Cover Page

The handle http://hdl.handle.net/1887/33101 holds various files of this Leiden University dissertation

Author: Kazandjian, Mher V.
Title: Diagnostics for mechanical heating in star-forming galaxies
Issue Date: 2015-06-03

Diagnostics for Mechanical Heating in Star-forming Galaxies

Mher V. Kazandjian

Diagnostics for Mechanical Heating in Star-forming Galaxies

Proefschrift

door

Mher V. Kazandjian
geboren op 6 April 1983
te Beiroet, Libanon

Promotiecommisie

Table of Contents

I

Introduction

Matter between the stars occupies most of the volume of galaxies and it is referred to as the interstellar medium (ISM). The ISM comprises mainly of gas and dust. Part of the remaining volume is occupied by stars. In addition to these, it is believed that dark matter is a major component of a galaxy, but we will not refer to it in this thesis. Interstellar gas densities range from 10^{-3} cm^{-3} at the outer edge of a galaxy near the intergalactic medium (Bregman 2007), up to 10^{10} cm^{-3} in proto-planetary disks (Mac Low & Klessen 2004). However, most of this gas is in the 0.3 to 30 cm^{-3} range (Draine 2010).

The ISM represents about 10% of the total mass of a spiral galaxy. On average 1% of the mass of the ISM is in the form of dust. Different densities and thermal conditions are found in the ISM. Various phases have been recognized in the ISM (Wolfire et al. 1995, Tielens 2005, Snow & McCall 2006). The properties of these phases are summarized in Table-1.1. The subject of study in this thesis will be the molecular ISM.

Stars are easy to observe since they emit brightly in the visible range of the electromagnetic spectrum, but detection of the gas is not as easy. The various species can be detected and distinguished by analyzing the emission or absorption spectra of the various transitions among their discrete quantum states. In order for the emission of the gas to be observed, the species in the gas should be excited, so that the various transitions among these internal states can occur; eventually the photons emitted from these transitions are detected by our telescopes. To give a general idea of the sizes of the objects involved: the typical length scale of a galaxy is on the order of 10 to 100 kpc whereas the sizes of molecular clouds, where star formation occurs, range between 0.1 and 100 pc.

phase	density (cm^{-3})	temperature (K)	volume filling factor
Hot ionized medium	$\sim 3 \times 10^{-3}$	$\sim 5 \times 10^5$	$0.5^{\dagger}$
Warm ionized medium	~ 0.3	$\sim 10000 - 8000$	0.1
Warm neutral medium	~ 0.3	~ 8000	0.4
Cold neutral medium	~ 30	~ 50	0.01
Diffuse molecular clouds	$> 100 - 500$	$\gtrsim 25 - 100$	$\sim 10^{-3}$
Dense molecular clouds	$> 10^4$	$\gtrsim 10 - 50$	$< 10^{-4}$

Table 1.1 – Typical gas densities and kinetic temperatures of the phases of the ISM (Tielens 2005, Draine 2010).
† The volume filling factor for this phase of the ISM is uncertain (Draine 2010).

1.1   Chemistry and radiation

Most of the gas of the ISM is in the form of ionized hydrogen, HII, in the hot and warm ionized media. Neutral hydrogen, HI, is found in the warm neutral and the cold neutral media (labeled with the acronyms CNM and WNM, respectively, see Table-1.1). H is the simplest species in the ISM and it is the essential ingredient to form molecular hydrogen H_2. The formation of H_2 takes place mostly on the surface of dust grains (Gould & Salpeter 1963). Regions of the interstellar medium where the bulk of hydrogen is in the form of H_2 are known as molecular clouds. H_2 does not have a permanent electric dipole moment, since it is formed of two identical H atoms. Thus, it can not emit due to $\Delta J = \pm 1$ transitions, which are strictly forbidden. On the other hand H_2 does have a quadrupole moment which allows for $\Delta J = \pm 2$ transitions. The energy of these transitions is quite high, the least energetic of which is the $J = 2 - 0$ with $E/k_b = 512$ K, which renders its emission too weak in environments such as molecular clouds where the temperatures are too low (Shull & Beckwith 1982, Stahler & Palla 2005). The molecular ISM is mostly cold (~ 10 K) and dense (see Table-1.1), hence the gas is prone to gravitational instabilities which induce the clumpy and filamentary structure in the molecular ISM (Larson 1981, Falgarone & Phillips 1990, de Vega et al. 1996); it is believed that stars are born in these unstable regions. To have a good understanding of the overall mechanisms regulating galaxy formation and evolution it is essential to have a deep knowledge of the underlying physics and chemistry of star-forming regions.

Visible light in molecular clouds is highly obscured by dust. Infrared radiation emitted by the dust in these clouds can penetrate large column densities of H_2 (N(H) $\gtrsim$ 10^{24} cm^{-3}) and is used instead of visible light to study star forming regions.

The far-ultraviolet (FUV) radiation (6 < E < 13.6 eV) of stars heats the gas surrounding them and excites the internal energy levels of H gas. Regions of the ISM which are dominated by such radiation and where the gas changes from ionized to neutral to molecular are called "photon-dominated regions" (Tielens & Hollenbach 1985). A schematic diagram of a typical PDR showing the important chemical transitions, is shown in Figure-1.1
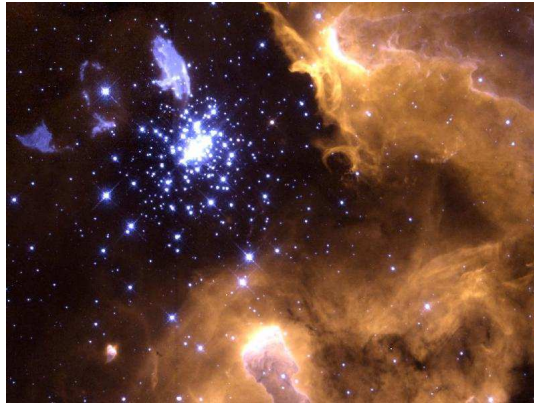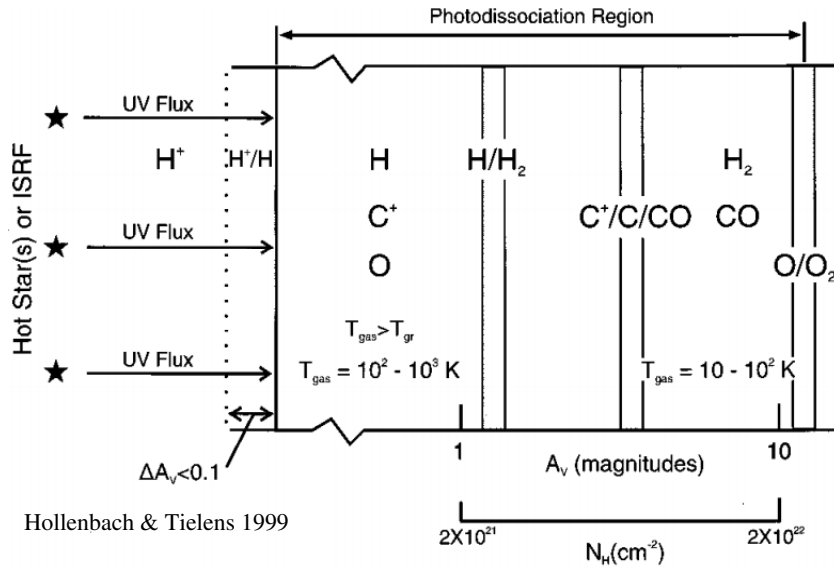
Figure 1.1 – *Top*: schematic diagram of a PDR; *bottom*: HST image of the nebula NGC 3603. NASA, Wolfgang Brandner (JPL/IPAC), Eva K. Grebel (Univ. Washington), You-Hua Chu (Univ. Illinois Urbana-Champaign)

In PDRs the surface layer of the clouds is heated by FUV and ionized by extreme ultraviolet (EUV, 13.6 eV < E < 0.1 keV) photons. The flux of these photons is rapidly attenuated at greater columns of hydrogen (N(H)), where the temperatures decrease. As the kinetic temperature decreases, ionized hydrogen, H^+, recombines with free electrons to form neutral hydrogen, HI. At higher column densities HI is transformed into H_2 via gas-grain processes. The dust catalyzes the formation of H_2 via a three-body process, two HI atoms and the dust grain. An HI atom has a certain probability of sticking on the surface of a dust grain. Once on the surface, it can recombine with another HI atom

3

which is also wandering on the surface to form H_2, which then leaves the surface of the grain (Gould & Salpeter 1963). In fact, the direct recombination of two hydrogen atoms in the gas phase is a very slow process compared to the three-body processes[1]. In the shielded region of the cloud, where the flux of FUV photons is progressively more diluted relative to the surface, molecular species other than H_2 form. Many species have been detected: see for instance the review by Tielens (2013). Most commonly observed in the sub-millimeter and the infrared wavelengths are species such as CO, ^{13}CO, HCN, HNC, HCO^+, CS, CN, SiO, H_2O, where CO is the most abundant species. The energy levels of these species are excited by collisions with H_2 (para- and ortho-) in addition to H, He, H^+, e^-. It should be noted that excitation due to the collisions with the last two partners is less significant in the shielded region of the PDR because of the low ionization fraction in these environments (Tielens & Hollenbach 1985), and is relevant in environments with enhanced ionization due to for example X-rays (Maloney et al. 1996b) or cosmic rays (Papadopoulos 2010). The excited population levels eventually tend to decay to lower energy states by spontaneous radiative emission. The densities of the colliding species necessary to excite the higher transitions and consequently to enable emission to be observed depend on their radiative properties. At local thermal equilibrium (LTE) the population densities of the levels between which the transition occurs are determined by the partition function. Usually LTE population densities are achieved whenever the density of the colliding species $>> n_{crit}$, where n_{crit} is the critical density defined as $n_{crit} \equiv A_{ij}/K_{ij}$ (cf. Tielens 2005); K_{ij} is the collisional rate coefficient of the transition from the ith to the jth level and A_{ij} is the spontaneous de-excitation rate, the Einstein A coefficient[2]. Generally, the ISM is not in LTE because $n < n_{crit}$. Thus, a good knowledge of the intensities of the emission provides insight on the underlying physical excitation mechanisms of the species (van der Tak 2011).

The main heating mechanism in PDRs is photo-electric heating, which is the heating of the gas due to the photo-electric effect on dust grains. Electrons ejected due to absorption by FUV photons in these grains collide elastically with the gas and heat it up (Bakes & Tielens 1994). This is the mechanism through which the gas, the FUV radiation and the dust are coupled to each other. In this thesis we do not focus on modeling HII regions since the medium is fully ionized and no molecules are present; this renders HII regions irrelevant for the molecular emission we are interested in. Cosmic rays can also play an important role in the heating of the gas in the UV-shielded region of the cloud. It has been proposed that the cosmic ray ionization rate in extreme star-burst regions could be as high as 10^4 times the ionization rate of the solar neighborhood (Papadopoulos 2010, Meijerink et al. 2011, Ao et al. 2013). These regions are referred to as cosmic-ray dominated regions (CRDRs). Moreover, in active galactic nuclei, X-ray heating is also potentially important. Similar to cosmic rays, energetic X-rays can penetrate through large columns of HI and H_2 ($N(H) \gtrsim 10^{24}$ cm^{-3}) and heat up the gas in the regions where FUV photons

---

[1] In the chemistry of the early Universe, the only channel for the formation of H_2 are gas phase reactions, in particular the so-called H_2^+ and H^- channels (Abel et al. 1997, Galli & Palla 1998, Lepp et al. 2002, Coppola et al. 2011). The former consists on the charge transfer between H_2^+ and H and the latter is represented by the associative detachment of H and H^-

[2] See Krumholz 2007 for the modified definition of the critical density which takes self-shielding into account

4
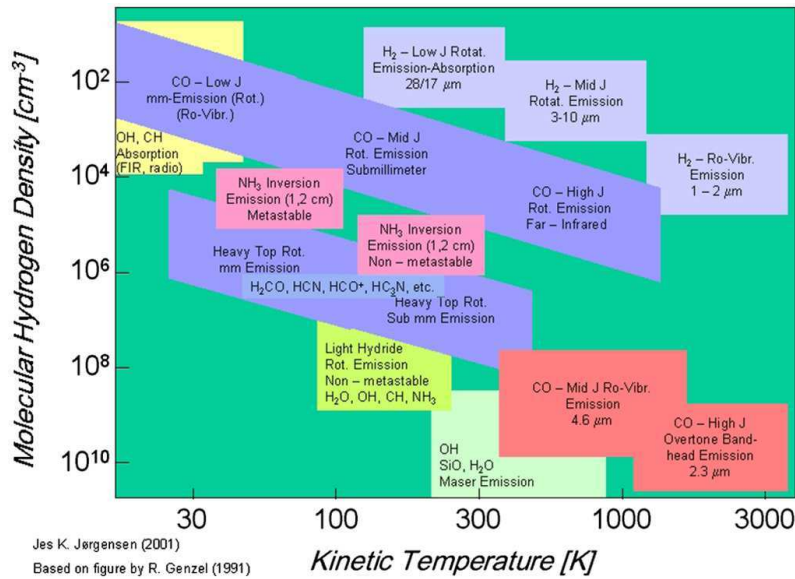
Figure 1.2 – Temperatures and density ranges in the ISM probed by some molecular lines. This diagram is taken from Tielens (2013) which in turn is a modified version from Genzel (1991) and is provided by Jes Jørgensen.

are shielded. These regions are referred to as X-ray dominated regions (XDRs: Maloney et al. 1996a, Bradford et al. 2003, Meijerink & Spaans 2005, Papadopoulos et al. 2011, Bayet et al. 2011, Meijerink et al. 2011). Unlike a PDR where the thermal and chemical properties vary steeply as a function of the column density of H_2 (see left panel of Figure-1.1), in XDRs and CRDRs a decrease in temperature and ionization is realized throughout these regions. In addition to the three excitation mechanisms discussed above, we will demonstrate in this thesis that mechanical feedback plays an important role in the thermal budget of PDRs which are at chemical and thermal equilibrium. So far we have only mentioned the important heating mechanisms in PDRs. Thermal equilibrium is achieved through fine structure line cooling of atomic and ionized species; the most dominant of which are [CII] 158 μm and [OI] 63 μm line cooling (Kaufman et al. 1999). For example, observations of 29 extreme star-forming environments by Rosenberg et al. (2015) in the HerCULES survey reveal that [CII] 158 μm and [OI] 63 μm contribute up to $\sim 70\%$ of the far infrared emission of these galaxies, with a significantly lower contribution by CO (see Table-4 by Rosenberg et al. 2015).

The gas in the ISM can emit at different wavelengths depending on the difference in the energies of the levels involved in the transition. The most important transition types are summarized in Table-1.2.

For instance, the ionization of a hydrogen atom requires 13.6 eV ($\sim 160,000$ K), corresponding to photons in the EUV spectrum. On the other hand, transitions among

5

	Process	Energy [eV]	Example
Atoms			
	Ionization	$3 \rightarrow 25$ (first ionization)	
	Excitation	few$\rightarrow 10$	
	Spin-Spin (HI)	5.9×10^{-6}	
Molecules			
	Dissociation	few	4.5 eV for H_2
			11.2 eV for CO
	Vibration	$(10^{-3} \rightarrow 1)$ (infra-red)	1 eV for H_2
			0.27 eV for CO
	Rotation	$< 10^{-2}$ (micro-wave)	0.04 eV for H_2
			4.7×10^{-4} eV for CO

Table 1.2 – Energies for some specific chemical processes (Tielens 2005)

the quantum states of molecular species can be rotational, vibrational and electronic, or various combinations of these. These transitions obey selection rules, that allow for some of them to take place and forbid others. The energies of electronic transitions are on the order of a few eV. Thus, they can be used to probe gas with $T > 10,000$ K. In order to probe lower temperature gas, $T < 100$ K typical for molecular clouds, transitions with low energies must be considered, such as the CO(1-0) rotational transition which has an energy $E_{\mathrm{upper}}/k_b = 5.5$ K and a rest frame wavelength of 2.6 μm, placing it in the sub-mm regime of the electromagnetic spectrum. In Figure-1.2, the species commonly used to probe different ranges in density and temperature are shown.

1.2 Star formation, mechanical feedback and turbulence

The distribution of stellar masses is empirically described by a set of power-law functions, referred to as the initial mass function (IMF), which determines the probability of finding a star within a certain mass range. Stellar masses range from ~ 0.1 to ~ 100 M$_\odot$, where the IMF is a decreasing function of stellar mass (Salpeter 1955, Kroupa 2001). These very hot and very bright massive stars are (much) less numerous than low-mass stars. Although these form about 0.1% of the total stellar population, stars with $M \sim 100$ M$_\odot$ emit about 3×10^4 times more ionizing photons than stars of lower mass such as the Sun (Avedisova 1979, Sternberg et al. 2003). The ionizing photons from massive stars, particularly in star-forming and star-bursting regions[3], play a very important role in regulating the star formation rate. The pressure feedback from the photo-ionized gas around such stars may drive a thermal wind that can diminish the accretion due to the self-gravity of molecular gas, thus reducing the star formation efficiency and in some extreme cases halting the process of forming new stars (see review by Krumholz 2015).

---

[3] Star-bursting regions are regions where the star formation rate is very high > 1 M$_\odot$ yr^{-1} (e.g. Gao & Solomon 2004), compared to the mean estimate of 0.3 M$_\odot$ yr^{-1} in our galaxy (Robitaille & Whitney 2010).

Massive stars are also important because they are very short lived. They detonate as supernovae liberating typically 10^{51} ergs per event (Norman & Ferrara 1996). The shock waves of the blast propagate in its surrounding molecular gas, disturbing the ISM and inducing turbulence and providing mechanical feedback (see review by Mac Low & Klessen 2004). A few percent of the energy of a supernova is re-absorbed by the ISM which is heated up. FUV radiation in PDRs, X-rays in XDRs and cosmic rays in CRDRs heat and ionize the ISM locally, where the efficiency of the heating decreases for increasing column densities of H; this attenuation is less efficient for cosmic rays. The main difference between these three types of regions of the ISM, and regions that are mechanically heated by, e.g., supernovae, is that shocks and turbulence in the latter heat the ISM globally on larger scales down to the smallest scales, few pc and up to a kpc. In this thesis, we study the influence of increasing amounts of turbulent heating on the chemical and radiative properties of the ISM in a statistical manner.

1.3 Modeling

The modeling of the physical and chemical processes taking place in a galaxy and the comparison of the results to observations represents a major challenge. While the modeling of self-gravitating systems is a relatively well-defined problem, the hydrodynamic modeling with various cooling, heating and chemical processes is not. For instance, uncertainties in the reaction rates of chemical pathways for the formation and destruction of species affect the solution of the ordinary differential equations that describe the time evolution of the fractional abundances. As a consequence, the cooling and heating mechanisms can easily be either under- or over- estimated. Moreover, since about one per cent of the ISM by mass is composed of dust, all the major gas-phase and gas-grain reactions should be taken into account in order to properly describe the chemistry. The fast formation rate of H_2 required for its high abundance in the ISM was explained by Gould & Salpeter (1963), who showed that dust catalyzes the reaction of HI on the surface of grains that have a temperature in the range of 5 K – 20 K. The formation efficiency of H_2 on grain surfaces is close to unity for $T_{kin} < 20$ K. It decreases to $\sim 0.1 - 0.2$ for $T_{kin} \sim 500$ K which is still efficient for astrophysically relevant conditions in the ISM (Cazaux & Tielens 2002, 2004).

Another more practical challenge in self-consistent realistic modeling of molecular clouds is the computing times (CPU time) presently required. There have been many attempts of understanding the evolution of molecular clouds, but resolved galaxy-scale self-consistent simulations treating the chemical, radiative transfer and thermal processes accurately and simultaneously require prohibitively long CPU time.

1.4 The inverse problem and diagnostics

Recovering the physical conditions of the gas of the ISM can be thought of as an inverse problem; where given information on the emission, for example, the observed spectra,
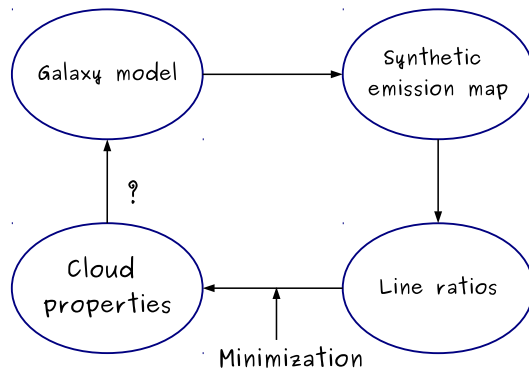
7

Figure 1.3 – Flow chart diagram of the procedure with which observations are matched to model predictions; The quantity minimized in recovering the "cloud parameters" from the "line ratios" is particular to the approach of this thesis. Any other quantity of interest can be minimized in-order to match the model predictions to the observations.

the challenge is to reconstruct the physical conditions of the gas that have given rise to the observed emission. Unlike the forward modeling process, the inverse problem is not uniquely defined; it tends to suffer from various degeneracies. The general scheme of the modeling procedure is presented in Figure-1.3, where model (or synthetic) emission are computed and compared to observed line ratios for an idealized galaxy; eventually individual cloud properties are recovered.

Computation of the synthetic maps involves the solution of a radiative transfer problem, for an assumed chemistry. The physics and chemistry incorporated in the modeling provide us with different amounts and levels of information, depending on the sophistication of the models and the degree of information and detail with which a galaxy or cloud is studied. For instance, using large-velocity-gradient (LVG) models of the line emission, various authors (e.g. Sobolev 1960, Henkel et al. 1983, Jansen et al. 1994, Hogerheijde & van der Tak 2000, van der Tak et al. 2007, Krumholz 2014) have shown that it is possible to constrain the gas temperature, the density of H_2, the velocity gradient, and the column density of the species emitting the observed radiation. However, the parameters driving the underlying physics, such as the FUV flux, are not easily constrained using only LVG modeling, and abundances must be assumed in order to derive the mass of the molecular gas. In-order to constrain the FUV flux, in star-forming regions, PDR modeling is usually used where the FUV flux is an important source of heating. Observations of luminous (LIRGS: L_{IR} (8-1000 μm) ~ 10^{11} $L_\odot$) and ultra-luminous (ULIRGs: L_{IR} ~ 10^{12} $L_\odot$) infra-red galaxies, that are a sub-class of star-forming galaxies, can not be modeled using PDR models alone, since PDR models are not able to fully match the observed atomic and molecular line intensity ratios (e.g. Loenen et al. 2008). XDRs models provide an alternative approach in modeling the emission of LIRGS and ULIRGS in a more satisfactory manner (e.g. Meijerink et al. 2007) but in some cases these models are not consistent with

the required X-ray fluxes in AGN (for e.g. Maloney et al. 1996b, Papadopoulos 2010, Meijerink et al. 2011, Rosenberg et al. 2014a,b).

In this thesis we explore how mechanically heated PDR models can be used to solve this problem by matching the observed line ratios. We will also use such models to constrain the amount of mechanical heating needed and find a diagnostic for it.

1.5 Thesis outline

The work presented in this thesis is divided into two parts. In the first part a parametric study of PDRs is performed to probe the effect of mechanical heating under different physical conditions and to identify possible diagnostics for mechanical feedback. In the second part, the PDR models of this parametric study are applied to galaxy models to produce emission maps of molecular species and analyze them. More specifically, the work done in each chapter is as follows.

In **Chapter 2** the effect of mechanical heating on the thermal and chemical properties of PDRs is investigated; in particular, the effect on the kinetic temperature of the gas, abundance, column density, as well as column density ratios of the molecular species CO, HCN, HNC, HCO$^+$ and H$_2$O are studied.

We solve the equilibrium state of all model clouds by using the Leiden PDR-XDR code developed by Meijerink & Spaans (2005). In this code the PDR region irradiated from one side by a FUV source is discretized into 1D semi-infinite parallel zones (slabs). The chemical and thermal properties of the zones are solved for iteratively at equilibrium. An escape probability formalism is used to treat the radiative transfer through the discretized slabs. The full internal details of the code are described by Meijerink & Spaans (2005) and the optimization details are discussed in the methods section of Chapter 2. Most possible conditions of the interstellar medium relevant to galaxies are covered by the parameter space of the PDR models. The grids of the models include hydrogen gas density ($1 < n < 10^6$ cm^{-3}), FUV radiation field ($0.32 < G_0 < 10^6$) measured in so-called Habing units, G_0, and mechanical heating rate ($10^{-24} < \Gamma_{mech} < 10^{-16}$ erg cm^{-3} s^{-1}).

The chemical and thermal properties of clouds determine the radiation emanating from them. In **Chapter 3** we extend the work done in the previous chapter by investigating the effect of mechanical heating on atomic and molecular lines, and their ratios. We try to use those ratios as a diagnostic to constrain the amount of mechanical heating in a region and also study its significance on estimating the H$_2$ mass. The emission of the PDR grids are computed assuming the Large Velocity Gradient approximation where the equilibrium state of the PDR models is used as input to RADEX (van der Tak et al. 2007) where the emission is computed in post-processing mode.

Emission of CO(1-0) is ubiquitously detected in galaxies and is commonly used to estimate the molecular mass in a galaxy or giant molecular cloud (Solomon et al. 1987, Bolatto et al. 2013, and references therein). In **Chapter 4**, we study the effect of mechanical heating on diagnostic line ratios of CO and ^{13}CO in model galaxies. In particular we determine whether these diagnostic line ratios can be used to probe the presence and constrain the magnitude of mechanical heating in actual galaxies. We make use of the PDR

models of Chapter 3 and apply them to the gas of a simulated disk and dwarf galaxy in post-processing mode and produce emission maps for the rotational transitions of the CO molecule and its ^{13}CO isotopologue up to $J = 4 - 3$. The disk and dwarf galaxies are simulated using solar and 1/5 solar metallicities. The emission maps of these model galaxies are used to compute line ratio maps of the CO and ^{13}CO transitions. These maps are used to illustrate the effect of mechanical feedback on the physical parameters obtained from the molecular line intensity ratios.

In **Chapter 5** we extend the work of the previous chapter to species other than CO and ^{13}CO. We include rotational transitions with critical densities $n \gtrsim 10^4$ cm^{-3}, for instance $4 - 3 < J \leq 15 - 14$ transitions of CO and ^{13}CO, also $J \leq 7 - 6$ transitions of HCN, HNC and HCO$^+$. In this chapter, we focus only on the disk galaxy, where the density field of the interstellar medium of the model galaxy is re-sampled to account for the lack of resolution and for the emission of gas with densities $> 10^3$ cm^{-3}. The re-sampling is done by assuming that the probability density function (PDF) of the density is a log-normal function inferred from the resolved low density scales. Following a similar approach as in Chapter 4, we fit the line-ratios of the synthetic emission maps for the central 2 kpc of the galaxy using one model PDR.

Furthermore, in the second part of this chapter, we investigate the impact of different log-normal density PDFs on the distribution of the luminosity as a function of density. The aim of this exercise it to check the conditions under which significant emission is obtained from gas with densities $n > 10^4$ cm^{-3}, and to test for the possibility of constraining the PDF using line ratios of high density tracers. In super-sonically turbulent clouds the Mach number, $\mathcal{M}$, is related to the dispersion of a log-normal distribution. We use this relationship to estimate the Mach number of the ISM by constraining the parameters of the density PDF using molecular line emission intensity ratios.

In the final chapter we put the work done in the thesis into the perspective of recent observations by the *Herschel* Space Observatory (Pilbratt et al. 2010) and discuss the importance and possible applications of our models to data obtained with Atacama Large Millimeter Array[4] (ALMA). We also discuss the major caveats of our present modeling and ways of improving future modeling, the limitations and some estimates on the requirements for improved modeling of the chemistry and the radiative transfer.

---

[4] http://www.almaobservatory.org/

II

Diagnostics of the Molecular Component of PDRs with Mechanical Heating

Multitransition CO observations of galaxy centers have revealed that significant fractions of the dense circumnuclear gas have high kinetic temperatures, which are hard to explain by pure photon excitation, but may be caused by dissipation of turbulent energy. We aim to determine to what extent mechanical heating should be taken into account while modeling PDRs. To this end, the effect of dissipated turbulence on the thermal and chemical properties of PDRs is explored. Clouds are modeled as 1D semi-infinite slabs whose thermal and chemical equilibrium is solved for using the Leiden PDR-XDR code, where mechanical heating is added as a constant term throughout the cloud. An extensive parameter space in hydrogen gas density, FUV radiation field and mechanical heating rate is considered, covering almost all possible cases for the ISM relevant to the conditions that are encountered in galaxies. Effects of mechanical heating on the temperature profiles, column densities of CO and H_2O and column density ratios of HNC, HCN and HCO^+ are discussed. In a *steady-state* treatment, mechanical heating seems to play an important role in determining the kinetic temperature of the gas in molecular clouds. Particularly in high-energy environments such as starburst galaxies and galaxy centers, model gas temperatures are underestimated by at least a factor of two if mechanical heating is ignored. The models also show that CO, HCN and H_2O column densities increase as a function of mechanical heating. The HNC/HCN integrated column density ratio shows a decrease by a factor of at least two in high density regions with $n \sim 10^5 \, \text{cm}^{-3}$, whereas that of HCN/$HCO^+$ shows a strong dependence on mechanical heating for this same density range, with boosts of up to three orders of magnitude. The effects of mechanical heating cannot be ignored in studies of the molecular gas excitation whenever the ratio of the star formation rate to the gas density (SFR / $n^{3/2}$) is close to, or exceeds, $7 \times 10^{-6} \, \text{M}_\odot \, \text{yr}^{-1} \, \text{cm}^{4.5}$. If mechanical heating is not included, predicted column densities (such as those of CO) are underestimated, sometimes (as in the case of HCN and HCO^+) even by a few orders of magnitude. As a lower bound to its importance, we determined that it has non-negligible effects already when mechanical heating is as little as 1% of the FUV heating in a PDR.

M. V. Kazandjian, R. Meijerink, I. Pelupessy, F. P. Israel, M. Spaans

2.1 Introduction

Radiation originating from the molecular gas in various galaxy environments, including galaxy centers, provides information about the physical state of these environments such as the gas mass and temperature, or the source of its excitation. The far-ultraviolet radiation (FUV; $6.0 < E < 13.6$ eV) emitted by newly formed luminous stars and X-rays ($E > 1$ keV) produced by black hole accretion have very distinct effects on the thermo-chemical balance of the gas. Strong FUV illumination results in so-called photon-dominated regions (PDRs; Tielens & Hollenbach (1985)), while X-ray irradiation creates X-ray dominated regions (XDRs; Maloney et al. (1996b)). In PDRs and XDRs, the thermal and chemical structure is completely determined by the radiation field, and directly reflects the energy balance of the interstellar gas. For example, in PDRs the CO is generally much cooler (T~ 10-30 K) than in XDRs ($T \sim 20-500$ K), therefore XDRs generally exhibit CO emissions to much higher J levels. Thus, observations of the CO ladder allow us to discriminate between the different types of radiation fields.

Recently, it has become clear that PDR and XDR excitation is not sufficient to fully explain observed molecular line emission ratios. For instance, Loenen et al. (2008) have found that the HCN, HNC, and HCO$^+$ line ratios observed towards (ultra-)luminous infrared galaxies span a parameter space that cannot be reproduced by models in which FUV or X-ray radiation dominates. In their study they showed that an additional heating mechanism is required, which they suggest to be mechanical heating caused by dissipating supernova shocks, injected on large scales and cascading down through turbulent dissipation to the smallest scales. More recently, Papadopoulos (2010) has suggested that cosmic ray ionization rates in such galaxies may exceed those measured in the Milky Way by factors of 10^3 to 10^4, hence significantly affect the ionization balance and thermal-chemical structure of interstellar clouds. The effects of high cosmic ray rates on ISM chemistry is studied in detail by Meijerink et al. (2011) (who consider mechanical heating as well only for selected models) and Bayet et al. (2011).

However, neither the models by Loenen et al. (2008) nor those by Meijerink et al. (2011) treat mechanical heating self-consistently, as it is only implemented as an additional heating term and not as feedback from hydrodynamics. The dynamical evolution of the interstellar medium in galaxies in general and close to a super-massive black hole in particular, has been studied in 3D hydrodynamic simulations (Wada & Norman 2002, Wada & Tomisaka 2005) but these in turn lacked chemistry, and line emission maps of the various molecules were created by using constant abundances. A study by Pérez-Beaupuits et al. (2011) improved on this by using chemical abundances obtained from the Meijerink & Spaans (2005) XDR code. Nevertheless, these simulations still lack FUV input and feedback from the hydrodynamics on the chemistry still needs to be done self-consistently.

The dominant coolants in the ISM which are commonly observed are the [CI] 609 μm, [CII] 158 μm and the [OI] 63 μm lines. These fine-structure lines are not sensitive to additional mechanical heating, when the clouds are already illuminated by FUV radiation Meijerink et al. (2011). This is in contrast to the molecular species that are formed in regions of the cloud, that are shielded from irradiation. Thus, in this paper we consider

molecular species as possible candidates for tracing regions which are dominated by mechanical heating. Although a simple dust model is taken into account (Meijerink & Spaans 2005), dust diagnostics are not discussed since these diagnostics are out of the scope of this paper. We will explore the possible tracers in a number of steps. In this paper, we will first establish under which physical conditions mechanical heating is important. We will estimate what range of mechanical heating rates we may expect for the different densities in the ISM. We will then determine how this affects the thermo-chemical balance in the models, and, by way of first application, discuss the effect on the integrated column densities of common molecular species such as CO, H_2O, HNC, HCN and HCO^+, and some of their ratios. In subsequent papers, we will calculate line emission maps that can be compared directly to the detailed observations obtained with (sub)millimeter telescopes, notably the Atacama Large Millimeter Array. Ultimately, our aim is to couple chemistry and hydrodynamics in order to treat the relevant physical effects in a self-consistent manner.

2.2   Methods

We solve the equilibrium state of all model clouds by using an optimized version[1] of the Leiden PDR-XDR code developed by Meijerink & Spaans (2005) (Details of the optimization and further improvements are mentioned in Sect. 2.2.2). In its present form, the code assumes a 1D PDR geometry where various heating and cooling processes are included in solving for the thermal and chemical balance. The radiative transfer for the cooling lines and the escape probabilities are computed based on the work by de Jong et al. (1980). We refer the reader to Meijerink & Spaans (2005) for further details on the thermal processes and chemical network used in solving for the steady state equilibria.

2.2.1   Parameter space and reference models

In order to reduce the number of free parameters, we considered three metallicity levels, the benchmark being $Z = Z_\odot$ (solar metallicity) to which we added $Z = 0.5Z_\odot$ (characteristic of moderately metal-poor dwarf galaxies) and $Z = 2Z_\odot$ (characteristic of spiral galaxy center conditions). Throughout the paper, our discussion concentrates on the $Z = Z_\odot$ models[2]. For the cosmic-ray ionization rate, we adopted the value $5 \times 10^{-17} s^{-1}$ used in Meijerink & Spaans (2005) which is close to that in the solar neighborhood. The grids consisted of models spanning a wide range of physical conditions, uniformly sampled (in $\log_{10}$ scale) in ambient gas density $1 < n < 10^6 \, cm^{-3}$, incident radiation field $0.32 < G_0 < 10^6$ and mechanical heating $10^{-24} < \Gamma_{mech} < 10^{-16} \, erg \, cm^{-3} \, s^{-1}$. In the absence of mechanical heating, n and G_0 dominate the characteristics of a PDR. The ambient gas density n is the total number density of hydrogen nuclei, which is set constant throughout the slab. The values considered cover the full range of densities encountered in the diffuse interstellar medium to those of dense molecular cloud cores. The incident

---

[1] The optimized code is called PDR-XDR-1.1

[2] The analogous grids for the other two metallicities are presented in the Appendix

FUV radiation field G_0 is measured in so-called Habing units (Habing 1969) correspond-ing to 1.6×10^{-3} erg cm^{-2} s^{-1}. The values considered here include radiation fields ranging from only a few times stronger than the relatively low solar neighborhood field to the in-tense fields irradiating clouds close to young OB associations; the upper limit corresponds to the radiation field intensity at a distance of about 0.1 pc from an O star.

In constraining a physically relevant range of mechanical heating rates, we took a combination of values recovered from softened particle hydrodynamics simulations (SPH hereafter; Pelupessy 2005), and added estimates of mechanical heating rates induced by turbulence caused by supernova shocks that are dissipated in the ISM (Loenen et al. 2008). The SPH simulations are of dwarf galaxies with n up to $\sim 10^3$ cm^{-3} where the mechan-ical heating rates ranged from $\sim 10^{-30}$ to 10^{-22} erg cm^{-3} s^{-1} for such densities. When naively extrapolated to densities of 10^6 cm^{-3}, rates up to 10^{-18} erg cm^{-3} s^{-1} are expected. In the Loenen et al. (2008) recipe, it is assumed that $\eta = 10\%$ of the supernova blast energy ($E_0 = 10^{51}$ erg per SN event) is absorbed throughout the continuous starburst re-gion (a region which by definition sustains a considerably high SFR, which is steady, by consuming the available gas), whose size is taken to be $D_{SB} = 100$ pc. Eq. 2.1, which is a combination of Eq. 3 and 4 in Loenen et al. (2008), relates Γ_{mech} to the supernova rate (SNR).

$$\Gamma_{mech} = \frac{SNR E_0 \eta}{V_{SB} V_{PDR} n_{PDR}} \qquad (2.1)$$

where V_{SB} is the volume of the starburst region, whereas V_{PDR} and n_{PDR} are the volume and number density of PDRs in that starburst region respectively. They also assumed that the absorbed energy is distributed evenly among the PDRs in this starburst region. The number of the PDRs in the starburst region is estimated by assuming a gas density contrast of 10 (the inverse of the filling factor) between that of the PDRs and the ambient ISM of the starburst. Considering a Salpeter IMF for the stellar population, the star formation rate (SFR) is related to the SNR via SNR/SFR = 0.0064 (see Dahlén & Fransson 1999). In computing the SNR, they assumed that stars with $M > 8$ M$_\odot$ end up as supernovae (see Loenen et al. 2008 for more details on the estimates and assumptions). A Kroupa (2001) IMF, over the mass range from $0.1 M_\odot$ to $125 M_\odot$ considered, would result in a marginally higher SNR/SFR ~ 0.01. This higher rate reflects a slightly enhanced mechanical heating rate. However, the difference in the resulting Γ_{mech} between both IMFs over the same mass range is $\sim 40\%$, thus for simplicity we adopted the Salpeter IMF.

By way of example, a mechanical heating rate Γ_{mech} of 2×10^{-20} erg cm^{-3} s^{-1} is expected in a quiescent disc, such as that of the Milky Way with an SFR ~ 1 M$_\odot$ yr^{-1} and a SNR of ~ 0.01 yr^{-1} . In regions with active star formation (SFR~ 50 M$_\odot$ yr^{-1} and SNR~ 0.3 yr^{-1}) the mechanical heating rate is much higher, $\Gamma_{mech} = 1 \times 10^{-18}$ erg cm^{-3} s^{-1} . For extreme starbursts with (SFR~ 1000 M$_\odot$ yr^{-1} and SNR~ 6.4 yr^{-1}) mechanical heating rates $\Gamma_{mech} = 2 \times 10^{-17}$ erg cm^{-3} s^{-1} are possible. Another source of mechanical energy input is the outflows of young stellar objects (YSOs). The outflow phase is short-lived, and as discussed by Loenen et al. 2008 a nearby dense cloud ($n > 10^5$ cm^{-3}) is required for a significant amount of energy to be absorbed by the surrounding ISM (compared to the mechanical heating due to supernovae). Hence energy input due to

YSOs is ignored in this study. Based on a similar order of magnitude estimate, mechanical energy input due to stellar winds are also ignored, since they would contribute up to 6% to the total mechanical heating (Pelupessy 2005, Leitherer et al. 1999).

It is of interest to determine the effects of mechanical heating by comparing the results obtained from models with and without a mechanical heating term. To this end, we have selected from the grids calculated for analysis and discussion in this paper the same reference models that were studied in detail by Meijerink & Spaans (2005) without taking into account mechanical heating. These models are summarized in Table 2.1.

Model Name	$\log n$ (cm^{-3})	$\log G_0$
M1	3.0	3.0
M2	3.0	5.0
M3	5.5	3.0
M4	5.5	5.0

Table 2.1 – Parameters of the reference models. These are identical to the ones in Meijerink & Spaans (2005). M1 and M2 correspond to low density clouds in galactic centers in the presence of a starburst event, whereas M3 and M4 correspond to much denser clouds where excitation of high density gas tracers such as HCN is possible.

In this first exploration, Γ_{mech} is added per unit volume. In doing so for a certain grid, each model in the $n - G_0$ parameter space has an extra Γ_{mech} added to its heating budget. Another choice could have been the addition of Γ_{mech} per unit mass, where for a certain grid the amount of added mechanical heating would be proportional to the gas density of the model in the grid. For simplicity we considered adding mechanical heating per unit volume.

2.2.2 Numerical schemes

Finding the thermal and chemical equilibrium for each slab is an $(N + 1)$-dimensional numerical root finding problem. N being the number of species (atomic and molecular species and electrons) in the chemical network in addition to the thermal balance. It involves solving the set of non-linear equations Eqs. 2.2 and 2.3.

$$d\mathbf{n}(T)/dt = \mathbf{0} \qquad (2.2)$$

$$\Gamma(T, \mathbf{n}) - \Lambda(T, \mathbf{n}, t) = 0 \qquad (2.3)$$

The first equation (chemical balance) is the rate of change of the density of the species at a certain temperature T. We solved for this vector equation of length N following the recipe by Tielens & Hagen (1982) in using the multi-dimensional Newton-Raphson method. The thermal balance is solved for in the second equation, where Γ and Λ are the total heating and cooling rates. These two terms are a 1D function of $\mathbf{n}$ (used as input from the previous equation) and T. This process is repeated iteratively until convergence with a tolerance of

15

10^{-6} for the chemical balance and 10^{-3} for the thermal balance. Two major improvements lead to a speed-up by a factor of ~ 30 over the original PDR-XDR code. These are (a) tweaking the LU decomposition (optimizing compiler flags and matrix elements storage scheme) used in the multi-dimensional Newton-Raphson root finding, and (b) using in the thermal balance root finding the secant method (with a convergence order of ~ 1.6) instead of the bisection method which has a linear convergence rate.

The distance from the surface of the cloud is measured in terms of the visual extinction (A_V) due to interstellar dust. It is related to the total column density of hydrogen nuclei N(H) according to Eq. 2.4 (Bohlin et al. 1978).

$$A_V = 5.34 \times 10^{-22} \, N_{\mathrm{H}} \, Z \, \mathrm{mag \, cm^{-2}} \tag{2.4}$$

Once the equilibrium state of the surface slab (with zero thickness) is solved for, the width of the remaining slabs is chosen adaptively while resolving the transition zone, which has large temperature gradients compared to the small temperature gradients at the surface of the slab and at high depths. This is also one of the changes over the original implementation. In choosing the slab width adaptively, the maximum allowed relative difference in the temperature between consecutive slabs was set to 5%. Smaller values were tested as well, where no significant difference was noticed.

It is assumed that the mechanical heating due to turbulence is absorbed by the ISM at all scales. Hence for simplicity Γ_{mech} is added *uniformly* throughout the cloud.

Molecular clouds may have a visual extinction up to 200 mag (Tielens & Hagen 1982). Beyond $A_V \sim 5$ mag most of the species become molecular whereas for $A_V > 10$ mag all abundances are almost constant since physical conditions do not change anymore. The maximum depth, we allowed for, in all the models, was $A_V = 20$ mag. This corresponds to N(H) $= 7.5 \times 10^{22}$, 3.7×10^{22} and 1.8×10^{22} cm^{-2} for metallicities of $Z = 0.5$, 1 and $2Z_\odot$ respectively. This enables us to compare clouds of different metallicities up to the same column density. In doing so, a fixed N(H) $= 1.8 \times 10^{22}$ cm^{-2} (the maximum N(H) for $Z = 2Z_\odot$) was adopted in the illustrations where column densities of molecular species were used.

For each value of mechanical heating and metallicity, 25×25 models equally spaced in $\log_{10} n$ and $\log_{10} G_0$ were calculated, up to a total of $\sim$16000 models. When there is no or very little mechanical heating, the temperature may drop below 10 K at a certain depth in the cloud. Since the code is designed to work for $10 < T < 10^4$ K[3], for slab elements where the lower limit is reached we solved the chemical network for a fixed temperature of 10 K. In making the convergence more robust, we built a small database of guess values (used as input in the root finding) for the surface slab. This enabled us to explore regions in the parameters where the original implementation failed.

---

[3] The lower bound in the temperature is set to 10 K since many reaction constants become inaccurate below that value (Röllig 2011). He and Fe$^+$ cooling become important above 10^4 K which make the thermal balance inaccurate since these are not included in the current version (in addition to other dielectronic recombination processes). But below 10^4 K, the contribution of these processes is negligible to the total cooling. Also for $T > 10^4$ K, the heating efficiency expression becomes inaccurate. However, not many models exceed 10^4 K, but we allowed that since it is needed to make the models converge as the solution is progressed into the cloud.

In running the models, an improved version of the PDR-XDR code was incorporated into the Astrophysical Multi-purpose Software Environment (AMUSE) framework. The AMUSE package allows astrophysical codes from different domains to be combined to conduct numerical experiments (see Pelupessy & Portegies Zwart 2012 for a more complete description). It is a development of the Multi-physics and Multi-scale Software Environment (MUSE, Portegies Zwart et al. 2009) and is freely available for download[4]. (The PDR code itself will be made available in the future). The interface to the Meijerink PDR-XDR code takes the main parameters G_0, n, Γ_{mech} as input and calculates the PDR equilibrium properties. This will allow the code to eventually be used as an equilibrium sub-grid model for,e.g., galaxy scaled hydrodynamic simulations. In the present work this feature is not used, only the capability to run many models in parallel is.

2.3 Results

In this section we present the comparisons for thermal and chemical diagnostics of the grids modeled with and without mechanical heating. We start by discussing the temperatures at the cloud surface, and at the maximum cloud depth considered since for a given model, the gas temperature to a large extent determines the chemical composition. Following this, we will discuss the statistical properties of the CO, H_2O, HCN, HNC and HCO^+ molecules which are important diagnostics for moderate and dense gas. Throughout this section, we use the reference models (M1 to M4) to illustrate the impact of mechanical heating on the properties of the PDRs as a function of depth.

2.3.1 Gas temperature

In the absence of other heating terms (such as due to mechanical heating) PDRs are characterized by rapid decreases in temperature, from ~1000 K at the surface down to ~10 K in regions where A_V exceeds 10 mag. Since mechanical heating may be expected to considerably change the temperature structure, we will first explore this.

2.3.1.1 Temperature at the surface

At the surface we only need to solve for the equilibrium of a single slab (with zero thickness). Because this can be done much faster than in the case of a full slab, a higher resolution is possible for the surface grids. These surface grids therefore consisted of 2500 (50 × 50) models uniformly sampled in $\log_{10} n$ and $\log_{10} G_0$. In Fig. 2.1 the surface temperature, without mechanical heating ($\Gamma_{\mathrm{mech}} = 0$ erg cm^{-3} s^{-1}), is shown for three different metallicities. The temperature contours are in good agreement with the profiles recovered by Kaufman et al. (1999) and Meijerink et al. (2007)(which uses the original implementation). We note that metallicity has little effect on the overall topology of the contour plots, except for regions where $G_0 > 10^4$, especially where $n > 10^4$ cm^{-3}. The temperature almost doubles as Z is increased from $Z_\odot$ to $2Z_\odot$, with no noticeable change between

---

[4] `www.amusecode.org`

$Z = 0.5 Z_\odot$ and $Z = Z_\odot$. This is because cooling scales as Z whereas the dominant heating term scales almost as Z for low n but increases to $\sim Z^2$ as n increases to 10^6 cm^{-3}. This temperature dependence on metallicity has also been observed by Röllig et al. (2006). It is worth noting that in the lower right-hand corner of the grid ($n > 10^{5.5}$ cm^{-3}, $G_0 < 5$) three equilibria were found, one unstable and two stable ones. The stable equilibria correspond to a low (~ 50 K) and a high temperature (~ 300 K) state with the unstable one in-between. Here we have shown the low-temperature equilibrium. In any case, we note that this part of the parameter space is not of physical relevance for systems that interest us here..
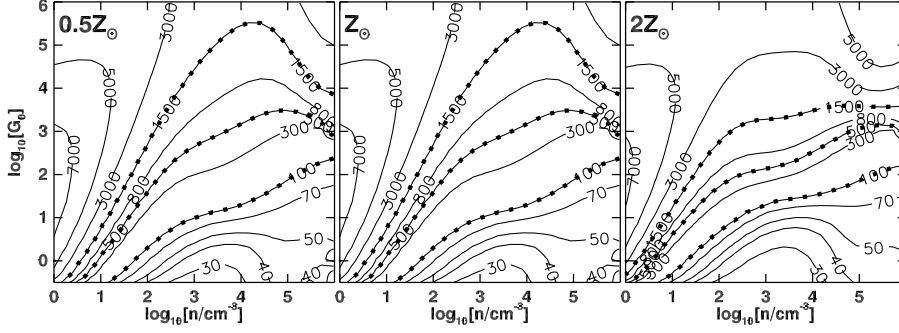

Figure 2.1 – Temperature profile (without mechanical heating) at the cloud surface for different metallicities. Generally, the temperature rises as a function of G_0 and constant n, since the dominant heating term is the photo-electric heating, which is proportional to G_0. However, the behavior for constant G_0 as a function of n is not as trivial. See Section 3.1 of Kaufman et al. (1999) and Section 3 of Meijerink et al. (2007) for more discussion of the topology of the contours. This version of the code covers a larger parameter range than Meijerink et al. (2007) . Solid lines with filled squares highlight the temperature contours for 100, 500 and 1500 K . The most significant change when comparing the three panels is for the 1500 K contour, where for $Z = 2Z_\odot$ higher temperatures are attained (compared to the lower metallicities) in the same part of the parameter space ($n > 10^3$ cm^{-3} , $G_0 > 10^4$) .

The dominant heating term at the cloud surface is photo-electric heating, where electrons ejected from the dust grains collide elastically with the gas and heat it. The typical efficiency (ϵ) of this process is quite low, 0.5 to 1%, with a maximum of $\sim 5\%$ (Black & Dalgarno 1977). The photo-electric heating rate (Γ_{photo}) at the surface is given by the expression (Bakes & Tielens 1994):

$$\Gamma_{\text{photo}} = 10^{-24} \epsilon G_0 n \text{ erg cm}^{-3}\text{s}^{-1} \qquad (2.5)$$

where ϵ depends on electron density (n_e), G_0 and gas temperature. The expression for ϵ is given in Eq-2.6 (Bakes & Tielens 1994).

$$\epsilon = \frac{4.87 \times 10^{-2}}{1 + 4 \times 10^{-3} \left(G_0 T^{1/2}/n_e\right)^{0.73}} + \frac{3.65 \times 10^{-2} \left(T/10^4\right)^{0.7}}{1 + 2 \times 10^{-4} \left(G_0 T^{1/2}/n_e\right)} \qquad (2.6)$$

18

Hence the log_{10} of Eq. 2.5 is linear in $\log_{10} n$ and $\log_{10} G_0$ whenever ϵ is constant. Fig. 2.2 shows the total heating in the $n - G_0$ plane. In the top part of the plot, the contours are almost straight lines. This is not surprising, Γ_{photo} accounts in most cases for more than 95% of the total heating budget. To illustrate this, we look at the logarithm of Eq. 2.5, which in expanded form becomes :

$$\log_{10} \Gamma_{photo} = -24 + \log_{10} \epsilon + \log_{10} G_0 + \log_{10} n \qquad (2.7)$$

which is linear in both $\log_{10} G_0$ and $\log_{10} n$. This means that the heating efficiency is almost constant wherever the contours are straight lines. This is not true in the regions below the break in the contour lines which occurs in the region under the $G_0 = n$ line in Fig. 2.2. In that part of parameter space, photo-electric heating is complemented by H_2 photo-dissociation heating. However, this is a small part of the total parameter space, so that we are justified in using photo-electric heating as a good approximation for the total heating. Hence, we expect total heating to have a linear dependence on $\log_{10} n$ for constant values of G_0. This is achieved by fitting horizontal cuts of Γ_{total} in Fig. 2.2 as a function of n for different values of G_0.
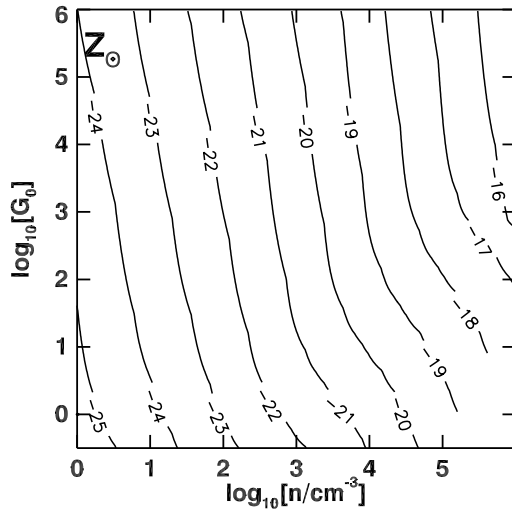
Figure 2.2 – Total heating at the cloud surface without mechanical heating. The main characteristic of this plot is that above the diagonal, the contours are parallel straight lines; whereas below the diagonal ($G_0 = n$ line), there is a break in the slope, indicating that photo-electric heating is no longer the dominant mechanism in that region. The minimum total heating is of the order of $10^{-25.5}$ erg cm^{-3} s^{-1} at the lower left corner and $10^{-15.2}$ erg cm^{-3} s^{-1} at the top right corner.

From the fits, we could see that the minimum surface heating for the lowest density gas considered ($n = 1$ cm^{-3}) ranges from $10^{-25.6}$ erg cm^{-3} s^{-1} (for low G_0) to $10^{-24.0}$ erg cm^{-3} s^{-1} (for high G_0). In contrast, the maximum surface heating for $n = 10^6$ cm^{-3}, is

$10^{-15.2}$ erg cm^{-3} s^{-1}. We also observe that the surface heating scales as $n^{1.21}$ for $G_0 < 10^2$ and $n^{1.55}$ for $G_0 > 10^4$.

The equilibrium temperature is expected to vary depending on the amount of extra heating introduced via Γ_{mech}. Following this simple assumption, we expect to have significant changes in the equilibrium temperature when Γ_{mech} is comparable to the total surface heating, with a varying impact on different parts of the parameter space. In order to determine the zone in the parameter space where Γ_{mech} alters the equilibrium state, we solve for n in Eq. 2.7 by equating it to Γ_{mech}. In other words, we solve for n in $\Gamma_{total,surface}(n) = \Gamma_{mech}$ for the range in Γ_{mech} we have considered in our parameter space. These solutions, n_c, listed in Table 2.2 mark the lines in the $G_0 - n$ plane where mechanical heating is the same as the total surface heating. To the left of these lines, $\Gamma_{mech} > \Gamma_{surface}$.

$\log_{10}[\Gamma_{mech}/\text{erg cm}^{-3}\,\text{s}^{-1}]$	-24	-22	-20	-18	-16
$\log_{10}[n_c/\text{cm}^{-3}]$	0.6	1.9	3.2	4.5	5.9

Table 2.2 – Estimated values of gas density, where clouds with lower densities (listed in the bottom row), the shape and equilibrium temperature of the contours of Fig. 2.1 are significantly effected by Γ_{mech} (top row). For $\Gamma_{mech} < 10^{-18}$ erg cm^{-3} s^{-1}, the fitting parameters for $\log_{10} G_0 = 2$ are used. For higher mechanical heating rates, those for $\log_{10} G_0 = 5$ are used since in that region of the parameter space Γ_{mech} is more relevant to high G_0.

In Fig. 2.3 the equilibrium temperature of the surface slab is shown for the range of Γ_{mech} that we consider. Regions, that are first affected by the mechanical heating input, are the ones where Γ_{mech} is comparable to the surface heating without mechanical input (see Fig. 2.2). This behavior can be traced by following the location of the dashed vertical lines (where $\Gamma_{mech} = \Gamma_{total,surface}$) and comparing the values of Γ_{mech} to the total surface heating contours in Fig. 2.3. It is clear that whenever the value of Γ_{mech} is comparable to the total surface heating, the temperature contours become almost vertical in the $n - G_0$ plane in Fig. 2.3. The locations where $\Gamma_{mech} = \Gamma_{total,surface}$ are marked by the dashed vertical lines where $n = n_c$ (see Table 2.2). For instance, in the first panel in Fig. 2.3 ($\Gamma_{mech} = 10^{-24}$ erg cm^{-3} s^{-1}), regions where temperatures increase significantly are when $\Gamma_{total,surface} < 10^{-24}$ erg cm^{-3} s^{-1}(see Fig. 2.3, and compare first panel in Fig. 2.3 to the middle panel in Fig. 2.1). Also we notice that the temperature increases from ~ 3000 K (for $G_0 \sim 10^2$) to ~ 10000 K at the density $n = n_c$, whereas it increases from ~ 5000 K (for $G_0 \sim 10^{5.0}$) to ~ 7000 K at the same density. This can be explained by the fact that heating at the surface is mainly due to photo-electric heating, thus as G_0 increases (for a fixed n), the amount total heating increases. Hence a fixed amount of mechanical heating would contribute less to the total heating budget, leading to a lower increase in the surface temperature. Subsequent panels in Fig. 2.3 which correspond to higher amounts of Γ_{mech} can be interpreted in the same fashion. The main feature of these panels is the shift in the position of the line marking $n = n_c$ towards higher densities. In the last panel where $\Gamma_{mech} = 10^{-16}$ erg cm^{-3} s^{-1} , the whole parameter space is dominated by mechanical heating.

Regions with a SFR of ~ 1 M$_\odot$ yr^{-1}are dominated by mechanical heating up to

densities of $\sim 10^3 \, \text{cm}^{-3}$. In Extreme starburst, where SFR of $\sim 1000 \, \text{M}_\odot \, \text{yr}^{-1}$ are possible, all clouds with $n < 10^{5.5} \, \text{cm}^{-3}$ become dominated by mechanical heating. In both cases, surface temperatures of $\gtrsim 5000 \, \text{K}$ are reached, and the temperature contours become independent of FUV heating.

2.3.1.2   Temperatures deep into the cloud

Now we turn our attention to the molecular region. The solution was terminated at $A_V = 20 \, \text{mag}$, where everything is molecular, well beyond $A_V \sim 1 \, \text{mag}$ where mainly atomic and radicals exist. As the FUV radiation penetrates the cloud, it is attenuated by dust absorption. Thus, the photo-electric heating that was the dominant at the surface, rapidly becomes less important and almost vanishes because (a) Γ_{photo} has a $\exp(-A_V)$ dependence on A_V, and (b) the heating efficiency ϵ becomes very small as electron abundances decrease significantly by recombination. Thus, in the absence of Γ_{mech}, heating by cosmic rays and dust (especially at high G_0) become the dominant ones in the molecular region.

In Fig. 2.4 we show contours of the equilibrium temperature at $A_V = 20$. In the absence of any mechanical heating, and in contrast to the situation for the surface slab, the topology of the contours is quite simple. The highest temperatures, with a maximum of $\sim 80 \, \text{K}$, are in the upper right corner at $n = 10^6 \, \text{cm}^{-3}$ and $G_0 = 10^6$. Temperatures decrease monotonously along the diagonal until they reach 10 K, which is the minimum temperature we allowed for. The main characteristic of a PDR is that the surface is heated to high temperatures, which is a thin layer. Beyond this layer, in the transition zone, the temperature drops sharply. Although the temperature profile in Fig. 2.4 is simple, it is counter-intuitive. We might expect the temperature to decrease as the density increases at a fixed G_0, but the opposite occurs. We explain this by the fact that as n increases, the coupling between gas and dust also increases. Dust temperature depends on G_0 and decreases as a function of A_V. Nevertheless, for very high $G_0 > 10^3$, the decreasing dust temperatures are still high enough to heat the gas ($\sim 30 \, \text{K}$).

The temperature profile throughout the cloud is shown in Fig. 2.5 for the selected models M1 to M4. The temperature generally decreases as a function of A_V. For some models which have high mechanical heating rates, the temperature increases and then saturates at higher values than those obtained at for the surface. As for the models whose temperature decreases, we see that as the density decreases, more specifically as the ratio G_0/n increases, the point of saturation of the temperature gets shifted further away from the surface of the cloud ($A_V = 0 \, \text{mag}$). For instance, when looking at clouds illuminated with a high FUV flux of $G_0 = 10^3$, the saturation point gets shifted from $A_V \sim 5 \, \text{mag}$ for $n = 10^3 \, \text{cm}^{-3}$ (low density gas) to $A_V \sim 2 \, \text{mag}$ for $n = 10^{5.5} \, \text{cm}^{-3}$ (high density gas, compare left panels of Fig. 2.5). A similar behavior is seen for the right panels which have a higher FUV flux with $G_0 = 10^5$. However, we note that the saturation point remains almost constant for a fixed G_0/n, which can be seen in comparing M1 and M4, where G_0/n are of the same order of magnitude. The temperature saturation point is also related to the H/H$_2$ and C$^+$/C/CO transition zones. For example, along the lines (in $n - G_0$ parameter space) where $G_0/n = 0.003$, 1 and 300, the location of the transition zones in

21
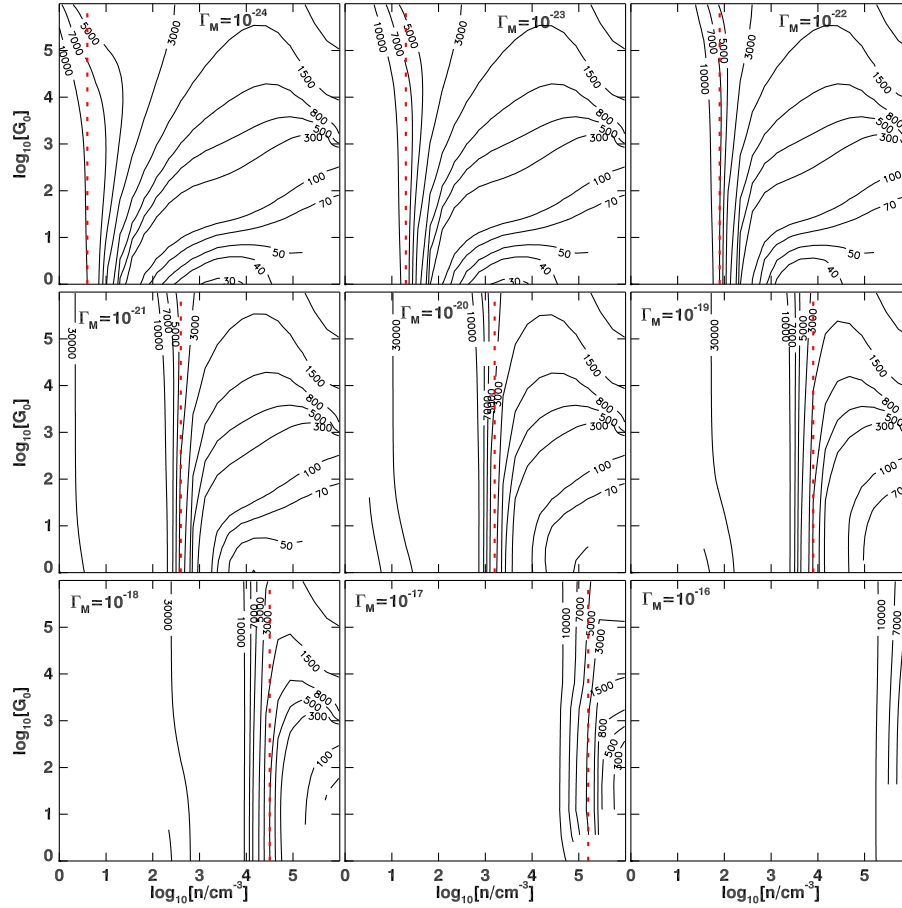
Figure 2.3 – Surface temperature (for $Z = Z_\odot$) for different values of mechanical heating. Each panel shows the surface temperature contours for a different value of Γ_{mech} mentioned at the top of each panel. In probing the effect of mechanical heating, each panel should be compared to the middle panel of Fig. 2.1 which is also for $Z = Z_\odot$. Different parts of the parameter space in n and G_0 are affected differently, depending mainly on the gas density. For $\Gamma_{mech} < 10^{-21}$ erg cm^{-3} s^{-1} , regions in density with $n < 10^3$ cm^{-3} have their temperatures increase significantly. The vertical dashed red lines mark densities $n = n_c$ where $\Gamma_{mech} = \Gamma_{total,surface}$. The location of these lines moves from very low densities ($n \sim 10^{0.5}$ cm^{-3}) to very high densities ($n > 10^5$ cm^{-3}) as Γ_{mech} increases from 10^{-24} to 10^{-16} erg cm^{-3} s^{-1}, sweeping the parameter space in density (for a certain grid) from left to right. In general the contour lines at $n = n_c$ become vertical, indicating that the surface temperature becomes independent of G_0. In subsequent plots, those lines are plotted only for $Z = Z_\odot$ grids, since the fits from which $n = n_c$ were derived were done only for solar metallicity.

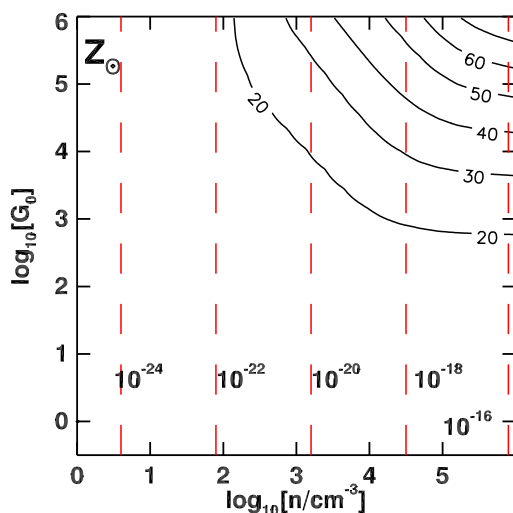Figure 2.4 – Temperature at $A_V = 20$ without mechanical heating. Higher equilibrium temperatures are attained for dense molecular clouds (top right corner) with decreasing equilibrium temperature towards low n and G_0. Below the 20 K contour, all temperatures are set to 10 K – the minimum allowed in the code. The red dashed lines mark the densities $n = n_c$ where $\Gamma_{\mathrm{mech}} = \Gamma_{total,surface}$ from Table 2.2.

the chemical species are almost unchanged.

In a PDR, the total heating at the surface it is dominated by $\Gamma_{\mathrm{photo},\, A_V=0} \sim \Gamma_{\mathrm{total},\, A_V=0} = \Gamma_{\mathrm{surface}}$, and decreases as a function of increasing A_V. Also total heating generally decreases as a function of A_V. In Section. 2.3.1.1 it was demonstrated that mechanical heating increases the surface temperatures significantly whenever $\Gamma_{\mathrm{mech}} = \Gamma_{\mathrm{surface}}$. In such situations, since mechanical heating is added uniformly throughout the PDR, we expect it to have a stronger impact (on the physical and chemical properties) at high depths compared to those at the surface. Hence Γ_{mech} should be the most dominant heating term beyond the surface, even more dominant than heating due to cosmic rays which attains a maximum of $10^{-21.5}$ erg cm^{-3} s^{-1} for $n = 10^6$ cm^{-3}. In Fig. A.1 we show the corresponding parameter grids as a function of Γ_{mech}; the thermal profile in these grids has almost no dependence on G_0 and depends solely on n.

In order to illustrate the degree by which Γ_{mech} increases temperatures throughout the cloud, we look at the curves in Fig. 2.5 corresponding to $\Gamma_{\mathrm{mech}} \neq 0$. We note that for densities where $\Gamma_{\mathrm{mech}} = \Gamma_{\mathrm{surface}}$, listed in Table 2.2, gas temperatures increase by almost two orders of magnitude for the low density models M1 and M2, and by at least one order of magnitude for the high density models M3 and M4. In fact, it suffices to have a mechanical heating rate 10 to 100 times smaller than the total heating at the cloud surface for gas temperatures to increase by a factor of ~2 (for high densities) and up to a factor of ~10 (for low densities). Thus, even relatively small mechanical heating rates

23

will substantially modify the physical parameters deduced from a pure PDR model. In a continuous starburst with an SFR = 1 $M_\odot$ yr^{-1} (which corresponds to Γ_{mech} ~ 2 × 10^{-20} erg cm^{-3} s^{-1} using Eq. 2.1), the mechanical luminosity (heating) is about 1% of the bolometric luminosity (Leitherer et al. 1999). Which implies that the ratio of mechanical luminosity to FUV luminosity (where the emission of star forming regions peak) is larger than 1% . Especially if we consider higher a SFR ~ $10M_\odot$ yr^{-1} which translates to a Γ_{mech} ~ 2 × 10^{-19} erg cm^{-3} s^{-1} . Assuming that half the FUV radiation is absorbed by the ISM of the galaxy, we would still be in the range where Γ_{mech} is at least 1% of the surface heating (which is due to FUV radiation), thus significantly altering the equilibrium temperatures of PDRs.
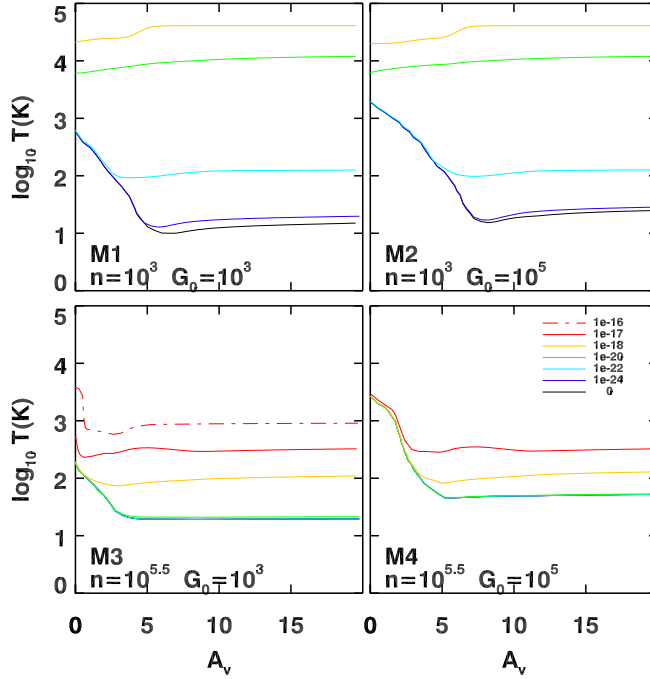
Figure 2.5 – Gas temperature as a function of the visual extinction for selected models. In the top two panels, for Γ_{mech} > 10^{-22} erg cm^{-3} s^{-1} (green and orange curves) the transition from H to H$_2$ does not occur. For the high density models the transition fails only for M4 when Γ_{mech} > 10^{-17} erg cm^{-3} s^{-1}.

2.3.2   Molecular gas tracers

Now that we have determined the degree to which mechanical heating alters the thermal properties of PDRs, we examine its effect on the chemical properties. Molecular clouds consist mainly of molecular hydrogen which is not directly observable except under very

special circumstances. Thus, we must depend on the (sub)millimeter line emission from various transitions of much less abundant tracer molecules. Each molecular line represents its own critical density and temperature.

In the following sections, we will consider the effect of mechanical heating on a few species commonly used as tracers. These are CO for relatively low gas densities and HCO^+, HCN, and HNC for relatively high densities, in addition to H_2O which has been also recently observed in very dense gas environments, $n \sim 10^6$ cm^{-3}.

2.3.2.1 CO

Properties of molecular H_2 gas are generally studied through observations of CO, which is the next most abundant species. The critical density (n_{cr}[5]) for the ground-state J=1-0 ^{12}CO transition is $n_{cr} \sim 2000$ cm^{-3}. This is in the middle section of range of densities n considered in our grids. Thus, the response of CO to mechanical heating may have important consequences for estimates of the amount of molecular gas and, for instance, may also explain the high gas temperature of 100-150 K which have been estimated for molecular gas in the centers of galaxies with densities of 100-1000 cm^{-3} (Israel 2009b).

In Fig. 2.6, we show the abundance of CO as a function of depth inside the cloud. For the models with densities close to n_{cr} (M1 and M2), CO abundances decrease sharply for $\Gamma_{mech} > 10^{-18}$ erg cm^{-3} s^{-1} and almost disappears when $\Gamma_{mech} > 10^{-20}$ erg cm^{-3} s^{-1}, where $x_{CO} < 10^{-13}$ caused by very high temperatures $T > 10000$ K (abundances of species relative to the total number of hydrogen nuclei are denoted by $x_i = n_i/(n_H + 2n_{H_2})$). At such high temperatures, no molecules, including CO, are formed. This is due to the very low abundance of H_2 which drops from ~ 0.5 to $\sim 10^{-9}$ beyond the radical region. This drop breaks the chemical network which leads to the formation of CO. In addition, the higher abundances of the ionic species H_3^+ and He^+ enhance the destruction of CO through the reactions $H_3^+ + CO \rightarrow HCO^+ + H_2$ and $He^+ + CO \rightarrow O + C^+ + He$. On the other hand, for $\Gamma_{mech} \leq 10^{-18}$ erg cm^{-3} s^{-1} the first obvious effect of mechanical heating on CO is the shift of the C/CO transition zone towards the surface of the slab. This shift is caused by the enhanced abundance of O_2 and OH and higher temperatures in the radical region (see Fig. 2.6).

In the high density models M3 and M4, the abundance of CO decreases by a factor of two as Γ_{mech} increases from 10^{-18} erg cm^{-3} s^{-1} to 10^{-17} erg cm^{-3} s^{-1}. As Γ_{mech} is pushed further to 10^{-16} erg cm^{-3} s^{-1} x_{CO} decreases from 10^{-4} to 10^{-16} for M3 and becomes under-abundant for M4 ($x_{CO} < 10^{-12}$). This behavior can be explained by the enhanced abundance of the ionized species He^+ and H_3^+, which destroy CO through ion-neutral reactions. Also, the significant drop in abundance of H and HCO (by three orders of magnitude) reduce the formation of CO through the reactions $H + HCO \rightarrow CO + H_2$ and $O + C_2 \rightarrow CO + C$.

In Figs. 2.7 and A.2, the column density of CO is shown without and with increasing values of mechanical heating respectively. The general trend is an increase in N(CO)

---

[5] The critical density n_{cr} should not be confused with n_c, defined earlier, which is the gas density where $\Gamma_{mech} = \Gamma_{total,surface}$

whenever the added Γ_{mech} is comparable to the surface heating of a PDR with no mechanical heating. This occurs at densities (n_c) marked by vertical dashed lines in Fig. A.2. For higher densities in the grids (to the right of these lines) $\Gamma_{mech} < \Gamma_{surface}$ and the opposite is true for lower densities (to the left the lines). At densities a factor of 3 higher than n_c (a distance of 0.5, in $\log_{10}$ scale, to the right of n_c) where $\log_{10} n = \log_{10} n_c + 0.5$ we can see a change in the shape of the contours in $N(CO)$. This change corresponds to an increase up to a factor of two in $N(CO)$, with no noticeable change in regions where $\log_{10} n > \log_{10} n_c + 0.5$. From our fits of surface heating these regions have $\Gamma_{surface} < \Gamma_{mech}/20$. It is also noticed that the increase of $N(CO)$ is more pronounced for high values of G_0/n as Γ_{mech} increases (compare left and right panel of Fig. 2.6). We can explain this by looking at the the $C^+/C/CO$ transition zone, which gets shifted towards the surface of the cloud as Γ_{mech} dominates. This shift is more pronounced for higher G_0, thus resulting in more CO in the column of H we are considering ($N(H) = 1.8 \times 10^{22} cm^{-2}$).

For conditions similar to that of the Milky Way, SFR ~ 1 M$_\odot$ yr^{-1} which corresponds to a Γ_{mech} of 2×10^{-20} erg cm^{-3} s^{-1}, $N(CO)$ estimates would be marginally ($\sim 20\%$) lower when Γ_{mech} is not taken into account. However, for starbursts with $n \sim 10^4$ cm^{-3} and $G_0 \sim 10^3$ and a significantly higher SFR (~ 50 M$_\odot$ yr^{-1}) the $N(CO)$ estimates would be a factor of two less when the Γ_{mech} of 1×10^{-18} erg cm^{-3} s^{-1} is ignored (compare Fig. 2.7 to the panel corresponding to $\Gamma_{mech} = 10^{-18}$ erg cm^{-3} s^{-1} in Fig. A.2, where the $N(CO)$ contour is shifted to the right, from $n \sim 10^3$ to $n \sim 10^{4.5}$ cm^{-3}). For low metallicity grids we considered $Z = 0.5 Z_\odot$, which may represent systems such as dwarf galaxies (where the metallicity may be as low as 0.1 $Z_\odot$), the increase in $N(CO)$ may be up to one order of magnitude, reaching 10^{17} cm^{-2}. This occurs even for a low mechanical heating rates corresponding to an SFR of ~ 1 M$_\odot$ yr^{-1}. The increase in $N(CO)$ is visible in the central part of the parameter space (compare the grids when $\Gamma_{mech} = 10^{-21}$ erg cm^{-3} s^{-1} and $\Gamma_{mech} = 10^{-20}$ erg cm^{-3} s^{-1} in Fig. A.4). In contrast, for the highest metallicity we considered, the $Z = 2 Z_\odot$ grids, which represents a more likely condition for galactic centers, the increase is less prominent even for the extreme mechanical heating rates of $\Gamma_{mech} = 10^{-17}$ erg cm^{-3} s^{-1} corresponding to ~ 500 M$_\odot$ yr^{-1} (see Fig. A.3).

Thus, we conclude that we would potentially severely underestimate the amount of CO in the system if mechanical heating is ignored, especially for metallicities less than $Z_\odot$, i.e., in dwarf galaxies.

2.3.2.2   H$_2$O

Until the launch of the Herschel Space Observatory, it was not possible to observe water lines in the far-infrared from nearby extra-galactic sources, as their emission is blocked by the Earth's atmosphere. Now, water line emission has been detected by several Herschel key programs, and a striking example is provided by the water lines observed in Markarian 231 (González-Alfonso et al. 2010). In this object, water lines intensities are comparable to those of the CO lines. This is very different from what is observed for, e.g., the starburst galaxy M82 (Weiß et al. 2010) and the Orion Bar in the Milky Way (Habart et al. 2010).

Water can be formed through a neutral-neutral reaction chain, O + H$_2$ $\rightarrow$ OH + H,
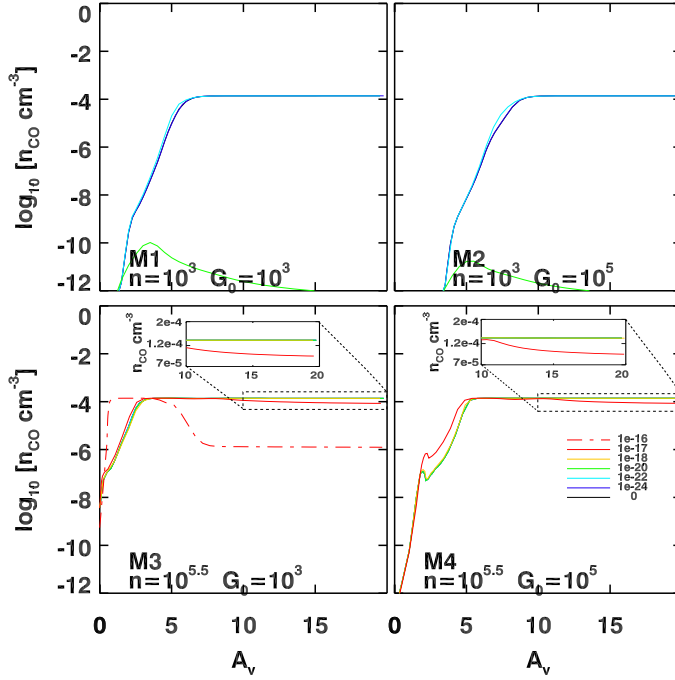
Figure 2.6 – CO abundance as a function of A_V for selected models. In all the diagrams, the C/CO transition zone is shifted towards the surface as a function of increasing Γ_{mech}. For M1 and M2, the abundance of CO is below the displayed range for $\Gamma_{mech} > 10^{-20}$ erg cm^{-3} s^{-1} (these curves are not shown). The other curves almost overlap except for $\Gamma_{mech} = 10^{-20}$ erg cm^{-3} s^{-1}. In models M3 and M4 the abundance of CO drops slightly beyond the transition zone compared to the case of no mechanical heating. The curves overlap except for $\Gamma_{mech} = 10^{-16}$ erg cm^{-3} s^{-1}, where the C$^+$/C/CO transition does not fully take place.

followed by $OH + H_2 \rightarrow H_2O + H$. In order to obtain significant abundances, the medium has to be molecular and sufficiently warm, as the reactions have barriers of $\sim$ 2000 K. In X-ray exposed environments, it is possible to obtain a significant water abundance $x_{H_2O} \sim 10^{-10}$ at high temperatures ($T \sim 3000$ K), produced by an ion-molecule reaction chain. A recent paper by Meijerink et al. (2011) shows that water production can be enhanced by an order of magnitude in these warm atomic environments, when the grains are stripped from their ice layers, as is possibly the case in violent environments around an AGN.

As we have seen in the previous sections, the temperatures in the molecular regions of the mechanically heated PDR can be increased to temperatures $T >> 100$ K, which is favorable for the production of water through the neutral reaction chain.

In Fig. 2.8 the abundance of H_2O is shown as a function of depth. The low-density models are marginally affected as long as $\Gamma_{mech} < 10^{-20}$ erg cm^{-3} s^{-1}. For higher mechanical heating rates the H/H$_2$ transition does not occur, thus H_2O does not form. However,

Figure 2.7 – CO total column density up to $N(H) = 1.8 \times 10^{22}$ cm^{-2} or $A_V \sim 10$ mag for $Z = Z_\odot$ without mechanical heating.

the impact on the abundance of H_2O is more significant for the the high-density (M3 and M4), where the abundance of H_2O is enhanced by at least one order of magnitude when $\Gamma_{mech} > 10^{-17}$ erg cm^{-3} s^{-1} . The reference grid for the column density of H_2O at solar metallicity (without mechanical) heating is shown in Fig. 2.9. In comparing this reference grid to Figs. A.5-A.7 (corresponding to grids for lower and higher metallicities), the column densities range between $N(H_2O) \sim 10^{14}$ (very low densities, $n < 10^1$ cm^{-3}) and up to $10^{16.5}$ cm^{-2} ($n > 10^2$ cm^{-3}). These column densities increase when the gas density if close to $n = n_c$ especially for $\Gamma_{mech} > 10^{-19}$ erg cm^{-3} s^{-1} where an optimum of ($N(H_2O) \sim 10^{18}$ cm^{-2}) is reached (see last row of Fig. A.5). When the mechanical heating rate becomes too high (in the regions where $n \ll n_c$), the column densities drop again, because there is insufficient H_2, which is destroyed through collisional dissociation, to form water. Therefore, one finds that this optimum moves from lower to higher densities for increasing mechanical heating rates.

Thus, the high column densities of H_2O accompanied by high temperatures make this molecule an excellent diagnostic tool for galaxy environments where mechanical heating dominates.

2.3.2.3 HCN and HNC

The critical density for the HCN and HNC $J = 1$-0 collisional excitation by H is $\sim 1 \times 10^6$ and $\sim 0.5 \times 10^6$ cm^{-3} respectively. Together with their relatively high abundance, makes them valuable high gas density tracers. Here we will be first looking at the abundances of HNC and HCN, x_{HNC} and x_{HCN} respectively up to $A_V = 20$ mag. Then we will study the
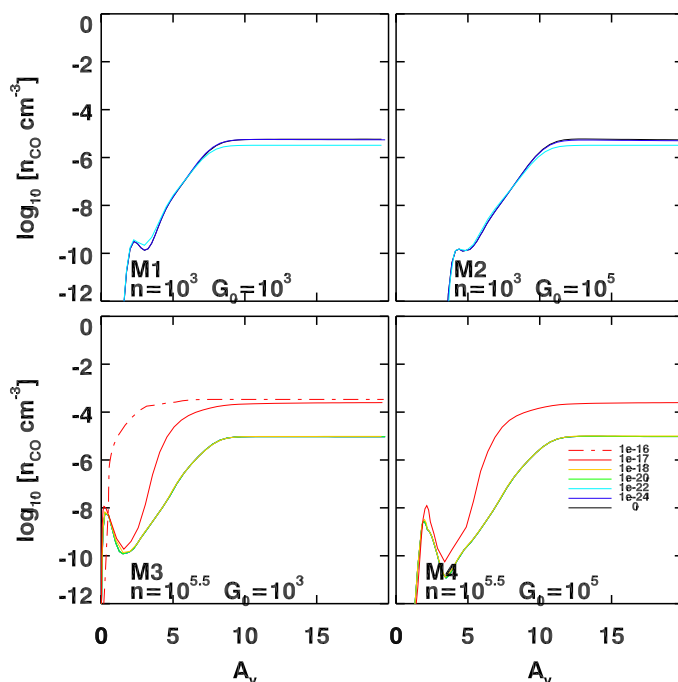
Figure 2.8 – H$_2$O abundance as a function of A_V for selected models.

effect of mechanical heating on the column density ratios of these two species.

Although included for completeness in Figs. 2.10 and 2.11, the low-density models M1 and M2 are of no physical interest, since they refer to densities at least two order of magnitude below the critical density of HCN and HNC. The more relevant high-density models M3 and M4 show (in contrast to the low-density models), an increase by four orders of magnitude in x_{HCN} when Γ_{mech} exceeds 10^{-18} erg cm^{-3} s^{-1}; whereas an increase of three orders in x_{HNC} is observed. The increase in the abundance of HCN was also noted by Loenen et al. (2008) and Meijerink et al. (2011). Mechanical heating causes the equilibrium temperature, in the molecular region, to increase from 100 K, when $\Gamma_{mech} = 10^{-18}$ erg cm^{-3} s^{-1}, to $\sim$ 900 K when $\Gamma_{mech} = 10^{-16}$ erg cm^{-3} s^{-1} (see Fig. 2.5). Consequently HNC is converted more effectively to HCN via the reaction HNC + H $\rightarrow$ HCN + H whose activation barrier of $\sim$ 200 K is surpassed (Schilke et al. 1992). This explains the drop in the fractional abundance of HNC with respect to HCN with $x_{HNC}/x_{HCN} \sim 0.1$.

The abundance of HCN and HNC increases by few orders of magnitude with increasing Γ_{mech} . This increase is because of the enhanced production of both species via the neutral-neutral reaction H$_2$ + CN $\rightarrow$ HCN + H. Also HCN and HNC are formed with equal probability through recombination reactions of HCNH$^+$, which has been also noted by Aalto (2005). These two processes are more dominant than the reaction HNC + H $\rightarrow$
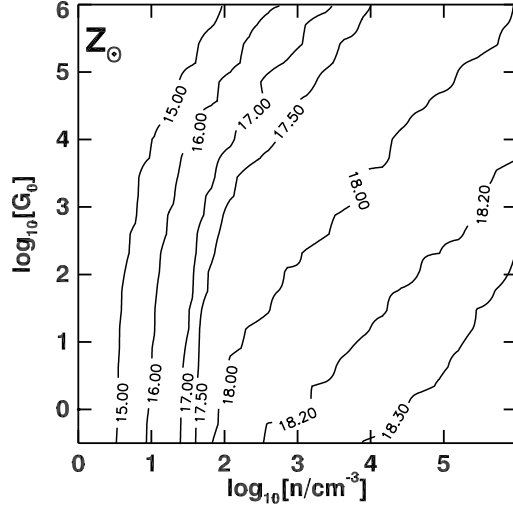
29
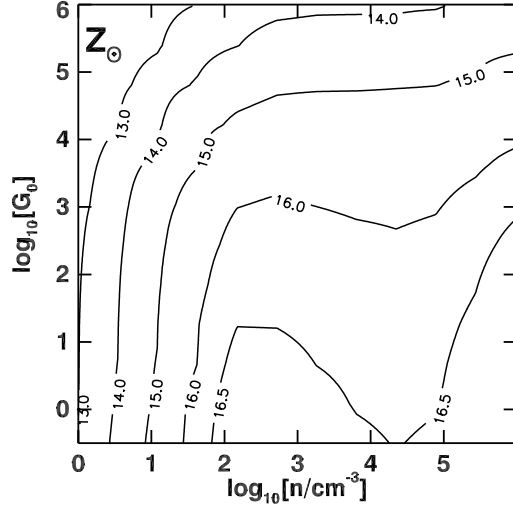
Figure 2.9 – H_2O total column density up to $N(H) = 1.8 \times 10^{22}$ cm^{-2} or $A_V \sim 10$ mag for $Z = Z_\odot$ without mechanical heating.

HCN + H, which is just a re-shuffling the bonds of HNC that leaves $x_{HCN} + x_{HNC}$ constant. However, HNC + H $\rightarrow$ HCN + H is responsible for the bias in the abundance of HCN with respect to HNC.

Now we look at the column density ratio $N(HNC)/N(HCN)$ in order to gauge the effects of mechanical heating in the $G_0 - n$ parameter space. These are computed by integrating x_{HNC} and x_{HCN} up to $N(H) = 1.8 \times 10^{22}$ cm^{-2} and taking their ratio. The same column density is considered for the other metallicities when the ratio $N(HNC)/N(HCN)$ is computed. In Fig. 2.12 the column density ratio of HNC to HCN is shown for the whole grid with no mechanical heating (pure PDR). Since HCN is a good tracer for dense molecular clouds with $n \geq 10^4$ cm^{-3} (Solomon et al. 1992), we focus on that part of the parameter space for this diagnostic. In the absence of mechanical heating, in this range of density, $N(HNC)/N(HCN) < 1$ for all G_0. When mechanical heating is added, specifically for Γ_{mech} larger than 10^{-19} erg cm^{-3} s^{-1}, the column density ratio starts decreasing even more with almost no dependence on G_0. For instance, in the upper right corner $N(HNC)/N(HCN)$ decreases from 0.7 to 0.55 (see Fig. A.8). This decrease affects regions where $\log_{10} n = \log_{10} n_c + 1.0$. At $\log_{10} n = \log_{10} n_c$ (dashed vertical lines in Fig. A.8) $\Gamma_{mech} = \Gamma_{surface}$ as described in Sect. 2.3.1.1, so mechanical heating dominates everywhere in the cloud. Whereas at $\log_{10} n = \log_{10} n_c + 1.0$ mechanical heating is up to 100 times smaller than the total heating at the surface of the pure PDR case. For the largest Γ_{mech} considered 10^{-16} erg cm^{-3} s^{-1} the $N(HNC)/N(HCN)$ decreases below 0.1 over the whole parameter space (see Fig. A.8). This is also observed for the other metallicities in Figs. A.9 and A.10.

Thus, we find that the ratio $N(HNC)/N(HCN)$ is sensitive to low mechanical heating
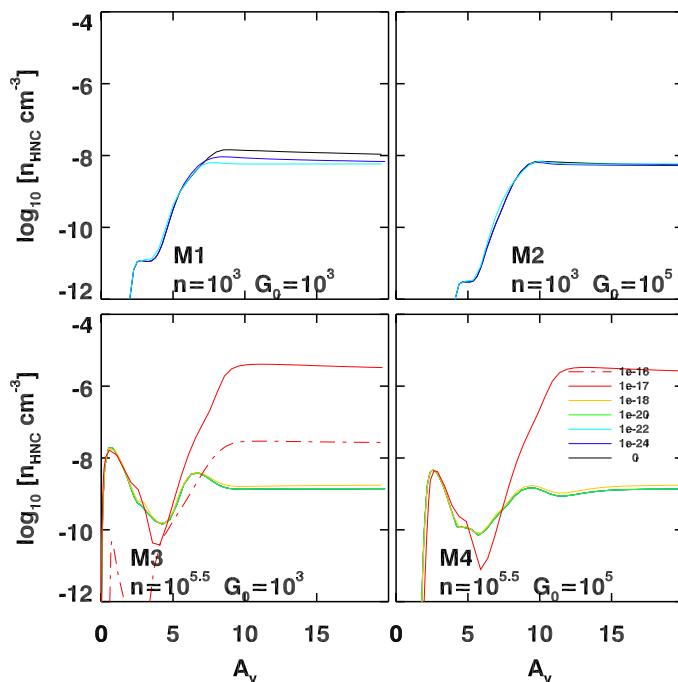
Figure 2.10 – HNC abundance as a function of A_V for selected models. In the top panels the curves for $\Gamma_{mech} > 10^{-22}$ erg cm^{-3} s^{-1} are not shown since the C$^+$/C/CO transition does not take place.

rates, a factor of a hundred smaller than the total heating at the surface of a pure PDR. For higher mechanical heating rates that are 20 times smaller than those at the surface, N(HNC)/N(HCN) decrease at least by a factor of two.

2.3.2.4   HCN/HCO$^+$

HCO$^+$ is another high density gas tracer with $n_{cr} \sim 10^5$ cm^{-3} for J=1-0 transition. It has been suggested that in AGNs, where X-ray heating dominates, HCN is less abundant than HCO$^+$ (Lepp & Dalgarno 1996), suggesting that the HCN/HCO$^+$ ratio is a diagnostic for the determination of the physical nature of a source object. A detailed study of the effect of cosmic rays (Meijerink et al. 2011) shows that the abundance of HCO$^+$ is inhibited by high cosmic ray rates. Since cosmic rays have a large penetrating depth, they may raise the temperature of clouds up to large column densities. Since Γ_{mech} is added uniformly throughout the slab and the temperatures are likewise enhanced, a behavior similar to that caused by cosmic rays should be seen. In a similar fashion as for HNC and HCN, we look at abundances and column density ratios with and without mechanical heating to see how it affects the N(HCN)/N(HCO$^+$) ratios.

In the low- density models (top row of Fig. 2.13) a slight increase in the abundance
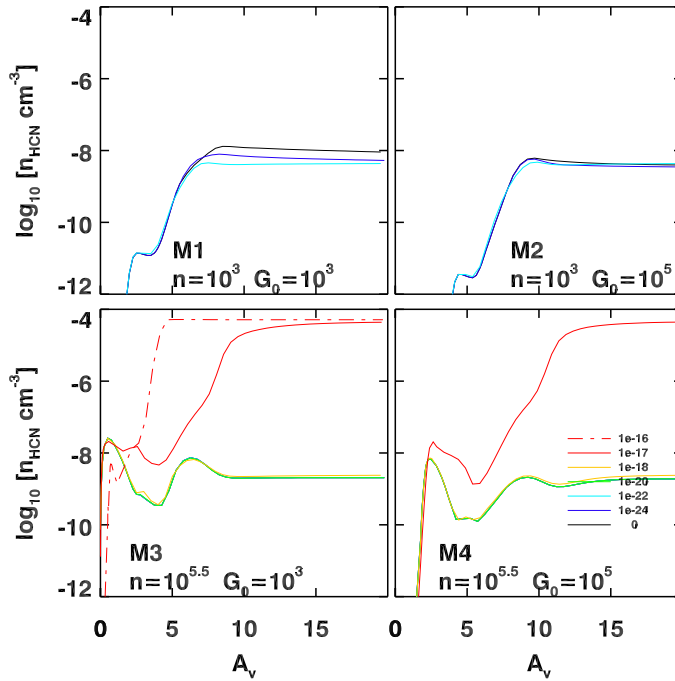
Figure 2.11 – HCN abundance as a function of A_V for selected models. The same convention of Fig. 2.10 are used.

of HCO$^+$ is observed up to $\Gamma_{mech} = 10^{-22}$ erg cm^{-3} s^{-1}. This is caused by a slightly slower destruction rate of HCO$^+$ through the reaction HCO$^+$ + e$^-$ → CO + H. For $\Gamma_{mech} > 10^{-22}$ erg cm^{-3} s^{-1}, the two orders of magnitude drop in the abundance of HCO$^+$ in the molecular region is caused mainly by ion-neutral reactions with H$_2$O, HCN (which we demonstrated to increase in the previous section) and C. The abundance of HCO$^+$ is unaffected by Γ_{mech} in M3 and M4 unless it is larger than 10^{-17} erg cm^{-3} s^{-1}. For that amount of mechanical heating x_{HCO^+} becomes $\sim 10^{-11}$ beyond the radical region. In this case, the reactions H$_2$O + HCO$^+$ → CO + H$_3$O$^+$ and HCN + HCO$^+$ → HCNH$^+$ + CO dominate (again because of enhanced abundances of H$_2$O and HCN) in destroying HCO$^+$ by two orders of magnitude compared to the other reactions. However, an increase of one to four orders of magnitude in x_{HCO^+} is observed for $A_V < 5$ mag. This contributes significantly to the column density of HCO$^+$ in clouds with low N(H), which could make a significant impact on the interpretation of line ratios for clouds with small column densities as opposed to those with high N(H).

Looking at the column density ratios of HCN to HCO$^+$, N(HCN)/N(HCO$^+$), we see in Fig. 2.14 a non-trivial dependence. The ratio varies from $10^{-0.7}$ (in the high-density and high-FUV flux zone) to $10^{0.7}$ (in the high-density, moderate- to low-FUV flux zone).

An interesting feature of this column density ratio, quite different from the HNC/HCN

Figure 2.12 – HNC/HCN integrated column density ratios (integrated up to $N(H) = 1.8 \times 10^{22}$ cm^{-2} or $A_V \sim 10$ mag for $Z = Z_\odot$) without mechanical heating. The column density ratio decreases from left to right. For dense molecular clouds, the ratio is ~0.7 and it is almost constant as a function of G_0.

situation, is the fact that the $N(\text{HCN})/N(\text{HCO}^+)$ ratio increases to ~ 10 and $\sim 10^3$, as opposed to a decrease of *only* a factor of two in the ratio $N(\text{HNC})/N(\text{HCN})$ as a function of increasing Γ_{mech}. For high densities when $\Gamma_{\text{mech}} > 10^{-20}$ erg cm^{-3} s^{-1} the contours become almost parallel for $\log_{10} n_c < \log_{10} n < \log_{10} n_c + 1.0$. This implies that the $N(\text{HCN})/N(\text{HCO}^+)$ ratio does not depend on G_0/n (as far as this ratio is concerned), but is dominated by mechanical heating down to values ~ 100 times smaller than the surface heating of a pure PDR. This is shown in Fig. A.11 where $N(\text{HCN})/N(\text{HCO}^+)$ ranges between 10 and 10^4 in the density range mentioned. Similar behavior is seen for the other metallicities considered.

This, and the fact that $N(\text{HCN})/N(\text{HCO}^+)$ is very sensitive to very small values of mechanical heating makes this ratio an excellent diagnostic for mechanically heated regions.

2.4   Conclusion and discussion

The goal of this paper is to assess when we should take into account mechanical heating in modeling the observed line emission properties of the interstellar medium in PDRs. We have calculated the equilibrium thermal and chemical properties of interstellar clouds as 1D semi-infinite slabs for a large range of hydrogen gas densities ($1 < n < 10^6$ cm^{-3}) and radiation fields ($0.3 < G_0 < 10^6$). As a result, we covered more or less *all* conditions physically relevant for the ISM, from the diffuse ISM in the outskirts of quies-
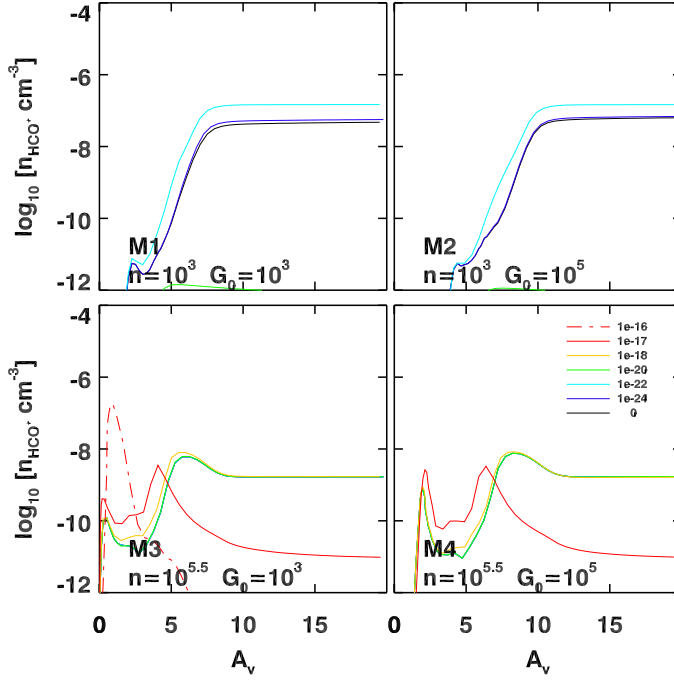
Figure 2.13 – HCO$^+$ abundance as a function of A_V for selected models.

cent galaxies ($G_0 < 1$, $n = 1 - 100\,\text{cm}^{-3}$), to the dense, FUV-exposed environments ($G_0 \sim 10^5$, $n \sim 10^{5.5}\,\text{cm}^{-3}$) of active galaxy centers. We have also explored three levels of heavy-element abundance, $Z = 0.5$, 1.0 and $2.0 Z_\odot$, thus considering the low metallicities of dwarf galaxies as well as the enhanced metallicities in galaxy centers. We have done this by adding a mechanical heating term resulting from dissipating turbulence of supernovae. The heating rates included are between $10^{-24} < \Gamma_\text{mech} < 10^{-16}$ erg cm^{-3} s^{-1}, which corresponds to star-formation rates ranging from SFR ~ 0 to $\sim 1000\,\text{M}_\odot\,\text{yr}^{-1}$ under the assumptions explained in section 2.1. We first explored the effect on the thermal balance at the surface and deep into the cloud at high column densities, and then the chemistry of a few commonly observed species in the ISM of galaxies, namely, CO, H$_2$O, HCN, HNC, and HCO$^+$. We demonstrated that mechanical heating radically changes the resulting chemical and thermal structure. The following conclusions can be drawn :

(i) The equilibrium temperature in a PDR is significantly altered, i.e., increased by an order of magnitude, for ratios $\Gamma_\text{mech}/n^{1.5} \sim 10^{-25}$ erg cm$^{-4.5}$ s^{-1}. This is a lower bound in the sense that when $\Gamma_\text{mech}/n^{1.5} = 10^{-25}$ the temperature inside the cloud (even for the densest clouds $n \sim 10^6$ cm^{-3}) increases by a factor of 10. Thus, Γ_mech *must* be taken into account while solving for the equilibrium state of a PDR. In translating this relation into one relating gas density to the star formation rate, it can be expressed as SFR$/n^{3/2} = 7 \times 10^{-6}$. For higher values the temperature increases even more. Also, the H/H$_2$ transition
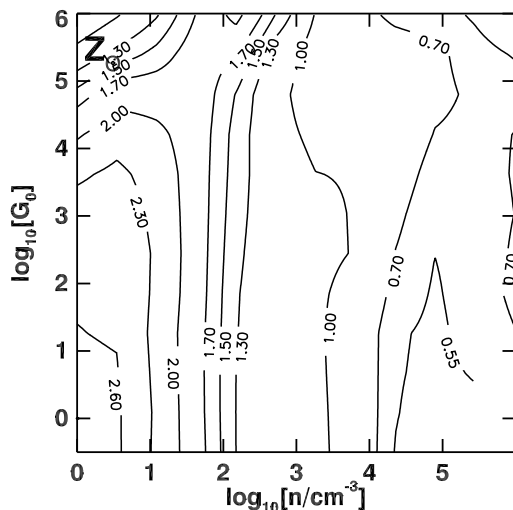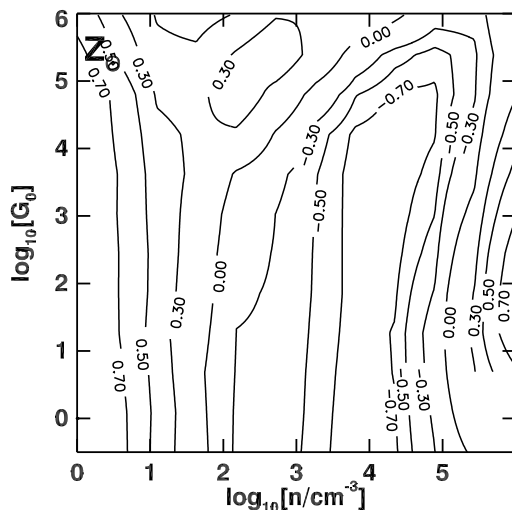
Figure 2.14 – HCN/HCO$^+$ integrated column density ratios (integrated up to $N(\text{H}) = 1.8 \times 10^{22}$ cm^{-2} or $A_V \sim 10$ mag for $Z = Z_\odot$) without mechanical heating.

may not occur for very high mechanical heating rates ($\Gamma_{\text{mech}}/n^{1.5} \gg 10^{-25}$), especially for the low density clouds with $n \sim 10^3$ cm^{-3}.

(ii) Mechanical heating rates that are two orders of magnitudes smaller than the surface heating nevertheless are high enough to increase the temperature by an order of magnitude in low-density clouds and up to a factor of two in high-density clouds $n \sim 10^6$ cm^{-3}. For instance, inclusion of a mechanical heating rate of 10^{-18} erg cm^{-3} s^{-1} in the high-density cloud models M3 and M4 of Meijerink & Spaans (2005) increases the temperatures inside the clouds from $T \sim 30$ K to ~ 100 K and from $T \sim 70$ K to ~ 110 K, respectively. Such heating rates Γ_{mech} are expected to occur in star-burst galaxies, and correspond to an SN rate of approximately 0.3 per year and a SFR rate of 9.4 M$_\odot$ yr^{-1} (Loenen et al. 2008).

(iii) We observe that $N(\text{CO})$ is easily doubled when mechanical heating is included in modeling PDRs, especially for gas with $n \sim 10^3$ cm^{-3}. As such, mechanical heating should be considered, when interpreting observed CO data. We also observe that the implied column density strongly depends on metallicity. This column density decreases from 10^{18} cm^{-2} at solar metallicity to 10^{17} cm^{-2} at half-solar metallicity; whereas it increases up to 10^{19} cm^{-2} at double-solar metallicity. This is particularly interesting for galaxy centers where the metallicity is expected to be higher than that of the solar neighborhood.

(iv) Our results show that the brightness of emission lines observed in galaxy centers may at least partly be due to high mechanical heating rates. The models with $Z = 2Z_\odot$ require higher column densities, and temperatures are enhanced by a factor 2 to 10. It also suggests that CO column densities in low-metallicity dwarf galaxies are even lower than assumed otherwise. Mechanical heating excites the gas to high temperatures, but the

column density $N(CO)$ is significantly lower (by almost an order of magnitude) compared to $Z = Z_\odot$). In addition to that, the relative gas fraction is lower in dwarf galaxies, as supernovae easily disperse gas from the galaxy.

(v) Like CO, H_2O also exhibits an increase in column density. The temperature increase induced by mechanical heating results in implied column densities $N(H_2O)$ three orders of magnitude higher (up to $\sim 10^{18}$ cm^{-2}) compared to models without mechanical heating. This gives H_2O approximately the same column density as CO, for the highest mechanical heating rate. Based on this, H_2O lines could also provide an excellent diagnostic in combination with CO, when studying mechanical heating in galaxies.

(vi) HCN, HNC, HCO+ line ratios have been used to discriminate between PDRs and XDRs (Meijerink et al. 2007, Loenen et al. 2008). Although we do not compute line intensity ratios in this paper, we have studied the signature of mechanical heating on the integrated column density ratios of HNC/HCN and HCN/HCO+. We find that model HNC/HCN column density ratios decrease by a factor of at least 5 for gas densities $n > 10^5$ cm^{-3}, when $\Gamma_{mech} > 10^{-17}$ erg cm^{-3} s^{-1}. This effect is mitigated in clouds subjected to lower mechanical rates, but only at densities $n < 10^4$ cm^{-3}. HCN and HNC do not produce significant line emission at these densities as they are well below the critical density for excitation. On the other hand, the HCN/HCO$^+$ column density ratio strongly depends on mechanical heating. This ratio increases from ~ 10 to ~ 100, for dense molecular clouds ($n > 10^5$ cm^{-3}), when $\Gamma_{mech} = 10^{-19}$ erg cm^{-3} s^{-1} and up to 10^4 for $\Gamma_{mech} = 10^{-18}$ erg cm^{-3} s^{-1} for $Z = 0.5, 1.0, 2Z_\odot$. In general for these conditions the column densities of HCO$^+$ decrease from $\sim 10^{14}$ cm^{-2} to $\sim 10^{13}$ cm^{-2}, those for HCN increase from $\sim 10^{13}$ cm^{-2} to $\sim 10^{16.5}$ cm^{-2}, whereas $N(HNC)$ drop to $\sim 10^{13}$ cm^{-2} from $\sim 10^{14}$ cm^{-2}. The abundance of HCO$^+$ drops by at least three orders of magnitude at column densities higher $N_H > 1.8 \times 10^{21}$ cm^{-2} for the aforementioned Γ_{mech}. In galaxy centers, higher A_V are easily possible compared to $Z = Z_\odot$. This translates into higher $N(H)$, which in turn would imply a smaller $N(HCO^+)$ compared to $N(HCN)$. Hence resulting in even higher HCN/HCO+ column density ratio. The lack of HCO$^+$ in combination with bright HCN line emission might be useful in tracing regions with high mechanical heating rates.

The integrated column density ratios do not translate directly into line intensity ratios. Instead, one should compute these ratios by solving the radiative transfer equations. We will consider predictions for the actual line intensities of HCN, HNC and HCO$^+$ in the next paper, where we will also assess time-dependent effects. The equilibrium treatment is certainly valid for the low-metallicity dwarf galaxies, and the benchmark-metallicity of solar neighborhood galaxy discs, but this may not be the case for the high-metallicity galaxy centers, where the chemical, thermal, and dynamical timescales are quite comparable in the inner < 100 pc, especially at densities $n < 10^3$ cm^{-3}. For example, the formation timescale of H_2 (Hollenbach & Tielens 1999) is < 5 Myr at an ambient gas density $n \sim 10^3$ cm^{-3} and a kinetic temperature of $T \sim 100$ K. The stellar orbital periods (which stir up the ISM) are comparable to or shorter than this, namely between 0.1 and 15 Myr. Hence, a time-dependent treatment is necessary, and we aim to accomplish this in upcoming papers by adapting the current PDR-XDR code. We will allow for time-dependent chemical evolution, and couple it with an SPH code through AMUSE. As such,

the chemistry, gas and stellar dynamics are being evolved self-consistently.

Acknowledgements

Appendices

Figures A.1 – A.10 can be found in the online version at:
`http://www.aanda.org/articles/aa/pdf/2012/06/aa18641-11.pdf`

III

Diagnostics of the Molecular Component of PDRs with Mechanical Heating II: Line Intensities and Ratios

CO observations in active galactic nuclei and star-bursts reveal high kinetic temperatures. Those environments are thought to be very turbulent due to dynamic phenomena such as outflows and high supernova rates.

We investigate the effect of mechanical heating on atomic fine-structure and molecular lines, and their ratios. We try to use those ratios as a diagnostic to constrain the amount of mechanical heating in an object and also study its significance on estimating the H_2 mass.

Equilibrium photo-dissociation models (PDRs hereafter) were used to compute the thermal and chemical balance for the clouds. The equilibria were solved for numerically using the optimized version of the Leiden PDR-XDR code. Large velocity gradient calculations were done as post-processing on the output of the PDR models using RADEX.

High-J CO line ratios are very sensitive to mechanical heating (Γ_{mech} hereafter). Emission becomes at least one order of magnitude brighter in clouds with $n \sim 10^5$ cm^{-3} and a star formation rate of 1 $M_\odot$ yr^{-1} (corresponding to $\Gamma_{mech} = 2 \times 10^{-19}$ erg cm^{-3} s^{-1}). Emission of low-J CO lines is not as sensitive to Γ_{mech}, but they do become brighter in response to Γ_{mech}. Generally, for all of the lines we considered, Γ_{mech} increases excitation temperatures and decreases the optical depth at the line center. Hence line ratios are also affected, strongly in some cases. Ratios involving HCN are a good diagnostic for Γ_{mech}, where the HCN(1-0)/CO(1-0) increases from 0.06 to 0.25 and the HCN(1-0)/HCO$^+$(1-0) increase from 0.15 to 0.5 for amounts of Γ_{mech} equivalent to 5% of the surface heating rate. Both ratios increase to more than 1 for higher Γ_{mech}, as opposed to being much less than unity in pure PDRs.

The first major conclusion is that low-J to high-J intensity ratios will yield a good estimate of the mechanical heating rate (as opposed to only low-J ratios). The second one is that the mechanical heating rate should be taken into account when determining A_V or equivalently N_H, and consequently the cloud mass. Ignoring Γ_{mech} will also lead to large errors in density and radiation field estimates.

M. V. Kazandjian, R. Meijerink, I. Pelupessy, F. P. Israel, M. Spaans

3.1 Introduction

The study of molecular gas in external galaxies dates back to the mid-seventies, with the detection of ground-state emission from CO (the most abundant molecules after hydrogen) in a small number of bright nearby galaxies. At present observations CO and many other molecules exist for a very large number of galaxies, near and far. It is important to be able to interpret the emission in the various lines from those galaxies, since that gives us insight in the physics dominating the interstellar medium in the star forming regions of these extra-galactic sources.

For decades, line observations had to be done from the ground in a frequency range limited by atmospheric opacity, so that for most molecular species only the low transitions were accessible. Level transitions at higher rest frame frequencies, were only possible for distant galaxies for which the high-frequency lines were red-shifted into atmospheric windows accessible from the ground. In the past few years the *Herschel* Space Observatory (Pilbratt et al. 2010) operating outside the Earth's atmosphere has provided direct observations of spectral lines at frequencies hitherto impossible or hard to access.

By way of example we mention the determination of extensive ^{12}CO rotational transitions ladder in galaxies such as M82 (Loenen et al. 2010, Panuzzo et al. 2010, Kamenetzky et al. 2012) and Mrk231 (van der Werf et al. 2010, González-Alfonso et al. 2012). *Herschel* ran out of coolant in April 2013, but at about the same time, the Atacama Large Millimeter Array (ALMA) became operational. With ALMA, a large fraction of the important submillimeter spectrum is still accessible, at vastly superior resolution and sensitivity, allowing detection and measurement of diagnostic molecular line transitions largely out of reach until then.

Conducting detailed studies of the physical properties of the molecular gas of close-by star-forming galaxies involves a challenging inversion problem, where resultant line intensities are used to constrain gas densities, molecular content, kinetic temperatures and the nature and strengths of the radiation field exciting the gas. In order to solve this problem, it is necessary to get a clearer understanding of the underlying physics and phenomena characterizing specific regions such as galaxy centers, including our own.

A good starting point to analyze molecular gas emission is the application of the so-called large-velocity-gradient (LVG) models (Sobolev 1960). This assumes an escape probability formalism for photons in different geometries which simplifies solving for the radiative transfer significantly. LVG models have been widely used by the ISM community with some other basic assumptions to estimate the molecular density of the gas, species abundances and the kinetic temperature (Henkel et al. 1983, Jansen et al. 1994, Hogerheijde & van der Tak 2000, Schöier et al. 2005, Krumholz 2014, among others). These models provide only an insight for the physical and chemical properties of the clouds; the actual nature of the source of energy cannot be determined using those LVG models, see for example Israel (2009a,b). The next level of sophistication over LVG modeling involves the application of photon-dominated region (PDR) models (Ferland et al. 1998, Hollenbach & Tielens 1999, Le Petit et al. 2006, Röllig et al. 2007, Bisbas et al. 2012). These models self-consistently solve for the thermal and chemical structure of clouds irradiated by FUV photons.

In PDRs, energy sources other than FUV photons could dominate the thermal and chemical balance. In the vicinity of an active galactic nucleus (AGN), PDR models can be augmented by models for X-ray dominated region (XDRs Maloney et al. 1996a, Bradford et al. 2003, Meijerink & Spaans 2005, Papadopoulos et al. 2011, Bayet et al. 2011, Meijerink et al. 2011).

In both these models, the underlying assumption is that the thermal balance is dominated by radiation. The physical situation in galaxy centers, star-bursts and dense cores (Pineda et al. 2010) is, however, more complicated. There are other processes, such as mechanical feedback that may also excite the gas mechanically (Loenen et al. 2008, Ossenkopf & Mac Low 2002, Ossenkopf 2002, Kazandjian et al. 2012).

Although these models are much more sophisticated than LVG models, a simplified comparison of many PDR codes[1] (Röllig et al. 2007) has shown that they shed a statistical view on the underlying processes. This is particularly true in the transition zone from atomic to molecular gas, where an order of magnitude difference between the various quantities compared in the models is not uncommon. Such discrepancies are mainly due to the uncertainties in the chemical reaction constants, which in turn influence the reaction rates, abundances and thermal balance (Vasyunin et al. 2004). In addition to those uncertainties observations of extra-galactic sources have spatial resolution limitations. For example the resolution of *Herschel* for the nucleus of NGC 253 is on the order of 1 kpc. The surface area covered by such a beam size contains a large number of clouds. In modeling the nucleus of such galaxies one might need to consider two or more PDRs simultaneously. Although considering more than one PDR component improves the fits significantly, the increased number of free parameters usually has a negative impact on to the statistical significance of those fits. This is particularly valid whenever the number of lines being fitted is low.

Here we follow the modeling of paper I (Kazandjian et al. 2012) where we studied the effect of mechanical heating (Γ_{mech}) by considering its impact on the thermal and chemical structure (abundances, column densities and column density ratios of species) of PDRs. Hence our basic modeling premise will be the same in this paper. Namely, a 1D semi-infinite plane-parallel geometry is adopted. It is assumed that the slab is illuminated with a FUV source from one side. Another major assumption is that the clouds are in an equilibrium state. Since equilibrium is assumed, we consider a simplified recipe in accounting for mechanical feedback. For simplicity, the contribution of mechanical heating to the total heating budget is added in an ad-hoc fashion uniformly throughout the cloud.

Our approximation of the effect of mechanical heating by a single homogeneous heating term is a simplification. In practice, the mechanical energy which could be liberated by supernova events or gas outflows, is deposited locally in shock fronts. In these fronts, which are the interaction surfaces between high speed flows and the ambient medium, the energy is not necessarily distributed uniformly throughout the cloud volume. On the other hand, this energy will eventually cascade to smaller spatial scales and thermalize en route to equilibrium. The efficiency of the "thermalization" is conservatively taken to be

---

[1] In the comparison benchmark the chemistry involved 4 elements (H, He, O and C) and 30 species. For more details on the benchmarks and the codes used see `http://goo.gl/7Hf6mD`

10%. Consequently the approximation we adopt may be less applicable to systems where the dynamical time-scales are comparable to the thermal and chemical time-scales; this occurs for example in clouds in the inner kpc of galaxy centers. Our choice for the ranges in mechanical heating explored is based primarily on estimates by Loenen et al. (2008). They found that fits for the line ratios of the first rotational transition ($J = 1 - 0$) of the molecules HCN, HNC and HCO$^+$ are greatly enhanced by using PDR models which included "additional" heating. They attributed this extra heating to dissipated turbulence and provided an estimate for it. The major conclusion of Paper I was that even small amounts of mechanical heating, as low as 1% of the surface FUV heating, has significant effects on the molecular abundances and column densities. Those effects are mainly manifested as enhanced CO abundances which could increase by up to a factor of two. Although this might not seem a significant effect, the column densities of the high density tracers such as HCN and HNC increase (or decrease) by an order of magnitude depending on the amount of Γ_{mech}.

The aim of this paper is to understand both the ground-state and the more highly excited states of molecular gas in galaxy centers and to determine whether turbulence or shocks can make a major contribution to the molecular emission. In other words, we thus extend the work done in Paper I, which focused on the chemical abundances and column densities only, by studying the signature of mechanical feedback on selected atomic and molecular emission lines.

The models presented in this paper also apply to other regions where the gas is, e.g., (1) heated by young stellar objects (YSO's), (2) stirred up turbulently by the fast motions of stars, or (3) violently heated by supernovae. Since we assume equilibrium, applying our models to those regions is of course an approximation. In all cases, non-negligible amounts of mechanical energy may be eventually injected into the ISM (Leitherer et al. 1999). Part of this energy is then converted to mechanical heating, particularly important in so-called star-burst galaxies.

Since the amount of turbulent energy absorbed by the ISM is a priori unknown, we explore a wide range of possibilities of turbulent heating contributions to PDRs. In our approach, the additional heating self-consistently modifies the emission. In this paper we provide two new estimates of mechanical heating rates and re-enforce our assumptions of Paper I (see the methods section below).

Although we introduce an extra free parameter (the amount of absorbed turbulent energy), the basic molecular abundances and gas parameters are self-consistently determined by the equilibria that we solve for in the PDR models. In the following we explore, using those 1D equilibrium PDR models, the effect of mechanical heating (Γ_{mech}) on atomic and molecular line intensities for a range of densities, FUV flux (G_0), metallicities and column densities. In doing so we aim to find good diagnostics for Γ_{mech} and to check for the usefulness of such PDR models with an additional "ad-hoc" heating term in constraining mechanical heating.

3.2   Methods

A PDR is primarily characterized by its gas number density, the FUV flux of the environment and its spatial extent (usually measured in A_V or alternatively the column density of H). The conversion of A_V to N_H is given by $N_H = 1.87 \cdot 10^{21} A_V (Z_\odot/Z)$ cm^{-2}. In PDRs, the main heating sources are typically the FUV photons irradiating the cloud surface. In addition to FUV heating, cosmic-rays penetrating the molecular interior of clouds also contribute to heating the gas. To this, we now apply increased amounts of (mechanical) heating which might be due to absorbed turbulent energy. We discuss in section-3.2.1 the details of the inclusion of mechanical heating into the PDR models.

In modeling a PDR, we used an optimized version of the PDR code described by Meijerink & Spaans (2005) and Meijerink et al. (2007). For a detailed description of the code, we refer the reader to the methods section of Paper I and to Meijerink & Spaans (2005). The ISM is modeled as a homogeneous cloud of uniform gas density illuminated by a FUV source from the side. For simplicity, the cloud is assumed to be an equilibrium plane-parallel semi-infinite slab. The thermal state and the chemical abundances of all the species within the cloud are solved for self-consistently (for more details see 3.2.2). We explore a parameter space similar to that in Paper I where $1 < n < 10^6$ cm^{-3} and $1 < G_0 < 10^6$. In Fig. 3.1, we show a schematic diagram (a template grid) for the (n, G_0) parameter space, where we highlight some situations in which the ISM could be. We divide the grid into three grades in density: low $(0 < n < 10^2$ cm$^{-3})$, medium $(10^2 < n < 10^5$ cm$^{-3})$ and high $(10^5 < n < 10^6$ cm$^{-3})$. In addition to those two fundamental parameters specifically for a PDR, we study the response of a cloud's emission on increasing amounts of Γ_{mech} for different depths A_V. We specifically consider emission in atomic fine-structure lines of [OI], [CII], and [CI] in addition to the various molecular line transitions of CO, ^{13}CO, HCN, HNC, HCO$^+$, CN, and CS.

A full range of possible "extra" heating rates is explored. From pure PDRs, where heating is dominated by the FUV source, to regions where the heating budget is dominated by turbulence. This allows us not just to constrain the effect of turbulent heating (as we will demonstrate throughout the paper), but also to improve on estimates of molecular cloud column densities in cases where turbulent heating contributions are ignored.

A difference with respect to the approach in Paper I lies in the choice of the Γ_{mech}, parametrization. Based on the conclusions of Paper I, we decided that in a scheme for probing the effects of Γ_{mech} on a grid of PDR models, it is more convenient to include it in the heating budget as a per unit mass term, rather than a per unit volume one (see next section).

In this paper, we consider higher H column densities than included in Paper I, expanding coverage from columns corresponding to $A_V = 10$ mag to columns corresponding to $A_V = 30$ mag. The main constraint on this depth is the limit in the interpolation tables used in the PDR code for computing the self-shielding of CO. In general, the properties deep inside the molecular cloud $(A_V > 10$ mag) are constant. This fact can be exploited to approximate the cloud properties at even higher A_V values.

We note that all figures shown in main text of this paper correspond to PDRs of solar metallicity. We have, in fact, also considered other metallicities, including those as low
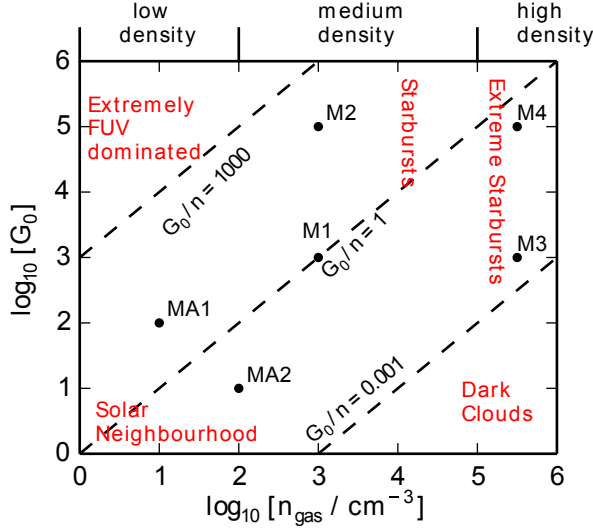
Figure 3.1 – Diagram indicating different regimes in the (n, G_0) parameter space. The labeled points correspond to our reference models used throughout the paper (see Table-3.2).

as $Z = 0.1Z_\odot$ which characterize the most metal-poor dwarf galaxies as well as $Z = 2Z_\odot$ typical to galaxy centers. At any fixed A_V, the corresponding H column density ($N_H = N(H) + 2N(H_2)$) is taken to depend inversely on the cloud metallicity in a linear fashion. We illustrate this as follows. PDRs with the lowest metallicity and highest $A_V = 30$ mag considered will have $N_H = 5.6 \times 10^{23}$ cm^{-2} compared to $N_H = 9.4 \times 10^{21}$ cm^{-2} for clouds with a $Z = 2Z_\odot$ and an $A_V = 10$ mag. Figures corresponding to non-solar metallicity conditions can be found in the Appendix.

3.2.1   Mechanical heating

A major conclusion of Paper I was that mechanical heating must not be neglected in calculating heating-cooling balances. Addition of a modest amount of mechanical heating to the cloud volume, corresponding to no more than a small fraction of the FUV surface heating, already suffices to alter the chemistry of the PDR significantly.

The PDR model grids in Paper I were parametrized by n (first axis - horizontal axis), G_0 (second axis - vertical axis) and Γ_{mech} (per unit volume, third axis). The parameter space was sampled by picking equidistant points in log space for each axis. The disadvantage of such a representation is that for all the models each grid (as a function of n and G_0) has the same amount of Γ_{mech} independent of n. For example, a cloud with $n = 1$ cm^{-3} would have the same amount of Γ_{mech} added as one with $n = 10^6$ cm^{-3}. What might be a huge amount for the former cloud would be negligible for the latter. It is thus preferable to parametrize Γ_{mech} adaptively for each density level. In the following,

the third axis is replaced by the new parametrization of Γ_{mech}. This new parametrization is defined using the symbol α where :

$$\alpha = \frac{\Gamma_{mech}}{\Gamma_{surf}} \sim \frac{\Gamma_{mech}}{\Gamma_{photo}} \tag{3.1}$$

where Γ_{surf} is the total heating rate at the surface of the PDR (at $A_V = 0$ mag), and Γ_{photo} is the photo-electric heating rate. The expression relating it to n and G_0 is $\Gamma_{photo} = \epsilon_0 G_0 n$, where ϵ is the heating efficiency. The treatment of mechanical heating in terms of the total surface heating is to a high degree of accuracy equivalent to a parametrization as a function of Γ_{photo}. Γ_{photo} is linearly proportional to n. For a certain section in α (in the third axis) each model thus has a Γ_{mech} proportional to its density. We note that this new parametrization is also equivalent to saying that Γ_{mech} is added per unit mass, since multiplying n by m_H (the mass of a hydrogen atom) corresponds to a mass density.

To make this clear, we will now consider an example. The case $\alpha = 0$ corresponds to a situation where no mechanical heating is present in the PDR (what we call this a reference or pure PDR model). On the other hand, the case $\alpha = 1$ represents a model where the amount of mechanical heating added to the reference model, is equivalent to the heating at its surface. We now point the reader to the right panel of Fig. 3.2, which is a grid of reference models (i.e, a section in $\alpha = 0$). For example, the surface heating for a model with $n = 10^4$ cm^{-3} and $G_0 = 10^3$ is $\sim 10^{-19}$ erg cm^{-3} s^{-1}. In a grid with $\alpha = 0.01$, this model would have an amount $\Gamma_{mech} = 0.01 \times 10^{-19} = 10^{-21}$ erg cm^{-3} s^{-1} added to its heating budget. More such examples are summarized in Table-3.1.
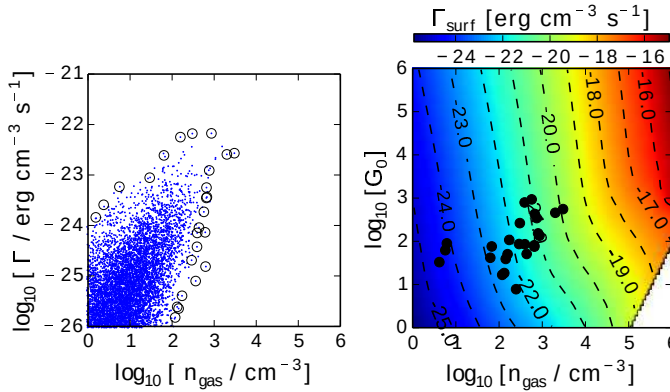
Figure 3.2 – (Left) Mechanical heating rates applied to the SPH simulation of a dwarf galaxy (Pelupessy 2005, Pelupessy & Papadopoulos 2009). The maximum heating rate is $\sim 10^{-22}$ erg cm^{-3} s^{-1}. (Right) Surface heating (Γ_{surf}) for zero mechanical heating ($\alpha = 0$) for Z = Z$_\odot$. The heating rates range from $\sim 10^{-22}$ to $\sim 10^{-20}$ erg cm^{-3} s^{-1} at $n \sim 10^3$ cm^{-3}. An SPH particle with $n \sim 10^3$ cm^{-3} and a maximum Γ_{mech} (in the simulation) would have an $\alpha = 1$ and 0.1 if its G_0 is 1 and 10^3 respectively. The black points in the right panel correspond to the boundary points in n and Γ_{mech} distribution (plotted as open circles in the left panel) .

n	G_0	Γ_{mech}	α	SFR density
(cm^{-3})		(erg cm^{-3} s^{-1})		(M$_\odot$ yr^{-1} kpc^{-3})
10^2	1.0	3.5×10^{-27}	1×10^{-4}	< 0.01
10^4	10^3	2.1×10^{-22}	2×10^{-3}	~ 2
10^4	10^4	2.1×10^{-21}	4×10^{-3}	~ 20
$10^{4.5}$	10^5	2.1×10^{-20}	1×10^{-2}	~ 200
10^6	10^5	3.4×10^{-17}	0.3	> 1000

Table 3.1 – Mechanical heating rates for different densities and FUV luminosities for models whose metallicity is Z = Z$_\odot$. These models span the full density and FUV ranges we have explored. Almost the full range of mechanical heating rates are also covered, from quiescent discs (first row) to highly turbulent star-bursts (last row).

A simple recipe (also adopted in Paper I) for estimates of Γ_{mech} in a star-burst is presented in Loenen et al. (2008). One of the main assumptions concerns the fraction of the energy of a super-nova (SN hereafter) event transferred into heating the ISM (η_{trans}), which was assumed to be 10%. However, η_{trans} is not well known in general. The amount of turbulent energy transferred into heating the ISM, Γ_{mech}, is also related to η_{trans}. For this reason we consider values of α ranging for 0 to 1. This range would cover most heating rates that would be a result from the full range of η_{trans}. As an example, α could be related to the local SFR in a star-burst. In general, a higher SFR would result in a high SN rate, thus a larger α as shown in Table-3.1.

Moreover, we used the mechanical luminosity curves in Leitherer et al. (1999) as an independent method of estimating the amount of Γ_{mech} that can be disposed into the ISM. In Leitherer et al. (1999), stellar population synthesis models are used to predict spectrophotometric properties of active star-forming regions. Fig. 111 to 114 in that paper, provide predictions for the mechanical luminosity over a time-span of 1 Gyr, both for an instantaneous star-burst ($L_{\mathrm{mech}} = 10^{40} - 10^{41}$ erg/s) and a continuous one ($L_{\mathrm{mech}} = 10^{42}$ erg/s). The mass of the stars formed during these two scenarios is 10^6 M$_\odot$. If we assume that this occurs in a box whose size is 100 pc (the same spatial scale used in Loenen et al. 2008), we obtain a $\Gamma_{\mathrm{mech}} \sim 10^{-20}$ erg cm^{-3} s^{-1} and $\Gamma_{\mathrm{mech}} \sim 10^{-22} - 10^{-21}$ erg cm^{-3} s^{-1} for the continuous and the instantaneous star-burst scenarios respectively. In computing those estimates, we assumed that the mechanical luminosity is fully absorbed by the ISM since they occur over a time-span of at least 50 Myr, which is much longer than the chemical time-scale.

Our final attempt to estimate Γ_{mech} relied on extracting the mechanical feedback from softened particle hydrodynamics simulations of dwarf galaxies (Pelupessy & Papadopoulos 2009). There, the mechanical heating is computed self-consistently in the SPH code. In the left panel of Fig. 3.2, we show the mechanical heating rate (per unit volume) as a function of the gas density of the SPH particles. It is quite comforting to note that, although the previous two methods were quite simplistic, the estimated mechanical heating rates are close to those obtained by the SPH simulation for the same density range.

3.2.2   Radiative transfer

Two methods were used in computing the radiative transfer of the atomic and molecular lines. Those of the atomic fine-structure (hereafter FS) lines were computed self-consistently within the PDR code (for the details see Meijerink & Spaans 2005). For these lines the temperature gradient within the slab has been taken into account.

In computing the emission of the molecular species the statistical equilibrium non-LTE radiative transfer code RADEX (Schöier et al. 2005) was used. In order to account for clouds with different depths, the various emission were computed for different A_V. This is equivalent to saying that we considered a semi-finite slab illuminated by a FUV source from one side (the primary FUV source). In using this approximation the FUV flux from a source, which could be on the other side of the truncated slab model, is ignored. Accounting for that second source would be important in the case when A_V is low (< 1 mag) and when the lines are optically thin. Although the lowest A_V we considered was 5 mag, the worst case scenario even for high A_v is when the secondary FUV source (from the other side) has the same strength as the primary. In this case, ignoring the secondary FUV source would reduce the emission by at least half the amount. For our purposes, since we would be looking at line ratios and at clouds with $A_V > 5$ mag, we expect this approximation to be satisfactory. Hence, for simplicity we assume that the semi-infinite slab is illuminated by a FUV source from one side only. There are PDR codes which allow for a secondary FUV source, for example Le Petit et al. (2006). An even more advanced PDR code which allows for an arbitrary 3D geometry has been developed by Bisbas et al. (2012).

The large velocity gradient (LVG) approximation upon which RADEX is based does not take into account a PDR temperature gradient. For the molecular species, this is not crucial, for two reasons: firstly, molecules are only abundant in regions beyond $A_V \gtrsim 5$ mag. In those regions the molecular abundances are at least two orders of magnitude higher than those close to the surface of the PDR ($A_V = 0$ mag). Secondly, deep into the cloud where $A_V \gtrsim 5$ mag temperatures are practically constant, very different from the steep temperature gradients close to the PDR surface.

Although the temperature is almost constant in the molecular zone, we tried to account for the contribution of the temperature gradient of the atomic and radical zones by using a weighted average of the quantities required to compute the emission. The gas kinetic temperature and the densities of the colliding species (mainly H_2) were weighted against the density of the species of interest. The weighted temperatures are $\sim 3\%$ higher than the saturated kinetic temperatures in the molecular zone. This is due to higher kinetic temperatures at the surface compared to those in the molecular zone. In contrast the weighted density of the colliding species was about 5% lower than those in the molecular zone. This reflects the fact that H_2 has a much lower abundance near the surface of the cloud compared to that at the molecular zone. These two counteracting effects, higher temperature and lower abundances result in a 1% increase in the emission compared to the case where no weighting was done.

The densities of the colliders are also weighted with respect to the abundances of species whose emission are being computed. The colliders considered were H_2, H^+, He

47

and e$^-$. Finally, a background radiation field corresponding to that of the current day CMB is used by RADEX. One of the assumptions we adopted, which affects the outcome of the line ratios of ^{13}CO to CO, is the elemental abundance of C and ^{13}C. Since we opted to keep the number of parameter low for this exploratory investigation, we chose C / ^{13}C = 40 for all our models, even for models with higher and lower metallicities. The actual ratio could be as high as 90 and as low as 20 in our galaxy (Savage et al. 2002). Since we picked a lower value, we expect that variations over the possible range would only decrease the emission of ^{13}CO; hence leading for line ratios involving ^{13}CO/CO to decrease.

One of the main advantages offered by the use of RADEX (one-zone approximation) over a calculation based on the temperature gradient is the much greater speed of computation. For each model, the LVG approximation requires only one computation of the population densities. In contrast, it would have been necessary to compute the population densities for each slab of the discretized PDR when taking the temperature gradient into account.

It still remains to decide what micro-turbulence line width to use. Since most molecular line emission emanates from the shielded region where $A_V > 5$ mag and where the gas is relatively cold, the line widths there are expected to be low. Again, here we resort to the simulations of Pelupessy & Papadopoulos (2009), where for such clouds, the mean velocity dispersion is on the order of few km/s. We considered other line widths as well but the qualitative dependence of the line ratios was not affected. Hence, for simplicity we used a micro-turbulence line-width of 1 km/s for all our models. We note that this line width should not be confused with the measured (observed) line-width. The measured line-width would be due to the contribution of multiple clouds along the line of sight. For extra-galactic sources, this line-width would be much larger than the micro-turbulence line-width.

As a check on the validity of using LVG models, we compared the emission grids computed with the LVG approximation to those computed by Meijerink et al. (2007). Although the grids in Meijerink et al. (2007) have been computed taking into account the temperature gradient in the PDR , they agree quite well with the ones we computed here with RADEX. As an independent check, the grids without Γ_{mech} agreed quite well with the ones computed by Kaufman et al. (1999).

3.3   Results

Atomic fine-structure and molecular emission lines are studied in order to see how mechanical feedback could affect their emission and their various line ratios. Here we present results from the reference models summarized in Table-3.2, and highlight some emission grids. The grids for different column densities are presented in the Appendix. We start by presenting results of the atomic lines, followed by those for molecular species. For each of the species considered we highlight the main chemical and radiative factors which effect their emission. Once we have characterized the effect of mechanical feedback on the emission of the reference models and the model grids, we proceed by highlighting trends

in the line ratios which could be used as diagnostics for mechanical feedback in the ISM.

Model Name	$\log n$ (cm^{-3})	$\log G_0$
MA1	1.0	2.0
MA2	2.0	1.0
M1	3.0	3.0
M2	3.0	5.0
M3	5.5	3.0
M4	5.5	5.0

Table 3.2 – This is a list of the reference models for typical PDRs used in this paper. The models in the top part (MA1 and MA2) are particularly useful for studying the line emission of the atomic species (the FS lines). Since molecular line emission is too low to be relevant in these two low-density models, higher density models are also considered (M1 to M4). All these models are identical to the reference models from Paper I and Meijerink & Spaans (2005). M1 and M2 correspond to low-density clouds in star-bursting galaxy centers, whereas M3 and M4 correspond to much denser clouds where excitation of high density gas tracers such as HCN are possible. These models are also shown in our template grid in Fig. 3.1.

3.3.1   Atomic species - intensities

FS lines such as [OI] 63 μm and [CII] 158 μm are the dominant coolants in PDRs. High temperatures (> 100K) are necessary to have a bright emission of those lines. Thus, most of the emission originates from the surface layer of the PDR where $N_{\mathrm{H}} < 10^{21}$ cm^{-2}. The temperatures drop with increasing N_{H} as such column densities are optically thick for FUV photons (Hollenbach & Gorti 2009). In Fig. 3.3 we show the integrated cooling rate as a function of depth (A_V) for M1. From a qualitative point of view, the cooling budgets for the remaining models are similar. The purpose of this figure is to illustrate the steep dependence of the FS cooling as a function of A_V. We also see here that the cooling due to the lowest transition of the molecular species considered adds up to less than ~1% of the total cooling.

Although most of the FS emission emanates from the PDR's surface section, the molecular zone also contributes. This contribution of the molecular zone to the FS cooling is important when considering line ratios. It depends on the location of the C$^+$/C/CO transition zone. A fast transition (as a function of A_V) from C$^+$ to C, would result in a lower abundance of C$^+$ (thus lower emission). Usually, the A_V where the C$^+$/C/CO transition zone occurs is closer to the surface for PDRs with high densities than clouds with low densities. This phenomenon is described in more detail in Kazandjian et al. (2012). For example, in low-density PDRs the abundances of C$^+$ (x_{C^+}) decreases slightly from $\sim 10^{-4}$ (at the surface) to $\sim 10^{-5}$ in the molecular zone. However, a much greater decrease in x_{C^+} is observed in the molecular zone of medium and high-density PDRs; there x_{C^+} decreases to $\sim 10^{-10}$. Consequently, we expect to find higher contributions to C$^+$ cooling from the molecular zones in low- density clouds than in high-density clouds.
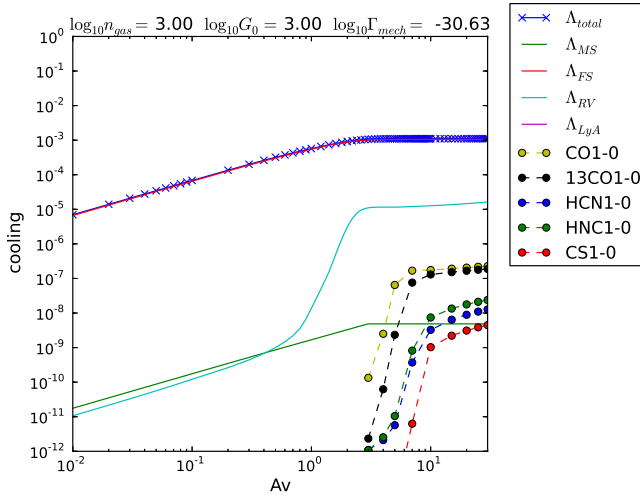
Figure 3.3 – Integrated cooling rates (in erg cm^{-2} s^{-1}) $\int_0^{A_v} \Lambda(A'_v)dA'_v$ as a function of A$_V$ for the various cooling mechanisms included in the PDR code. The curves for the total cooling (blue with crosses) and the FS cooling curve overlap. The remaining solid curves (MS for meta-stable line cooling, RV for ro-vibrational cooling of H$_2$, and LyA for the Lyman-alpha cooling) are shown for completeness. The dotted curves (with filled circles) are the first rotational transitions for the molecular species computed using LVG models.

A similar analysis applies to the other FS lines of C and O. For example in clouds which are highly dominated by FUV radiation (see Fig. 3.1) atomic abundances remain relatively high in the molecular zone. At the surface $10^{-6} < x_{C^+} < 10^{-4}$ and $x_C \sim 10^{-4}$ due to the high flux of FUV photons which can penetrate deep into the clouds. Hence recombination is less effective in locking the atoms into molecules. At densities $n > 10^3$ cm^{-3}, the FUV photons are blocked by higher columns of CO resulting in $x_{C^+} < 10^{-8}$ and $x_C < 10^{-6}$.

The intensity of the emission depends mainly on the chemical abundances of the species in question (discussed in the previous two paragraphs) and strongly on the kinetic temperature of the gas. Here we investigate the effect of Γ_{mech} on the emission from the atomic and molecular zones, by looking at its effect on the kinetic temperature of the gas. In general, we expect the emission to be enhanced as Γ_{mech} is introduced into a PDR. At the surface, mechanical feedback increases the temperatures at most by a factor of three, even for the highest Γ_{mech} considered. As an example, in the low G_0/n ($\sim 0.01 - 10$) models such as MA1 and MA2, the surface temperature increases from 110 K to 300 K without mechanical heating ($\alpha = 0$, see Eq. 3.1 and Fig. 3.2) and from 2200 K to 4500 K for maximum Γ_{mech} ($\alpha = 1.0$), respectively. Note that the surface of low density PDRs is a lot more sensitive to Γ_{mech} compared to the high density ones. Moreover, the temperature increase in the molecular zone is much greater. For instance in the low density PDRs, we

50

line	ν (GHz)	λ (μm)	n_{cr} (cm^{-3})	E/k_b (K)
Atomic				
[OI]	4759	63	5.0×10^5 (H)	228
[CI]	809	369	3.0×10^2 (L)	63
[CI]	492	609	2.0×10^3 (M)	24
[CII]	1897	158	2.8×10^3 (M)	92
Molecular				
CO(1-0)[a]	115	2602	2.2×10^3 (M)	5.53
CO(2-1)	230	1301	1.2×10^4 (M)	16.6
CO(3-2)	346	867.6	3.8×10^4 (M)	33.2
CO(4-3)	461	650.7	9.1×10^4 (M)	55.3
CO(6-5)	691	433.9	3.0×10^5 (H)	116
CO(7-6)	806	371.9	4.6×10^5 (H)	155
CO(10-9)	1151	260.4	1.1×10^6 (H)	304
CO(16-15)	1841	162.9	3.5×10^6 (H)	751
^{13}CO(1-0)[a]	110	2722	1.9×10^3 (M)	5.29
^{13}CO(2-1)	220	1361	1.0×10^4 (M)	15.9
^{13}CO(3-2)	330	907.5	3.3×10^4 (M)	31.7
^{13}CO(6-5)	661	453.8	2.6×10^5 (H)	111
HCN(1-0)[b]	88.6	3384	2.0×10^6 (H)	4.25
HCN(4-3)	354	846.3	2.1×10^8 (H)	42.5
HNC(1-0)[b]	90.7	3309	3.6×10^5 (H)	4.35
HNC(4-3)	362	827.6	2.1×10^7 (H)	43.5
HCO$^+$(1-0)[c]	89.2	3363	2.1×10^5 (H)	4.28
HCO$^+$(4-3)	356	841.0	9.3×10^6 (H)	42.8
CS(1-0)[d]	45.0	6123	5.4×10^4 (M)	2.35
CS(4-3)	196	1531	3.0×10^6 (H)	23.5
CN($1_{1/2}$-$0_{1/2}$)[e]	113	2651	1.8×10^6 (H)	5.43
CN($2_{3/2}$-$1_{3/2}$)	226	1325	4.7×10^6 (H)	16.3

Table 3.3 – Critical densities and the transition (excitation) energies for the atomic FS lines and the molecular lines. The critical densities for the molecular lines displayed were computed for a kinetic temperature of 50K; whereas the one for the FS lines were computed at 500K. The values of n_{cr} are shown to give the reader an idea of the regime for the densities where the species would be at LTE or not. The symbols "L" (low), "M" (medium), "H" (high) indicate the range in density where the n_{cr} of the corresponding transition lies..

[a] Yang et al. (2010)

[b] Dumouchel et al. (2010), Green & Thaddeus (1974)

[c] Botschwina et al. (1993)

[d] Lique et al. (2006)

[e] Klisch et al. (1995), Lique et al. (2010)

see a boost from ~ 10K to 100K in MA2 and MA1 whenever $\Gamma_{\text{mech}} = 0.1\Gamma_{\text{surf}}$.

We now turn our attention to the contribution of the molecular zone to the integrated luminosity of the FS lines. In pure PDRs ($\alpha = 0$) which are in the $G_0/n \gg 1$ regime, at least 2% of the integrated luminosity comes from depths with $A_V > 5$ mag. Since Γ_{mech} increases temperatures in the molecular zone, we expect the FS line emission to increase as well (this is explained in more detail in section-3.3.3). For instance, when $\alpha = 0.25$ the contribution of the molecular zone increases to $\sim 10\%$ for clouds with $A_V = 10$ mag. For clouds with higher A_V (~ 30 mag) this contribution increases further up to 50%.

In the top panel of Fig. 3.4, we show the emission grid of the [CII] 158 μm FS line. This grid agrees very well with that shown in Fig. 3 in Kaufman et al. (1999). In the lower panel, we illustrate the relative changes in the emission of that same grid as a function of α. We see that the [CII] 158 μm FS line emission depends weakly on Γ_{mech} whenever it is below 0.5 Γ_{surf} ($\alpha < 0.5$). Whenever $\alpha \geq 0.5$ low density PDRs such as MA1 and MA2 show an increases in the emission by up to a factor of two. The mid- and high-density PDRs whose $G_0 > 10^2$ are hardly affected. The emission of [OI] 63 μm, [CI] 369 μm , and [CI] 609 μm exhibit a stronger dependence on Γ_{mech}. These grids are shown in Fig. A.1 in Appendix-A.

As a basis for discussion, we first highlight some of the main features of the FS emission grids in the absence of any Γ_{mech} contribution. (1) Emission intensities increase as G_0 increases (see the top panels of Fig. 3.4 and Fig. A.1). This is caused by the ability of the FUV photons to penetrate deeper into the cloud at fixed n but higher G_0, thus leading to a thicker atomic region. (2) Emission peaks near the critical densities of the lines (n_{cr} hereafter). Those n_{cr} are around 10^3 cm^{-3} with the exception of the critical density of the [OI] line which lies in the high density region. Both excitation energy E_{ul}/k_B and n_{cr} for all the lines are listed in Table-3.3. (3) The emission intensities range from 10^{-6} erg cm^{-2} s^{-1} to 10^{-2} erg cm^{-2} s^{-1} , spanning four orders of magnitude. This is significantly brighter than the molecular emission (see section-3.3.3), which peaks at 10^{-5} erg cm^{-2} s^{-1}. The range in the intensities of the atomic fine-structure lines is narrower than that of the molecular lines. (4) When Γ_{mech} is introduced the emission in enhanced for $n < n_{cr}$; the opposite is observed for $n > n_{cr}$. This is particularly valid for the neutral and atomic species (see the bottom panels of Fig. 3.4 and Fig. A.1).

Here we focus on the last point mentioned in the previous paragraph. Particularly we try to determine the reason causing the different behavior of the emission for $n < n_{cr}$ vs $n > n_{cr}$. The boost in the emission could be due to an increase in temperature, or in abundance, or both. By analyzing the chemistry we see that the dominant reactions remain the same (up to $\alpha \sim 0.1$) for $n < n_{cr}$. Moreover, there are no fundamental changes in the abundances for $n < n_{cr}$. This ties the emission boost to the increasing amounts of Γ_{mech} that raise the gas temperature, particularly in the molecular region.

Let us now consider the part of the parameter space in the grid where $n > n_{\text{cr}}$. The emission tends to decrease whenever $\alpha > 0.1$. The only exception to this occurs in the emission grid for the [OI] 63 μm line (see rightmost panel in the bottom row of Fig. A.1). At such densities, O maintains a much higher abundance than C$^+$ in the molecular zone. Hence the strongest decrease is seen for the two neutral carbon lines [CI] 369 μm and
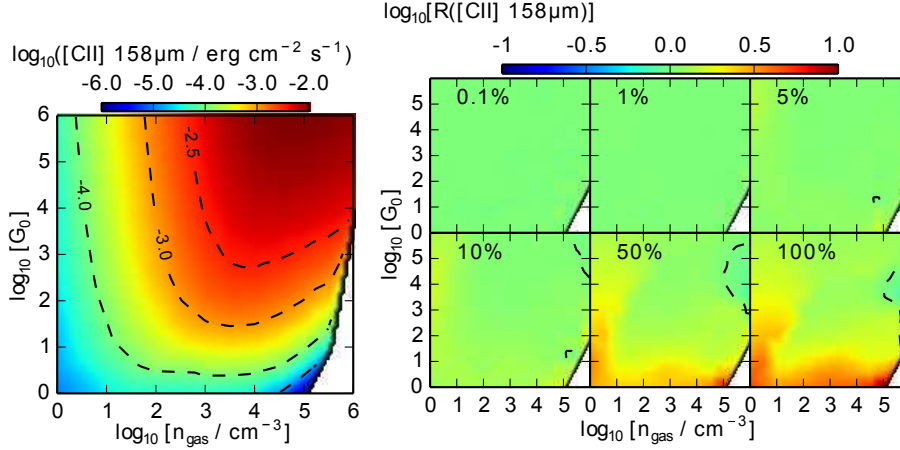
Figure 3.4 – [**Left**] The reference grid for the [CII] 158 μm line emission for PDRs without mechanical heating. [**Right**] [CII] 158 μm line emission corresponding to different value of α labeled at the top of each panel. Each model in the grid has an additional amount of heating introduced to its energy budget. The added Γ_{mech} is in terms of a percentage of the surface heating (as explained in the methods section). Each grid shows the percentage change (increase or decrease) in emission relative to that in the reference grid in the left panel. For instance, when $\Gamma_{mech} = 0.5\Gamma_{surf}$ ($\alpha = 0.5$) (panel with the 50% label), the emission in MA1 is enhanced by a factor of ~ 3. A decrease in emission is observed only when $\Gamma_{mech} > 0.5\Gamma_{surf}$ to the right of the contour line at M4. We define the relative change as $R = I(\alpha)/I(\alpha = 0)$, where $I(\alpha)$ is the emission intensity of the line at a specific value of α. Here and in all such subsequent plots the dashed contour line traces $R = 1$. On this line the emission with and without extra heating are the same. In other words, models on this line experience no change in the emission because of Γ_{mech}. In general 'redder' regions correspond to enhanced emission, whereas 'bluer' regions indicated regions where emission are suppressed.

[CI] 609 μm (see left and middle panels of Fig. A.1) whereas the opposite is observed for [OI] 63 μm . We will discuss each of those below.

The high density region of the [CII] 158 μm grid reveals a decrease in the emission only in extreme cases ($\alpha > 0.5$). This is seen most clearly to the right of the dashed line in the panels for $\alpha = 0.1$, 0.5 and 1 in Fig. 3.4). This is simply because C$^+$ becomes un-abundant at high densities ($n \gtrsim 10^5$ cm^{-3}).

The emission of [OI] 63 μm is more interesting but less trivial to explain, since it is the result of an interplay between the cooling due to the FS lines and the additional Γ_{mech}. We have already mentioned that [OI] 63 μm is the dominant cooling line in all the models. As Γ_{mech} is added more cooling is required to maintain a thermal balance. This occurs by increasing the gas temperature throughout the PDR which in turn boosts the total cooling rate by increasing the [OI] 63 μm emission. At the densities of interest here ($n > 10^4$ cm^{-3}) and with $\alpha > 0.5$, x_O decreases from 10^{-4} to 10^{-8} in the molecular zone due to the dominant reaction of O with OH. Notwithstanding the steep decrease in x_O, the [OI] 63 μm emission increases because of the much higher temperatures.

Finally, the reduction in the [CI] emission (at high densities) when Γ_{mech} is introduced, is due to x_C decreasing by an order of magnitude in the atomic region of the PDR; dropping from $\sim 10^{-4}$ to $\sim 10^{-5}$ where most of the emission comes from. We discuss this for an extreme PDR with conditions typical for an extreme star-burst ($n = 10^6$ cm^{-3} and $G_0 = 10^6$). There the emission decrease is greatest. This decrease is due to the reduced production rate (by one order of magnitude) of C through the neutral-neutral reaction of H with CH. Moreover, higher abundances of H_2 in the atomic region enhance the radiative association reaction of C with H_2, leading to a faster destruction of C. These two processes results in a reduction of x_C throughout the PDR leading to lower emission.

The different dependence on Γ_{mech} throughout the grids of the lines encourages us to look in detail at the various combinations of line ratios in an attempt to identify effective diagnostics for Γ_{mech}. We first summarize the most important model emission features that play a role in determining the ratios:

- For pure PDRs (without Γ_{mech}) we can safely say that the majority of the FS emission are from the surface of the cloud and up to $A_V = 10$ mag. Particularly, [OI] 63 μm and [CII] 158 μm saturate at $A_V \sim 5$ mag.

- When Γ_{mech} is introduced, the molecular zone contributes increasingly to the integrated emission of the lines, especially those of [CI]. When $n < n_{cr}$ more than half of the emission in these lines is from the molecular zone. Hence, line ratios might depend on the column densities of the PDRs considered.

- As Γ_{mech} increases, emission of the FS lines for clouds with $n < n_{\text{cr}}$ increases; whereas it tends to decrease above that density (except for [OI]).

3.3.2   Atomic species - line ratios

So far we have touched upon the intensities of the emission of FS lines. What actually matters is the relative enhancement of one emission line compared to another (i.e., the line ratio); this is a commonly used technique since understanding line ratios sheds insight on the underlying excitation mechanism(s) of such emission. In Fig. 3.5, we show (for the reference models) all the possible combinations of line-ratios of the FS lines that we considered. The analogous figures for metallicities either higher or lower than solar are presented in Fig. A.2. We note that the line ratios apply to fixed cloud sizes ($A_V = 10$ mag).

The very low-density models (MA1 and MA2) show a distinctive response to Γ_{mech} in comparison to the rest of the models. Only in these two models, some of the line ratios (expressed on log-scales) change sign i.e., the ratio changes from being below unity to above unity or vice-versa due to one line becoming brighter than the other.

For instance, in MA1, the ionized to neutral atomic carbon line ratio [CII] 158μm/[CI] 369μm shows a very nice dependence on Γ_{mech}. It decreases from ~ 15 to unity as Γ_{mech} increases. A similar behavior is observed for MA2, but the ratio saturates to ~ 3 at high α. Another interesting line ratio is that of neutral oxygen to neutral carbon ([OI] 63μm/[CI] 369μm), which exhibits a very strong response to Γ_{mech}. The ratio decreases

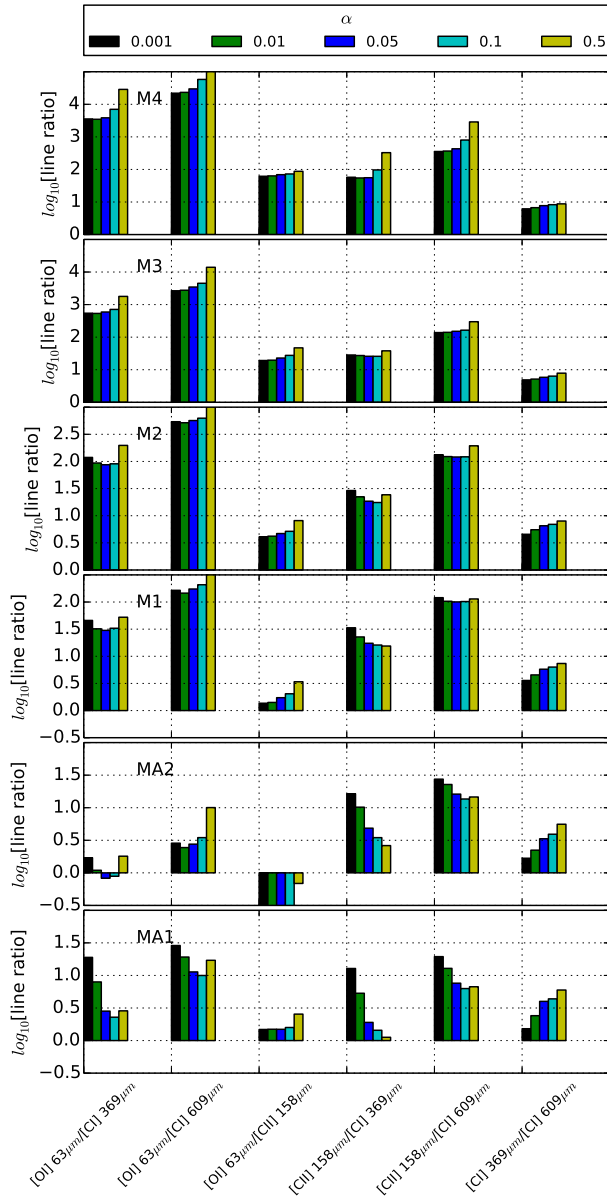Figure 3.5 – Fine-structure line ratios for different values of Γ_{mech} ($Z = Z_\odot$) for the reference models.

as α increases. The reason for this is the fact that the [CI] 369μm line is enhanced (and becomes stronger than the [OI] 63μm line) due to the low energy of the [CI] 369μm transition (24 K) compared to the 228 K of the [OI] 63μm line. Hence, the [OI] 63μm emission remains restricted to the surface, whereas the total emission of [CI] 369μm gets a significant contribution from the deeper molecular interior. This line ratio decreases by approximately a factor of ten for MA1 (from $\sim$ 20 to $\sim$ 3) when Γ_{mech} is as low as 5% of the surface heating. A less distinctive behavior is observed in MA2, where the line ratio decreases from $\sim$ 2 to $\sim$ 1 and increases again to above 2 for $\alpha = 0.5$. In MA1, the ratio of the principal cooling lines, neutral oxygen to singly ionized carbon ([OI] 63μm/[CII] 158μm), has a weak dependence on Γ_{mech}. It increases only for extreme mechanical heating rates corresponding to $\alpha = 0.5$. More interestingly, in MA2 the ratio has a stronger dependence of Γ_{mech} approaching unity (from $\sim$ 0.3) as α increases. This is explained by the fact that as α increases, temperatures increase as well. Since x_{O} is about 100 times higher in the molecular zone than x_{C}, the [OI] 63μm emission increases. This occurs despite the fact that the transition energy for the [CII] 158 μm line is less than half that of the [OI] 63 μm line. A similar behavior is observed in M1, but there the ratios increase from 1 to $\sim$ 3.

The neutral carbon-carbon line ratio [CI] 369μm/[CI] 609μm is particularly interesting since it involves FS lines of the same atomic species; hence the line ratio depends purely on the radiative properties of the lines and neither on the chemistry nor the column density. In MA1, we see a steady increase in the ratio from 1 to $\sim$ 5 for $\alpha = 0.05$. This can be easily explained. As Γ_{mech} causes temperatures to rise, the upper levels become more populated, so that the third level involving the [CI] 369 μm line becomes brighter than [CI] 609μm. For a detailed discussion on level populations see section-3.3.3. The C[II] 158μm/[CI] 609μm and [OI] 63μm/[CI] 609μm ratios do not exhibit any very interesting dependence on Γ_{mech}. They are shown just for completeness.

The high-density models M1 to M4 exhibit a slow monotonous (either increasing or decreasing) dependence on Γ_{mech}. The ratios in these models are generally $\gtrsim$ 10 even for $\alpha = 0$. This is also true for extreme mechanical heating rates $\alpha = 1$ (except for [OI] 63μm/[CII] 158μm in M1). Unlike the low density models, models M1 to M4 exhibit a jump in the line ratios only when $\alpha \gtrsim 0.5$.

In summary, what we have found in this section that [CII] 158μm/[CI] 369μm, [OI] 63μm/[CI] 369μm and [CI] 369μm/[CI] 609μm are good diagnostic line ratios for low density clouds. One can use those lines to constrain Γ_{mech} if the density, G_0 and the A_V of the object are known. Those line ratios show a stronger dependence on Γ_{mech} at higher or lower metallicities as well, except in models at $Z = 0.1 Z_{\odot}$ (see Fig. A.2). However, further investigation is needed in-order to see if atomic line ratios are good diagnostics of mechanical feedback for the whole range in density, G_0 and A_V. In addition to the reference models, the grids of the line ratios from which those models were picked are presented in Fig. A.3.

56

3.3.3 Molecular species

The molecular emission lines were computed with LVG models , unlike those of the atomic species which were computed within the discretized PDR. We utilized the LVG code RADEX (Schöier et al. 2005) in computing all the emission intensity grids. In this paper, we have limited ourselves to the rotational line emission from CO, ^{13}CO, HCO$^+$, HCN, HNC, CS, and CN.

We first present an analysis that is common to most of the molecular lines considered. In pure PDRs ($\alpha = 0$), the gas temperatures in the molecular region are very low (10 $\sim$ 15 K) and vary little within the grid (see the grids corresponding to $\alpha = 0$ in Appendix B for all the molecular species). Thus, whenever the gas density of a cloud is below the critical density (n_{cr}) of the line considered, the chemistry determines the shape of the contours in the emission grid. There the contour lines are independent of G_0 and appear as almost vertical lines. Also in the absence of Γ_{mech} , the emission contours follow the shape of the temperature contours of the molecular region. This is particularly valid in the case of the high-J transitions. However, when we introduce Γ_{mech}, the chemistry is altered significantly along with the gas temperature. This causes the emission to increase by orders of magnitude (cf, the figures for CO with Γ_{mech} in the Appendix).

On the other hand, for densities above n_{cr}, the contours in the emission grids depend mainly on temperature. This is not surprising, as we may demonstrate by considering a simple two level system. The ratio of the upper population density (x_2) to the lower one (x_1) at equilibrium is (Draine 2010):

$$\frac{x_2}{x_1} = \frac{1}{1 + n_{cr}/n_{col}} \frac{g_2}{g_1} \exp\left(-\frac{T_{12}}{T_{kin}}\right) \tag{3.2}$$

where n_{col} is the density of the colliding species (mainly H$_2$). g_1 and g_2 are the degeneracies of the lower and upper levels respectively and T_{12} is the energy difference of the two levels in Kelvin (E_{12}/k_b). For simplicity, we assume $n_{col} = n(H_2)$, and also ignore a second term on the right involving the radiation temperature (T_{rad}) that introduces only minor changes in the LVG treatment (since $T_{rad} = T_{cmb} \ll T_{kin}$ in general).

When $n_{col} \gg n_{cr}$, this equation reduces to:

$$\frac{x_2}{x_1} = \frac{g_2}{g_1} \exp\left(-\frac{T_{12}}{T_{kin}}\right), \tag{3.3}$$

which is independent of the gas density, and depends only on the kinetic gas temperature. Also, when $n_{col} > n_{cr}$, all the lines are thermalized, and the excitation temperature is effectively equal to the gas temperature. Although these equations are for a two-level system, they provide a general idea of what might be happening in a multi-level systems (which might include multiple colliding species whenever the rates are available).

As Γ_{mech} is introduced, the higher transitions gain prominence since relative temperature increases are high. This in turn leads to increased high-level populations (see the left panel of Fig. 3.6). Another way to look at the pumping of the higher levels is by looking at the collision rate coefficients K_{12} and K_{21}. Ignoring degeneracies, those two are related via $K_{12} \sim K_{21} \exp(-T_{12}/T_{kin})$.

57

Another interesting common feature is the optical depth at the line center, τ_0. We observe that it decreases as a function of increasing Γ_{mech}. As temperatures increase, more levels get populated leading to smaller optical depths. These are shown in Fig. 3.6, which shows the CO ladder along with curves for τ_0 for a range in Γ_{mech}. In the right panel, the trend in τ_0 is clearly visible.
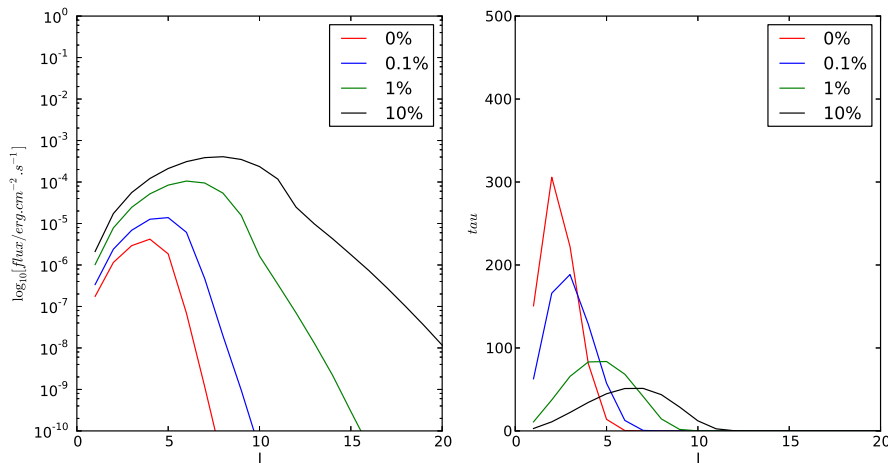

Figure 3.6 – CO ladders for a PDR model with $n = 10^3$ cm^{-3} and $G_0 = 10^3$ for different values of mechanical heating. The numbers in the legend correspond to Γ_{mech} in terms of the surface heating. **(left)** CO line intensities as a function of the rotational level J. Notice the boost in the intensities is much larger at high-J compared to low-J. **(right)** Optical depth at the line centers (τ_0) for the same lines. The optical depth generally decreases as a function of increasing Γ_{mech}, but the most significant effect is that the low-J CO lines become optically thinner with $\tau_0 \sim 1$.

CO and ^{13}CO

CO is the second most abundant molecule in the ISM after H_2. Since the critical density of the CO(1-0) rotational line is moderate (see Table-3.3), it is a good tracer of molecular gas with average densities. The critical densities increase gradually as we go higher up the CO ladder, reaching $\sim 10^{6.5}$ cm^{-3} for the 16-15 transition[2]. In Fig. 3.7, we show the grids for CO J=1-0 emission. In Fig. 3.8, we show the relative increase/decrease in CO J=1-0 emission as a function of Γ_{mech}. The analogous grids for the CO J=2-1, 3-2, 4-3, 6-5, 7-6, 10-9 and 16-15 transitions are presented in Fig. B.1 (and a subset of those for the ^{13}CO lines) are displayed in Fig. B.2. We note that we will be using ^{12}CO and CO interchangeably in referring to carbon monoxide.

At low densities ($n < 10$ cm^{-3}), the emission of CO is very weak ($\sim 10^{-10}$ erg cm^{-2}

---

[2] The critical densities depend only lightly on temperature. For instance n_{cr} for the 16-15 transition changes only by 5% as the gas temperature changes from 10K to 1000K
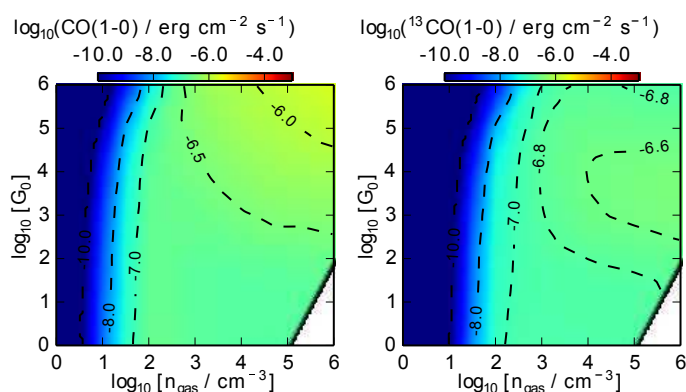
Figure 3.7 – Emission intensity grids of CO($J = 1 - 0$) and ^{13}CO($J = 1 - 0$) transitions for the 1D-PDR models. The emission of the models in the grid correspond to an $A_V = 10$ mag, which amounts to a column density of H, $N_H \sim 10^{22}$ cm^{-2} at solar metallicity. The intensities were computed using the RADEX LVG code. A line-width of 1 km s^{-1} was used. No mechanical heating is added for the models in this grid. This is used as a reference grid for the ones in which Γ_{mech} is introduced (see Fig. 3.8).
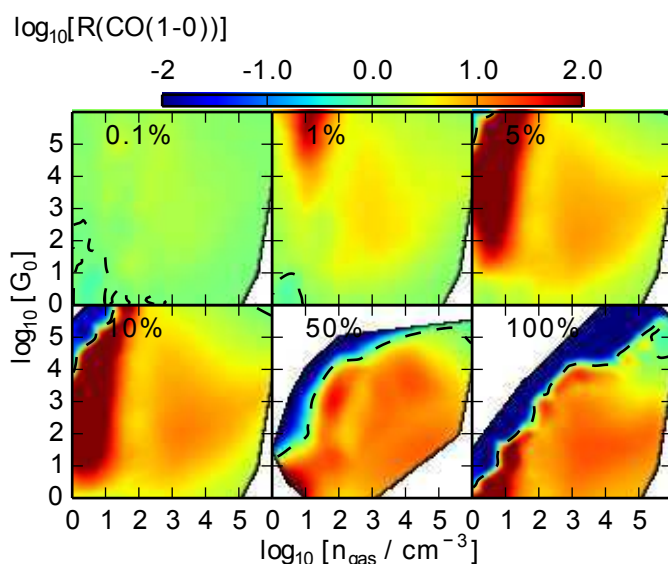
Figure 3.8 – Relative change in the emission of the CO J=1-0 rotational line for different values of Γ_{mech}. The colors in the panels correspond to the relative change of the emission with respect to the reference grid in the left panel of Fig. 3.7. See also the caption of Fig. 3.4.

s^{-1}) compared to emission at mid- to high-densities ($n > 10^3$ cm^{-3}). This is obvious in Fig. B.2. As was mentioned also earlier, we notice that at such low densities the emission contours show almost no dependence on G_0. This is simply explained by the fact that there are few collisions to excite the upper rotational levels, and that the background dust emission (which is only weakly dependent on G_0) is dominating. Another contributing factor is the low gas temperature (~ 10 K) in the molecular zone. On the other hand at mid- and high-densities, where $n \gtrsim n_{cr}$ of CO(J = 1-0), we start seeing a strong dependence of these emission on G_0.

In general the emission intensity is positively correlated with Γ_{mech}, i.e. it increases with increasing $\Gamma_{mech}$ (see Fig. 3.8, B.1, B.2). The only exception occurs at some of the high density regions in the CO(1-0) and ^{13}CO grids. We can see such a behavior in the upper right corner of the CO grids when $\alpha = 0.5$ and 1. In the ^{13}CO grids the emission decrease is clearest (and covers a larger part of the grid), for example see the J=1-0, J=2-1 and J=3-2 grids in Fig. B.2.

In well-irradiated, low-density regions ($n < n_{cr}$ and $G_0 > 10$), the emission increases up to two orders of magnitude (see red regions in Fig. 3.8). This is caused by (1) a rise in the temperature induced by Γ_{mech}, and (2) a higher abundance of CO (and ^{13}CO), causing a double increase. The abundance of CO is boosted because its is accelerated via the reaction H + CO$^+$ $\rightarrow$ CO + H$^+$.

At the higher densities ($n > n_{cr}$) the response to Γ_{mech} becomes weaker. More than one factor contributes to this. From the thermal perspective the temperatures in the molecular regions are already high (~ 50 to 100 K). This is due to the tight coupling between dust and gas. Hence the relative increase in the gas temperature is small, in contrast to what happens in the low-density models. Another contributing factor is the decrease in the abundance of CO. In the absence of Γ_{mech}, most C atoms are locked in CO molecules. For extreme Γ_{mech} ($\alpha \geq 0.5$) the abundance of most molecules, including H$_2$, decreases drastically (Kazandjian et al. 2012), leading to x_{CO} lower by almost 3 orders of magnitude (from $\sim 10^{-4}$ to $\sim 10^{-7}$).

Although we would suspect that the higher temperatures (due to Γ_{mech}) would lead to enhanced emission, the reduced abundance and column density of CO counteracts that enhancement. These two effects combined lead to a small relative increase in emission. As an example, for low densities an increase in the emission by one order of magnitude is easily attained for $\alpha = 0.01$. On the other hand an $\alpha = 0.1$ is required to enhance the CO emission by the same factor in the high density region of the grids (cf, bottom-left panel of Fig. 3.8). The only exception where a decrease in the emission is observed occurs in the CO(1-0) line. This is not surprising, since in looking at the left panel of Fig. 3.6 we see that the 1-0 transition is weakly effected by Γ_{mech} (compared to the higher transitions). So a reduced N(CO) leads to lower emission of the 1-0 line.

A similar behavior is observed for the ^{13}CO emission which is, however, more sensitive to Γ_{mech} than ^{12}CO. In particular, as Γ_{mech} increases, the mid- and high-density regions show a stronger decrease in the emission of the first three J transitions. This decrease is due to a reduced N(^{13}CO) and an already low optical depth. N(^{13}CO) is about 20 times lower than N(^{12}CO). Moreover the Einstein A coefficients of ^{13}CO are about 20% lower than those of ^{12}CO. Hence the upper levels, which are mainly excited collisionally, are

de-populated less frequently, and a higher upper-level population density is maintained. We see that these two factors lead to the reduced optical depth of ^{13}CO. At mid- and high-densities $N(^{13}$CO) decreases as α increases. Since the optical depth is already low, it neither plays a significant role in blocking the emission nor in enhancing the emission by allowing "trapped" radiation to escape from the cloud; this is also true when the cloud becomes more transparent as α increases. Consequently, since intensity is proportional to the column density of the emitting species, a decrease in $N(^{13}$CO) results in lower emission. On the other hand, the $J > 3 - 2$ transitions show enhanced emission all over the grid. This occurs despite the reduced column densities of ^{13}CO. High kinetic temperature due to Γ_{mech} enhances the strong pumping of the associated level populations; eventually, this counteracts the effect of the reduced $N(^{13}$CO) on the emission.

Although the generic behavior of the CO and ^{13}CO grids are similar, the differences among them are interesting enough to have a closer look at their line ratios. Especially for ones involving the low-J lines where the ^{13}CO lines are optically thin.

In Fig. 3.9, we show the line ratios for our reference models. These ratios include transitions for lines within the CO ladder (left panel), the ^{13}CO ladder (middle panel), and the ^{13}CO to ^{12}CO line ratios (right panel). The ratios between high-J and low-J transitions show a strong dependence on Γ_{mech}. For example, in M3 the CO(16-15)/CO(1-0) ratio changes abruptly from $\lesssim 0.1$ to > 100 when $\alpha > 0.05$. A similar behavior is observed for the corresponding ^{13}CO ratio. In Fig. 3.6, we see that the optical depth of $J = 16$-15 CO is almost unaffected as Γ_{mech} increases, whereas that of the $J = 1$-0 line decreases rapidly from ~ 100 to ~ 1. The opposite is observed when it comes to the intensity, where the $J = 16$-15 CO line emission increases by $\sim$ four orders of magnitude. This explains the huge increase in the ratio of those lines. This line ratio along with the ratio CO(16-15)/CO(10-9) are the only ones (among the ratios we looked at) that show a significant change for the high-density model M5 (see the top row of the middle panel in Fig. 3.9).

In medium- to high-density models, ratios involving low-J transitions are less sensitive to Γ_{mech}. Those ratios are almost constant in the high density models, since the lines are thermalized and the population densities do not change relative to each other. However, in the low- and medium-density models MA1, MA2, and M1 the CO(4-3)/CO(1-0) ratio might be a good diagnostic for Γ_{mech}. In MA1 we see that this line ratio increases by a factor of ~ 10 (as well as the corresponding ^{13}CO ratio). Because these are ratios within the same species, the increase is a pure measure of the radiative properties of the species. As in the cases of MA1 and MA2, we are in the non-LTE phase. As the temperature increases, the upper levels are populated faster leading to stronger emission in, e.g., the CO(4-3) line, which drives up the ratio.

The most interesting and useful behavior of the ^{13}CO/^{12}CO (right panel of Fig. 3.9) occurs in the high density models M3 and M4. The ratios decrease monotonously from ~ 0.5 (for $\alpha = 0$) to ~ 0.1 (for $\alpha = 1$).

We showed previously that the optical depth of CO decreases with increasing α. Also ^{13}CO is optically thin in general. So for column densities corresponding to $A_V > 10$ mag, we expect to have a steeper dependence of the line ratios of CO and ^{13}CO on Γ_{mech}.

We summarize the main results of this section by emphasizing that in low density PDRs, the ratios of high-J to low-J emission lines of CO and ^{13}CO might be useful diag-
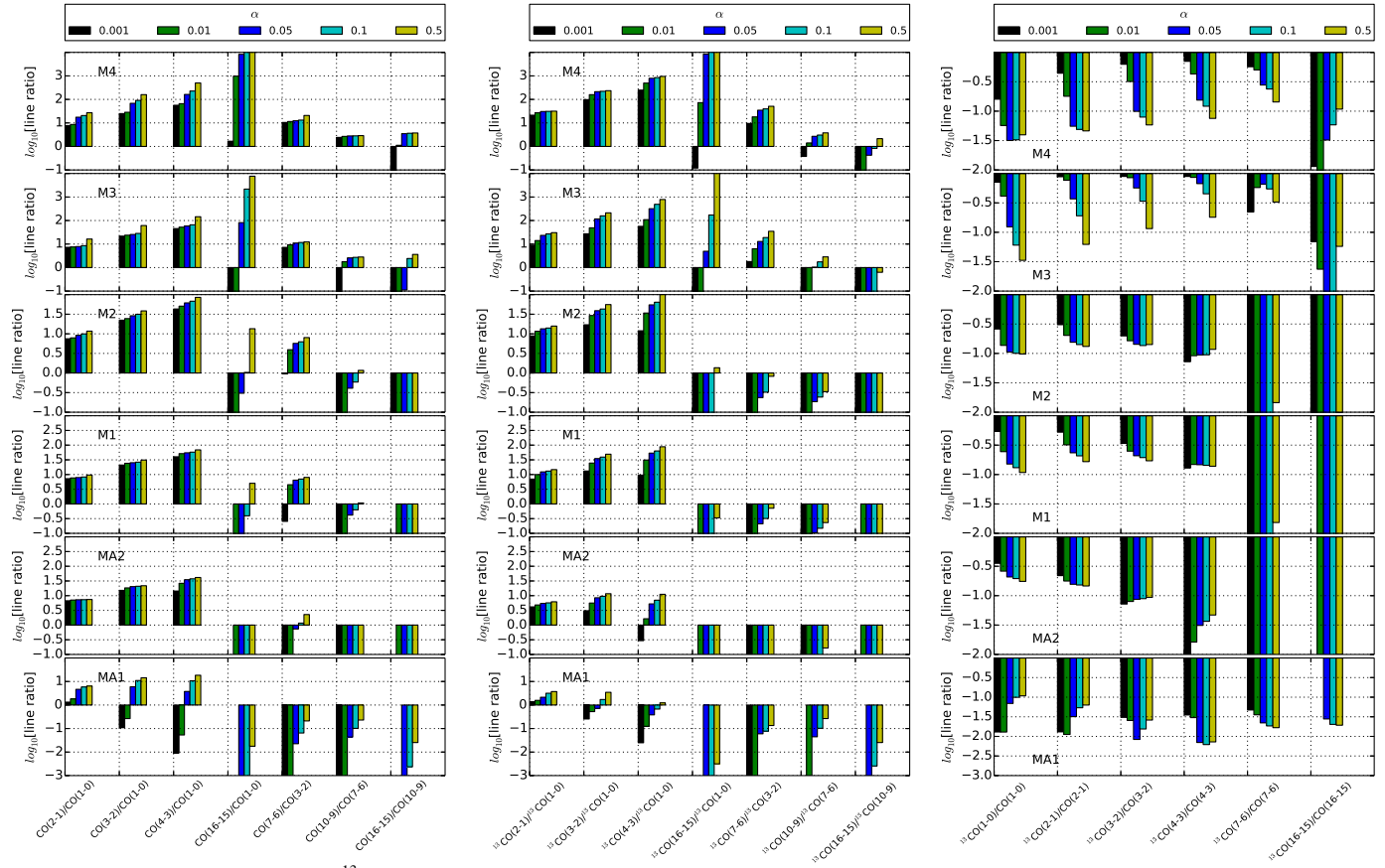
Figure 3.9 – Line ratios of CO and ^{13}CO for different amounts of Γ_{mech} ($Z = Z_{\odot}$) or the reference models.

nostics for Γ_{mech}. The line ratio of ^{13}CO with its isotopologue CO are good diagnostics for Γ_{mech} in high-density PDRs. They show a strong and clear trend.

HCN and HNC

HNC and HCN are linear molecules with very similar radiative properties in the infra-red regime. Both have (a) large dipole moments (3.05 and 2.98 respectively, Botschwina et al. 1993) that allow them to be easily observed (b) high critical densities $> 10^5$ cm^{-3} for the 1-0 transition (see Table-3.3) that render them as good tracers for high-density molecular gas. In this paper, we consider the rotational transitions from $J = 1 - 0$ up to $J = 4 - 3$, which are commonly observed. Since the emission of these lines is very sensitive to temperature changes, they might be useful in identifying molecular clouds dominated by mechanical feedback. In Paper I we studied the column density ratios of the two species. We showed that HCN becomes more abundant than HNC as Γ_{mech} increases. Here we study the effect of Γ_{mech} on the emission of these two species and their ratios.

In the absence of any Γ_{mech} the emission grids show a very weak dependence on G_0, as compared to their dependence on n. This dependence is illustrated in Fig. 3.10. This kind of dependence is generic to cases where the gas density is (much) lower than the critical density of the line considered, which is also the case here.
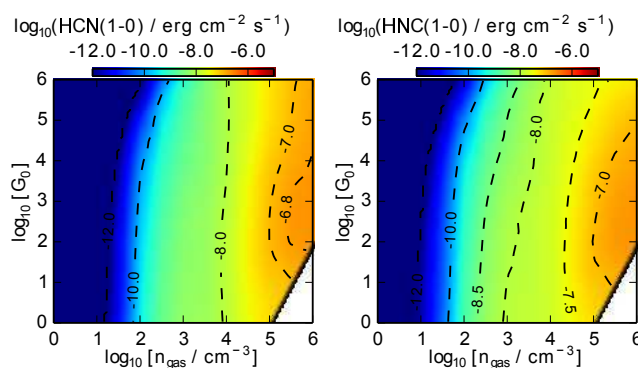
Figure 3.10 – HCN and HNC emission of the 1-0 line in the absence of Γ_{mech} ($Z = Z_\odot$).

In contrast to the weak dependence on G_0, the dependence on Γ_{mech} is quite strong. The enhancements in the emission of HCN are stronger than those of HNC (the bottom two rows of Fig. B.3). This is simply because HCN becomes more abundant than HNC. The main channel through which the conversion occurs is via the reaction H + HNC $\rightarrow$ H + HCN (see Meijerink et al. 2011, for a more elaborate discussion on the chemistry). This process becomes dominant for $T_{kin} > 150$K in the molecular region (Schilke et al. 1992), which is achieved when $\alpha > 0.1$. Below that threshold in α, HNC is equally destroyed via ion-neutral reactions with H$_3$O$^+$, especially at low densities. Another contributing factor to the increase in the abundance of HCN is its efficient formation via the neutral-neutral reactions with H$_2$. For completeness, we note that the relative change in the emission of the $J = 4-3$ line is stronger than that of the 1-0 line for reasons discussed in section-3.3.3.

63
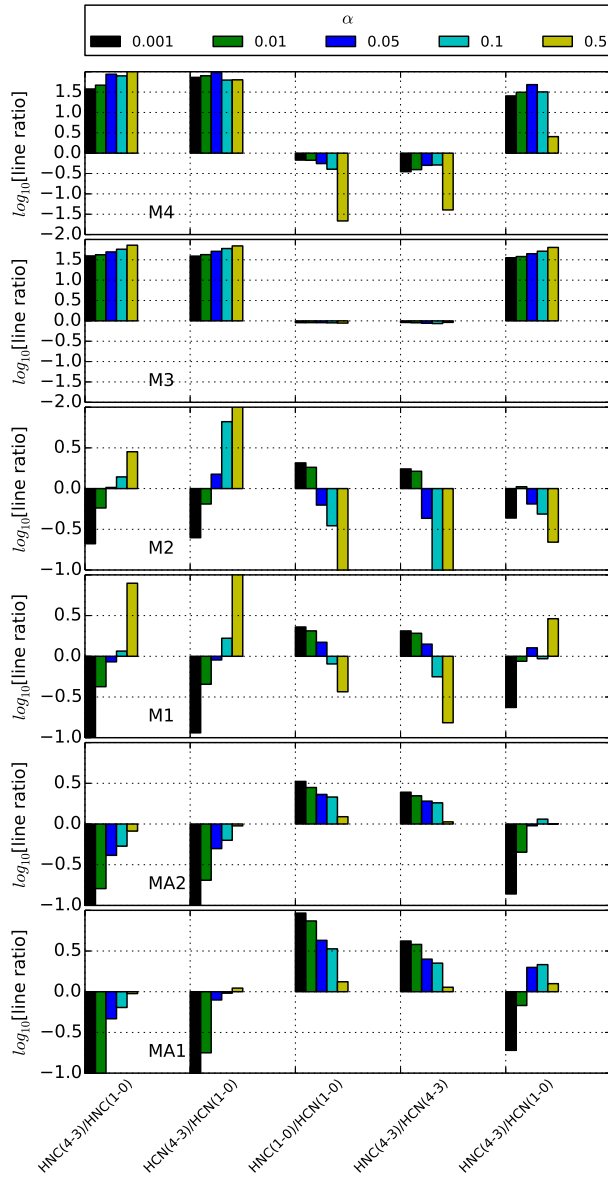
Figure 3.11 – Various line ratios of HNC and HCN as a function of Γ_{mech} ($Z = Z_\odot$) for the reference models.

In Fig. 3.11 we show the line ratios considered for HCN and HNC. Transition ratios such as HNC(4-3)/HNC(1-0) and HCN(4-3)/HCN(1-0) behave as expected (first two columns in the figure): with increasing α, they increase as well (since the higher levels are populated more easily at higher temperatures). In M1 and M2, the ratio increases quite fast linearly in log scale. Unfortunately, in M3 and M4 the ratios are almost constant and are thus of little use as a diagnostic for high-density PDRs.

Again in M1 and M2, the inter-species ratios HNC(1-0)/HCN(1-0), HNC(4-3)/HCN(4-3) and HNC(4-3)/HCN(1-0) are strongly dependent on Γ_{mech}. We see that for $\alpha = 0.5$, the ratio HNC(1-0)/HCN(1-0) drops from ~ 2 to ~ 0.3. This is caused primarily by the difference in column densities caused by the chemical effects discussed above. Since those ratios depends monotonously on α (see M2 in Fig. 3.11), we may consider them as as a good diagnostic for such PDRs. This is not the case for M3 and M4. The line ratios have a weaker dependence on mechanical heating whenever $\alpha < 0.1$. However, an abrupt decrease (from ~ 0.3 to < 0.01) is observed for $\alpha \gtrsim 0.5$.

Interestingly enough at metallicities typical for galactic center regions ($Z = 2\, Z_\odot$), clouds such as M4 show a significant dependence on α (see Fig. B.4). This is simply a result of the fact that a higher metallicity implies a higher column density of the gas and the species in question. In such situations, fluctuations of the abundances in the radical region play a minor role.

In summary, line ratios such as HNC(1-0)/HCN(1-0) and HNC(4-3)/HCN(4-3) are good diagnostics for Γ_{mech} in PDRs in the following cases : (a) at gas densities less than the critical densities of the lines mentioned, and (b) in high-density PDR environments such as galaxy centers with super-solar metallicities and star-burst regions.

HCO$^+$

HCO$^+$ is another high density tracer. The critical densities (at 50K) of its $J = 1 - 0$ and $J = 4 - 3$ emission lines are $\sim 2 \times 10^5$ cm^{-3} and $\sim 10^7$ cm^{-3} respectively. The emission grids for both lines are shown in Fig. 3.12. The corresponding grids as a function of α are presented in Fig. B.5.

We will discuss only mid- and high-density models ($n > 10^3$ cm^{-3}), since at lower densities the lines would be too weak to be observed. With increasing Γ_{mech} , the emission of the J=1-0 line in the high density region (and $G_0 > 10^5$) decreases by a factor of ~ 2. At such high densities, x_{HCO^+} drops by three orders of magnitude, leading to the reduced emission. We trace the source of the reduced abundance of x_{HCO^+} to its slow production rates; which is reduced by an order of magnitude as α increases. This slowing down is mainly due to the reaction of the ionic species HOC$^+$ and CO$^+$ with H$_2$ through which HCO$^+$ is formed. The abundance of these two ionic reactants drops by factors of two and two hundred respectively as α increases, hence the slow production rate of HCO$^+$. As long as the HCO$^+$($J = 1 - 0$) grid is concerned, the emission is enhanced everywhere else throughout the grid. See the dashed line in Fig. B.5.

For PDRs with moderate densities i.e., in the non-LTE phase of the rotational line of HCO$^+$, the coupling between dust and gas is weak compared to that in high-density clouds. This weaker coupling results in a weaker dependence of the abundance on Γ_{mech} (since the physical conditions do not change much). However, the temperature does in-
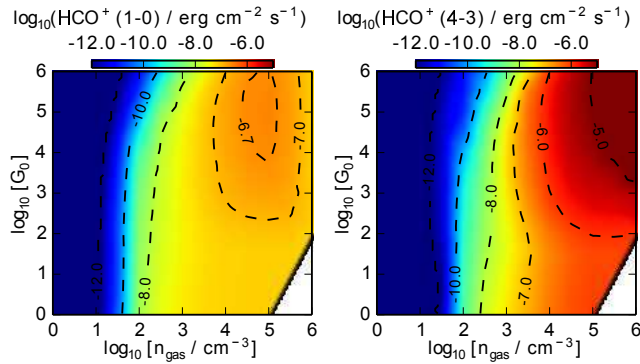
65

Figure 3.12 – HCO$^+$ $J = 1 - 0$ and $J = 4 - 3$ emission in the absence of Γ_{mech} for solar metallicity ($Z = Z_\odot$).

crease in the molecular zone where HCO$^+$ is present. This increase in the temperature enhances the emission of the $J = 1 - 0$ line for densities $n < 10^4$ cm^{-3} .

The $J = 4 - 3$ line responds in similar way to changes in Γ_{mech}, but the emission decrease only for $\alpha = 0.05$ and 0.1. This emission is more sensitive to temperature changes because of the ease of populating upper levels. Thus, the emission is boosted again for $\alpha > 0.1$, even though x_{HCO^+} decreases for $n > 10^5$ cm^{-3}.

HCO$^+$ is interesting because it behaves quite differently in the mid- and high-density regimes. It can be used as a diagnostic for both regimes in combination with other species (as we discuss below).

CN
The critical densities of the CN($1_{1/2}$-$0_{1/2}$) and CN($2_{3/2}$-$1_{3/2}$) is in the high density part of the parameter space (see Table-3.3). Similar to HCO$^+$, the emission grid of those lines also exhibits a peculiar dependence on increasing amounts of mechanical feedback. In looking at the abundance of CN, we see that at high densities x_{CN} correlates negatively with α. The reduction in the abundance is caused by the high temperatures in the molecular zone of the PDR. The high temperatures leads to the destruction of CN, at a rate which is an order of magnitude higher compared to pure PDRs, through the reaction H$_2$ + CN $\rightarrow$ HCN + C. The reduced abundance of CN results in the dimming emission as Γ_{mech} is introduced, which is evident in Fig. -B.6. Beyond $\alpha = 0.1$ N(CN) becomes too low, where the intensities (in both lines considered) decrease by a factor of 10.

On the other end of the parameter space (at mid- and low densities), N + CN $\rightarrow$ N$_2$ + C is the dominant reaction for the full range in α. This reaction maintains a high x_{CN} in that part of the parameter space, i.e the region bounded by the dashed contour line in the bottom row (where $\alpha = 0.1, 0.5, 1.0$) of the panel corresponding to CN in Fig. B.6.

CS
This species has a very distinctive dependence on Γ_{mech} (compared to the other molecular

species we have so far considered). In Fig. 3.13, we see that a region of suppressed emission sweeps across the grid from high- to low- density as α increases. This non-trivial behavior is difficult to explain in detail.
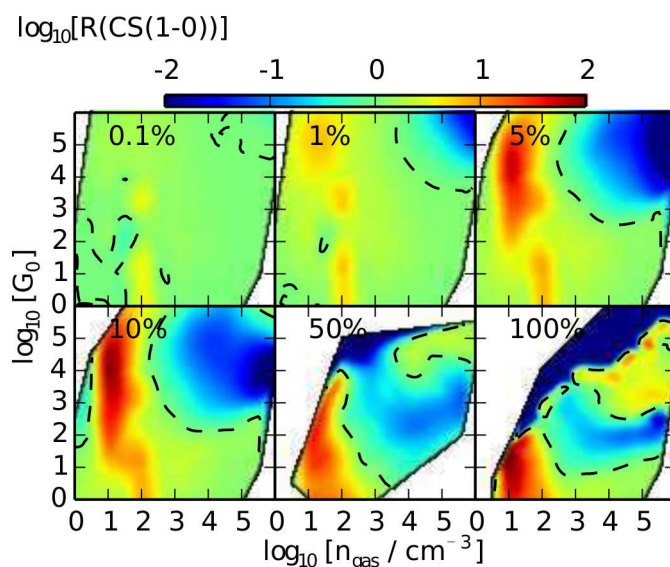
$\log_{10}[R(CS(1-0))]$

Figure 3.13 – Grids of the relative changes in the emission of the CS(1-0) line for different values of α ($Z = Z_\odot$). See also Fig. 3.4 for a description of the colors.

The n_{cr} for CS is $\sim 5 \times 10^4$ cm^{-3} and $\sim 3 \times 10^6$ cm^{-3} for the $J = 1 - 0$ and $J = 4 - 3$ lines respectively (at 50 K). Up to $\alpha = 0.05$ both grids indicate a strong decrease in the emission for $n > 10^3$ cm^{-3} and $G_0 > 10^3$. The reduction in the emission is as low as a factor of 50 for high density PDRs. As α increases further the emission of those PDRs starts to increase again relative to the case of $\alpha = 0$. This increase reaches a factor of 50 for $J = 4 - 3$ transition. Meanwhile, the region where the emission are suppressed is pushed to lower densities and lower G_0. This is a consequence of the chemistry. At the high densities, the drop in the emission is due to reactions with cosmic rays. Those reactions become dominant in destroying CS instead of the neutral-neutral reaction O + CS $\rightarrow$ S + CO; which otherwise is the dominant reaction in pure PDRs. The strong dependence of the CS lines on α makes it a useful candidate for mechanical feedback.

In Fig. 3.14 we show the line ratio for CS, CN, and HCO$^+$. In all the reference models the line ratio of HCO$^+$(4-3)/HCO$^+$(1-0) and particularly the inter-species CS/HCO$^+$ ratios vary over more than one order of magnitude as a function of α. The CS(4-3)/CS(1-0) ratio shows some dependence on Γ_{mech}, but again those variations are small compared to the ones mentioned before. The line ratios CS(1-0)/HCO$^+$(1-0) and CS(4-3)/HCO$^+$(4-3) are more interesting. In looking at the CS grids in Fig. 3.13, we see that variations are well described in the CS/HCO$^+$ ratios, which allows them to be used diagnostically to constrain
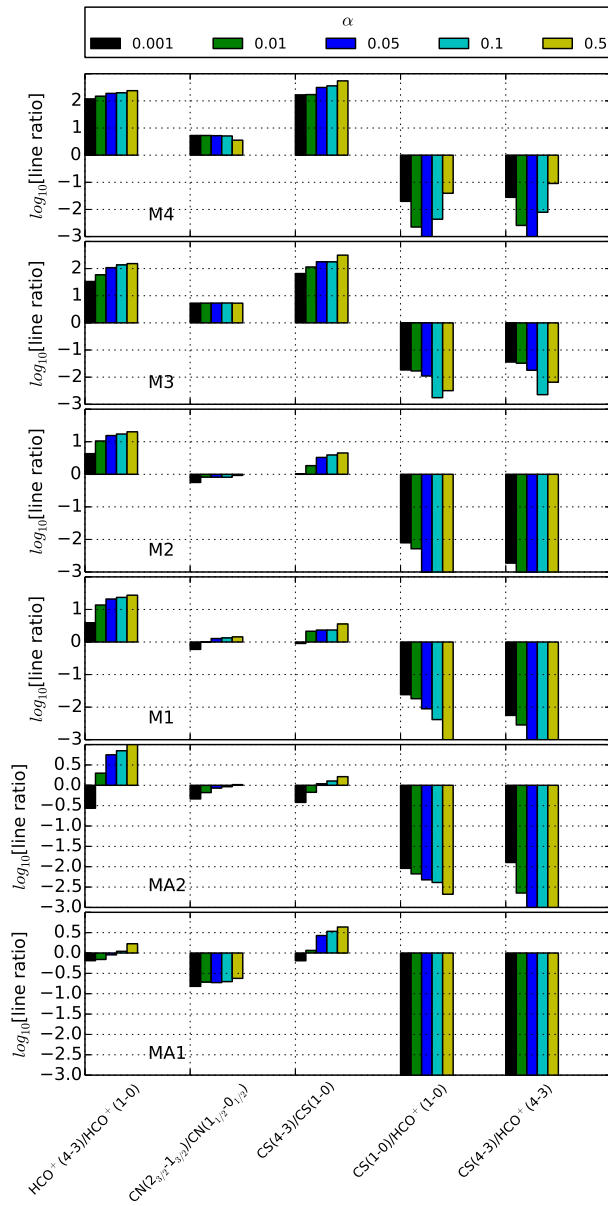
Figure 3.14 – Line ratios of HCO$^+$, CN and CS for $Z = 1Z_\odot$ and $A_V = 10$ mag for the reference models.

Γ_{mech} in extreme star-bursts. For instance a ratio less than 0.01 would imply an $\alpha \sim 0.05$; whereas a ratio around 0.1 implies $\alpha > 0.1$ (see last column in Fig. 3.14).

In M1 and M2, the line ratio behavior is the same at higher or lower metallicities (see Fig. B.7). In M3 and M4, this ratio's response to changes in α is slightly weaker at $Z = 0.5 \, Z_\odot$. In the lowest metallicity case, $CN(2_{3/2}\text{-}1_{3/2})/CN(1_{1/2}\text{-}0_{1/2})$ decreases to unity as α increases. This might be useful in probing Γ_{mech} in e.g. dwarf galaxies.

3.3.4   Other line ratios

Fig. 3.15 shows some other molecular line ratios, selected to illustrate their importance as a diagnostic for Γ_{mech} in PDRs. Most of the line ratios exhibit an order of magnitude change for $\alpha \lesssim 0.25$. Typical examples are $HCO^+(1\text{-}0)/CO(1\text{-}0)$ and $HCN(1\text{-}0)/CO(1\text{-}0)$ in the high-density models such as M3 and M4. On the other hand, $HCO^+(1\text{-}0)/^{13}CO(1\text{-}0)$ shows an irregular increase as a function of α in these models, but a strictly monotonous increase (from ~ 0.01 to 1) is observed in the lower density models M1 and M2.

Ratios involving lines of HCN with CO and HCO^+ are excellent candidates for constraining Γ_{mech}. This is also the case at lower and higher metallicities (see Fig. B.8) for all the representative models. In some cases, such as $HCN(4\text{-}3)/HCO^+(4\text{-}3)$ in M4, the ratio increase from ~ 0.3 to 10 for $\alpha \sim 0.1$. One drawback in the $HCN(1\text{-}0)/CO(1\text{-}0)$ ratio is the degeneracy in its dependence on Γ_{mech} in M3. For example in the absence of Γ_{mech}, this ratio has a value of 0.3. It reaches a minimum of 0.01 (for $\alpha = 0.1$) and increases to ~ 0.3 for extreme cases where $\alpha = 0.5$. Cases of such degeneracies can be resolved by simultaneously considering other line ratios, as we will demonstrate at the end of this section.

We draw special attention to the CN/HCN inter-species ratios. They have a very strong dependence on Γ_{mech}, showing a decrease by an order magnitude for the lowest transition ratios as α increases from 0 to 1.

In summary, we found that line ratios between CN, HCN and HCO^+ are quite useful in constraining Γ_{mech}. This is true in particular for CN since Γ_{mech} seems to drive ratios to values well below unity for most clouds when $\alpha > 0.1$. In high-density clouds whose heating budget is dominated by Γ_{mech}, line ratios of HNC/HCO^+ tend to exceed unity.

3.4   Application

We have presented model predictions for line intensities and line ratios of many molecular species. However, we have not yet reflected on any observational data to which these models can be applied. In this section we use actual data and demonstrate (a) the importance of molecular line ratios as a diagnostic for mechanical heating and (b) their usefulness as a tool for constraining it.

In Table-3.4, we present the range of line ratios involving HCN, HNC, CO and HCO^+ for infra-red luminous galaxies taken from Table-B.2 in Baan et al. (2008).

We follow a simplistic approach to an ambitious goal. Our aim is to constrain $(n, G_0,$
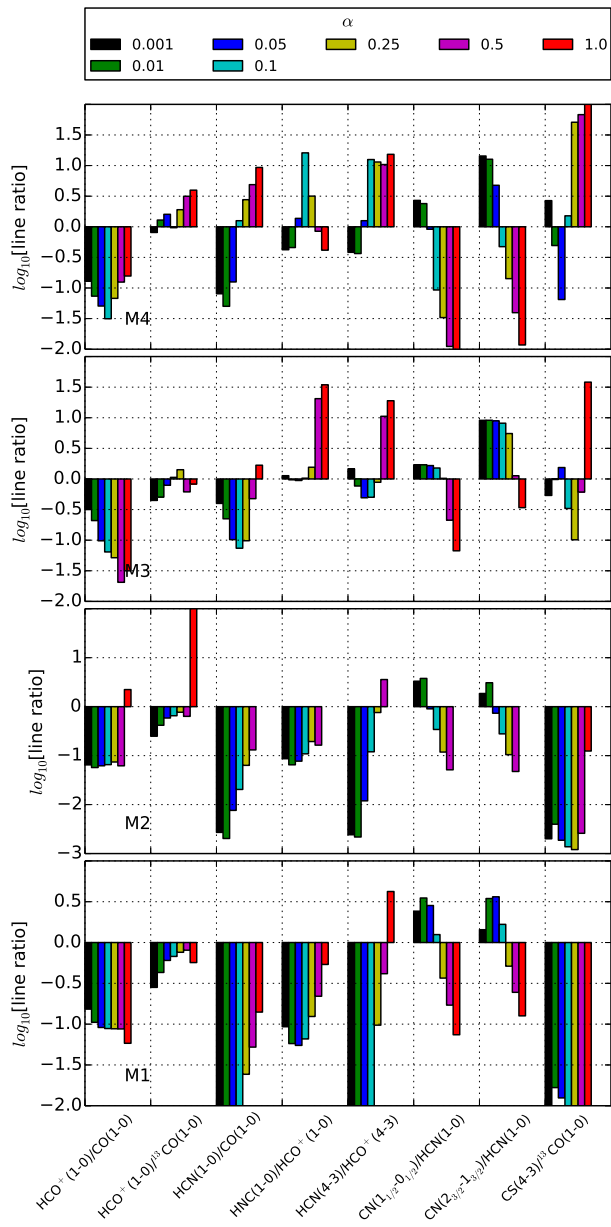
Figure 3.15 – Line ratios with strong dependence on Γ_{mech} for $Z = Z_\odot$ for the reference models.

ratio	range	reference
HCN(1-0)/HNC(1-0)	1.5 – 4.0	Baan et al. (2008)
HCN(1-0)/HCO$^+$(1-0)	0.6 – 3.2	Baan et al. (2008)
HNC(1-0)/HCO$^+$(1-0)	0.3 – 1.0	Baan et al. (2008)
HCO$^+$(4-3)/CO(1-0)	0.1 – 0.5	Israel et al. (1995), Knudsen et al. (2007)

Table 3.4 – Observed ranges of molecular line ratios for some starburst galaxies.

A_V, α) using the data at our disposal. The only major assumption we make is the metallicity of the source. Here we will assume solar metallicity.

In Fig. 3.16 we present a step-by-step procedure to constrain (n, G_0, A_V, α) using line ratio grids parametrized with those four quantities. Each small square represents a grid as a function of n (horizontal axis) and G_0 (vertical axis), like all the previous grids that we have shown so far. Each collection of grids illustrates the constraining procedure for a certain A_V. The collection of grids in Fig. 3.16 corresponds to $A_V = 5$ mag. The ones for $A_V = 10$ and 30 mag can be found in the appendix in Fig. C.7 and C.8. In each column, grids for different α are presented.

In the top row of each collection, regions where the line ratio of HCN(1-0)/HNC(1-0) is within the observed range (see Table-3.4), are delineated in light blue. Clearly, the HCN(1-0)/HNC(1-0) ratio does not constrain all four parameters. However, if A_V and α are known, one can constrain the range in n and G_0 for the source. For example, if we know a priori that $A_V = 5$ mag and $\alpha = 0$ (pure PDR), then the FUV flux is constrained to $G_0 > 10^5$ (see the grid with $\alpha = 0$ in the first row of Fig. 3.16) while the gas density is not constrained. On the other hand, if α is known to be 0.5 (which is quite extreme), then n and G_0 are constrained to a much narrower region. Including the information about HCN(1-0)/HCO$^+$(1-0) from Table-3.4 helps us better constrain all four parameters (see the second row in the mentioned Figures). Although now n and G_0 are better constrained (cyan regions), α is still degenerate. Similarly, HNC(1-0)/HCO$^+$(1-0) fails in achieving our goal (yellow zones in the third row).

Based on our observation in the results section that Γ_{mech} has a strong signature on high-J transitions (which was more or less ubiquitous for all species), we attempt adding ratios of observed lines involving a high-J and a low-J transition. We use the $J = 4 - 3$ transition of HCO$^+$ of NGC253 as a guide. It is clear that this ratio manages to constrain all four parameters, with moderate certainty to $A_V \sim 5$ mag, $10^{3.5} < n < 10^4$, $10^4 < G_0 < 10^{4.5}$ and $\alpha \sim 0.1$. This may not be a unique find. However, we expect the χ^2 value (or the minimum for a proper statistical fit) to be close to the range constrained by this proof of concept simple demonstration.

3.5   Conclusion and discussion

We have studied the effect of Γ_{mech} on a wide range of parameter space in n and G_0 covering six order of magnitude in both ($1 < n < 10^6$ cm^{-3} and $1 < G_0 < 10^6$). Throughout
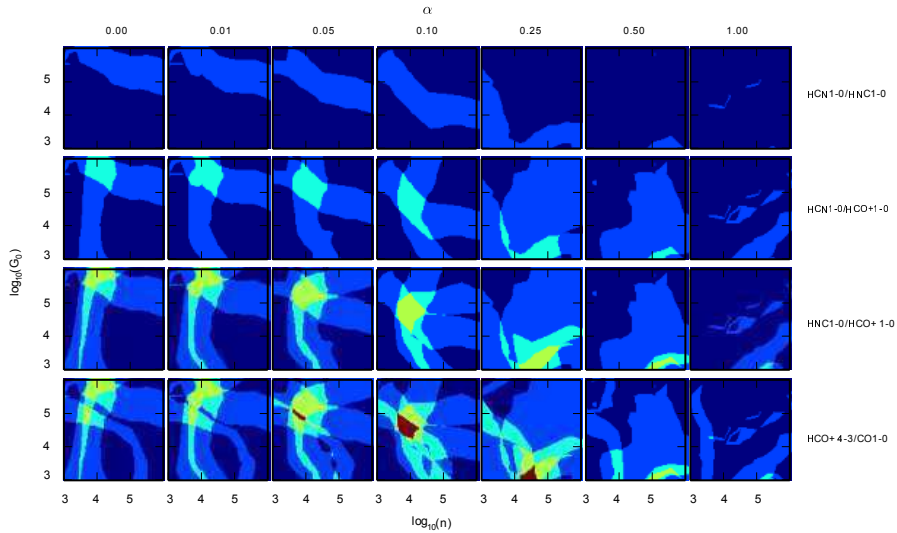
Figure 3.16 – Constraining the Γ_{mech} , A_V, n and G_0 for starburst galaxies. In this figure we illustrate the procedure used to constrain those parameters for $A_V = 5$ mag, the figures for the remaining A_V are in Fig. C.7 and C.8. Each row corresponds to a certain line ratio, and each column corresponds to a certain α. The colors correspond to regions where the observed line ratio in each grid is within the observed range of Table-3.4. In the first row regions where HCN(1-0)/HNC(1-0) is between 1.5 and 4.0 is shaded in light blue. In the second row we include HCN(1-0)/HCO$^+$(1-0). The regions which are within the observed line ratios for both HCN(1-0)/HCO$^+$(1-0) and HCN(1-0)/HNC(1-0) are shaded in cyan. In the third row, we introduce HNC(1-0)/HCO$^+$(1-0), the region satisfying all three line ratios is shaded in green. We notice that green regions exist for all values of α in the third row. Hence we can not constrain α so far. It is only when HCO$^+$(4-3)/CO(1-0) is included, α is constrained to 0.1 (red region in the $\alpha = 0.1$ column) in the last row. Although much smaller red regions are also visible for $\alpha = 0.05$ and $\alpha = 0.25$, the global minimum would be most likely around $\alpha = 0.1$ region. In applying a similar procedure to grids corresponding to $A_V = 10$ and 30 mag, we do not observe any red region.

this parameter space we investigated the most important and commonly observed molecular emission and atomic fine-structure lines and their ratios. The explored range in mechanical heating (Γ_{mech}) covers quiescent regions, with almost no star-formation, as well as violently turbulent star-bursts. The star-formation rates for those range from 0.001 $M_\odot$ yr^{-1} to ~ 100 $M_\odot$ yr^{-1} respectively.

The two fundamental questions we try to answer in this paper are: (a) is it possible to constrain the mechanical heating rate in a star-forming region by using molecular line ratios as a diagnostic? (b) how important is Γ_{mech} in recovering the molecular H$_2$ mass of a star-forming region using observed molecular line emission such as those of CO?

Before discussing these questions, we state the main characteristics of mechanically

heated PDRs we observed in our grids:

- The most significant contribution of Γ_{mech} to the atomic fine-structure line intensities results from enhanced temperatures in the molecular zone. This is especially the case for the [CI] lines. For clouds whose density is below the critical density of those lines, half of the emission intensity emanates from the molecular zone. FS line ratios, such as [CII] 158μm/[CI] 369μm, [OI] 63μm/[CI] 369μm and [CI] 369μm/[CI] 609μm, are good diagnostics for Γ_{mech} in low-density PDRs ($n < 10^3$ cm^{-3}).

- High-J to low-J transitional ratios of ^{12}CO and ^{13}CO, such as CO(16-15)/CO(1-0), are good diagnostics for Γ_{mech} over the whole density range considered. In contrast low-J CO line ratios, such as CO(2-1)/CO(1-0) or CO(4-3)/CO(1-0), are useful as diagnostics[3] only for clouds with $n < 10^3$ cm^{-3}.

- The line ratios of ^{13}CO/^{12}CO (in both low-J and high-J transitions) have a strong dependence on Γ_{mech}. They decrease as Γ_{mech} increases. This complements the range in density where low-J transitions of ^{12}CO (and ^{13}CO) can be used as diagnostics for Γ_{mech}.

- At high metallicities ($Z = 2\ Z_\odot$), HCN and HNC are very good diagnostics for Γ_{mech} when $G_0 \gtrsim 10^5$, such sources include star-bursts in galaxy centers.

- Line ratios such as HCN(1-0)/CO(1-0), HCN(1-0)/HCO$^+$(1-0), CN($1_{1/2}$-$0_{1/2}$)/HCN(1-0), CN($2_{3/2}$-$1_{3/2}$)/HCN(1-0), CS(1-0)/HCO$^+$(1-0) show a strong dependence of Γ_{mech}, hence they are a good diagnostic of it.

One major conclusion of the paper, which we demonstrated in the application section is: low-J transitions alone are not good enough to constrain mechanical heating, while ratios involving high-J to low-J transitions do a much better at that.

Another major conclusion is the importance of Γ_{mech} in constraining A_V or, equivalently, the hydrogen column density N_H, which can be used to determine the molecular mass of the cloud. In comparing Fig. 3.16 to the ones of higher A_V in the appendix, one can see that if Γ_{mech} is ignored, it is easy to under- or over-estimate the A_V by a factor of five (or more). Ignoring Γ_{mech} also results in more than an order of magnitude error in estimating the n and G_0. For instance in looking at the last row of Fig. 3.16, one can see that when Γ_{mech} is ignored, an error up to two orders of magnitude can be done in constraining the ranges of n and G_0.

We emphasis that our approach in constraining the physical parameters of clouds using the observed line ratios is just a proof of concept demonstration. Ultimately one must use more elaborate minimization methods to attempt to constrain the physical parameters. However, it is most likely that the parameters, which best fit the observations, will be very close to the ones obtained using the method adopted in the application section. We leave

---

[3] We refer the reader to the end of this section for a small discussion on the difference about regions dominated by cosmic-rays in comparison to ones dominated by Γ_{mech}.

73

it to the interested reader to make use of the grids which are published as well with this paper (see Fig. C.3, C.4 C.5).

We finalize our discussion by touching on the effect of cosmic rays (CR). Although it is outside the scope of this paper, we explored the effect of enhanced CR rates. Diagnostic line ratio grids for HCN, HNC and HCO$^+$ are fundamentally different from those which are dominated by Γ_{mech} (see Fig. C.6). Hence, we expect that in using diagnostics presented in this paper, clouds which are embedded in environments where the CR rate is enhanced, would not be mistaken with clouds whose heating budget is dominated by Γ_{mech}.

Acknowledgements

Appendices

Figures A.1 – A.3, B.1 – B8 and C.1 – C.8 can be found in the online version at:
`http://www.aanda.org/articles/aa/pdf/2015/02/aa22805-13.pdf`

IV

CO and ^{13}CO Emission Map Construction for Simulated Galaxies

We apply photo-dissociation (PDR) molecular line emission models to the gas of simulated galaxies in post-processing mode and produce emission maps for the rotational transitions of the CO molecule and its ^{13}CO isotope up to $J = 4 - 3$. We use these maps to investigate the occurrence and effect of mechanical feedback on the physical parameters obtained from molecular line intensity ratios. We consider two galaxy models: a small disk galaxy of solar metallicity and a lighter dwarf galaxy with 0.2 $Z_\odot$ metallicity. Elevated excitation temperatures for CO$(1 - 0)$ correlate positively with mechanical feedback, which is enhanced towards the central region of both model galaxies. The emission maps of these model galaxies are used to compute line ratios of CO and ^{13}CO transitions. These line ratios are used as diagnostics where we attempt to match them using a single component mechanically heated equilibrium PDR. We find that PDRs ignoring mechanical feedback in the heating budget over-estimate the gas density by a factor of 100 and the far-UV flux by factors of $\sim 10 - 1000$. In contrast, PDRs that take mechanical feedback into account are able to fit all the line ratios for the central < 2 kpc of the fiducial disk galaxy quite well. The mean mechanical heating rate per H atom that we recover from the line ratio fits of this region varies between $10^{-27} - 10^{-26}$ erg cm^{-6} s^{-1}. Moreover, the mean gas density, mechanical heating rate, and the A_V are recovered to less than half dex. On the other hand, our single component PDR model fit is not suitable for determining the actual gas parameters of the dwarf galaxy, although the quality of the fit line ratios are comparable to that of the disk galaxy.

M. V. Kazandjian, I. Pelupessy, R. Meijerink, F. P. Israel, M. Spaans
submitted to *A&A*

4.1   Introduction

Most of the molecular gas in the universe is in the form of H$_2$. However, this simple molecule has no electric dipole moment. The rotational lines associated with its quadrupole moments are too weak to be observed at gas temperatures less than 100 K, where star formation occurs. This is also true for the other emission of H$_2$; hence it is hard to detect directly in cold molecular environments by applying techniques common to those used to detect warmer gas. CO is the second most abundant molecule after H$_2$, and it has been detected ubiquitously. CO forms in shielded and cold regions where H$_2$ is present. Despite its relatively low abundance, it has been widely used as a tracer of molecular gas. Solomon & de Zafra (1975) were the first to establish a relationship between CO$(1-0)$ flux ($W_{\text{CO}(1-0)}$) and H$_2$ column density ($N(\text{H}_2)$). Since then, this relationship has been widely used and it is currently known as the so-called X-factor. The applicability and limitations of the X-factor are discussed in a recent review by Bolatto et al. (2013).

Environments where cool H$_2$ is present allow the existence of CO, and many other molecular species. In such regions, collisions of these molecules with H$_2$ excite their various transitions, which emit at different frequencies. The emission line intensities can be used to understand the underlying physical phenomena in these regions. The line emission can be modeled by solving for the radiative transfer in the gas. One of the most direct ways to model the emission is the application of the large velocity gradient (LVG) approximation (Sobolev 1960). LVG models model the physical state of the gas such as the density and temperature, they do not differentiate among excitation mechanisms of the gas, such as heating by shocks, FUV, or X-rays, and they do not provide information about the underlying physics.

The next level of complexity involves modeling the gas as equilibrium photon dominated regions, PDRs (Tielens & Hollenbach 1985, Hollenbach & Tielens 1999). These in turn are limited when it comes to their applicability to star forming regions and starbursts. Modeling of Herschel and other observations for, e.g., NGC 253, NGC 6240 and M82, using these PDRs show that these models lack particular heating sources, such as heating due to AGN or enhanced cosmic ray ionization (Maloney et al. 1996b, Komossa et al. 2003, Martín et al. 2006, Papadopoulos 2010, Meijerink et al. 2013, Rosenberg et al. 2014a, among many others). Another heating source, which is not accounted for in PDR modeling and is relevant to this paper, is mechanical heating due to turbulence (Loenen et al. 2008, Aalto 2013).

Various attempts have been made in this direction in modeling star-forming galaxies and understanding the properties of the molecular gas. However, because of the complexity and resolution requirements of including the full chemistry in the models, self-consistent galaxy-scale simulations have been limited mainly to CO (Kravtsov et al. 2002, Wada & Tomisaka 2005, Narayanan et al. 2008, Pelupessy & Papadopoulos 2009, Xu et al. 2010, Pérez-Beaupuits et al. 2011, Narayanan et al. 2011, Shetty et al. 2011, Feldmann et al. 2012, Narayanan & Hopkins 2013).

The rotational transitions of CO up to $J = 4-3$ predominantly probe the properties of gas with densities in the range of 10^2 - 10^5 cm^{-3}, and with temperatures around ~ 50K.

Higher J transitions probe denser and warmer molecular gas around ~ 200K for the $J = 10 - 9$ transition. In addition to high-J CO transitions other high-density tracers, such as CS, CN, HCN, HNC and HCO$^+$, are good probes of cold gas with $n \sim 10^6$ cm^{-3}. Thus, having a broad picture on how these species and their line emission are related to their environment provide a full picture on the underlying physical processes.

In Kazandjian et al. (2012, 2015a) we studied the effect of mechanical feedback on diagnostic line ratios of CO, ^{13}CO and other high density tracers for grids of mechanically heated PDR models in a wide parameter space relevant to quiescent disks as well as turbulent galaxy centers. We found that molecular line ratios between $J \geq 4 - 3$ and lower transitions are good diagnostics of mechanical heating. In this paper, we build on our findings in Kazandjian et al. (2015a) to apply them to the chemistry models to simulated galaxies with sub-grid modeling in post-processing mode to construct CO and ^{13}CO maps for transitions up to $J = 4 - 3$. Our approach is similar to that by Pérez-Beaupuits et al. (2011) where the sub-grid modeling is done using PDR modeling that includes a full chemical network based on Le Teuff et al. (2000), which is not the case for the other references mentioned above. The main difference of our work from Pérez-Beaupuits et al. (2011) is that our sub-grid PDR modeling takes into account the mechanical feedback in the heating budget; on the other hand we do not consider X-ray heating effects due to AGN. The synthetic maps are processed in a fashion that simulates what observers would measure. These maps are used as a guide to determine how well diagnostics such as the line ratios of CO and ^{13}CO can be used to constrain the presence and magnitude of mechanical heating in actual galaxies.

In the method section we start by describing the galaxy models used, although our method is generally applicable to other grid and SPH based simulations. We then proceed by explaining the procedure through which the synthetic molecular line emission maps were constructed. In the results section we study the relationship and the correlation between the luminosities of CO, ^{13}CO, and H$_2$. We also present maps of the line ratios of these two molecules and see how mechanical feedback affects them, how well the physical parameters of the molecular gas can be determined, when the gas is modeled as a single PDR with and without mechanical feedback. In particular, we try to constrain the local average mechanical heating rate, column density and radiation field and compare that to the input model. We finalize with a discussion and conclusions.

4.2 Methods

In order to construct synthetics emission maps of galaxies, we need two ingredients: (1) A model galaxy, which provides us with the state of the gas, and (2) a prescription to compute the various emission of the species. We start by describing the galaxy models in Section-4.2.1 along with the assumptions used in modeling the gas. The parameters of the gas, which are necessary to compute the emission of the species and the properties of the model galaxies chosen, are described in Section-4.2.2. In Section-4.2.3, we describe the method with which the sub-grid PDR modeling was achieved and from which the emission of the species were consequently computed. Sub-grid modeling is necessary

since simulations which would resolve scales where H/H$_2$ transitions occur (Tielens & Hollenbach 1985), and where CO forms, need to have a resolution less than ~ 0.01 pc. This is not the case for our model galaxies, but this is achieved in our PDR models. The procedure for constructing the emission maps is described in Section-4.2.4.

4.2.1 Galaxy models

In this paper, we will use the model galaxies of Pelupessy & Papadopoulos (2009), which are TreeSPH simulations of isolated dwarf galaxies in a steady state. The simulation code calculates self-gravity using a Oct-tree method (Barnes & Hut 1986) and gas dynamics using the softened particle hydrodynamics (SPH) formalism (see e.g. Monaghan 1992), in the conservative formulation of Springel & Hernquist (2002). It uses an advanced model for the ISM, a star formation recipe based on a Jeans mass criterion, and a well-defined feedback prescription. More details of the code and the simulations can be found in Pelupessy & Papadopoulos (2009). Below we will summarizes main ingredients.

The ISM model used in the dynamic simulation is similar, albeit simplified, to that of Wolfire et al. (1995, 2003). It solves for the thermal evolution of the gas including a range of collisional cooling processes, cosmic ray heating and ionization. It tracks the development of the warm neutral medium (WNM) and the cold neutral medium (CNM) HI phases. The latter is where densities, $n > 10$ cm^{-3}, and low temperatures, $T < 100$ K, allow the H$_2$ molecules to form. Our assumption is that the short time-scales in these dense regions, which are associated with non-equilibrium effects, may play an important role in the formation and emission of the molecular species. For instance, in star-bursts in galaxy centers, the chemical time-scale of H$_2$ formation out of HI (Hollenbach & Tielens 1999) is comparable to the time-scale of the build-up of the FUV field (Parravano et al. 2003), the orbital period of molecular gas in the central few parsec of galaxy centers (Kim et al. 2006), the dynamical time-scale of spherical clouds, as well as the time-scale of the occurrence of these star-bursts.

The FUV luminosities of the stellar particles, which are needed to calculate the photo-electric heating from the local FUV field, are derived from synthesis models for a Salpeter IMF with cut-offs at 0.1 M$_\odot$ and 100 M$_\odot$ by Bruzual & Charlot (1993), and updated by Bruzual & Charlot (2003). Dust extinction of UV light is not accounted for, other than that from the natal cloud. For a young stellar cluster we decrease the amount of UV extinction from 75% to 0% in 4 Myr (see Parravano et al. 2003).

For an estimate of the mechanical heating rate we extract the local dissipative terms of the SPH equations, the artificial viscosity terms (Springel 2005). These terms describe the thermalization of shocks and random motions in the gas, and are in our model ultimately derived from the supernova and the wind energy injected by the stellar particles that are formed in the simulation (Pelupessy 2005). We realize that this method of computing the local mechanical heating rate is very approximate. To be specific: this only crudely models the actual transport of turbulent energy from large scales to small scales happening in real galaxies, but for our purposes it suffices to obtain an order of magnitude estimate of the available energy and its relation with the local star formation.

We selected two galaxy types from the set of galaxy models by Pelupessy & Papadopoulos (2009), and applied our PDR models to them. These galaxies are star-forming galaxies and have metallicities representing typical dwarfs and disk-like galaxies, which enable us to study typical star-bursting regions. The first model galaxy is a dwarf galaxy with low metallicity ($Z = 0.2\ Z_\odot$). The second model is a heavier, disk like, galaxy with metallicity ($Z = Z_\odot$). The basic properties of the two simulations are summarized in Table-4.1.

abrv	name	mass ($M_\odot$)	Z ($Z_\odot$)	gas fraction
dwarf	coset2	10^9	0.2	0.01
disk	coset9	10^{10}	1.0	0.1

Table 4.1 – Properties of the galaxies used.

4.2.2 Ingredients for further sub-grid modeling

While our method of constructing molecular emission maps is generally applicable to grid based or SPH hydrodynamic simulations of galaxies, we use the simulations of Pelupessy & Papadopoulos (2009) since they provide all the necessary ingredients to allow for our sub-grid modeling prescription. These are necessary for the post-processing of the snapshots of the hydrodynamic density field, and to produce realistic molecular line emission maps. Our method is applicable to a simulation if it provides a number of physical quantities for each of the resolution elements (particles, grid cells): the densities resolved in the simulation must reach $n \sim 100 - 1000$ cm^{-3}in-order to produce reliable CO and ^{13}CO emission maps up to $J = 4-3$, and the simulation must provide estimates of the environmental temperature, far-UV field flux and local mechanical heating rate. In essence, the simulation must provide realistic estimates of the CNM environment in which the molecular clouds develop. In the next section, we describe in detail the assumptions with which the CNM was modeled. A number of such galaxy models exist (see the introduction for references), and with the increase in computing power, more simulations, also in a cosmological context, are expected to become available. Pelupessy & Papadopoulos (2009) present a sweep of SPH models of disk and dwarf galaxies. We note that the gas temperature estimated from the PDR models is not the same as the gas temperature of the SPH particle from the simulation. The reason for this is the assumption that the PDR is present in the sub-structures of the SPH particle. This sub-structure is not resolved by the large scale galaxy simulations, and hence not probed. We have compared the temperature at the surface of the PDR to that of the SPH particle, where we find a good agreement between them. This is a good check, since the SPH particle provides a boundary condition to the embedded PDR model. We want to stress that we can apply our methodology to any simulation that fulfills the above criteria.

4.2.3 Sub-grid PDR modeling in post-processing mode

In order to model the emission emanating from the SPH particles, we model the substructure that is present on scales below that probed by the SPH particles using a sub-grid model. For this we assume (1) local dynamical and chemical equilibrium and (2) that the substructure where H_2 forms complies to the scaling relation of Larson (1981), from which the prescription, by Pelupessy et al. (2006), of the mean A_V given in Eq-4.1 is derived.

$$< A_V >= 3.344Z \left(\frac{P_e/k_B}{10^4 \text{ cm}^{-3}K} \right)^{1/2} \tag{4.1}$$

Z is the metallicity of the galaxy in terms of $Z_\odot$, P_e is the boundary pressure of the SPH particle and k_B is the Boltzmann constant. Using the boundary conditions as probed by the SPH particles and this expression for the mean A_V, we proceed to solve for the chemical and thermal equilibrium using PDR models.

We assume a 1D semi-infinite plane-parallel geometry for the PDR models whose equilibrium is solved for using the Leiden PDR-XDR code Meijerink & Spaans (2005). Each semi-infinite slab is effectively a finite slab illuminated from one side by an FUV source. This is of course an approximation, where the contribution of the FUV sources from the other end of the slab is ignored, and the exact geometry of the cloud is not taken into account. The chemical abundances of the species and the thermal balance along the slab are computed self-consistently at equilibrium, where the UMIST chemical network (Le Teuff et al. 2000) is used. In this paper we keep the elemental abundance ratio of ^{12}C/^{13}C fixed to a value of 40, that is the lower limit of the suspected range in the Milky way. This ratio is important in the optically thin limit of the CO line emission at the edges of the galaxies. It plays a less significant role in the denser central regions of galaxies. We have outlined the major assumptions of the PDR models used in this paper, for more details on these see Meijerink & Spaans (2005) and Kazandjian et al. (2012, 2015a).

The main parameters which determine the intensity of the emission of a PDR are the gas number density (n), the FUV flux (G) and the depth of the cloud measured in A_V. In our PDR models we also account for the mechanical feedback. We refer to these as mechanically heated PDRs (mPDR), which affects the chemical abundances of species (Loenen et al. 2008, Kazandjian et al. 2012), as well as their emission (Kazandjian et al. 2015a). Hence the fourth important parameter required for our PDR modeling is the mechanical feedback (Γ_{mech}). In addition to these four parameters, metallicity plays an important role, but this is taken constant throughout each model galaxy (see Table-4.1). The SPH simulations provide local values for n, G, and Γ_{mech}.

Based on the PDR model grids in Kazandjian et al. (2015a), we can compute the line emission intensity of CO and ^{13}CO given the four parameters (n, G, Γ_{mech}, A_V) at a given metallicity. We briefly summarize the method by which the emission was computed by Kazandjian et al. (2015a). For each PDR model, the column densities of CO and ^{13}CO, the mean density of their main collision partners, H_2, H, He and e$^-$, and the mean gas temperature in the molecular zone are extracted from the model grids. Assuming the LVG approximation, these quantities are used as input to RADEX (Schöier et al. 2005) which computes the line intensities. In the LVG computations a micro-turbulence line-width,

v_{turb}, of 1 km s^{-1} was used. Comparing this line width to the velocity dispersion of the SPH particles, we see that the velocity dispersion for particles with $n > 10$ cm^{-3}, where most of the emission comes from and which have $A_V > 5$ mag, is on the order of unity. The choice of the micro-turbulence line-width does not affect the general conclusions of the paper. This is discussed in more detail in Section-4.5.1.

In this paper, the parameter space used by Kazandjian et al. (2015a) was extended to include $10^{-3} < n < 10^6$ cm^{-3}, $10^{-3} < G < 10^6$, where G is measured in units of $G_0 = 1.6 \times 10^{-3}$ erg cm^{-2} s^{-1}. Moreover the emission was tabulated for $A_V = 0.01, 0.1, 1...30$ mag. The range in Γ_{mech} was wide enough to cover all the states of the SPH particles. For each emission line of CO and ^{13}CO we constructed 4D interpolation tables. Consequently, given any set of the four PDR parameters for each SPH particle, we can compute the intensity of all the lines of these species. About 0.1% of the SPH particles had their parameters outside the lower bounds of the interpolation tables, mainly $n < 10^{-3}$cm^{-3} and $G < 10^{-3}$. The disk galaxy consists of 2×10^6 particles, half of which contribute to the emission. The surface temperature of the other half is larger than 10^4K, which is caused by high Γ_{mech} where no transition from H to H$_2$ occurs in the PDR, thus CO and ^{13}CO are under-abundant. We ignore these SPH particles since they do not contribute to the mean flux of the emission maps and the total luminosities.

The use of interpolation tables in computing the emission is compelled by CPU time limitations. Computing the equilibrium state for a PDR model consumes, on average, 30 seconds. Most of the time, about 50%, is spent in computing the equilibrium state up to $A_V = 1$ mag near the H/H$_2$ transition zone. Beyond $A_V = 1$ mag, the solution advances much faster. Finding the equilibria for a large number of SPH particles requires a prohibitively long time, thus we resort to interpolating. Although interpolation is less accurate, it does the required job. On average it takes 20 seconds to process all these SPH particles and produce an emission map for each of the line emission of CO and ^{13}CO, with the scripts running serially on a single core.

4.2.4 Construction of synthetic emission maps and data cubes

The Construction of the flux maps is achieved by the following steps :

1. Bin the region of interest over a spatial domain.

2. For each bin (pixel) compute the mean flux in units of energy per unit time per unit area.

3. Repeat steps 1 and 2 for each emission line.

In practice a flux map is constructed from the brightness temperature of a line, measured in K, that is spectrally resolved over a certain velocity range. This provides a spectrum at a certain pixel as a function of velocity. The integrated spectrum over the velocity results in the flux. The velocity coordinate, in addition to the spatial dimensions projected on the sky, at every pixel can be thought of as a third dimension; hence the term "cube". Using a flux map, for a certain line computed from the simulation, we can do the opposite

and construct the data cube. Each SPH particle has a different line-of-sight velocity and a common FWHM micro-turbulence line width of 1 km s^{-1} . By adding the contribution of the Gaussian spectra of all the SPH particles within a pixel, we can construct a spectrum for that pixel. This procedure can be applied to all the pixels of our synthetic map producing a synthetic data cube. The main assumption in this procedure is that the SPH particles are distributed sparsely throughout each pixel and in line of sight velocity space. We can estimate the number density of SPH particles per pixel per line-of-sigh velocity bin by considering a typical pixel size of $\sim$ 1 kpc and a velocity bin equivalent to the adopted velocity dispersion. The typical range in line of sight velocities is from -50 to +50 km/s, which results in 100 velocity bins. With an average number of 5000 SPH particles in a pixel, the number density of SPH particles per pixel per velocity bin is 50. The scale size of an SPH particle is on the order of $\sim$ 1 pc, which is consistent with the size derived from the scaling relation of Eq-1 by (Larson 1981) by using a velocity dispersion of 1 km/s. Thus, the ratio of the projected aggregated area of the SPH particles to the area of the pixel is $\sim 10^{-4}$. This can roughly be thought of as the probability of two SPH particles overlapping along the line of sight within 1 km/s.

4.3   Results

4.3.1   Emission maps

In Figure-4.1, we show the emission maps of the first rotational transition of CO and ^{13}CO, for the model disk and dwarf galaxy. These maps were constructed using the procedure described in Section-4.2.3. Emission in these maps trace the molecular gas. As the density and temperature of the gas increase towards the inner regions, the emission is enhanced. Comparing the corresponding top and bottom panels of Figure-4.1, we see that the emission of the dwarf galaxy is significantly weaker than that of the disk galaxy. The gas of the dwarf galaxy is 10 times lighter than the disk galaxy's. Moreover, the metallicity of the dwarf galaxy is 5 times lower than that of the disk galaxy. Hence the column densities of CO and ^{13}CO are about 100 times lower in the former galaxy. The mean gas temperatures used to compute the emission is $\sim$ 10 times lower in the PDR sub-grid modeling of the dwarf galaxy compared to the disk galaxy, which results in weak excitation of the upper levels of the molecules through collisions. All these factors combined result in a reduced molecular luminosity in the dwarf galaxy, which is $\sim 10^4$ times weaker than that of the disk galaxy.

We demonstrate the construction of the data cube, described in Section-4.2.4, by presenting the CO$(1-0)$ emission map of the disk galaxy in Figure-4.2. These maps provide insight on the motion of the individual clouds along the line-of-sight. In the coordinate system we chose, negative velocities correspond to gas moving away from the observer, where the galaxy is viewed face-on in the sky. Thus, the velocities of the clouds are expected to be distributed around a zero mean. The width in the velocity distribution varies depending on the spatial location in the galaxy. For example, at the edge of the galaxy the gas is expected to be quiescent, with a narrow distribution in the line-of-sight velocities
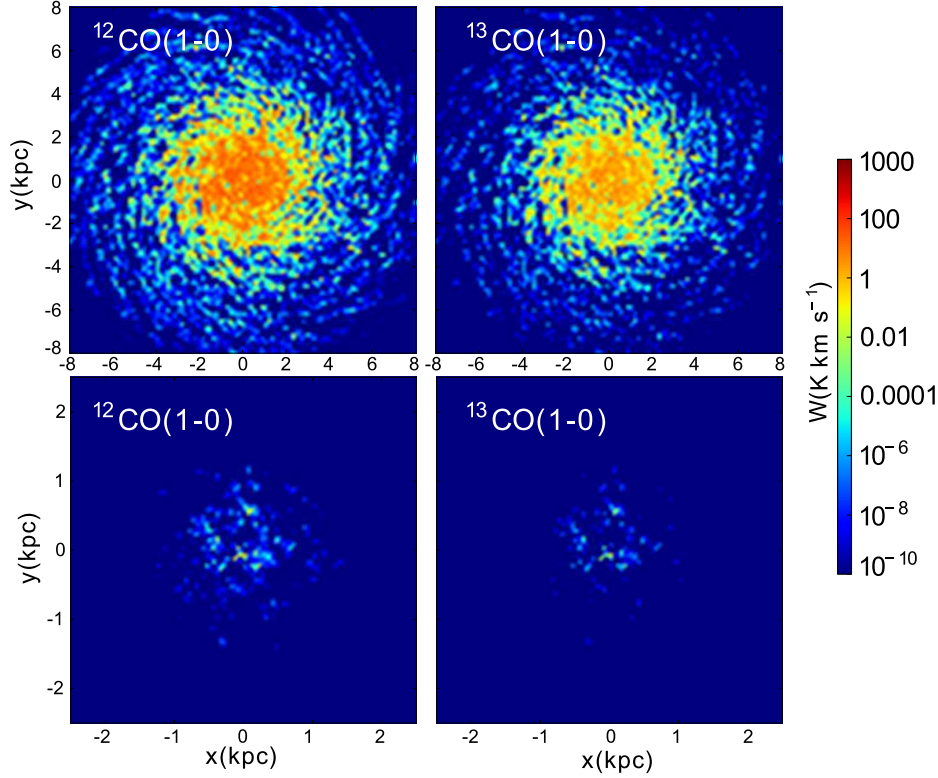
Figure 4.1 – (Top row) CO($1-0$) and ^{13}CO(1-0) fluxes of the disk galaxy. (Bottom row) CO(1-0) and ^{13}CO(1-0) emission for the dwarf galaxy. The pixel size in these maps is 0.16×0.16 kpc.

(V_{los}). This is seen clearly in the channel maps $|V_{los}| = 20$ km s^{-1} , where the CO($1-0$) emission is too weak outside the $R > 3$ kpc region. In contrast the emission of these regions are relatively bright in the $|V_{los}| = 0$ km s^{-1} map. In the inner regions, $R < 1$ kpc, the CO($1-0$) emission is present even in the 40 km s^{-1} channel, which is a sign of the wide dynamic range in the velocities of the gas at the central parts of the galaxy.

The relationship between mechanical feedback, excitation temperature, T_{ex} (see Eq-10 in van der Tak et al. 2007) of the CO($1-0$) line and the distance of the molecular gas from the center of the galaxy (R) is illustrated in Figure-4.3; we plot the averages of Γ_{mech}/n, the mechanical heating rate per H nucleus, and the mean T_{ex} of the SPH particles in each pixel of the emission maps. T_{ex} for each SPH particle is a by product of the RADEX LVG computations (Schöier et al. 2005). We highlight the two obvious trends in the plots: (a) The mechanical heating per H nucleus increases as the gas is closer to the center, (b) The excitation temperature correlates positively with mechanical feedback and correlates negatively with distance from the center of the galaxy. It is also interesting to note that, on average, the SPH particles with the highest Γ_{mech}/n have the
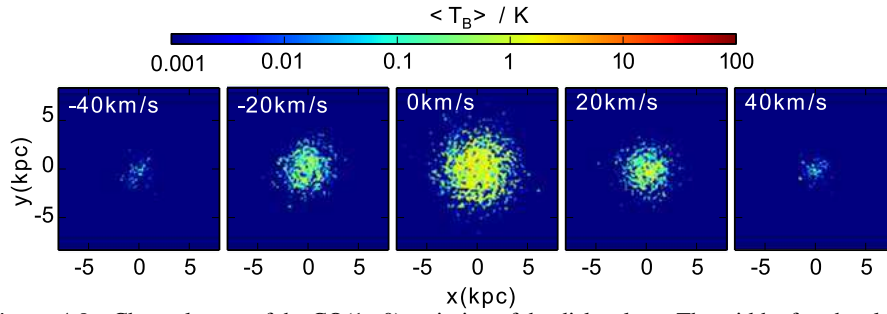
83

Figure 4.2 – Channel maps of the CO(1−0) emission of the disk galaxy. The width of each velocity channel is 20 km s^{-1} , where the average brightness temperature in the channels, indicated at the top of each panel, is shown. Since the galaxy is projected face-on at the sky, most of the emission emanates from the channel [-10, 10] km s^{-1} centered at $V_{los} = 0$ km s^{-1} .

highest excitation temperatures and are the closest to the center, see red points in the middle panel of Figure-4.3. On the other hand, gas situated at $R > 3$ kpc has average excitation temperatures less than 10 K and approaches 2.73 K, the cosmic microwave background temperature we chose for the LVG modeling, at the outer edge of the galaxy. This decrease in the excitation temperature is not very surprising, since at the outer region CO is not collisionally excited due to collisions with H$_2$, which has a mean abundance 10 times lower than that of the central region. Collisional excitation depends strongly on the kinetic temperature of the gas. In Kazandjian et al. (2012), it was shown that small amounts of Γ_{mech} are required to double the kinetic temperature of the gas in the molecular zone, where most of the molecular emission originate. However, Γ_{mech} is at least 100 times weaker in the outer region compared to the central region, which renders mechanical feedback ineffective in collisionally exciting CO.

4.3.2 The X factor: correlation between CO emission and H$_2$ column density

Since H$_2$ can not been observed through its various transitions in cold molecular gas whose $T_{kin} < 100$ K, astronomers have been using its proxy molecule CO to derive the molecular mass in the ISM of galaxies. It has been argued that the relationship between CO(1-0) flux and $N(H_2)$ is more or less linear (Solomon et al. 1987, Bolatto et al. 2013, and references therein) with $X_{CO} = N(H_2)/W_{CO(1-0)}$ nearly constant, where the proportionality factor X_{CO} is usually referred to as the *X*-factor. The observationally determined Milky Way X_{CO}, $X_{CO,MW}$, is given by $\sim 2 \times 10^{20}$ cm^{-2} (K km s^{-1})$^{-1}$ (Solomon et al. 1987). By using the emission map of CO(1-0) presented in Figure-4.1, and estimating the mean $N(H_2)$ throughout the map from the PDR models, we test this relationship in Figure-4.4.

It is clear that only for pixels with $W_{CO(1-0)} > 10$ K km s^{-1} X_{CO} approaches $X_{CO,MW}$. These pixels are located within $R \lesssim 2$ kpc of the disk galaxy, and $R \lesssim 0.2$ kpc of the
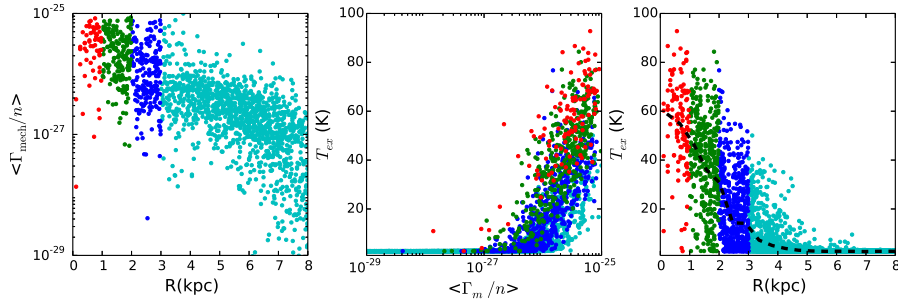
Figure 4.3 – (**Left**) Mean mechanical heating per hydrogen nucleus as a function of the distance from the center of the disk galaxy.(**Center**) Mean excitation temperature of the CO(1-0) line as a function of mechanical heating rate per hydrogen nucleus. (**Right**) Mean excitation temperature of the CO(1-0) line as a function of the distance from the center of the disk galaxy. The different colors correspond different galactocentric distance intervals. Red, green blue and cyan correspond to intervals [0, 1], [1,2] [2,3] and [3, 8] kpc respectively.
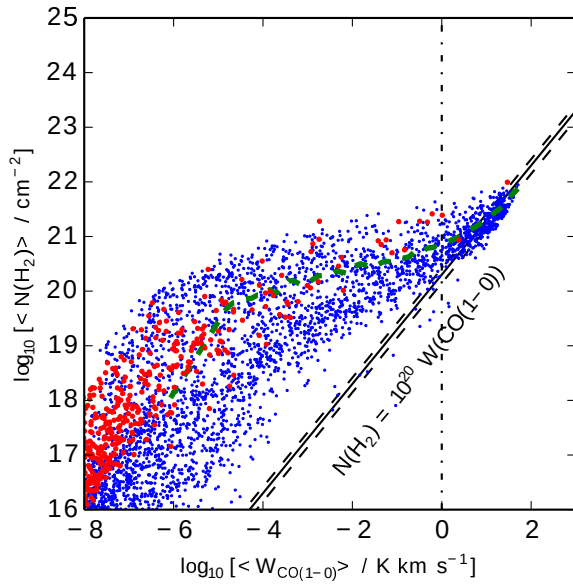
Figure 4.4 – $N(H_2)$ vs. CO(1-0) flux of the synthetic emission maps. The blue and red points correspond to the pixels of the disk and dwarf galaxies, respectively. The solid black line is the $W_{CO(1-0)} = X_{CO,MW} \, N(H_2)$ curve, with the observed ±30% uncertainty band shown by the black dashed lines. X_{CO} for pixels with $W_{CO(1-0)} < 10$ K km s^{-1} diverges from that of the Milky way, where the mean X_{CO} for the pixels is plotted in green. We note that 99% of the luminosity of the disk galaxy emanates from pixels whose $W_{CO(1-0)} > 1$ K km s^{-1} indicated by the dot-dashed line.

dwarf galaxy. Whenever $W_{CO(1-0)} < 10$ K km s^{-1}, X_{CO} increases rapidly reaching $\sim$ $1000X_{CO,MW}$. Looking closely at pixels within $W_{CO(1-0)}$ intervals of [0.1, 1], [1, 10] and > 10 K km s^{-1} we see that the gas average densities in these pixels are $\sim$ 20, 80 and 300 cm^{-3}respectively. This indicates that as the gas density becomes closer to the critical density of the CO(1-0) transition, which is $\sim 2 \times 10^3$ cm^{-3}, X_{CO} converges to that of the Milky Way. This is not surprising since as the density of gas increases, the mean A_V of an SPH particle increases to more than 1 mag. In most cases, beyond $A_V > 1$ mag, most of the H and C atoms are locked in H$_2$ and CO molecules respectively, where their abundances become constant. This leads to a steady dependence of the CO emission on A_V, and hence H$_2$. This is not the case for $A_V < 1$ mag, where fast variations in the abundances of H$_2$ and CO result in fast variations in the column density of H$_2$ and the CO emission, leading to the spread in X_{CO} observed in Figure-4.4. A more precise description on this matter is presented by Bolatto et al. (2013).

Most of the gas of the dwarf galaxy lies in the $A_V < 1$ mag range. Moreover, the low metallicity of dwarf galaxy results in a smaller abundance of CO in comparison to the disk galaxy, and thus a lower $W_{CO(1-0)}$. This results in an X_{CO} which is 10 to 100 times higher than that of the Milky Way (Leroy et al. 2011). Our purpose of showing Figure-4.4 is to check the validity of our modeling of the emission. Maloney & Black (1988) provide a more rigorous explanation on the $W_{CO(1-0)}$ and $N(H_2)$ relationship.

4.3.3 Higher J-transitions

So far we have only mentioned the CO(1-0) transition. The critical density of this transition is 2×10^3 cm^{-3}. The maximum density of the gas in our simulations is $\sim 10^4$ cm^{-3}. It is necessary to consider higher J transitions in probing this denser gas. The critical density of the CO(4-3) transition is $\sim 10^5$ cm^{-3}, which corresponds to densities 10 times higher than the maximum of our model galaxies. Despite this difference in densities the emission of this transition and the intermediate ones, $J = 2 - 1$ and $J = 3 - 2$, are bright enough to be observed due to collisional excitation mainly with H$_2$. To have bright emission from these higher J transitions, it also necessary for the gas to be warm enough, with $T_{kin} \gtrsim 50$ K, so that these levels are collisionally populated. In Figure-4.5, we show the luminosities of the line emission up to $J = 4 - 3$ of CO and ^{13}CO, emanating from the disk and dwarf galaxies. In addition to that, we present the luminosity of the inner, $R < 0.5$ kpc, region of the disk galaxy where Γ_{mech} is enhanced compared to the outer parts. This allows us to understand the trend in the line ratios and how they spatially vary and how mechanical feedback affects them (see next section). The ladders of both species are somewhat less steep for the central region, which can be seen when comparing the black and red curves of the disk galaxy in Figure-4.5. Hence, the line ratios for the high-J transitions to the low-J transitions are larger in the central region. This effect of Γ_{mech} was also discussed by Kazandjian *et al* (2015), who also showed that line ratios of high-J to low-J transitions are enhanced in regions where mechanical heating is high, which is also the case for the central parts of our disk galaxy. We will look at line ratios and how they vary spatially in Section-4.3.4.
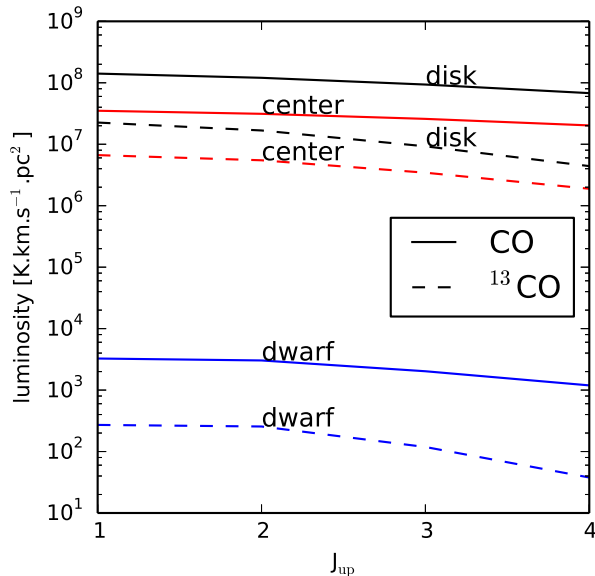
Figure 4.5 – Total luminosity of CO and ^{13}CO transitions up to $J = 4 - 3$ of the disk galaxy (black curves), the central $R < 2$ kpc region of the disk galaxy (red curves) and the dwarf galaxy (blue curves).

4.3.4   Diagnostics

In this section we use synthetic emission maps, for the $J > 1-0$ transitions, constructed in a similar fashion as described in Section-4.3.1. These maps are used to compute line ratios among CO and ^{13}CO lines where we try to understand the possible ranges in diagnostic quantities. This can help us recover physical properties of a partially resolved galaxy.

In Figure-4.6, we show ratio maps for the various transitions of CO and ^{13}CO. In these maps, line ratios generally exhibit uniform distributions in the regions where $R < 2$ kpc. This uniform region shrinks down to 1 kpc as the emission from transition in the denominator becomes higher. This is clearly visible when looking at the corresponding ^{13}CO/CO transitions in the panels along the diagonal of Figure-4.6. This is also true for the CO/CO transitions shown in the upper right panels of the same figure. Exciting the $J > 1-0$ transitions requires enhanced temperatures, where Γ_{mech} plays an important role in addition to H_2 densities higher than 10^3 cm^{-3}. Such conditions are typical to the central 2 kpc region but not for the outer regions. Hence diminishing emission of $J > 1 - 0$ results in the compact peaks that we mentioned. The peak value of the line ratios of CO/CO transitions at the center is around unity, compared to 0.1 - 0.3 for ratios involving transitions of ^{13}CO/CO. Since $J > 1 - 0$ transitions are weakly excited outside the central region, the line ratios decrease, e.g., by factors of 3 to 10 towards the outer edge of the galaxy for CO(2-1)/CO(1-0) and CO(4-3)/CO(1-0), respectively. Another conse-

quence of the weak collisional excitation of CO and ^{13}CO is noticed by looking again at the ^{13}CO/CO transitions along the diagonal panels of Fig-4.6, where the small scale structure of cloud "clumping", outside the central region becomes evident by comparing the ^{13}CO(1-0)/CO(1-0) to ^{13}CO(4-3)/CO(4-3). This dense gas is compact and occupies a much smaller volume and mass, approximately 10% by mass.

Similar line ratio maps can be constructed for the dwarf galaxy, which are presented in Figure-4.10 of the Appendix. These maps can be used to constrain the important physical parameters of the gas of both model galaxies, as we will demonstrate in the next section.

4.4 Application: modeling extra-galactic sources using PDRs and mechanical feedback

Now that we have established the spatial variation of diagnostic line ratios in the synthetic maps, we can use them to recover the physical parameters of the molecular gas that is emitting in CO and ^{13}CO.

The synthetic maps that we have constructed assume a high spatial resolution of 100 × 100 pixels, where the size of our model disk galaxy is ∼ 16 kpc. If we assume that the galaxy is in the local universe at a fiducial distance of 3 Mpc (the same distance chosen by Pérez-Beaupuits et al. (2011)), which is also the same distance of the well known galaxy NGC 253, then it is necessary to have an angular resolution of 1" to obtain such a resolution. This can be easily achieved with ALMA whose highest angular resolution is 0.01" in its widest configuration. In order not to restrict ourselves to galaxies in the local universe, we adopted a resolution of 21 × 21, which corresponds to a pixel size of ∼ 0.8 kpc. This resolution places our galaxy five times further at the same angular resolution of 1".

In the top panel of Figure-4.7, we show the normalized $W_{CO(1-0)}$ map, normalized with respect to the peak flux, with an overlaid mesh of the resolution mentioned before. Each pixel in the mesh contains on average a few thousand SPH particles. For simplicity, and despite the fact that each pixel encloses many SPH particles with different distributions in the gas parameters, we model the emission of the gas as that coming out of a single PDR, instead of considering two or more components. Using model emission, we estimate the parameters n, G, Γ_{mech} and A_V, one pixel at a time. Since we consider transitions up to $J = 4 - 3$ for CO and ^{13}CO, we have a total of 8 transitions, hence $8 - 4 = 4$ degrees of freedom in our fits. The purpose of favoring one PDR component in the fitting procedure is not to reduce the degrees of freedom, since for every added PDR component we loose five degrees of freedom, which could result in fits that are less significant.

The statistic we minimize in the fitting procedure is :

$$\chi^2 = \sum_j \sum_i \left[\frac{(r_o^i - r_m^j)}{\sigma_o^i} \right]^2 \tag{4.2}$$

(Press et al. 2002), where r_o and σ_o are the observed values and assumed error bars of the line ratios of the pixel in the synthetic map. r_m is the line ratio for the single
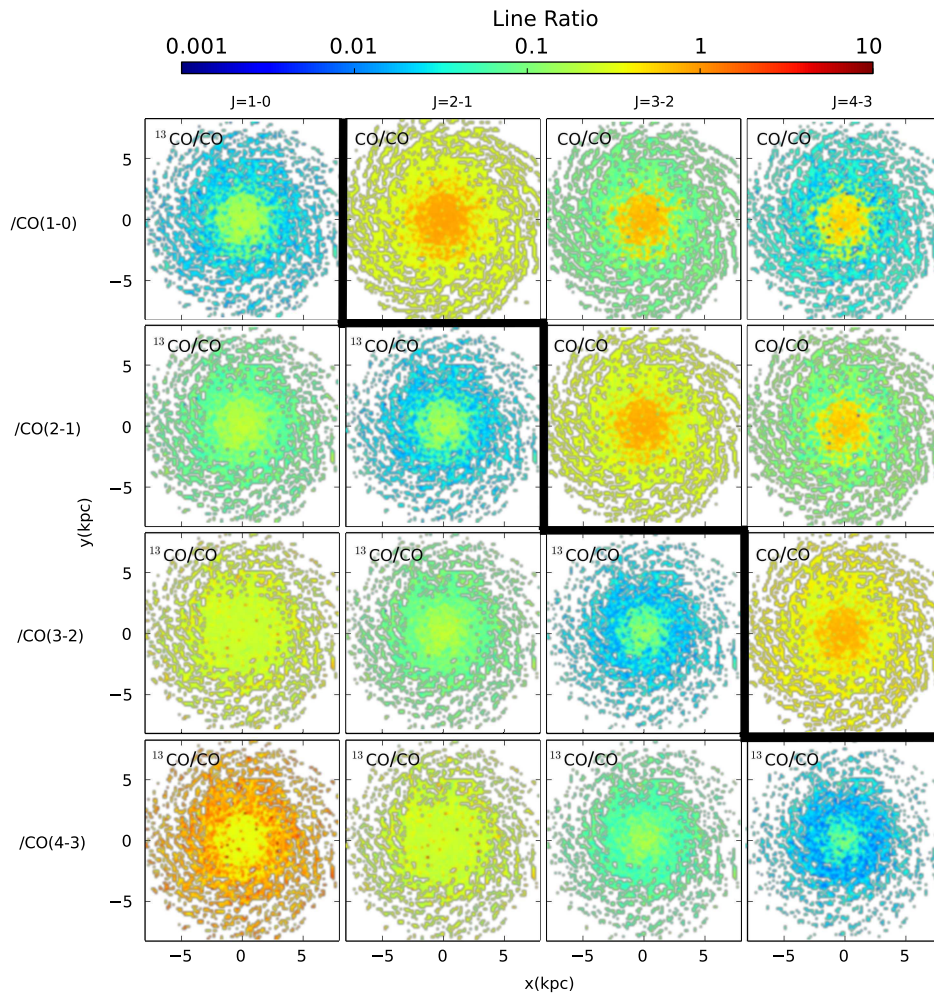
Figure 4.6 – Line ratio maps for various transitions of CO and ^{13}CO for the disk galaxy. The transition of the line in the numerator is specified at the top of each column, whereas that of the denominator is specified at the left of each row. For example, the panel in the third row of the second column corresponds to the line ratio map of ^{13}CO(2-1)/CO(3-2); the species involved in the line ratio are specified at the top left corner of each panel. Ratios larger than unity are typical to the central regions $R < 2$ kpc. Line ratio maps between CO transitions are to the left zig-zagged line, whereas the remaining maps are for line ratios between ^{13}CO and CO. Ratios involving $J \geq 3 - 2$ transitions trace the small scale structure of the molecular gas for $R > 2$ kpc.
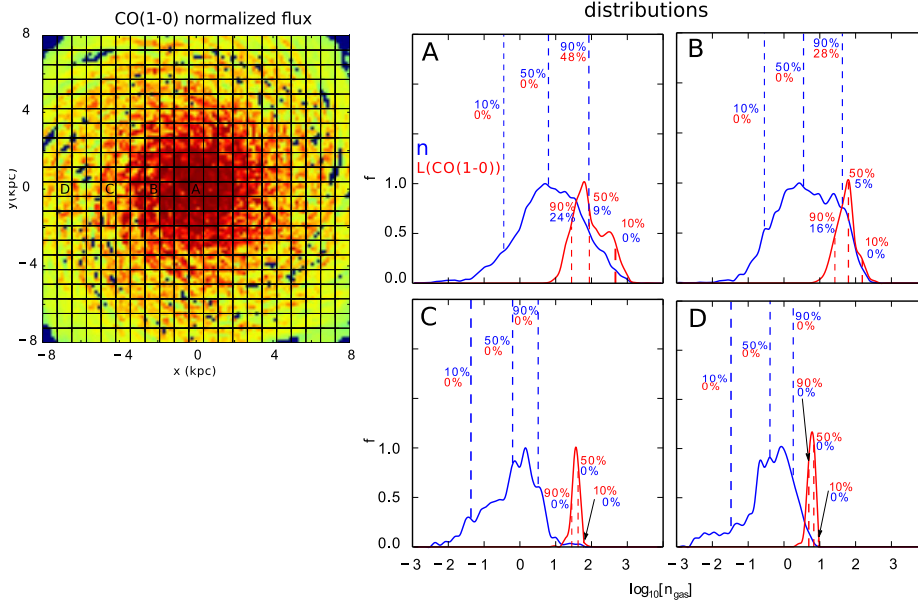
Figure 4.7 – Distributions of gas density and $W(CO(1-0))$ as a function of distance from the center of the disk galaxy. The normalized $W_{CO(1-0)}$ map, with the overlaid grid which has a resolution of 21×21 pixels is show in the **Left** panel. The labels A, B, C, D correspond to the pixels at distances of 0, 2, 4, and 7 kpc from the center of the galaxy. In the **right** panels we plot, in blue, the gas density distribution function, $f(n)$, of the SPH particles in these pixels. The fractional contribution of the SPH particles to the CO(1-0) luminosity of the pixel as a function of gas density, $f(L_{CO(1-0)})(n)$, is plotted in red. Both curves are scaled to their maximum value so that we can compare the ranges where they overlap. The cumulative distribution function is defined as $CDF(n) = \int_{10^{-3}}^{n} f(n)dn$. The blue dashed lines indicate the gas densities where the CDF $= 10, 50, 90\%$ respectively. Below these percentages, in red, are the fractional contribution of these SPH particles to the luminosity of the pixel. This contribution is defined as $LCDF(n) = \int_{10^{-3}}^{n} f(L_{CO(1-0)})(n)dn$. The red dashed lines represent the LCDF $= \int_{n}^{10^4} f(L_{CO(1-0)})(n)dn$ along with the analogous CDF integrated from $n = 10^4$ cm^{-3}. The corresponding distribution plots as a function of G_0, Γ_{mech} and A_V are shown in Figure-4.9 in the appendix.

PDR model whose parameter set we vary to minimize χ^2. The index i corresponds to the different combinations of line ratios. The line ratios we try to match are the CO and ^{13}CO ladders normalized to their $J = 1 - 0$ transition, in addition to the ratios of ^{13}CO to the CO ladder. These add up to 10 different line ratios which are not independent, and the number of degrees of freedom remains 4 for the mechanically heated model (mPDR), and 5 for the PDR which does not consider mechanical heating.

In Figure-4.8, we show the fitted line ratios of the pixels labeled (A, B, C, D) in Figure-4.7. The first row, labeled **A**, corresponds to the central pixel in the map. For this pixel, 90% of the emission emanates from gas whose density is higher than 10 cm^{-3},
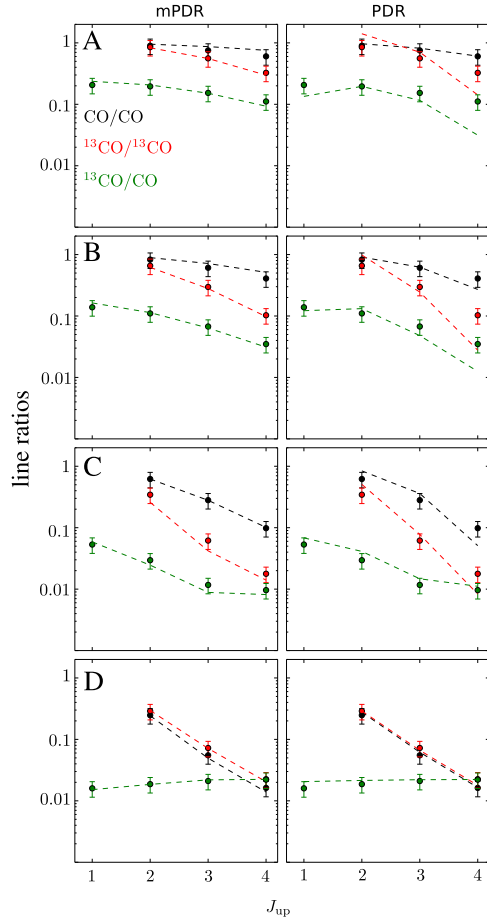
Figure 4.8 – Constraining the parameters for a resolved galaxy. The black dots correspond to the line ratios of CO($J \geq 2 - 1$) with CO(1-0) for a pixel in the emission map. The red dots correspond to the line ratios of ^{13}CO($J \geq 2 - 1$) with ^{13}CO(1-0) for the same pixel. The green dots correspond to the line ratios of the same transitions of ^{13}CO and CO for a pixel. The dashed line are the line ratios of these transitions of the best fit PDR model. The PDR models in the left column labeled "with mechanical heating" consider a range of possible Γ_{mech} in the heating budget while fitting these line ratios (the dots), while the plots labeled "without mechanical heating" do not take Γ_{mech} into account. The parameters of the best fit PDR models for each pixel are listed in Table-4.2.

constituting 24% of the mass in that pixel. The normalized cumulative distribution functions for the gas density (blue curves) and CO(1-0) luminosity (red curves) are shown in the bottom panels of Figure-4.7. The blue dashed lines indicates the density where 10, 50 and 90% of the SPH particles have a density up to that value. The numbers in red below these percentages indicate the contribution of these particles to the total luminos-

91

ity of that pixel. For instance, in pixel **A** 10% of the particles have a density less than ~ 0.03 cm^{-3}and these particles contribute 0% to the luminosity of that pixel; at the other end, 90% of the particles have a density less than ~ 100 cm^{-3}and these particle contribute 48% to the luminosity of that pixel. In a similar fashion, the red dashed lines show the cumulative distribution function of the CO(1-0) luminosity of the SPH particles, but this time integrated from the other end of the n axis. For example, 50% of the luminosity results from particles whose density is larger than 100 cm^{-3}. These particles constitute 9% of the gas mass in that pixel. The fits for PDR models that do not consider mechanical heating are shown in Figure-4.8. We see that these models fit ratios involving $J > 3 - 2$ transitions poorly compared to the mPDR fits, especially for the pixel A and B which are closer to the center of the galaxy compared to pixels C and D. In the remaining rows (**B,C,D**) of Figure-4.8, we show fits for pixels of increasing distances from the center of the galaxy. We see that as we move away further from the center, the CO to ^{13}CO ratios become flat in general, close to the elemental abundance ratio of ^{13}C/C which is 1/40 (see the green curve in the bottom row). This is essential, because the lines of both species are optically thin at the outer edge of the galaxy, hence the emission is linearly proportional to the column density, which is related to the mean abundance in the molecular zone. Another observation is that the distribution of the luminosity in a pixel becomes narrow at the edge of the galaxy. This is due to the low gas density and temperature in this region, where there are less SPH particles whose density is close to the critical density of the CO(1-0) line. We also see that Γ_{mech} plays a minor role, where both fits for a PDR with and without Γ_{mech} are equally significant. The parameters of the fits for the four representative pixels are listed in Table-4.2.

This fitting procedure can also be applied to the dwarf galaxy. The main difference in modeling the gas as a PDR in the disk and dwarf galaxy is that the mechanical heating in the dwarf is lower compared to the disk, thus it does not make a significant difference in the fits. In Figure-4.10, the line ratio maps show small spatial variation, thus it is not surprising in having small standard deviations in the fit parameters, in Table-4.2 of the dwarf galaxy compared to the disk galaxy.

4.5   Conclusion and discussion

In this paper, we have presented a method to model molecular species emission such as CO and ^{13}CO for any simulation which includes gas and provides a local mechanical heating rate and FUV-flux. The method uses this local information to model the spatial dependence of the chemical structure of PDR regions assumed to be present in the substructure of the gas in the galaxy models. These are then used to derive brightness maps assuming the LVG approximation. The method for the determination of the emission maps together with the interstellar medium model of the hydrodynamic galaxy models constitute a complete, self-consistent model for the molecular emission from a star forming galaxies' ISM. We compute the emission of CO and ^{13}CO in rotational transitions up to $J = 4 - 3$ for a model disk-like and a dwarf galaxy. From the emission maps, line ratios were computed to constrain the physical parameters of the molecular as PDRs.

		$\log_{10}\left[\frac{n}{\text{cm}^{-3}}\right]$	$\log_{10}\left[\frac{G}{G_0}\right]$	$\log_{10}\left[\frac{\Gamma_{\text{mech}}}{\text{erg cm}^{-3}\text{ s}^{-1}}\right]$	$\frac{A_V}{\text{mag}}$	χ^2_{red}
disk galaxy						
A	mPDR	1.8 ± 0.1	1.4 ± 1.0	-23.0 ± 0.1	22 ± 2	0.5 ± 0.1
0.5 kpc	PDR	3.5 ± 0.1	4.7 ± 0.3	–	7.6 ± 0.4	3.7 ± 0.1
	Actual	1.63 ± 0.1	1.71 ± 0.1	-23.1 ± 0.1	9.8 ± 0.7	–
B	mPDR	1.2 ± 0.3	0.6 ± 0.9	-23.5 ± 0.3	20.9 ± 3.1	0.7 ± 0.2
2 kpc	PDR	3.5 ± 0.1	2.8 ± 0.4	–	5.1 ± 0.6	3.6 ± 0.2
	Actual	1.16 ± 0.2	1.22 ± 0.1	-23.8 ± 0.2	4.7 ± 0.7	–
C	mPDR	1.5 ± 0.3	3.7 ± 1.1	-23.8 ± 0.3	10.1 ± 2.4	1.1 ± 0.2
4 kpc	PDR	2.7 ± 0.3	4.2 ± 0.7	–	6.6 ± 1.2	3.0 ± 0.8
	Actual	0.41 ± 0.1	0.53 ± 0.1	-24.9 ± 0.2	1.4 ± 0.1	–
D	mPDR	0.7 ± 0.5	1.6 ± 1.3	-26.5 ± 1.2	3.6 ± 1.7	0.3 ± 0.3
7 kpc	PDR	0.7 ± 0.6	3.3 ± 0.9	–	4.9 ± 1.5	0.6 ± 0.4
	Actual	-0.23 ± 0.1	-0.18 ± 0.1	-26.6 ± 0.2	0.4 ± 0.1	–
dwarf galaxy						
	mPDR	2.5 ± 0.3	3.4 ± 0.8	-23.4 ± 0.3	4.2 ± 0.6	0.6 ± 0.4
0.5 kpc	PDR	2.5 ± 0.3	4.7 ± 0.4	–	5.4 ± 0.4	0.5 ± 0.3
	Actual	1.1 ± 0.1	1.33 ± 0.1	-24.9 ± 0.2	0.8 ± 0.1	–

Table 4.2 – A comparison between the parameters fit using line ratios for the disk and dwarf galaxy. The listed numbers are the averages of the fit parameters for pixels at a specific distance from the center, these distances are listed on the left of the Table. For the dwarf galaxy we only show the fit parameters for the central 0.5 kpc. For each pixel, we present the fit parameter (first row) for a mechanically heated PDR (mPDR), a pure PDR which does not consider mechanical feedback into its heating budget (second row), and the actual mean and standard deviation for these quantities for the SPH particles within the pixel of the luminosity map. In the last column the statistic we minimize per degree of freedom, χ^2_{red} is listed to compare the quality of the fits of the mPDR and the pure PDR models.

We conclude the following:

1. Excitation temperature correlates positively with mechanical feedback in equilibrium galaxies. This in turn increases for gas which is closer to the center of the galaxy. The analysis presented in this paper allows estimates of mechanical feedback in galaxies which have high excitation temperatures in the center such as those observed by, e.g., Mühle et al. (2007) and Israel (2009b).

2. Fitting line ratios of CO and ^{13}CO using a single mechanically heated PDR component is sufficient to constrain the local Γ_{mech} throughout the galaxy within an order of magnitude, given the limitations of our modeling of the emission. The density of the gas emitting in CO and ^{13}CO is better constrained to within half dex. This approach is not suitable in constraining the gas parameters of the dwarf galaxy, although the statistical quality of the fits is on average better than that of the disk galaxy.

3. Our approach fails in constraining the local FUV-flux. It is under-estimated by two orders of magnitude in mechanically heated PDR fits, and over-estimated by more than that in PDRs, which do not account for mechanical feedback. This discrepancy is due considering one PDR component, where $J < 3-2$ CO lines are optically thick and trace very shielded gas. This discrepancy can also be explained by looking at the right column of Figure-4.9, where most of the emission results from SPH particles, which constitute a small fraction, and the rest of the gas is not captured by the PDR modeling.

The main features of our PDR modeling with mechanical feedback is the higher number of degrees of freedom it allows compared to LVG models and multi-component PDR modeling. We fit 10 line ratios while varying four parameters in the case where Γ_{mech} was considered, and 3 parameters when Γ_{mech} was not. We note that the actual number of *independent* measurements of line emission of CO and ^{13}CO up to $J = 4 - 3$ is 8. In LVG modeling the number of free parameters is at least 5, since in fitting the line ratios we need to vary T, $n(H_2)$, $N(CO)$, $N(^{13}CO)$ and the velocity gradient. On the other hand, PDRs assume elemental abundances and reaction rates. Moreover, the uncertainties in the PDR modeling could be much larger and depend on the micro-physics used in the PDR modeling (Vasyunin et al. 2004, Röllig et al. 2007). Thus, LVG models have more free parameters compared to single PDR models used in our method. On the other hand, considering two PDR components increases the number of free parameters to 9. Thus, rendering the fitting problem over-determined with more free parameters than independent measurements. Although LVG models are simple to run compared to PDR models, they do not provide information about the underlying physical phenomena exciting the line emission, which renders them useless for constraining Γ_{mech}. Although a two component PDR model produces better "Xi-by-eye" fits, these fits are statistically less significant than a single PDR model, but physically relevant. The main disadvantage of PDR modeling is the amount of bookkeeping required to run these models and they are computationally 10 times more demanding than LVG modeling, which is why we resorted to using interpolation tables.

4.5.1 Improvements and prospects

Our models have two main limitations: 1) we make implicit assumptions on the small scale structure of the galactic ISM and 2) we assume chemical equilibrium. The first limitation can be improved by performing higher spatial resolution simulations, which would result in gas that is better resolved and is denser than the current maximum of 10^4 cm^{-3}in the disk galaxy. A resolution of 10^6 cm^{-3} in the gas allows us to consider transitions up to $J = 15 - 14$ which are more sensitive to Γ_{mech} compared to the $J = 1 - 0$. Galaxy scale simulations, which reach densities higher than 10^4 cm^{-3} have been performed by Narayanan & Hopkins (2013) and required about 3×10^7 particles, and our method could be easily scaled to post-process such simulations.

Having more data to fit helps in finding better diagnostics of Γ_{mech} and narrower constraints for it. Another advantage in having emission maps for these high J transitions is

the increased the number of degrees of freedom in the fits, which renders the PDR models we fit statistically more significant. Moreover, it would be natural to consider multi-components PDR models in these fits, a dense-component fitting the $J > 4 - 3$ transitions and low-density component fitting the lower ones. These components are not independent, low-J emission is also produced by the high density PDR components. The high density component PDR would generally have a filling factor 10 to 100 times lower than the low density component, thus the high density model contributes mainly to the high-J transitions, whereas the low density models contributes mainly to the low-J emission and less to the high-J emission.

In producing the synthetic line emission maps, we have used the LVG emission from SPH particles, which assume PDR models as the governing sub-grid physics. The main assumption there was that the micro-turbulence line-width $v_{turb} = 1$ km/s. The peak of the distribution of v_{turb} of the SPH particles is located at ~ 3 km/s. The optical depth in the lines are thus in reality smaller than what we used in the calculations for the paper. When the lines become optically thick it effectively reduces the critical density of those transitions, and allows the excitation to higher energy states. The lines become more easily optically thick, for normal cloud sizes ($A_V = 5 - 10$) at $v_{turb} = 1$ km/s, which causes the peak of the CO ladder to be at a higher rotational transition. In order to quantify the shift of the peak of the CO ladder, we calculated a grid with different turbulent velocities, $v_{turb} = 1.0, 2.7, 5.0$, and 10.0 km/s, representative of the turbulent velocities in the SPH simulation, and used that grid to produce the resulting CO ladder. We found that the peak of the CO ladder is located at CO(4-3) transition, when computed from the distribution of v_{turb}, while the peak is located at CO(6-5) for the calculations where only $v_{turb} = 1.0$ km/s was used. Although this causes a significant quantitative change in the emission, it does not affect the general conclusions of the paper.

An accurate treatment of the radiative transfer entails constructing the synthetic maps by solving the 3D radiative transfer of the line emission using tools such as LIME (Brinch & Hogerheijde 2010). This would eliminate any possible bias in the fits. Currently, we construct the emission maps by considering the mean flux of the emission of SPH particles modeled as PDR within a pixel. This results in a distribution of the emission as a function of gas density as seen in Figure-4.7 and Figure-4.9. When fitting the line ratios, we recover the mean physical parameters of the molecular gas in that pixel associated with these emission. Using tools such as LIME, the micro-turbulence line width would be treated in a more realistic way by using the actual local velocity dispersions in the small scale turbulent structure of the gas, as opposed to adopting a fiducial 1 km s^{-1} as we have done throughout the paper.

Not all H$_2$ gas is traced by CO, since the H/H$_2$ transition zone occurs around $A_V = 0.1$ mag whereas the C/CO transition occurs around $A_V = 1$ mag. When looking at Figure-4.7 and Figure-4.9, we see that most of the CO emission emanates from a fraction of the gas. The remaining "major" part of the gas can contain molecular H$_2$, which is not traced by CO, but by other species such as C or C$^+$, that do have high enough abundances to have bright emission (Wolfire et al. 2010).

Finally, we note that we have ignored any "filling factor" effects in constructing the synthetic maps and the fitting procedure. This is not relevant to our method since in

95

considering line ratios, and filling factors cancel out in single PDR modeling of line ratios. However, it is important and should be taken into account, when considering multi-component PDR modeling and when fitting the absolute luminosities.

Acknowledgements

Appendix
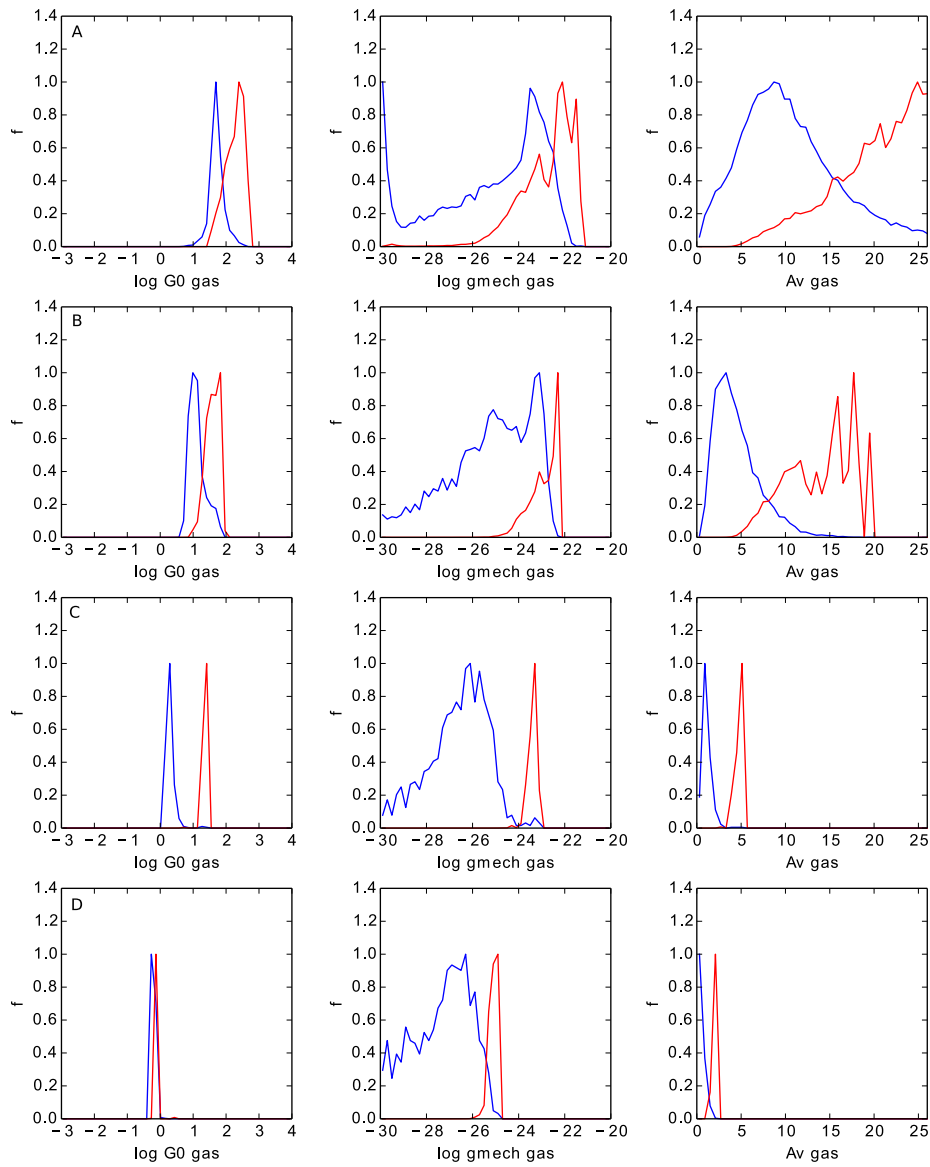
Figure 4.9 – Distribution functions as a function of G_0, Γ_{mech} and A_V for the representative pixels labeled A, B, C and D of Figure-4.7. The blue curves represent the distributions as a function of G_0 (first column), Γ_{mech} (second column) and A_V (third column). The red curves represent the fractional contribution of these distributions to the luminosity of their corresponding pixels. Both curves are normalized to their peak so that we can visually compare the subset of these distributions which contribute to the luminosity.
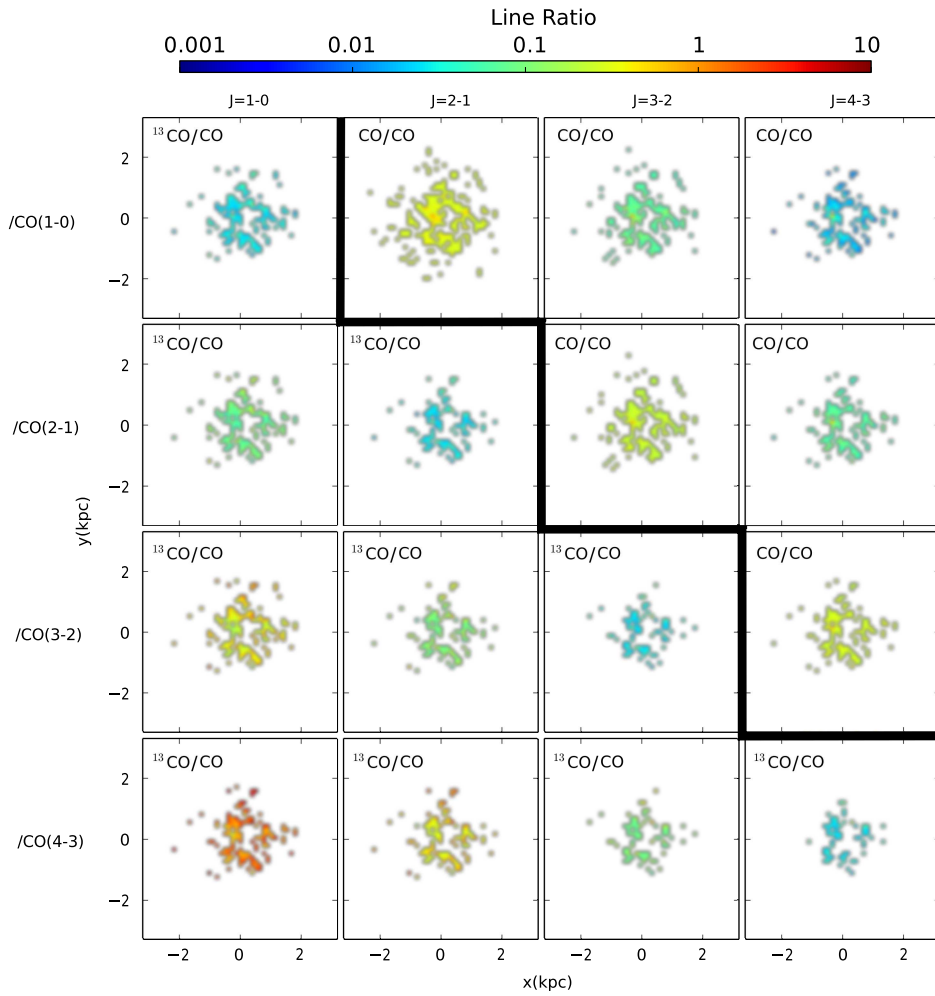
Figure 4.10 – Line ratio maps for various transitions of CO and ^{13}CO for the dwarf galaxy. The line ratios are generally spatially uniform and show slight variation, unlike the disk galaxy. These maps are also patchy, especially for line ratios involving $J = 3 - 2$ and $J = 4 - 3$ transitions. This is due to the low number of SPH particles with densities close to 10^4 cm^{-3} which are a pre-requisites for these transitions. See caption of Figure-4.6 for more details on interpreting the maps.

V

Constraining Cloud Parameters Using High Density Gas Tracers in Galaxies

Far-infrared molecular emission is an important tool to understand the excitation mechanisms of the gas in the ISM of star forming galaxies. In the present work, we model the emission from rotational transitions with critical densities $n \gtrsim 10^4$ cm^{-3}. We include $4 - 3 < J \leq 15 - 14$ transitions of CO and ^{13}CO, in addition to $J \leq 7 - 6$ transitions of HCN, HNC and HCO$^+$ on galactic scales. We do this by re-sampling high density gas in a hydrodynamic model of a gas-rich disk galaxy, assuming that the density field of the interstellar medium of the model galaxy follows the probability density function (PDF) inferred from the resolved low density scales. We find that in a narrow gas density PDF, with a mean density of ~ 10 cm^{-3} and a dispersion $\sigma = 2.1$ in the log of the density, most of the emission of molecular lines, even of gas with critical densities $> 10^4$ cm^{-3}, emanates from the 10-1000 cm^{-3} part of the PDF. We construct synthetic emission maps for the central 2 kpc of the galaxy and fit the line-ratios of CO and ^{13}CO up to $J = 15 - 14$ as well as HCN, HNC and HCO$^+$ up to $J = 7 - 6$, using one photo-dissociation region (PDR) model. We attribute the goodness of the one component fits for our model galaxy to the fact that the distribution of the luminosity, as a function of density, is peaked at gas densities between 10 to 1000 cm^{-3}, with negligible contribution from denser gas. Specifically, the Mach number, $\mathcal{M}$, of the model galaxy is ~ 10.

We explore the impact of different log-normal density PDFs on the distribution of the luminosity as a function of density, and we show that it is necessary to have a broad dispersion, corresponding to Mach numbers $\gtrsim 30$ in order to obtain significant ($> 10\%$) emission from $n > 10^4$ cm^{-3} gas. Such Mach numbers are expected in star-forming galaxies, Luminous Infrared Galaxies (LIRGS), and Ultra-Luminous Infrared Galaxies (ULIRGS). This method provides a way to constrain the global PDF of the ISM of galaxies from observations of molecular line emission. As an example, by fitting line ratios of HCN(1-0), HNC(1-0) and HCO$^+$(1-0) for a sample of LIRGS and ULIRGS, using mechanically heated PDRs, we constrain the Mach number of these galaxies to $29 < \mathcal{M} < 77$.

M. V. Kazandjian, I. Pelupessy, R. Meijerink, F. P. Israel, M. J. F. Rosenberg, M. Spaans
submitted to *A&A*

5.1   Introduction

The study of the distribution of molecular gas in star forming galaxies provides us an understanding of star formation processes and its relation to galactic evolution. In these studies carbon monoxide (CO) is used as a tracer of star-forming regions and dust, since in these cold regions (T < 100 K) H_2 is virtually invisible. The various rotational transitions of CO emit in the far-infrared (FIR) spectrum, and are able to penetrate deep into clouds with high column densities, which are otherwise opaque to visible light. CO lines are usually optically thick and their emission emanates from the C^+/C/CO transition zone (Wolfire et al. 1989), with a small contribution to the intensity from the deeper part of the cloud (Meijerink et al. 2007). On the other hand, other molecules whose emission lines are optically thin due to their lower column densities, probe higher depths of the cloud compared to CO. These less abundant molecules (e.g., ^{13}CO) have a weaker signal than CO, and a longer observation time is required in-order to observe them. Since ALMA became available, it has become possible to obtain well resolved molecular emission maps of star forming galaxies in the local universe, due to its high sensitivity, spatial and spectral resolution. In particular, many species have been observed with ALMA, including the ones we consider in this paper, namely CO, ^{13}CO, HCN, HNC and HCO^+ (e.g., Imanishi & Nakanishi 2013, Saito et al. 2013, Combes et al. 2013, Scoville et al. 2013, Combes et al. 2014).

Massive stars play an important role in the dynamics of the gas around the region in which they form. Although the number of massive stars (M > 10 $M_\odot$) is about 0.1% of the total stellar population, they emit more than 99% of the total ultra-violet (FUV) radiation. This FUV radiation is one of the main heating mechanisms in the ISM of star forming regions. Such regions are referred to as photon-dominated regions (PDRs) and they have been studied since the 1980's (Tielens & Hollenbach 1985, Hollenbach & Tielens 1999). Since then, our knowledge of the chemical and thermal properties of these regions has been improving. Since molecular clouds are almost invariably accompanied by young luminous stars, most of the molecular ISM forms as part of a PDR, and thus this is the environment where the formation of CO and other molecular species can be studied. In addition, the life-span of massive stars is short, on the order of 10 Myrs, thus they are the only ones that detonate as supernovae, liberating a significant amount of energy into their surroundings and perturbing it. A small fraction of the energy is re-absorbed into the ISM, which heats up the gas (Usero et al. 2007, Falgarone et al. 2007, Loenen et al. 2008). In addition, star-bursts (SB) occur in centers of galaxies, where the molecular ISM can be affected by X-rays of an accreting black hole (AGN) and enhanced cosmic ray rates or shocks (Maloney et al. 1996b, Komossa et al. 2003, Martín et al. 2006, Oka et al. 2005, van der Tak et al. 2006, Pan & Padoan 2009, Papadopoulos 2010, Meijerink et al. 2011, 2013, Rosenberg et al. 2014a, among many others), that ionize and heat the gas.

By constructing numerical models of such regions, the various heating mechanisms can be identified. However, there is no consensus about which combination of lines define a strong diagnostic of the different heating mechanisms. This is mainly due to the lack of extensive data which would probe the various components of star forming regions in extra-galactic sources. Direct and self-consistent modeling of the hydrodynamics, radia-

tive transfer and chemistry at the galaxy scale is computationally challenging, thus some simplifying approximations are usually employed. In the simplest case it is commonly assumed that the gas has uniform properties, or is composed of a small number of uniform components. In reality, on the scale of a galaxy or on the kpc scale of star-bursting regions, the gas density follows a continuous distribution. Although the exact functional form of this distribution is currently under debate (e.g. Nordlund & Padoan 1999), it is believed that in SB regions, where the gas is thought to be super-sonically turbulent (Norman & Ferrara 1996, Goldman & Contini 2012) the density distribution of the gas is a log-normal function (Vazquez-Semadeni 1994, Nordlund & Padoan 1999, Wada & Norman 2001, 2007, Kritsuk et al. 2011, Ballesteros-Paredes et al. 2011, Burkhart et al. 2013, Hopkins 2013). This is a universal result, independent of scale and spatial location, although the mean and the dispersion can vary spatially. Self-gravitating clouds can add a power-law tail to the density PDF (Kainulainen et al. 2009, Froebrich & Rowles 2010, Russeil et al. 2013, Alves de Oliveira et al. 2014, Schneider et al. 2014). However, Kainulainen & Tan (2013) claim that such gravitational effects are negligible on the scale of giant molecular clouds, where the molecular emission we are interested in emanates.

In Kazandjian et al. (2015a), we studied the effect of mechanical heating (Γ_{mech} hereafter) on molecular emission grids and identified some diagnostic line ratios to constrain cloud parameters including mechanical heating. For example, we showed that low-J to high-J intensity ratios of high density tracers will yield a good estimate of the mechanical heating rate. In Kazandjian et al. (2015b), KP15 hereafter, we applied the models by Kazandjian et al. (2015a) to realistic models of the ISM taken from simulations of quiescent dwarf and disk galaxies by Pelupessy & Papadopoulos (2009). We showed that it is possible to constrain mechanical heating just using $J < 4 - 3$ CO and ^{13}CO line intensity ratio from ground based observations. This is consistent with the suggestion by Israel & Baas (2003) and Israel (2009b) that shock heating is necessary to interpret the high excitation of CO and ^{13}CO in star-forming galaxies. This was later verified by Loenen et al. (2008), where it was shown that mechanically heated PDR models are necessary to fit the line ratios of molecular emission of high density tracers in such systems.

Following up on the work done by KP15, we include high density gas ($n > 10^4$ cm^{-3}) to produce more realistic synthetic emission maps of a simulated disk-like galaxy, thus accounting for the contribution of this dense gas to the molecular line emission. This is non trivial as global, galaxy wide models of the star forming ISM are constrained by the finite resolution of the simulations in the density they can probe. This paper is divided into two main parts. In the first part, we present a new method to incorporate high density gas to account for its contribution to the emission of the high density tracers, employing the plausible assumption, on theoretical grounds (e.g. Nordlund & Padoan 1999), that the density field follows a log-normal distribution. In the methods section, we describe the procedure with which the sampling of the high density gas is accomplished. Once we have derived a re-sampled density field we can employ the same procedure as in KP15 to model the line emission of molecular species. In Section-5.3.1, we highlight the main trends in the emission of the $J = 5 - 4$ to $J = 15 - 14$ transitions of CO and ^{13}CO tracing the densest gas, along with the line emission of high density tracers HCN, HNC and HCO$^+$ for transitions up to $J = 7-6$. In Section-5.3.2, we fit emission line ratios

using a mechanically heated PDR (mPDR hereafter) and constrain the gas parameters of the model disk galaxy. In the second part of the paper, Section-5.4, we will follow the reverse path and examine what constraints can be placed on the PDF from molecular line emissions, following the same modeling approach as in the first part. We discuss the effect of the shape and width of the different density profiles on the emission of high density tracers. In particular, we discuss the possibility of constraining the dispersion and the mean of an assumed log-normal density distribution using line ratios of high density tracers. We finalize with a summary and general remarks.

5.2   Methods

The numerical methods we implement in this paper are similar to those in KP15. We will focus exclusively on a single model disk galaxy, but the methods developed here could be applied to other models. We implement a recipe for the introduction of high density gas $n > 10^4$ cm^{-3}, which is necessary to model the emission of molecular lines with critical densities[1] (n_{crit}) in the range of $10^4 - 10^8$ cm^{-3}. In the following, we summarize briefly the methods used in KP15.

5.2.1   Galaxy model, radiative transfer and sub-grid modeling

The model galaxy we use in this paper is the disk galaxy simulated by Pelupessy & Papadopoulos (2009), with a total mass of 10^{10} M$_\odot$ and a gas content representing 10% of the total mass. This represents a typical example of a quiescent star forming galaxy. The code FI (Pelupessy & Papadopoulos 2009) was used to evolve the galaxy to dynamical equilibrium (in total for ~ 1 Gyr). The simulation code implements an Oct-tree algorithm which is used to compute the self-gravity (Barnes & Hut 1986) and a TreeSPH method for evolving the hydrodynamics (Monaghan 1992, Springel & Hernquist 2002), with a recipe for star formation based on the Jeans mass criterion (Pelupessy 2005). The adopted ISM model is based on the simplified model by Wolfire et al. (2003), where the local FUV field in the neighborhood of the SPH particles is calculated using the distribution of stellar sources and population synthesis models by Bruzual & Charlot (1993, 2003) and Parravano et al. (2003). The local average mechanical heating rate due to the self-interacting SPH particles is derived from the prescription by Springel (2005): the local mechanical heating rate is estimated using the local dissipation by the artificial viscosity terms, which in this model ultimately derive mainly from the localized supernova heating. For the work presented here the most important feature of these simulations is that they provide us with the information necessary for further sub-grid modeling in post-processing mode. Details about this procedure can be found in KP15. In particular, the gas density n, the mean local mechanical heating rate Γ_{mech}, the local FUV flux G and the mean A_V of the SPH particles are used. We refer to these as the main physical parameters of the gas, which are essential to parametrize the state of PDRs that are used, to obtain the emission maps.

---

[1] We use the following definition of the critical density, $n_{crit} \equiv k_{ij}/A_{ji}$, where k_{ij} is the collision coefficient from the level i to the level j and A_{ji} is the Einstein coefficient (of spontaneous decay from level j to level i.

This method of computing the emission can be generally applied to other simulations, as long as they provide these physical parameters.

The PDR modeling (Meijerink & Spaans 2005) consists of a comprehensive set of chemical reactions between the species of the chemical network by Le Teuff et al. (2000). The main assumption in the extended sub-grid modeling, is that these PDRs are in thermal and chemical equilibrium. We post-process an equilibrium snapshot of the SPH simulation by applying these PDR models to the local conditions sampled by each particle, and estimate the column densities of the molecules, abundances of the colliding species, and the mean gas temperature of the molecular clouds. These are the main ingredients necessary to compute the emission emanating from an SPH particle. PDR models are non-homogeneous by definition, as there are steep gradients in the kinetic temperature and the abundances of chemical species. By assuming the large velocity gradient (LVG) approximation (Sobolev 1960) using Radex (van der Tak et al. 2007), weighted quantities from the PDR models were used as input to Radex to compute the emission of the molecular species studied in this paper (Kazandjian et al. 2015a). For more details on computing the emission and constructing the emission maps we refer to Section-2.3 of KP15, where this method can be applied to any SPH simulation of a star-forming galaxy that provides the ingredients mentioned above. For the work in this paper, we do not include any AGN or enhanced cosmic ray physics, since these are not relevant for the simulation we have used. XDR and or enhanced cosmic ray models are necessary in modeling the ISM of ULIRGS, as was discussed by, e.g., Papadopoulos (2010) and Meijerink et al. (2011) and shown in the application of the models to Arp 299 by Rosenberg et al. (2014b).

5.2.2 Sampling the high density gas

One of the main purposes of this paper is to constrain cloud parameters using the molecular transitions mentioned earlier. The typical critical densities of these transitions are between $\sim 10^5$ and $\sim 10^8$ cm^{-3}. The highest density reached in the SPH simulation is 10^4 cm^{-3}, thus the rotational levels we are interested in are sub-thermally populated in the non-LTE (local thermal equilibrium) regime. Therefore the intensity of the emission associated with these transitions is weak. In-order to make a more realistic representation of the molecular line emission of the ISM of the simulated galaxy, we resort to a recipe to sample particles up to 10^6 cm^{-3}. In what follows, we describe the prescription we have used to sample particles to such densities.

The sampling scheme we adopt is based on the assumption that the gas density PDF of the cold neutral medium (CNM) and the molecular gas is a log-normal function, given by Eq-5.1 (Press et al. 2002):

$$\frac{dp}{d \ln n} = \frac{1}{\sqrt{2\pi\sigma^2}} \exp\left(-\frac{1}{2}\left[\frac{\ln n - \mu}{\sigma}\right]^2\right) \tag{5.1}$$

where μ is the natural logarithm (ln) of the median density (n_{med}), and σ is the width of the log-normal distribution. Such PDFs are expected in the inner ($\sim$ kpc) ISM of galaxies. For example, simulations by Wada & Norman (2001) and Wada (2001) reveal that the

PDF of the gas density is log-normally distributed over seven orders of magnitude for densities ranging from ~ 4 cm^{-3} to $\sim 4 \times 10^7$ cm^{-3}. Log-normal density distributions have been discussed by other groups as well, and we refer the reader to Section-5.1 for more references. The simulations by Wada are evolved using a grid based code with a box size ~ 1 kpc and include AGN feedback, whereas our simulation was evolved with an SPH code and without AGN feedback with a scale length of ~ 10 kpc. The major assumption in our sampling is that the gas of our model disk galaxy follows a log-normal distribution for $n > 10^{-2}$ cm^{-3}. Using this assumption we can sample and add high density gas beyond the maximum of 10^4 cm^{-3} of the simulated galaxy. Of course such re-sampling does not provide a realistic spatial distribution of high density gas, as the re-sampled particles are assumed to be placed randomly within the smoothing length of SPH particles that are dense enough to support star-formation. We can use this simplification as long as we do not try to construct maps resolving scales smaller than the original spatial resolution of ~ 0.05 kpc.

In Figure-5.1, we show the distributions of the gas density of our simulation along with that of the temperature. The SPH simulation consists of $N = 2 \times 10^6$ particles. The distribution of the temperature has a peak at low temperature and a peak at high temperature, similar to the PDF in Figure-4 in Wada (2001). The low temperature peak around $T = 300$ K corresponds to gas that is thermally stable, whereas the higher temperature peak around $T = 10000$ K corresponds to gas that is thermally unstable (Schwarz et al. 1972). On the other hand, the distribution of the density exhibits just one prominent peak near $n \sim 1$ cm^{-3}, with a small saddle-like feature at a lower density of $\sim 10^{-2}$ cm^{-3} (see the bottom panel of Figure-5.1). The histogram of the density of the stable gas in the bottom panel, shows that the density of this gas ranges between $10^{-2} < n < 10^4$ cm^{-3}. The lower bound of this interval is shifted towards higher densities as the gas populations are limited to lower temperatures, indicating efficient cooling of the gas for high densities. The temperature of the SPH particles represents its peripheral temperature. Thus, although the temperature might be too high for the formation of molecules at the surface, molecules could form in the PDRs present in the sub-grid modeling.

The 1000 K mark seems to be a natural boundary between the thermally stable and the unstable population (see top panel of Figure-5.1). Hence we use the minimum density range for this population, $n \sim 10^{-2}$ cm^{-3}, as the lower limit for the fit of the PDF that we apply. This is depicted in Figure-5.2, where we fit a log-normal function to the gas density around the peak at $n = 1$ cm^{-3}. The density range of the fit is $n_{\text{low}} = 10^{-2} < n < n_{high} = 10^2$ cm^{-3}. To find the best fit of the actual density PDF, we examined other values for n_{low} and n_{high}. For example, choosing $n_{\text{low}} = 10^{-1}$ cm^{-3} causes the fit PDF to drop faster than the original distribution for $n > 10^2$ cm^{-3}, which reduces the probability of sampling particles with $n > 10^5$ cm^{-3} to less than one particle in a sample of one billion. On the other hand, setting $n_{high} = 10^3$ cm^{-3} does not affect the outcome of the fit. Using the best fit density PDF, we notice that only the gas within the $10^{-2} < n < 10^2$ cm^{-3} range is log-normally distributed, where the original distribution starts deviating from the log-normal fit for $n > 10^2$ cm^{-3} (compare blue and red curves in Figure-5.2). The deviation from a log-normal distribution is likely due to the resolution limit of the SPH simulation. For example, the PDF of a simulation with 4×10^5 SPH particles start to deviate from

log-normality for $n > 10^{1.5}$ cm^{-3}. A similar deviation in the density distribution fit by Wada (2001) is observed in the $n \gtrsim 10^6$ cm^{-3} range, most likely due to similar resolution constraints. Here we will assume that the gas density will be distributed according to a log-normal function in the infinite N-limit.

For each SPH particle i, parent particle hereafter, we sample from the fit PDF an ensemble $\{n_s\}$ of 100 sub-particles within the smoothing length of the parent, where n_s and n_i are the gas number densities of the sampled and parent particles respectively. The ensemble $\{n_s\}$ is chosen such that $n_s > n_i$, which enforces having sampled particles that are denser than the parent. The particles with $n > 10^2$ cm^{-3} constitute 2% of the gas mass, as their total number is $\sim 40,000$. The PDF of the sampled particles is shown in green in Figure-5.2, where the sampled PDF follows the fit log-normal distribution very accurately for densities $n > 10^3$ cm^{-3}. The bias of sampling particles with $n_s > n_i$ affects the shape of the distribution between $n = 10^2$ cm^{-3} to 10^3 cm^{-3}. This discrepancy is resolved by adjusting the weights of the sampled and parent particles along bins in density range such that the new weights match the fit PDF. These weights are used to adjust the masses of the parent and sampled particles, which ensures that the total mass of the system is conserved. The combined PDF is overlaid as black crosses in Figure-5.2.

The re-sampling is restricted to particles with $n_i > 10^2$ cm^{-3} to ensure that the sub-particles are sampled in regions that are likely to support star-formation. Thus, most of the far-IR molecular emission results from this density range. In our sampling, we ignore any spatial dependence on the gas density distribution, where the PDFs correspond to that of all the particles in the simulation. Sampling new gas particles with $n > 10^2$ cm^{-3} ensures that these ensembles will lie in regions tracing CO and consequently H$_2$. At the outskirts of the galaxy, the H$_2$ column density is at least 100 times lower compared to the center of the galaxy. Moreover, since the density PDF is log-normal, the number of SPH particles with $n > 10^4$ cm^{-3} in the outskirts are so small, that no emission from high density tracers is expected. Thus, we would not have enhanced molecular emission due to the sampling, e.g. for the high density tracers, at the edge of the galaxy, where it is not expected to be observed. To address this point, we examine the shape of the gas density PDF for increasing galactocentric distances. We find that the median of the log-normal distribution is shifted to lower densities, while the dispersion becomes narrower towards the edge of the galaxy. Consequently, the relative probability of finding high density gas at the outer edge of the galaxy is reduced compared to that of the central region. In fact, the PDF in the region within $R < 2$ kpc is closely represented by the one we have shown in Figure-5.2. The dispersion of the density PDF for distances $R < 2$ kpc from the center is $\sigma = 2.05$ is very close to $\sigma = 2.1$ of the fit PDF in Figure-5.2. On the other hand, the dispersion is $\sigma = 1.2$ for $6 < R < 8$ kpc. Thus, in this paper we focus on the central region of the galaxy, where the same density PDF is used in sampling the gas particles within this region. It is worth noting that after the sampling procedure, gas with $n > 10^4$ cm^{-3} constitutes only 0.5% of the total gas mass. For example, this is consistent with the estimate of the filling factor of the densest PDR component derived from modeling the star-forming galaxy Arp 299 by Rosenberg et al. (2014b), even though our model galaxy is not necessarily representative of Arp 299.

The log-normality feature of the density PDF reflects non-linearity in the evolution

105

of the gas, which we use as an argument for the cascade of turbulence into small spatial scales where high density gas forms. Here we will take the Γ_{mech} of the sampled particles to be the same as their parent SPH particle, although in Figure-2 of Kazandjian et al. (2015a) we have shown that there is some dependence of Γ_{mech} on the gas density. However, this dependence is not trivial (see Nordlund & Padoan 1999). Note that for our models Γ_{mech} would never be the dominant heating mechanism for high density gas ($> 10^4$ cm^{-3}), while this could change for modeling ULIRGs. A similar assumption was made for the A_V and G of the sampled particles, where the same values as that of the parent were used. As a check we picked a typical region in the central kpc of the galaxy and quantified the mean and the standard deviation of Γ_{mech}, G and A_V relative to the parent particle compared to other gas particles within its smoothing length. We found that the spread in Γ_{mech} is within a factor of two, whereas this spread decreases to within 0.1 for G and A_V. Therefore, the assumption of using the same parameters as the parent for the sampled ones would have a small effect on the produced emission maps.

Various other authors have tried to overcome the resolution limit of their simulations. For example, the sampling procedure by Narayanan et al. (2008) is motivated by observations of GMCs. Their approach entails the sampling of GMCs by assuming that half of the gas mass is represented by molecules. Moreover, these GMCs are modeled as spherical and gravitationally bound with power-law density profiles provided by Rosolowsky (2005), Blitz et al. (2007) and Solomon et al. (1987). These sampling methods are similar to the work presented here, in the sense that they make a (different) set of assumptions to probe high density gas not present in the simulation. Our basic assumption is a physically motivated extension of the log-normal distribution.

5.3   Modeling dense gas in galaxy disks

5.3.1   Luminosity ladders and emission maps

The contribution of the high density particles to the total luminosity of each transitions is illustrated in Figure-5.3. The luminosity of a SPH particle is approximated as the product of the line flux (F) with the projected area (A) of the SPH particle. The total luminosity of a certain emission line of the galaxy is computed as $L = \sum_{i=1}^{i=N} F_i A_i$, where i is the index of the SPH particles and N is the number of SPH particles. In the current implementation, the "area" of each sampled particle is assumed to be A_i/N_s, where $N_s = 100$ is the number of the sampled particles. This ensures that the total area of the sampled particles adds up to the area of the parent particle. Such a normalization is consistent with the SPH formalism, where all particles have the same mass. The luminosities of the lines due to the sampling are marginally affected, with a weak dependence on the transition and the species. The increase in the luminosity is due to the dependence of the flux of the emission lines on the gas density, where in general, the flux increases as a function of increasing density. The dependence of the luminosity on density and its relationship to the density PDF will be addressed in Section-5.4.

The total luminosities as a function of J, luminosity "ladders", are computed by con-
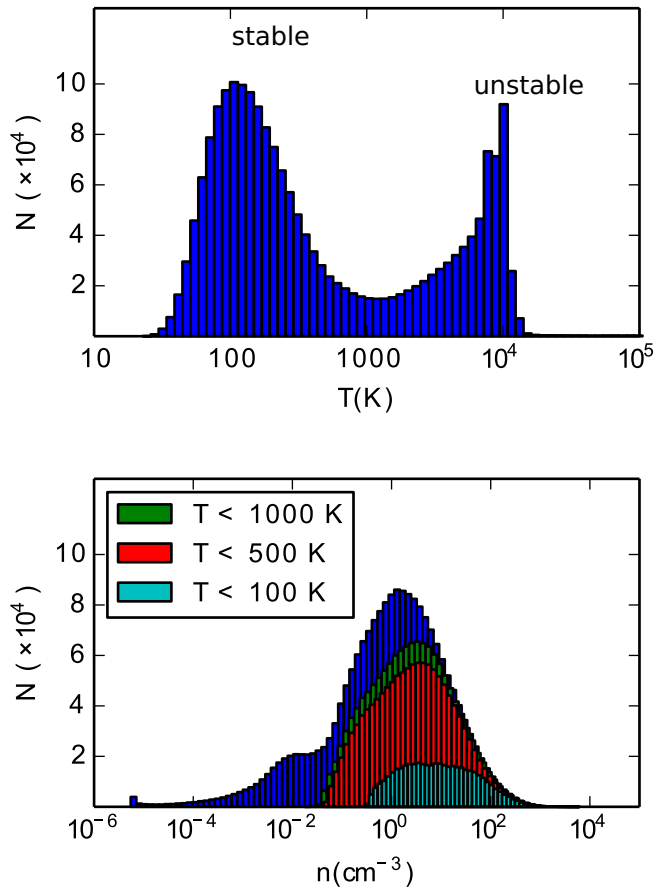
Figure 5.1 – (Top) Histogram of the kinetic temperature of the SPH particles. (Bottom) Histogram of the gas density of the SPH particles. In this same panel, the histograms for the gas densities of sub-populations of the gas are also shown. The red, green and cyan histograms correspond to gas particles with temperature below $T = 1000, 500, 100$ K respectively. These sub-populations of the gas particles are thermally stable corresponding to the peak around $T = 300$ K in the top panel. The vertical axis refers to the number of SPH particles within each bin.

sidering all the SPH particles within a projected box of 16×16 kpc. In Figure-5.4 we show the flux maps of a subset of the molecular lines. These maps give insight on the regions of the galaxy where most of the emission emanates. In the next section we will use line ratios in a similar manner to KP15 in order to constrain the gas parameters within pixels in the central region of the galaxy. The rotational emission lines we have used are listed in Table-5.1.
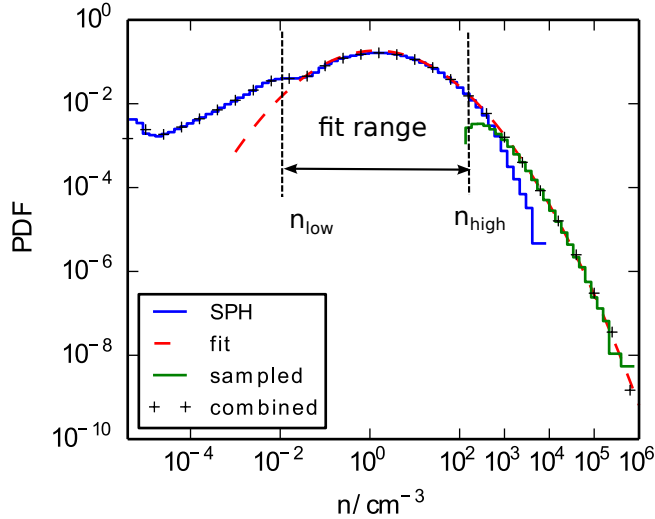
Figure 5.2 – Probability density function of the SPH particles. The blue curve corresponds to the PDF of gas density n and it is proportional to $dN/d\log(n)$; in other words this curve represents the probability of finding an SPH particle within a certain interval of $\log(n)$. The dashed-red curve is the log-normal fit of the PDF of the blue curve in the range 10^{-2} to 10^{4}. The green curve is the PDF of the sampled population from the original SPH particles while keeping the samples with $n > 10^{2}$ cm^{-3}. The black crosses trace the combined PDF of the sampled and the original set of the SPH particles. The median density and the dispersion are $n_{\mathrm{med}} = 1.3$ cm^{-3} and $\sigma = 2.1$ respectively.

5.3.2   Constraining cloud parameters using line ratios

With the synthetic luminosity maps at our disposal, we construct various line ratios and use them to constrain the mechanical heating rate in addition to the remaining gas parameters, namely n, G and A_V, throughout the central < 2 kpc region of the galaxy. We follow the same approach by KP15, where we minimize the χ^2 statistic of the line ratios of the synthetic maps against these of a mechanically heated PDR model.

   We fit the cloud parameters one pixel at a time and compare them to the mean physical parameters of the gas in that pixel. In Figure-5.5, we show a sample fit for the central pixel of the model galaxy that has a pixel size of 0.4×0.4 kpc, which is the same pixel size that has been assumed by KP15. For this fit we have considered the luminosity ladders of CO, ^{13}CO, HCN, HNC and HCO$^+$ normalized to the CO(1-0) transition. In addition to these, we have included the ladder of ^{13}CO normalized to ^{13}CO(1-0) transitions.

   The gas parameters derived from the fits for pixels of increasing distance from the center are shown in Table-5.2. In addition to the fit parameters, we show the mean values of these parameters in each pixel. This allows us to compare the fit values to the average
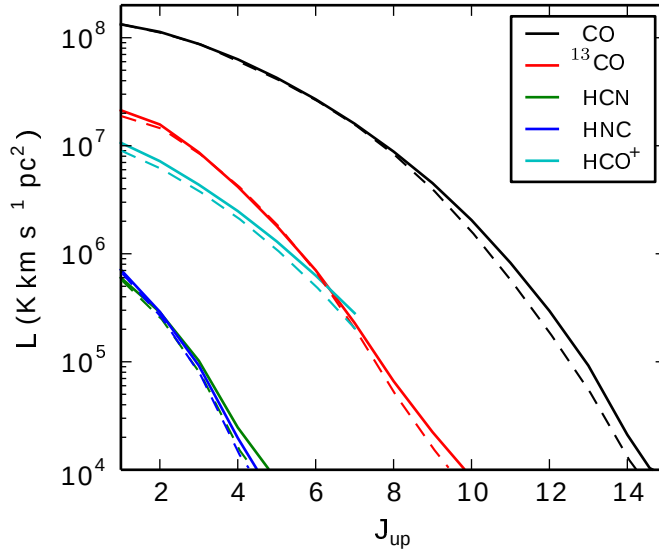
Figure 5.3 – Total luminosity of all the molecular transitions for the model galaxy over a region of 16×16 kpc. The dashed lines correspond to the original set of particles, whereas the solid lines represent the combined luminosity of the sampled and the original sets.

physical conditions, which is not possible when such fits are applied to actual observations. We find that a mPDR constrains the density and the mechanical heating rate to less than a half-dex and the visual extinction to less than a factor of two. On the other hand, the FUV flux (G) is largely unconstrained. We note that a pure PDR, that is not mechanically heated (not show here), fails in fitting most of the ratios involving $J > 4 - 3$ transitions, and leads to incorrect estimates of the gas parameters.

The molecular gas is indirectly affected by the FUV flux via the dust. The dust is heated by the FUV radiation, which in turn couples to the gas and heats it up. In addition to the FUV flux, this process depends also on the gas density, where it becomes very efficient for $n > 10^4$ cm^{-3} and $G \gtrsim 10^3$. In our case, the FUV flux is unconstrained mainly because the density of the gas is significantly lower than the critical densities of the $J > 4 - 3$ transitions of CO and ^{13}CO and the transitions of the high density tracers, where 99% of the gas has a density less than 10^3 cm^{-3}. These transitions are sub-thermally excited and their fluxes depend strongly on density. On the other hand, the emission grids of these transitions as a function of n and G show a weak dependence on the FUV flux. For example, see Figure-7 (Kazandjian et al. 2015a), where Γ_{mech} plays a more important role in heating the gas in the molecular zone compared to the heating due to the coupling of the dust to the gas.

Despite the fact that G is not well constrained using the molecular lines we have considered, which was also the case in KP15, we did succeed to fit the line ratios from the synthetic maps using a mechanically heated PDR. We also learn from this exercise that it
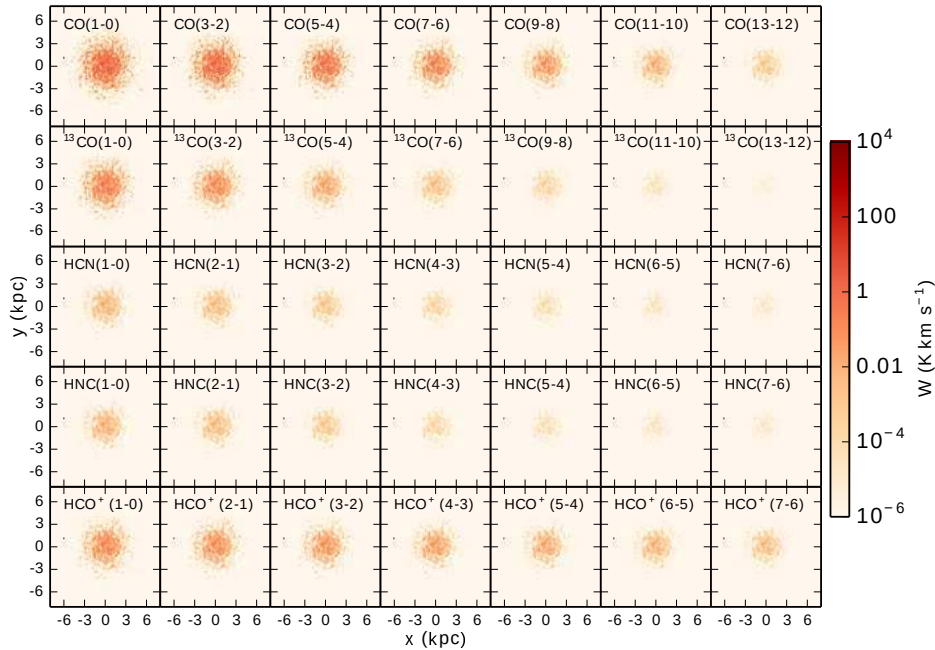
Figure 5.4 – Flux maps of the model galaxy of a selection of the CO and ^{13}CO lines, and all of the transitions of HCN, HNC, HCO$^+$.

is possible to constrain n, Γ_{mech} and A_V with high confidence within an order of magnitude using line ratios of high density tracers as well as CO and ^{13}CO. It is common to have large degeneracies when using line ratios to constrain cloud parameters. Such degeneracies arise mainly due to the small number of line ratios used in the fits, while including additional line ratios reduces the degeneracy in the parameter space. The reduction in the degeneracies in the parameter space is illustrated in Figure-16 by Kazandjian et al. (2015a), where using four independent line ratios of a sample of LIRGS shrinks the degeneracy to less than half a dex in the $n - G$ parameter. Possible ways of constraining G will be discussed in Section-5.5. The main reason why we manage to fit the synthetic line ratios well is because the range in the densities where most of the emission emanates is between 10 and 1000 cm^{-3} (see Figure-5.6). This narrow range in the density is due to the narrow density PDF of our galaxy model. In the next section, we explore the effect of increasing the median and the width of the density PDF on the relative contribution of the whole span of densities to the flux of molecular line emission of mechanically heated PDRs.

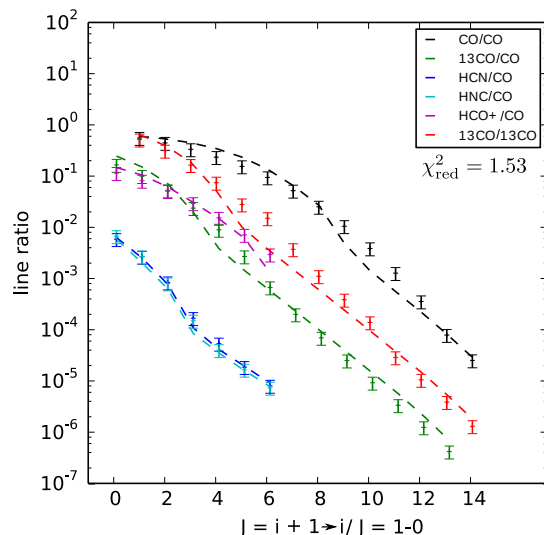| species	J-transitions
CO	1-0 → 15-14
^{13}CO	1-0 → 15-14
HCN	1-0 → 7-6
HNC	1-0 → 7-6
HCO$^+$	1-0 → 7-6

Table 5.1 – Rotational lines used in constructing the flux maps

Figure 5.5 – Sample fit of the line ratios of the central pixel (0.4 x 0.4 kpc^2) with a single PDR model. The points with error bars represent the line ratios of the specified species from the synthetic maps. The dashed curves correspond to the line ratios of the best fit PDR model. All the ratios are normalized to CO(1-0) except for the red ratios which are normalized to ^{13}CO(1-0).

5.4 Constraining the gas density PDF

The gas density PDF is a physical property of the ISM that is of fundamental interest because it gives information about the underlying physical processes, such as the dynamics of the clouds and the cooling and heating mechanisms. A log-normal distribution of the density is expected if the ISM is super-sonically turbulent (Vazquez-Semadeni 1994, Nordlund & Padoan 1999, Wada & Norman 2001, 2007, Burkhart et al. 2013, Hopkins 2013), and this simple picture can explain, amongst others, the stellar IMF, cloud mass functions, and correlation patterns in the star formation (Hopkins 2012b,a, 2013). A log-normal distribution was assumed in Section-5.2 which allows us to extrapolate the density structure in the simulation beyond the resolution limit, in a statistical sense.

The question remains whether it is possible to derive the properties of the density PDF

R		$\log_{10}[n]$	$\log_{10}[G]$	$\log_{10}[\Gamma_{\mathrm{mech}}]$	A_V	χ^2_{red}
< 0.4	mPDR	1.9 ± 0.2	-0.6 ± 1.9	-23.0 ± 0.2	12.2 ± 0.4	1.7 ± 0.5
	Actual	1.9 ± 0.2	1.8 ± 0.1	-23.4 ± 0.2	11.2 ± 1.3	–
~ 0.8	mPDR	1.9 ± 0.3	1.4 ± 3.0	-23.1 ± 0.3	12.8 ± 2.3	1.3 ± 0.2
	Actual	1.8 ± 0.1	1.7 ± 0.1	-23.3 ± 0.1	9.4 ± 1.1	–
~ 1.0	mPDR	1.9 ± 0.2	2.0 ± 2.3	-23.1 ± 0.1	12.0 ± 4.4	1.6 ± 0.2
	Actual	1.7 ± 0.1	1.7 ± 0.1	-23.3 ± 0.1	8.5 ± 0.6	–
~ 1.5	mPDR	1.7 ± 0.4	0.4 ± 2.0	-23.3 ± 0.1	8.2 ± 1.3	1.0 ± 0.1
	Actual	1.5 ± 0.1	1.3 ± 0.1	-23.7 ± 0.1	5.5 ± 0.4	–

Table 5.2 – Model cloud parameters fits for pixels of increasing distance R (in kpc) from the center of the galaxy. These parameters are n (in cm^{-3}), G (in units of G_0), Γ_{mech} (in erg cm^{-3} s^{-1}) and A_V (in mag). The values in the row (mPDR) correspond to the average fit parameters and the dispersion for pixels at a distance R from the center. The actual mean values of the cloud parameters are listed in the following row labeled "Actual". We use 51 transitions in these fits and minimize the χ^2_{red} by varying four parameters, thus the DOF of the fit are 51-4 = 47. In the last column we show the mean value of χ^2_{red}, which is the value of the χ^2 per degree of freedom minimizing the fits. Smaller χ^2_{red} imply better fits but not necessarily good estimates of the actual values of the cloud parameters.
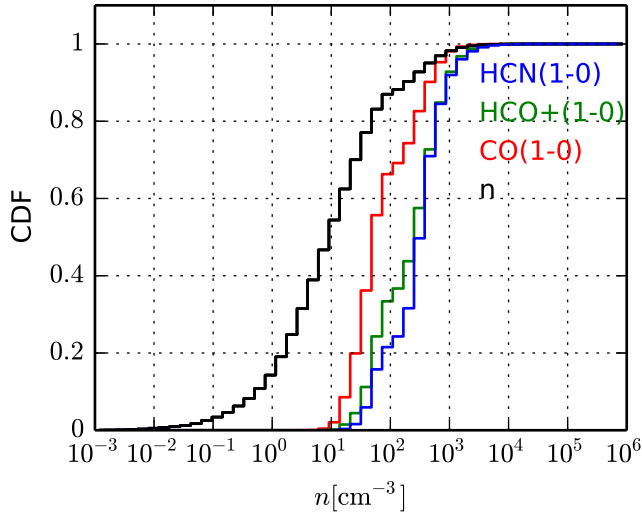

Figure 5.6 – Cumulative distribution of the densities and the luminosities of CO(1-0), HCO$^+$(1-0) and HCN(1-0). For example, $\sim 90\%$ of the gas particles have a density $n < 10^2$ cm^{-3}, whereas 75%, 40%, 20% of the emission of CO(1-0), HCO$^+$(1-0) and HCN(1-0) emanate from gas whose density is lower than 10^2 cm^{-3}.

from observations. This is probably only doable for the molecular ISM. There is limited scope for deriving the density PDF of the warm and cold neutral phase of the ISM, as the HI 21 cm line is not sensitive to variations in density. For the ionized phases, we do not expect a simple log-normal density PDF, as the turbulence may not be supersonic and or the length scales exceed the scale lengths in the galaxy disk. For the colder gas, where we expect a simple functional and relatively universal form, there is at least the prospect of probing the density structure using the molecular line species, which come into play at higher densities. Indeed, we may well reverse our approach taken in Sections-5.3.2, and try to constrain the density PDF (and the conditions in molecular clouds) using the emission of molecular species. Such an approach is possible, because we have assembled a large database of PDR models and resulting line emission, covering a wide range of parameter space.

In the remainder of this section, we will explore a limited part of the parameter space to examine the contribution from different line species for different density PDFs under some limiting assumptions. For completeness, we recapitulate the assumptions (some of which are implicit): 1) simple functional forms of the density PDF, where G, A_V and Γ_{mech} are taken constant (Nordlund & Padoan 1999); 2) emission from a given density is assumed to come from a PDR region at that density with a fixed A_V, with the density dependence coming from emission line-width and cloud size relation (e.g, Larson 1981). 3) chemical and thermal equilibrium is assumed for the PDR models.

We have seen in Section-5.3.1 that the high density tracers, in the simulation of the quiescent disk galaxy, have a limited effect on the emission ladders. That is because the density PDF drops off very fast in the simulation. This ultimately derives from the exponential decay in the assumed log-normal distribution. For this reason, we will consider broader dispersions in the PDF. In this paper, we adopt log-normal PDFs for the density, although a more relaxed power law distribution could also be considered. Such a power law decay of the density PDF is found in some models of supersonic turbulence when the effective equation of state has a polytropic index, γ, smaller than one, and temperatures strongly decrease with increasing density (Nordlund & Padoan 1999).

5.4.1   Parameter study

In this section, we compute the mean flux of molecular line emission emanating from a volume of gas whose density is log-normally distributed. In the first part, we explore the contribution of gas, of increasing density, to the mean flux. Particularly, we look for the necessary parameters of the PDF to obtain a significant ($> 10\%$) contribution of the high density gas to the mean flux. In the second part, we use line ratios of HCN(1-0), HNC(1-0) and HCO$^+$(1-0) for star-forming galaxies to constrain the parameters of the density PDF of such systems.

In computing the mean flux for the gas in the log-normal regime, the flux emanating from gas within a certain density range, should be weighted by the probability of finding it within that range. The mean flux is computed by summing all these fluxes for all the density intervals in the log-normal regime. In other words, the mean flux for a volume of gas is given by:

$$\bar{F} \quad = \quad N \int_{n_1}^{n_2} F(n) \times PDF(n) \, d \ln n \qquad\qquad (5.2)$$

$$M \quad = \quad N \int_{n_1}^{n_2} n \times PDF(n) \, d \ln n, \qquad\qquad (5.3)$$

where N is a normalization factor which scales the flux ($\bar{F}$) depending on the molecular gas mass (M) of the region, $PDF(n)$ is the gas density PDF we assume for the region considered, and $F(n)$ is the emission flux of a given line as a function of gas density (for a fixed G, Γ_{mech} and A_V). Typically the bounds of the integrals are dictated by the density of the molecular clouds, where the gas density is in the log-normal regime. A density of 1 cm^{-3} is a good estimate for the lower bound since no molecular emission is expected for gas with n less than that. The upper bound of the integral in Eq-5.2 can be as high as 10^6-10^8 cm^{-3}. $PDF(n)$ is a Gaussian in log scale, which decays rapidly whenever the gas density is 1-σ larger than the mean. While $PDF(n)$ is a decreasing function of increasing density, $F(n)$ is an increasing function of increasing n. Generally, the molecular gas mass in the central few kpc of star-forming galaxies is on the order of $10^9 - 10^{10}$ M$_\odot$ (Scoville et al. 1991, Bryant & Scoville 1999). This estimate, or a better one if available, can be used to compute N in Eq-5.2. We refer to the quantity $F(n) \times PDF(n) \, d \ln n$ as the weighted flux.

5.4.2   Weighted fluxes

The median density and the dispersion of the log-normal fit in Section-5.2 are $n_{med} = 1.3$ cm^{-3} and $\sigma = 2.1$ respectively, corresponding to a mean density of ~ 10 cm^{-3}. The mean density is much smaller than the critical densities of most of the transitions of HCN, HNC and HCO$^+$. For this reason all of the emission of HCN(1-0) and HCO$^+$(1-0) originates from gas with $n < 10^4$ cm^{-3} in Figure-5.6. In Figure-5.8, we show the weighted fluxes of gas of increasing density for HCN(1-0). The fluxes are determined by computing F in Eq-5.2 for intervals in $\log n$. Similar distributions can be computed for other emission lines of high density tracers, which are expected to be qualitatively similar. The rows in Figure-5.8 correspond to the PDFs in Figure-5.7. Along the columns we vary the physical cloud parameters over most of the expected physical conditions. G, Γ_{mech} and A_V are varied in the first, second and last column, respectively. In exploring the possible ranges in G and Γ_{mech} for the PDF of the SPH simulation, we see that the peak of the emission is restricted to $n < 10^3$cm^{-3}. The only situation where the peak is shifted towards densities higher than 10^3 cm^{-3} occurs when the mean A_V of the clouds in the galaxy is ~ 1 mag. However, in this case, the flux would be too weak to be observed. Hence with the combinations of these parameters, and with such a log-normal density PDF, it is not possible to obtain a double peaked PDF, or a gas density distribution with significant contribution from $n > 10^4$ cm^{-3} gas. Thus, most of the emission of the high density tracers is from gas with $n < 10^4$ cm^{-3}. The analogous plots of Figures-5.7 and 5.8 where the dispersion is varied for median densities of 12.5 cm^{-3} and 100 cm^{-3} are shown in the appendix.
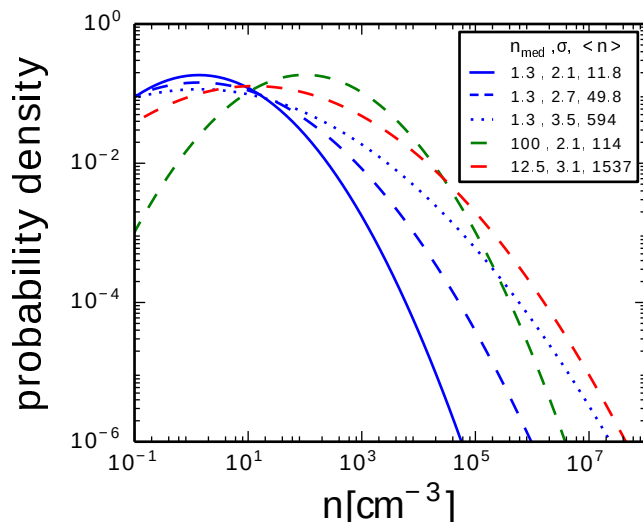
114

Figure 5.7 – An illustration which shows the effect of varying the median and the dispersion of a density PDFs. The blue curves represent PDFs that have the same median density as the one used in SPH simulation, but with increasing dispersions. The green curve has the same dispersion as that of the SPH simulation but with a higher median density. Finally, the red curve corresponds to the density PDF by Wada (2001). The mean densities corresponding to these PDFs are also listed in the legend.

For density PDFs with broader dispersions, $\sigma = 2.7$ and 3.5, respectively, it is possible to obtain luminosity distributions where at least 10% of the emission is from gas with densities $> 10^5 \text{cm}^{-3}$ (see second, third and last rows in Figure-5.8). In multi-component PDF fits, the filling factor of the "denser" component is on the order of a few percent (by mass or by area). In the Figure-5.8, we see that it is necessary to have a broad dispersion in the PDF in order to have a distribution of the luminosity where at least 10% of it emanates from gas with $n > 10^5 \text{ cm}^{-3}$.

When comparing the second and fourth[2] rows of the weighted fluxes in Figure-5.8, we see that they are quite similar. Thus, it seems that a low median density and a broad dispersion (second row) results in the same weighted fluxes as a PDF with a 100 times higher median density and a narrower dispersion (fourth row). To check for such degeneracies and constrain the PDF parameters using molecular emission of high density tracers, we construct line ratio grids as a function of n_{med} and σ.

It has been suggested that HCN(1-0) is a better tracer of star-formation than CO(1-0) because of its excitation properties (Gao & Solomon 2004). As a proof of concept, in Figure-5.9, we show a grid of line ratios of HCN(1-0)/HNC(1-0) and HCN(1-0)/HCO$^+$(1-0) as a function of the mean and the dispersion of the density PDF. The line ratios of a

---

[2] The PDF of the fourth row corresponds to that of the simulation by Wada (2001)
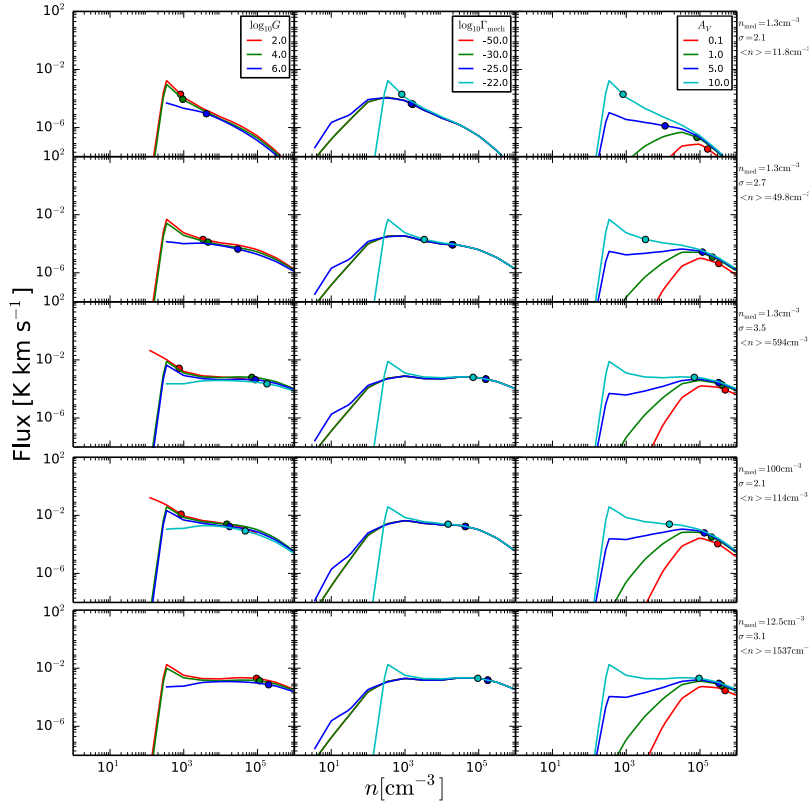
Figure 5.8 – Weighted fluxes for HCN(1-0) for different density PDFs. In the first three rows the median density of the PDFs corresponds to that of the SPH simulation, whereas the dispersion is increased from 2.1 to 3.5. In the fourth row, the median density is increased by a factor of 100 compared to that of the SPH simulation, but the dispersion is kept fixed. In the last row we show the weighted fluxes for the PDF obtained by the Wada 2001 simulation. In the first column the FUV flux is varied, from 100 times the flux at the solar neighborhood to $10^6 G_0$ corresponding to the FUV flux in extreme star-bursts ($A_V = 10$ mag, $\log_{10} \Gamma_{mech} = -22$). In the middle column we vary Γ_{mech} from the heating rate corresponding to quiescent disks to rates typical to violent star-bursts with a SFR of 1000 $M_\odot$ per year ($A_V = 10$ mag, $\log_{10} G = 2$). In the last column the A_V is varied from 0.1 to 10 mag, corresponding respectively to the typical values for a transition zone from H^+ to H and for dark molecular clouds ($\log_{10} G = 2$, $\log_{10} \Gamma_{mech} = -22$). The onset of emission is determined mainly by Γ_{mech}; for instance in looking at the middle column, we see that this onset of emission corresponds to $n \sim 10^2$ cm^{-3}, where for lower densities H_2 does not form, which is essential for other molecules such as HCN to form. For each curve in every panel we also plot the density, n_{90}, where 90% of the emission emanates from $n < n_{90}$. For example, in the top row, even for the most intense FUV flux $n_{90} \sim 10^{3.5}$ cm^{-3}. On the other hand, in bottom row, $n_{90} > 10^5$ cm^{-3}. Note that the curves corresponding to Γ_{mech} 10^{-50} (a pure PDR) and 10^{-30} erg cm^{-3} s^{-1} in the second column overlap.

sample of 117 LIRGS (Figures-1 and 2 by Loenen et. al 2008) show that in most of these galaxies $1 \lesssim$ HCN(1-0)/HNC(1-0)$\lesssim 4$ and $0.5 \lesssim$ HCN(1-0)/HCO$^+$(1-0)$\lesssim 3$. The overlapping regions in the line ratio grids in Figure-5.9 correspond to $2.54 < \sigma < 2.9$. The width of a log-normal density PDF is related to the Mach number, $\mathcal{M}$, in that medium via $\sigma^2 \approx \ln(1 + 4\mathcal{M}^2/3)$ (Krumholz & Thompson 2007, Hopkins 2012a). By applying this relationship to the range in σ constrained by the observations we find that $29 < \mathcal{M} < 77$. This range in $\mathcal{M}$ is consistent with that of violent star-bursts that take place in extreme star-forming regions and galaxy centers (Downes & Solomon 1998).

5.5 Discussion

The molecular emission of star-forming galaxies usually require more than one PDR component to fit all the transitions. Typically, a low density PDR components is needed to fit low-J transitions, e.g., for CO and ^{13}CO, whereas a high density $n > 10^4$ cm^{-3} component is needed to fit the $J > 6 - 5$ transitions of these two species and the high density tracers. In the inner $< 0.1 - 1$ kpc a mechanically heated PDR and/or an XDR might be necessary in the presence of an AGN or extreme star-bursts. In the first part of the paper, we sampled high density gas in our model star-forming galaxy simulation by assuming the gas density is a log-normal function, in order to account for the emission of the high density gas that was missing in the model galaxy due to resolution constraints. Since the dispersion of the density PDF of the model galaxy is narrow with $\sigma = 2.1$, corresponding to a Mach number $\mathcal{M} \sim 10$, the gas with density $n > 10^4$ cm^{-3} contributes $< 1\%$ of the total luminosity of each line. Consequently we were able to recover n, Γ_{mech} and A_V of the gas parameters within 2 kpc from line ratios of CO, ^{13}CO, HCN, HNC and HCO$^+$, reasonably well using a one component mechanically heated PDR model. The FUV flux was constrained less accurately, since Γ_{mech} is a dominant heating term at $A_V \gtrsim 1$ mag, where most of the molecular emission emanates. We have seen in Kazandjian et al. (2015a), that in the non-LTE regime, the molecular emission is almost independent of the FUV flux. This is not the case for $n \gtrsim 10^4$ cm^{-3}, however for such high densities the line ratio grids depend strongly on G, thus whenever the mean gas density is $> 10^4$ cm^{-3} and $G > 10^4$, e.g. in ULIRGS, we expect to constrain the FUV flux with high certainty. In this case it might be necessary to model the emission with more than one PDR component as was done by Rosenberg et al. (2014b). In this paper, the CO ladder of the ULIRG Arp 299 was fit using three PDR models and the FUV flux was well constrained only for the densest component with $n = 10^{5.5}$cm^{-3} (See Figure-5 by Rosenberg et. al. 2014b). Another possible way of constraining G is using diagnostic line ratios of atomic fine-structure lines. Since atomic fine-structure emission originates from $A_V < 1$ mag, it depends strongly on G. Consequently, these line-ratios show a strong dependence on G as well (Kaufman et al. 1999). This is valid even for the most extreme Γ_{mech} rates (see Fig-A3 by Kazandjian et al. (2015a)).

Modeling the ISM as discrete components is not a realistic representation, especially in ULIRGS, since the gas in such environments is expected to be distributed log-normally and in some cases the distribution could be a power-law (depending on the adiabatic index

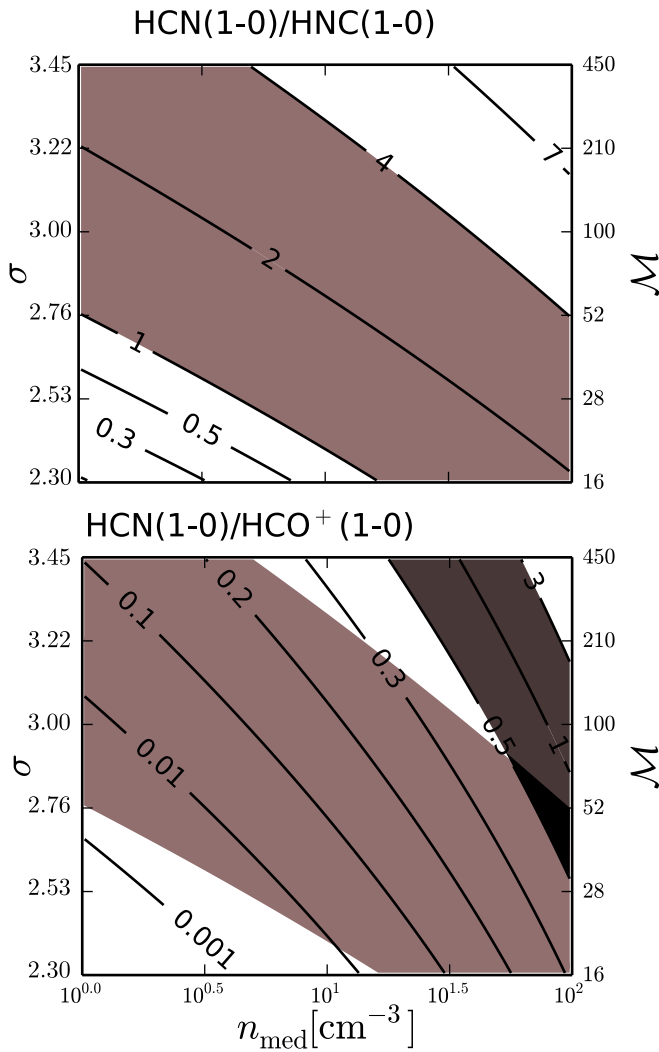Figure 5.9 – **Top** Line ratios of HNC(1-0)/HCN(1-0) as a function of the mean and the dispersion of the PDF. **Bottom** Line ratios of HCO$^+$(1-0)/HCN(1-0) as a function of the mean and the dispersion of the PDF. The overlapping region of these two line ratios is colored in black in the bottom panel. For all the grid points a typical $A_V = 10$ mag and $\Gamma_{\mathrm{mech}} = 10^{-22}$ cm^{-3} is used.

of the equation of state).

We have studied the contribution of the density function to the mean flux for different parameters defining a log-normal probability functions and showed that a broad dispersion is required to obtain significant emission for the $n > 10^4$ cm^{-3} clouds. The main advantage of such modeling is in interpreting un-resolved observations of star-forming galaxies where FUV heating and mechanical heating may play an important role. This approach is more appropriate than fitting the observations with one or more PDR components, since in such modeling the gas is assumed to be uniformly distributed with discrete densities. The number of free parameters arising from multi-component fits would be much higher than fitting the parameters of the gas density PDF, which has just two. This reduces the degeneracies and gives us information on the gas density PDF and about the turbulent structure and the Mach number, which is directly related to the density PDF and the mechanical heating rate. The main caveat in our approach is the assumption that the density PDF for $n > 10^{-2}$ cm^{-3} is a log-normal function and that the mechanical heating rate used in the PDR models is independent of the width of density PDF, A_V, G and the line-width. The reason for adopting this assumption is based on the fact that a relationship between gas density, and consequently the PDF, and the mechanical heating rate is lacking (Wheeler et al. 1980, Silich et al. 1996, Freyer et al. 2003, 2006). Ultimately the mechanical heating rate derives from the cascade of turbulence to the smallest scales due to a supernova event, where typically an energy transfer efficiency of 10% is assumed (Loenen et al. 2008). The outcome of recovering cloud parameters by independently varying them in the fitting exercise is a good step towards probing possible relationships between these parameters and mechanical heating. We have demonstrated the possibility of constraining the density PDF using line ratios of HCN(1-0), HNC(1-0) and HCO$^+$(1-0), where the derived Mach number is consistent with previous predictions. Grids of diagnostics involving other molecular species can also be computed (see reviews by Wolfire 2011, Bergin 2011, Aalto 2014, and references therein) in order to constrain the properties of the PDF, but that is beyond the scope of this paper. Moreover, we have used the flux ratios of molecular lines as diagnostics, but it is also possible to use the ratio of the star formation rate (SFR) to the line luminosity to constrain the PDF as is done by Krumholz & Thompson (2007). This is in fact quite interesting, since the SFR can be related to the mechanical heating rate as was done by Loenen et al. (2008). By doing so, a tighter constraint on the mechanical heating rate can be imposed, instead of considering it as a free parameter as we have done in our fitting procedure.

5.6   Summary and conclusion

We have constructed luminosity maps of some molecular emission lines of a disk-like galaxy model. These emission maps of CO, ^{13}CO, HCN, HNC and HCO$^+$ have been computed using sub-grid PDR modeling in post-processing mode. Because of resolution limitations, the density of the simulation was restricted to $n < 10^4$ cm^{-3}. We demonstrated that the density PDF is log-normal for $n > 10^{-2}$ cm^{-3}. Most of the emission of the high density tracers emanates from the gas with densities $\sim 10^2$ cm^{-3} for quiescent galaxies,

which is at least 1000 times lower in density than the critical density of a typical high density tracer. We attribute this to the fact that the dispersion of the PDF is narrow, and thus the probability of finding dense gas is low.

The main findings of this paper are:

- It is necessary to have a large dispersion in the density PDF ($\sigma > 2.7$), in order to have significant emission of high density tracers from $n > 10^4$ cm^{-3} gas.

- It is possible to constrain the shape of the PDF using line ratios of high density tracers.

- Line ratios of HCN(1-0), HNC(1-0) and HCO$^+$(1-0) for star-forming galaxies and star-bursts support the theory of super-sonic turbulence.

A major caveat for this approach is the assumption concerning the thermal and the chemical equilibrium. Care must be taken in interpreting and applying such equilibrium models to violently turbulent environments such as star-bursting galaxies and galaxy nuclei. Despite the appealing fact that the line ratios obtained from the example we have shown in Figure-5.9 favor high Mach numbers ($29 < \mathcal{M} < 77$) consistent with previous prediction of supersonic turbulence in star-bursts, a time-dependent treatment might be essential.

Acknowledgements

Appendix
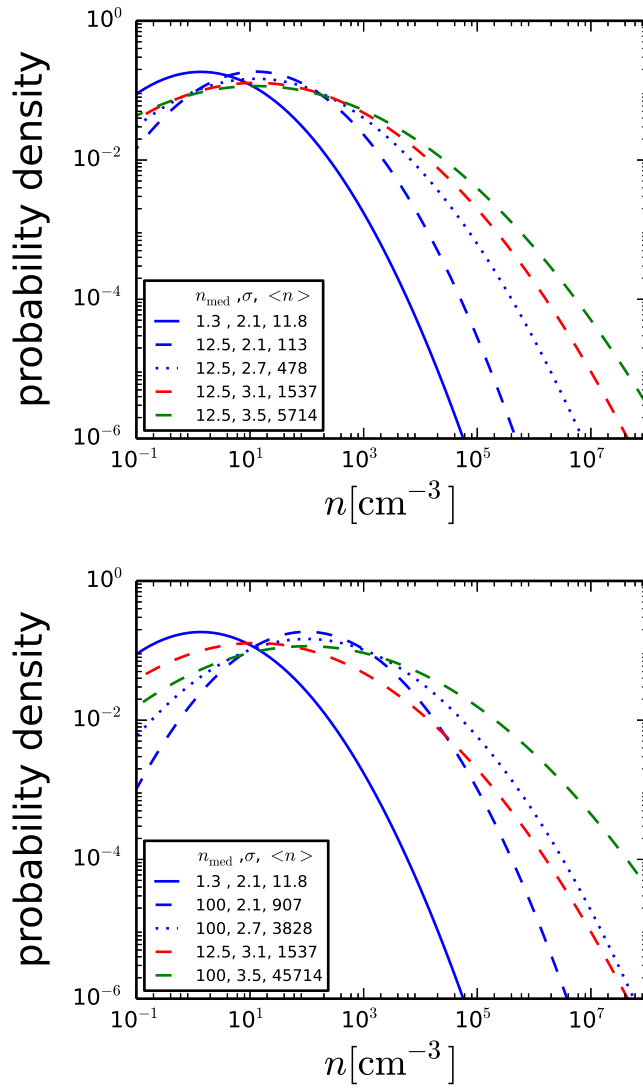
Figure 5.10 – Analogous plots of Figure-5.7 where the dispersion is varied for a fixed median density of 12.5 cm^{-3} in the left panel and 100 cm^{-3} in the right panel. In both cases the density PDF of the SPH simulation and the Wada 2001 simulation are also shown for reference and comparison.
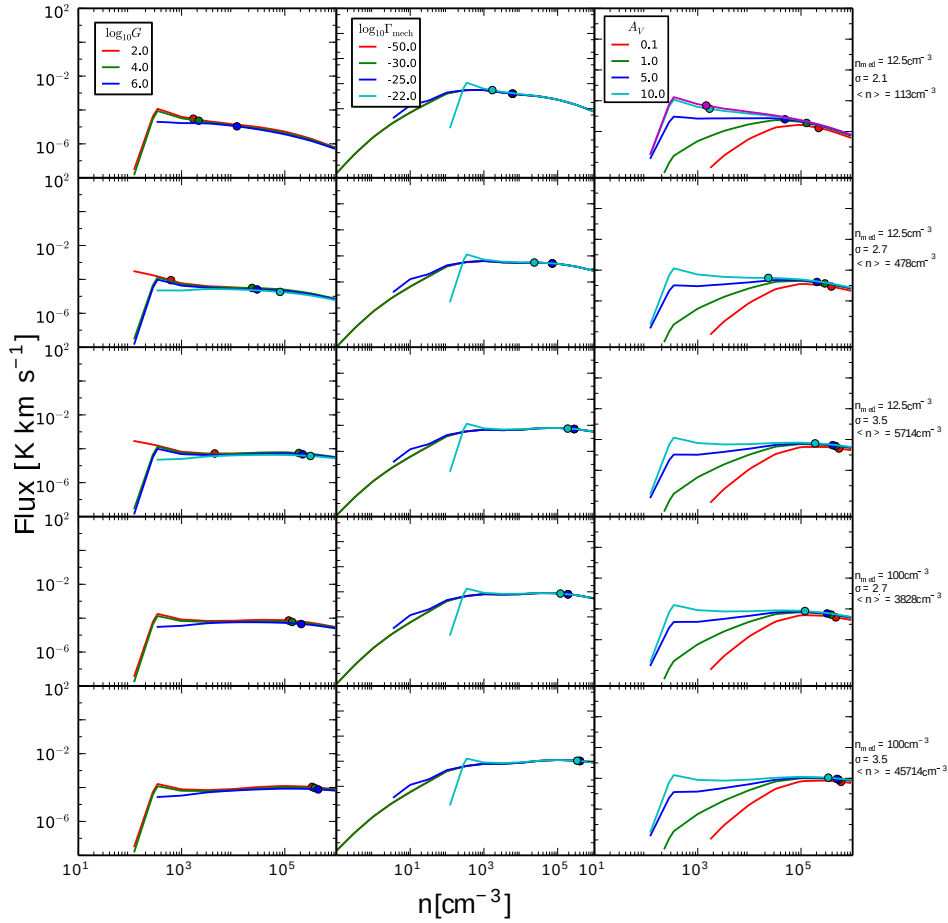
Figure 5.11 – Weighted fluxes of the PDFs of Figure-5.10 which are not shown in Figure-5.8

VI

General Discussion and Prospects

6.1 Thesis summary

In this thesis, I studied the effects of mechanical heating (Γ_{mech}) due to dissipating shocks and turbulence on diagnostics of regular star-burst galaxies (L_{IR} (8-1000 μm) $\sim 10^{9-10}$ $L_\odot$) as well as their extreme counterparts that are classified as luminous infrared galaxies (LIRGs) (L_{IR} (8-1000 μm) $\sim 10^{11}$ $L_\odot$) and ultra-luminous infra-red galaxies (ULIRGs) ($L_{IR} \sim 10^{12}$ $L_\odot$). These galaxies exhibit much higher star formation rates, up to 1000 $M_\odot$ yr^{-1}, compared to 0.01 $M_\odot$ yr^{-1} in a quiescent spiral galaxy such as the Milky way. The main questions I addressed in this thesis are: a) To what extent is mechanical heating important for the thermal and chemical balance of the ISM in star-burst galaxies? b) Does the inclusion of mechanical heating significantly change the interpretation of commonly used diagnostics such as line emission intensity ratios among [CI], [CII], ^{13}CO , CO and other high-density tracers? In particular, how important is mechanical heating in constraining cloud parameters in star-burst galaxies? c) How well can molecular line emission be used to probe the density distribution of super-sonically turbulent clouds in star-burst regions caused by shocks of supernova explosions and stellar outflows ?

In the scientific literature several authors have produced tables and diagrams of atomic and molecular line emission which enable the user to constrain the physical properties of PDRs, mainly the gas density and the FUV flux (e.g, Kaufman et al. 1999, Meijerink et al. 2007). These PDR models are partly able to explain multitransition CO observations of star-forming regions in galaxy centers (for e.g. Israel & Baas 2002), where the main problem arises in modeling the bright emission of CI which is consistently brighter in observations (Israel & Baas 2002). But as more data became available for LIRGS and ULIRGS by the Herschel Space Observatory (Pilbratt et al. 2010), it was clear that additional physical and (or) chemical processes must be included in these models to explain observations of modest star-busts in galactic nuclei (e.g. Israel & Baas 2003) as well as extreme star-forming regions (e.g. Loenen et al. 2008). For instance PDR models are unable to clearly define the parameters of the gas components of the star-bursts in galaxy centers using relative line intensities of ^{13}CO with [CI] and [CII] (for e.g. Israel & Baas

2002). The urge of using more sophisticated PDR modeling involving additional heating sources became evident in the work done by Loenen et al. (2008) and more importantly with the new *Herschel* data for high-J rotational lines of CO and other relevant molecular species (Israel & Baas 2002, Pilbratt et al. 2010, González-Alfonso et al. 2010, van der Werf et al. 2010, Meijerink et al. 2013).

In answering the questions we posed above, we extended the works by Meijerink et al. (2007), Loenen et al. (2008) and Meijerink et al. (2011) by including mechanical feedback as a free parameter in the heating budget of the PDR models. We constructed grids that allowed for constraining cloud parameters over the same parameter space considered by Kaufman et al. (1999), where pure PDR models without any mechanical heating were used to study the star-forming regions of M82, NGC 278, and the Large Magellanic Cloud.

In **Chapter-2** we explored a wide range of parameter space covering densities ranging from 1 to 10^6 cm^{-3} and FUV fluxes ranging from 1 G_0, for e.g. in the solar neighborhood, to fluxes of 10^6 G_0 typical at distances of 0.1 pc from an O star that are common in star-bursts. We concluded that mechanical heating for regions where star-formation rates ranging from SFR $\sim$ 0 to $\sim$ 1000 M$_\odot$ yr^{-1} corresponding to $10^{-24} < \Gamma_{\text{mech}} < 10^{-16}$ erg cm^{-3} s^{-1} impacts the thermal and chemical balance strongly. For example, an order of magnitude increase in the kinetic temperature of steady-state equilibrium clouds is not uncommon in the molecular zone. Moreover, in regions with star formation rates as large as $\sim$ 1000 M$_\odot$ yr^{-1}, the H/H$_2$ transition does not occur. As a consequence the abundances of other molecular species whose formation relies on the abundance of H$_2$ are also affected in these photo-dominated regions, leading to a strong reduction in their column densities. Thus, to answer question (a), we found that mechanical heating strongly affects the equilibrium state of clouds. As a lower bound to the influence of Γ_{mech}, we determined that for $\Gamma_{\text{mech}} \sim 0.01 \, \Gamma_{\text{photo}}$ the chemistry of the PDRs is significantly changed.

The emission of species depends primarily on their abundance and on the physical properties of the clouds, such as the kinetic temperature. In **Chapter-2** we found that Γ_{mech} also affects the abundances of chemical species and their column densities. We also found that generally, the column densities of CO, HCN and H$_2$O increase as a function of Γ_{mech}. The HNC/HCN integrated column density ratio shows a decrease by a factor of at least two in high-density regions with $n \sim 10^5$ cm^{-3}. On the other hand, the HCN/HCO$^+$ column density ratio increases by three orders of magnitude. We built on these results in **Chapter-3** where we calculated the emission grids of the atomic fine-structure lines of [OI], [CII], and [CI] in addition to the various molecular line transitions of CO, ^{13}CO, HCN, HNC, HCO$^+$, CN, and CS.

So far this has been a forward problem, where the effect of mechanical heating was probed on the physical and chemical properties of clouds. Typically, these properties are inferred from molecular line emission of star-forming regions where the measurements are matched against the product of models of such regions. We found that line ratios involving CO transitions with $J > 4-3$ are very sensitive to mechanical heating. The emission of these transitions becomes at least one order of magnitude brighter in clouds with $n \sim 10^5$ cm^{-3} and a star formation rate of 1 M$_\odot$ yr^{-1} (corresponding to $\Gamma_{\text{mech}} = 2 \times 10^{-19}$ erg cm^{-3} s^{-1}). The emission of the transitions of the species emanating from the

PDRs were computed using Large Velocity Gradient (LVG) models (e.g. Sobolev 1960, Henkel et al. 1983, Jansen et al. 1994, Hogerheijde & van der Tak 2000, van der Tak et al. 2007, Krumholz 2014). The input needed by these LVG models, for e.g. the column density of the species and the kinetic temperature of the gas, were extracted from the PDR models as averaged quantities, where the main assumption was that the line width is constant and is not related to the mechanical heating rate. Rotational transitions of CO with $J < 4 - 3$ are less sensitive to Γ_{mech} compared to the $J > 4 - 3$ transitions, however they do become brighter in response to Γ_{mech}. Generally, for all of the lines we considered, Γ_{mech} increases excitation temperatures and causes the optical depth at the line center to decrease; this effect is due to the reduced level populations for the lower excited states at higher temperatures. Γ_{mech} affects the emission of high density tracers as well. We found that ratios involving HCN are a good diagnostic for Γ_{mech}. For instance, the ratios HCN(1-0)/CO(1-0) and HCN(1-0)/HCO$^+$(1-0) increase to values larger than one whenever $\Gamma_{mech} \gtrsim 5\%$ of the surface photo-electric heating rate, while in pure PDRs these two ratios are much less than unity. The two major conclusions of chapter-3 are : (1) line ratios involving low-J to high-J transitions will provide good estimates of the mechanical heating rate, as opposed to line ratios involving only low-J ratios; (2) in determining A_V or equivalently N_H, the mechanical heating rate should be taken into account. Ignoring Γ_{mech} leads to a factor of two to three error in determining A_V, and more than one order of magnitude errors in the estimated density and radiation field.

En-route to answering (c), we applied mechanically heated PDR models to the sub-structure of the gas of simulated galaxies in Chapters 4 and 5. Two fiducial model galaxies were examined: a small disk galaxy of solar metallicity and a lighter dwarf galaxy with 0.2 $Z_\odot$ metallicity. Emission maps of CO and ^{13}CO (up to $J = 4 - 3$) were constructed for both galaxies in Chapter-4. This work was extended in Chapter-5 where emission maps up to $J = 15 - 14$ were constructed, in addition to emission maps of the high density molecular tracers HCN, HNC and HCO$^+$ up to $J = 7 - 6$. These maps were used to investigate the occurrence and the effects of mechanical feedback on recovering the physical parameters obtained from molecular line intensity ratios. The general conclusion of both chapters was that molecular line emission are very useful in constraining mechanical heating, especially in the central regions of galaxies. Moreover, since high-J to low-J line ratios are very sensitive to mechanical heating, they are good diagnostics for it. Possible degeneracies with XDR models will be discussed in the Section-6.4.

One of the important conclusions of Chapter-4 is that elevated excitation temperature for CO$(1 - 0)$ is correlated positively with mechanical feedback, which is enhanced towards the central region of the model galaxies. A second important conclusion of this chapter is closely related to the conclusion of Chapter-3; namely ignoring mechanical feedback in the heating budget over-estimates the derived gas density by a factor of 100 and the derived far-UV flux by factors of $\sim 10 - 1000$. We found that PDRs that take mechanical feedback into account are able to fit all the line ratios of CO and ^{13}CO quite well, up to the transition $J = 4 - 3$, for the central < 2 kpc of the fiducial disk galaxy. In the central region of the disk galaxy, the mean mechanical heating rate, mean gas density, and A_V recovered from these line ratios to less than half dex with their corresponding values in the model galaxy. In applying our modeling technique to the typical dwarf galaxy, we

concluded that single component PDR model fits are not suitable for determining the actual gas parameters of such systems although the quality of the fit line ratios comparable to that of the disk galaxy.

In recovering the cloud parameters in Chapter-4 it was assumed that the gas has uniform properties, or is composed of a small number of uniform components. In reality, on the scale of a galaxy or on the kpc scale of star-bursting regions common in LIRGS and ULIRGS, the gas density follows a continuous distribution. The exact functional form of this distribution is currently under debate, but it is believed that in star-burst regions, where the gas is thought to be super-sonically turbulent due to e.g. outflows and shocks, the density distribution of the gas is a log-normal function. It is also possible to have a more relaxed power-law distribution in models of supersonic turbulence where the effective equation of state has a polytropic index, γ, less than one (e.g. Nordlund & Padoan 1999). In **Chapter-5** we demonstrated that generalizing our models to fit line ratios by considering a set of clouds following an log-normal density distribution, it is possible to constrain the type of the turbulence in star-bursting galaxies. Particularly we demonstrated that the emission of high density tracers can be used to constrain the density distribution of super-sonically turbulent regions and the mach number as well which is tightly coupled to the width of the density distribution. We found that in a narrow gas density PDF, with a mean density of ~ 10 cm^{-3} and a dispersion $\sigma = 2.1$ in the log of the density, most of the emission of molecular lines even of gas with critical densities $> 10^4$ cm^{-3} emanate from the 10-1000 cm^{-3} part of the PDF. Since the distribution of the luminosity of the model galaxy, as a function of density, is peaked at gas densities between 10 to 1000 cm^{-3}, we found that one component PDRs fit the various line ratios well. In our exploration, we found that it is necessary to have a broad dispersion, corresponding to Mach numbers $\gtrsim 30$ in order to obtain significant ($> 10\%$) emission from $n > 10^4$ cm^{-3} gas; such Mach numbers are expected in LIRGS and ULIRGS. By applying our method to grid of line ratios of HCN(1-0), HNC(1-0) and HCO$^+$(1-0), we showed that it is possible to fit line ratios of a sample of LIRGS and ULIRGS using mechanically heated PDRs. We constrained the Mach number of these galaxies to be between $29 < \mathcal{M} < 77$, which is within the expected range.

In the following two sections we present two case studies where the grids of Chapters-2 and 3 have been applied to recent observation of NGC 253 and Arp 299. For these systems it has been shown by Rosenberg et al. (2014a,b) that mechanical heating is necessary for fitting and interpreting observations in such violent star-forming regions.

6.2   Application to NGC 253

NGC 253 is among the brightest galaxies that have been studied in wavelengths ranging from radio waves to X- and gamma rays. It is also one of the classic galaxies, similar to M82, Mrk 231 and Arp 299, that has very strong emission in the far-IR and sub-mm wavelengths due to the strong star-burst activity in the large molecular clouds that are present in its central kilo-parsec nuclear region (Israel et al. 1995, Mauersberger et al. 1996, Houghton et al. 1997, Bradford et al. 2003, Martín et al. 2009). Rosenberg et al.

(2014a) applied the models developed in Chapters 2 and 3 to recent observations of the ^{12}CO ladder (up to J=13-12) and the ^{13}CO (up to J=6-5) by Herschel, accompanied by older ground based observations of HCN and HNC by the James Clerk Maxwell Telescope (JCMT). They showed that mechanically heated PDR models successfully fit these observations where other models, such as pure PDR models, perform poorly.

Some of the key physical parameters of the gas derived from the observations of ^{12}CO and ^{13}CO in the central region of NGC 253, indicate a kinetic temperature of 120 K and an H_2 density of 4.5×10^4 cm^{-3} (Bradford et al. 2003). These estimates are reinforced by other observations of HCO$^+$ and HCN which predict a similar range in the density and temperature (Paglione et al. 1995, 1997). The two main suggestions for such high excitation temperatures, for otherwise cold $\sim$ 10 K molecular clouds, are heating by cosmic rays (Bradford et al. 2003) and heating by large-scale low-velocity shocks (Martín et al. 2006).

Rosenberg et al. (2014a) attempt to fit the full set of observations by Herschel and JCMT using : a) three-component LVG models only b) three component pure PDR models c) various combinations of composite PDR, mechanically heated cosmic ray dominated PDR (mCDR) and mechanically heated PDR (mPDR) models. In the case of LVG modeling only, the derived CO column density and the total gas mass were quite uncertain. This is mainly attributed to the fact that the fitting problem is over-determined, i.e., degenerate due to the large number of free parameters in the LVG modeling compared to the available observations (see Section 4.1 by Rosenberg et al. (2014a)). In the case of multi-component PDR modeling the derived mass of the clouds was about 30 times higher than previous estimates. Since the column density of H_2 is proportional to the gas mass, the over estimation of the gas mass was attributed to the high visual extinctions needed to match the bright emission of the High-J transitions due to the "un-accounted for" excitation source. Moreover, the fits of the high density tracers of HCN and HNC were poorly matched using these PDR only models. This led to the third attempt of considering mCDR and mPDR models, where the models proposed in this thesis have been used (see Figure-6.1).

The central region of NGC 253 is a fast star-forming region, i.e. a star-burst, where massive stars are common. These stars are short lived and end up detonating as supernovae, that are sources for cosmic rays. Supernovae cause wide spread shocks and turbulence, hence in modeling such environments it is natural to consider not only CRDRs as proposed by Papadopoulos et al. (2011), but also mCDRs as suggested by Meijerink et al. (2011). Since NGC 253 does not harbor an X-ray bright AGN (Pietsch et al. 2000), X-ray heating was not considered in the analysis by Rosenberg et al. (2014a). Bradford et al. (2003) has proposed that cosmic rays are responsible for most of the molecular gas excitation in NGC 253. Thus, Rosenberg et al. (2014a) used various combinations of mCRDs and mPDRs to model these new observations by Herschel. Among these combinations the best fitting model corresponds to the one in which two mPDR and one PDR models have been included, as shown in the right panels of Figure 6.2.

This model fits all the ^{12}CO, and ^{13}CO transitions within the error bars. In addition, the fluxes of the HCN and HNC transitions are much better fit compared to the two other cases, where these fluxes are over-estimated by at least a factor of two. By comparing all
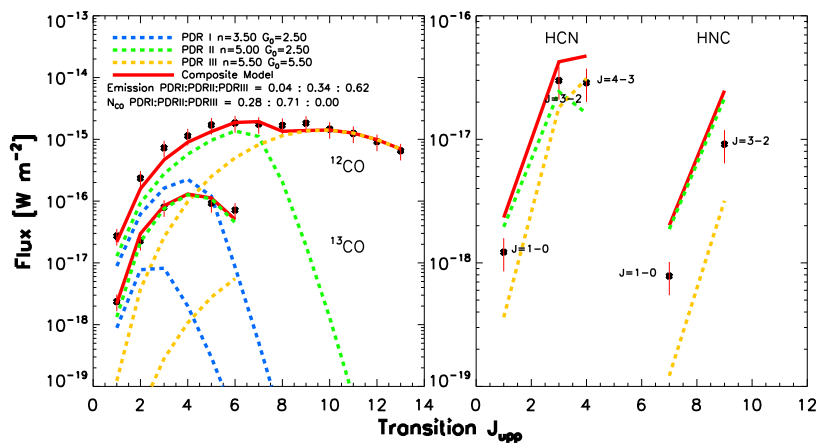
127

Figure 6.1 – Left: ^{12}CO and ^{13}CO excitation ladders, right: HCN and HNC excitation ladders of NGC 253 with flux of each transition plotted as black asterisks with red error bars. In blue, green and yellow dotted lines we plot the PDR I, II and III ISM phases with their filling factors. The composite model is plotted with a red solid line. The model density, G_0 and column density are shown in the legend along with the relative contribution of each phase in terms of emission and column density.

three panels, it is evident that mechanical heating is necessary to reproduce the observed emission, regardless of the amount of cosmic rays used in the modeling. This finding is similar to that of Nikola et al. (2011) in NGC 891 and Hailey-Dunsheath et al. (2008) for NGC 253 itself, where the emission of mid-J CO transitions have been modeled using a combination of micro-turbulence, shocks and PDRs.

6.3   Application to Arp 299

The mechanically heated PDR models developed and presented in this thesis have also been used by Rosenberg et al. (2014b) to explain the observational data collected by *Herschel* on Arp 299.

Unlike NGC 253, Arp 299 is a system of two colliding galaxies hosting three active galactic nuclei undergoing intense star formation. For this system several observations are available both by *Herschel* (PACS and SPIRE spectrometers) and JCMT. The former provided information about high-J CO lines (up to $J = 20 - 19$) (Rosenberg et al. 2014b), while for the latter ^{13}CO and HCN lines have been observed. The main difference between these observations and those of NGC 253 is the higher number of ^{12}CO transitions available. This is also true for HCN, where in this case HCN $J = 4 - 3$ has been detected. Several models were applied by (Rosenberg et al. 2014b) to explain the observed lines detected by *Herschel*; in particular, many heating mechanisms have been introduced to explain the excitation of the high-J transitions. Heating due to cosmic rays, X-rays and
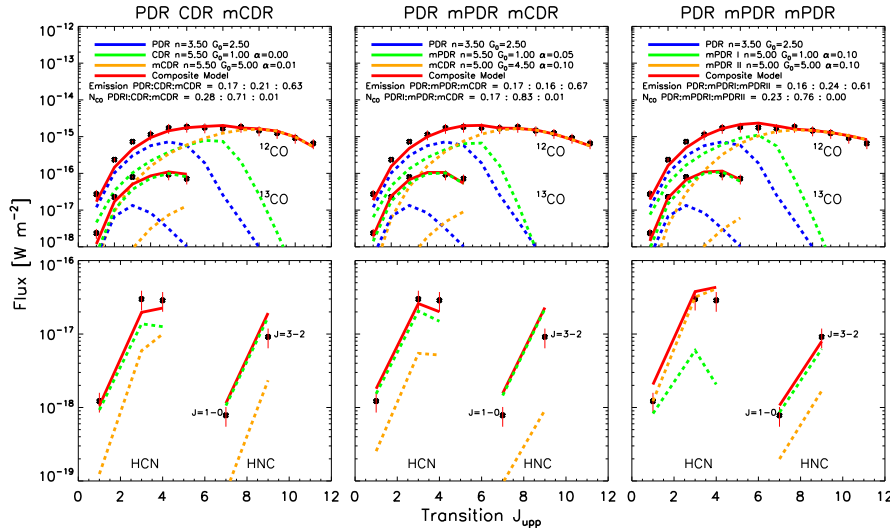
Figure 6.2 – ^{12}CO and ^{13}CO (top) with HCN and HNC (bottom) excitation ladders of NGC 253 with the flux of each transition are plotted as black asterisks with red error bars. In blue, green and yellow dotted lines PDR/CDR/mCDR (left), PDR/mPDR/mCDR (center), and PDR/mPDR/mPDR(right) ISM phases with their filling factors are plotted. The composite model is plotted with a red solid line. The model H_2 density [log cm^{-3}], G_0 [log Habing flux], and percentage mechanical heating (α) are shown in the legend along with the relative contribution of each phase in terms of emission and column density.

mechanical heating were considered.

In particular, mechanically heated Cosmic Rays Dominated Regions (mCDR) models overestimate the observed line intensities; the same results can be obtained for the HCN lines in X-rays dominated regions (XDR) models where the discrepancy reaches more than one order of magnitude (see Fig. 6.3). In a similar approach to the case of NGC 253 presented in the previous sub-section, mPDR models fit the observed ladder for high-*J* transitions within the error bars both for CO, ^{13}CO and HCN. This indicates the importance of mechanical heating in interpreting observations of violent star-bursting galaxies, especially for high-*J* transitions.

6.4 Prospects

6.4.1 Other possible applications

NGC 253 and Arp 299 are two galaxies which have been heavily studied due to their appealing property of being extremely bright in almost all parts of the electromagnetic spectrum. This makes them an ideal laboratory for astronomers to study star forming regions. Those galaxies have been recently observed by Herschel as many other star-
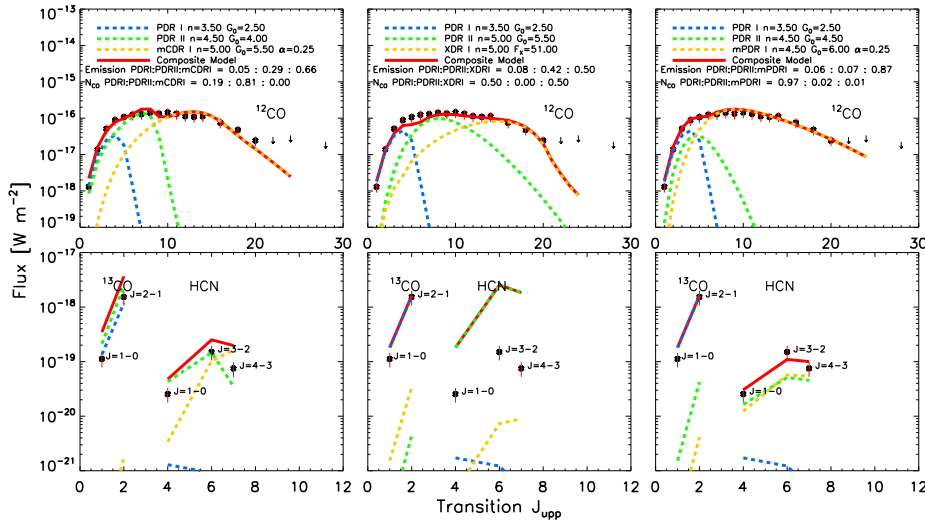
Figure 6.3 – ^{12}CO (top), ^{13}CO, and HCN (bottom) excitation ladders of Arp 299 with the flux of each transition plotted as black asterisks with red error bars. In blue, green and yellow dotted lines we plot the PDR/PDR/mCDR (left), PDR/PDR/mPDR (center), and PDR/PDR/XDR (right) ISM phases with their filling factors. The composite model is plotted with a red solid line. The model H_2 density [log cm^{-3}], G/G_0 [log Habing flux] or F_X [log erg s^{-1} cm^{-2}], and percentage mechanical heating (α) are shown in the legend along with the relative contribution of each phase in terms of emission and column density.

burst galaxies, LIRGS and ULIRGS, whose data are publicly available (Lemaux et al. 2014). The drawback of Herschel is that it has very high spectral resolution but low spatial resolution. For instance, although NGC 253 and Arp 299 are galaxies in the local universe, their star-burst regions which are on the scale of 1 kpc are almost covered by a single beam of Herschel, see e.g. Figure-1 by Rosenberg et al. (2014a). Another such situation is the case of Mrk 231 by van der Werf et al. (2010), where although a myriad transitions of CO and H_2O were observed within the spectral window of Herschel, no spatial information was provided.

Having spatially and spectrally resolved observations is important in addressing the fact that the filling factors of the mPDR component of the models of NGC 253 and Arp 299 is less than one per cent. This indicates that the emission of the high-J transitions in the best fit models of both systems emanates from mechanically heated regions that are dense and localized. There is stronger evidence for this localization in the best fit model of Arp 299 compared to NGC253, where $\alpha = 0.25$ and 0.1 are required, respectively. The higher α for Arp 299 could be due to the fact that Arp 299 is under-going a merger, hence the heating budget of the "best-fit model" is more dominated by mechanical heating compared to that of NGC253. Further hints for localized mechanically heating regions are provided by Pon et al. (2014), where Herschel observations of the Perseus B1-East

5 region are used where a filling factor of 0.15% of shock heated regions by dissipated turbulence was estimated. This filling factor is close to the 0.1% filling factor of the best fit model of NGC253 and about 5 times smaller that of Arp299. Although Perseus is a molecular cloud and not a star-burst galaxy like Arp299 and NGC253, it is a star-forming region where the same kind of shock heating and dissipation could be occurring. Despite the fact that the estimated filling factors mentioned earlier are very close, their proximity could be a mere coincidence. Thus, it would be an interesting application of the grids of Chapter-3 to try to constrain the mechanical heating rate of Perseus using the observations by Pon et al. (2014) and compare it to the rate they estimate. Moreover, the method presented in Chapter-5 can be applied to the data as well as to try to estimate the density PDF and consequently the Mach number in Perseus. A thorough study can be achieved with the Atacama Large Millimeter Array (ALMA), where at least the same spectral resolution of Herschel is matched with much higher spatial resolution. Thus, the answer to the localization of the mechanically heated regions could be checked systematically without the need of multi-component modeling. In fact, where multiple PDR models were necessary to model the emission of a region covered by the large beam of Herschel, single PDR models would be needed to model the emission of the resolved regions by ALMA within the same region of that beam. Recent observations of the central kpc region of NGC 1614, a LIRG with $L_{IR} \sim 10^{11.65}$ $L_{\odot}$ (Xu et al. 2015), hint to localized bright CO(6-5) emission compared to CO(2-1) that requires cooler gas to be excited. Takano et al. (2014) observed the central region of NGC 1068 which hosts an AGN where they present emission of a few shock and dust related species. Such spatially resolved emission maps along with future observations by ALMA could be used to find a definitive diagnostic discriminating XDRs from mPDRs.

6.4.2   General improvements

- In the PDR models we assumed that the micro-turbulence line-width is fixed throughout the parameter space. This assumption was based on galaxy scale ISM simulations by Pelupessy & Papadopoulos (2009) (see Chapter-4), where a canonical value of 1 km/s was used also in computing the emission maps in Chapters-4 and 5. The main limitation was the excessive computing time required to interpolate over the emission grids to compute the emission maps. Although this was good enough for our qualitative analysis of the trends in the diagnostic line-ratios, the use of a micro-turbulence line-width derived from the mechanical heating or computed self-consistently from the modeled gas, e.g. from an SPH simulation, could be essential for an accurate study.

- We focused our attention to high-J transitions, showing that they could be considered good tracers of the physical conditions present in the mechanically heated regions of the ISM . However, low-J transitions like the case of CO(1-0) still need to be accurately modeled in the low density case since the molecular mass of clouds is usually inferred from the luminosity of CO(1-0). A detailed simulation of the Milky Way by Smith et al. (2014) estimates that almost 42% of the molecular

mass is in gas not traced by CO, the so-called "CO-dark" gas. AREPO, which is a state of the art hydrodynamics code (Springel 2010), coupled with time dependent chemical evolution was used for that simulation, but very rough assumptions were done in the radiative transfer calculations. Namely, local thermal equilibrium was assumed in computing the CO(1-0) luminosity due to limited computational resources. A significant improvement over the LTE assumption would be able to produce the emission maps using the method presented in Chapter-3 where more accurate quantification of "CO-dark" gas can be achieved.

- Degeneracies between mPDR, CDRs and XDRs models: Meijerink et al. (2011) discuss the star-formation in environments with extreme mechanical feedback and cosmic ray rates with a comparison to X-ray dominated region. They find that OH^+, OH, H_2O^+, H_2O and H_3O^+ can be used as discriminants between XDRs and CDRs. Rosenberg et al. (2014b) find a similar behavior among XDR and CDR models where both perform poorly compared to mPDRs in fitting the molecular emission of Arp 299. It is worth noting that Rosenberg et al. (2014b) use CO, ^{13}CO, HCN, HNC and HCO^+ in their fitting procedure. On the other hand Meijerink et al. (2011) consider four models in their survey. Hence, it is interesting to increase the dimensionality of the grids by exploring possible ranges of X-ray heating and cosmic ray rates, in addition to considering the XDR – CDR discriminating species suggested by Meijerink et al. (2011), for the purpose of finding a unique diagnostic for these three types of regions.

- As an extension to the previous item, and to add more completeness to the modeling challenge, at the cost of further complexity, considering the $^{12}C / ^{13}C$ elemental ratio could have significant consequences on the outcome of the emission of the carbonaceous species. Ultimately for an accurate treatment of the huge minimization problem, i.e finding a best fit model with the proper statistical modeling, one must also consider the uncertainties involved in the chemical reaction constants and the Einstein coefficients and the collisional cross-sections used for computing the emission. An extensive review by Wakelam et al. (2010) discuss the challenges in modeling chemical networks one of which involves the propagation of uncertainties during the computations of the reaction rates. Clearly constructing grids, taking all the additional free parameters we mentioned, as was done in Chapter-2 and 3 is not a feasible solution. It is necessary to adopt sophisticated Monte-Carlo methods and smart-searching algorithms in finding a distinct diagnostic between XDRs, mPDRs and CDRs. In addition to such statistical modeling, it is also essential to have bigger data set against which the numerical modeling will be done. For example Papadopoulos et al. (2011) suggest that having more data such as multi-J transitions of CO, ^{13}CO and high density traces by ALMA could help find a unique diagnostic for CDRs.

- Needless to say, it is very important to have an accurate case study, a benchmark, against which the community can test the various numerical tools. The latest serious large scale comparison was done by Röllig et al. (2007). The "order-of-magnitude"

discrepancy among the tools for a reduced PDR model is indicative of lack of a reference against which an astronomer can test his/her tools. A case relevant to this thesis would be having a basic benchmark to probe the influence of mechanical heating in a star-forming region; it is necessary to have a self-consistent time-dependent hydrodynamics code, coupled to a radiative transfer code that is able to resolve the shocks accurately as well as treat the chemistry accurately. It is not necessary for this benchmark case to solve the problem fully, but to capture the physics and chemistry well enough to establish a solid foundation upon which more sophistication can be added.

Bibliography

Aalto, S. 2005, in IAU Symposium, Vol. 231, Astrochemistry: Recent Successes and Current Challenges, ed. D. C. Lis, G. A. Blake, & E. Herbst, 261–270

Aalto, S. 2013, in IAU Symposium, Vol. 292, IAU Symposium, ed. T. Wong & J. Ott, 199–208

Aalto, S. 2014, in IAU Symposium, Vol. 303, IAU Symposium, ed. L. O. Sjouwerman, C. C. Lang, & J. Ott, 15–28

Abel, T., Anninos, P., Zhang, Y., & Norman, M. L. 1997, New Astronomy, 2, 181

Alves de Oliveira, C., Schneider, N., Merín, B., et al. 2014, A&A, 568, A98

Ao, Y., Henkel, C., Menten, K. M., et al. 2013, A&A, 550, A135

Avedisova, V. S. 1979, Soviet Ast., 23, 544

Baan, W. A., Henkel, C., Loenen, A. F., Baudry, A., & Wiklind, T. 2008, A&A, 477, 747

Bakes, E. L. O. & Tielens, A. G. G. M. 1994, ApJ, 427, 822

Ballesteros-Paredes, J., Vázquez-Semadeni, E., Gazol, A., et al. 2011, MNRAS, 416, 1436

Barnes, J. & Hut, P. 1986, Nature, 324, 446

Bayet, E., Williams, D. A., Hartquist, T. W., & Viti, S. 2011, MNRAS, 414, 1583

Bergin, E. A. 2011, in EAS Publications Series, Vol. 52, EAS Publications Series, ed. M. Röllig, R. Simon, V. Ossenkopf, & J. Stutzki, 207–216

Bisbas, T. G., Bell, T. A., Viti, S., Yates, J., & Barlow, M. J. 2012, MNRAS, 427, 2100

Black, J. H. & Dalgarno, A. 1977, ApJS, 34, 405

Blitz, L., Fukui, Y., Kawamura, A., et al. 2007, Protostars and Planets V, 81

Bohlin, R. C., Savage, B. D., & Drake, J. F. 1978, ApJ, 224, 132

Bolatto, A. D., Wolfire, M., & Leroy, A. K. 2013, ARA&A, 51, 207

Botschwina, P., Horn, M., Flugge, J., & Seeger, S. 1993, J. Chem. Soc., Faraday Trans., 89, 2219

Bradford, C. M., Nikola, T., Stacey, G. J., et al. 2003, ApJ, 586, 891

Bregman, J. N. 2007, ARA&A, 45, 221

Brinch, C. & Hogerheijde, M. R. 2010, A&A, 523, A25

Bruzual, G. & Charlot, S. 1993, ApJ, 405, 538

Bruzual, G. & Charlot, S. 2003, MNRAS, 344, 1000

Bryant, P. M. & Scoville, N. Z. 1999, AJ, 117, 2632

Burkhart, B., Ossenkopf, V., Lazarian, A., & Stutzki, J. 2013, ApJ, 771, 122

Cazaux, S. & Tielens, A. G. G. M. 2002, ApJ, 575, L29

Cazaux, S. & Tielens, A. G. G. M. 2004, ApJ, 604, 222

Combes, F., García-Burillo, S., Casasola, V., et al. 2013, A&A, 558, A124

Combes, F., Garcia-Burillo, S., Casasola, V., et al. 2014, ArXiv e-prints

Coppola, C. M., Longo, S., Capitelli, M., Palla, F., & Galli, D. 2011, ApJS, 193, 7

Dahlén, T. & Fransson, C. 1999, A&A, 350, 349

de Jong, T., Boland, W., & Dalgarno, A. 1980, A&A, 91, 68

de Vega, H. J., Sánchez, N., & Combes, F. 1996, Nature, 383, 56

Downes, D. & Solomon, P. M. 1998, ApJ, 507, 615

Draine, B. 2010, Physics of the Interstellar and Intergalactic Medium, Princeton Series in Astrophysics (Princeton University Press)

Dumouchel, F., Faure, A., & Lique, F. 2010, MNRAS, 406, 2488

Falgarone, E., Hily-Blant, P., Pety, J., & Pineau Des Forets, G. 2007, in Molecules in Space and Laboratory

Falgarone, E. & Phillips, T. G. 1990, ApJ, 359, 344

Feldmann, R., Gnedin, N. Y., & Kravtsov, A. V. 2012, ApJ, 758, 127

Ferland, G. J., Korista, K. T., Verner, D. A., et al. 1998, PASP, 110, 761

Freyer, T., Hensler, G., & Yorke, H. W. 2003, ApJ, 594, 888

Freyer, T., Hensler, G., & Yorke, H. W. 2006, ApJ, 638, 262

Froebrich, D. & Rowles, J. 2010, MNRAS, 406, 1350

Galli, D. & Palla, F. 1998, Astronomy and Astrophysics, 335, 403

Gao, Y. & Solomon, P. M. 2004, ApJS, 152, 63

Genzel, R. 1991, in The Physics of Star Formation and Early Stellar Evolution, ed. C. J. Lada & N. D. Kylafis, NATO ASI Series No. 342 (Springer Netherlands), 155–220

Goldman, I. & Contini, M. 2012, in American Institute of Physics Conference Series, Vol. 1439, American Institute of Physics Conference Series, ed. P.-L. Sulem & M. Mond, 209–217

González-Alfonso, E., Fischer, J., Graciá-Carpio, J., et al. 2012, A&A, 541, A4

González-Alfonso, E., Fischer, J., Isaak, K., et al. 2010, A&A, 518, L43

Gould, R. J. & Salpeter, E. E. 1963, ApJ, 138, 393

Green, S. & Thaddeus, P. 1974, ApJ, 191, 653

Habart, E., Dartois, E., Abergel, A., et al. 2010, A&A, 518, L116

Habing, H. J. 1969, Bull. Astron. Inst. Netherlands, 20, 177

Hailey-Dunsheath, S., Nikola, T., Stacey, G. J., et al. 2008, ApJ, 689, L109

Henkel, C., Wilson, T. L., Walmsley, C. M., & Pauls, T. 1983, A&A, 127, 388

Hogerheijde, M. R. & van der Tak, F. F. S. 2000, A&A, 362, 697

Hollenbach, D. & Gorti, U. 2009, ApJ, 703, 1203

Hollenbach, D. J. & Tielens, A. G. G. M. 1999, Reviews of Modern Physics, 71, 173

Hopkins, P. F. 2012a, MNRAS, 423, 2016

Hopkins, P. F. 2012b, MNRAS, 423, 2037

Hopkins, P. F. 2013, MNRAS, 428, 1950

Houghton, S., Whiteoak, J. B., Koribalski, B., et al. 1997, A&A, 325, 923

Imanishi, M. & Nakanishi, K. 2013, AJ, 146, 47

Israel, F. P. 2009a, A&A, 493, 525

Israel, F. P. 2009b, A&A, 506, 689

Israel, F. P. & Baas, F. 2002, A&A, 383, 82

Israel, F. P. & Baas, F. 2003, A&A, 404, 495

Israel, F. P., White, G. J., & Baas, F. 1995, A&A, 302, 343

Jansen, D. J., van Dishoeck, E. F., & Black, J. H. 1994, A&A, 282, 605

Kainulainen, J., Beuther, H., Henning, T., & Plume, R. 2009, A&A, 508, L35

Kainulainen, J. & Tan, J. C. 2013, A&A, 549, A53

Kamenetzky, J., Glenn, J., Rangwala, N., et al. 2012, ApJ, 753, 70

Kaufman, M. J., Wolfire, M. G., Hollenbach, D. J., & Luhman, M. L. 1999, ApJ, 527, 795

Kazandjian, M. V., Meijerink, R., Pelupessy, I., Israel, F. P., & Spaans, M. 2012, A&A, 542, A65

Bibliography

Kazandjian, M. V., Meijerink, R., Pelupessy, I., Israel, F. P., & Spaans, M. 2015a, A&A, 574, A127

Kazandjian, M. V., Pelupessy, I., Meijerink, R., Israel, F. P., & Spaans, M. 2015b, submitted, ""

Kim, C.-G., Kim, W.-T., & Ostriker, E. C. 2006, ApJ, 649, L13

Klisch, E., Klaus, T., Belov, S. P., Winnewisser, G., & Herbst, E. 1995, A&A, 304, L5

Knudsen, K. K., Walter, F., Weiss, A., et al. 2007, ApJ, 666, 156

Komossa, S., Burwitz, V., Hasinger, G., et al. 2003, ApJ, 582, L15

Kravtsov, A. V., Klypin, A., & Hoffman, Y. 2002, ApJ, 571, 563

Kritsuk, A. G., Norman, M. L., & Wagner, R. 2011, ApJ, 727, L20

Kroupa, P. 2001, MNRAS, 322, 231

Krumholz, M. R. 2014, MNRAS, 437, 1662

Krumholz, M. R. 2015, in Astrophysics and Space Science Library, Vol. 412, Astrophysics and Space Science Library, ed. J. S. Vink, 43

Krumholz, M. R. & Thompson, T. A. 2007, ApJ, 669, 289

Larson, R. B. 1981, MNRAS, 194, 809

Le Petit, F., Nehmé, C., Le Bourlot, J., & Roueff, E. 2006, ApJS, 164, 506

Le Teuff, Y. H., Millar, T. J., & Markwick, A. J. 2000, A&AS, 146, 157

Leitherer, C., Schaerer, D., Goldader, J. D., et al. 1999, ApJS, 123, 3

Lemaux, B. C., Le Floc'h, E., Le Fevre, O., et al. 2014, VizieR Online Data Catalog, 357, 29090

Lepp, S. & Dalgarno, A. 1996, A&A, 306, L21

Lepp, S., Stancil, P. C., & Dalgarno, A. 2002, Journal of Physics B Atomic Molecular Physics, 35, 57

Leroy, A. K., Bolatto, A., Gordon, K., et al. 2011, ApJ, 737, 12

Lique, F., Spielfiedel, A., & Cernicharo, J. 2006, A&A, 451, 1125

Lique, F., Spielfiedel, A., Feautrier, N., et al. 2010, The Journal of Chemical Physics, 132, 024303

Loenen, A. F., Spaans, M., Baan, W. A., & Meijerink, R. 2008, A&A, 488, L5

Loenen, A. F., van der Werf, P. P., Güsten, R., et al. 2010, A&A, 521, L2

Mac Low, M.-M. & Klessen, R. S. 2004, Reviews of Modern Physics, 76, 125

Maloney, P. & Black, J. H. 1988, ApJ, 325, 389

Maloney, P. R., Begelman, M. C., & Pringle, J. E. 1996a, ApJ, 472, 582

Maloney, P. R., Hollenbach, D. J., & Tielens, A. G. G. M. 1996b, ApJ, 466, 561

Martín, S., Martín-Pintado, J., & Viti, S. 2009, ApJ, 706, 1323

Martín, S., Mauersberger, R., Martín-Pintado, J., Henkel, C., & García-Burillo, S. 2006, ApJS, 164, 450

Mauersberger, R., Henkel, C., Wielebinski, R., Wiklind, T., & Reuter, H.-P. 1996, A&A, 305, 421

Meijerink, R., Kristensen, L. E., Weiß, A., et al. 2013, ApJ, 762, L16

Meijerink, R. & Spaans, M. 2005, A&A, 436, 397

Meijerink, R., Spaans, M., & Israel, F. P. 2007, A&A, 461, 793

Meijerink, R., Spaans, M., Loenen, A. F., & van der Werf, P. P. 2011, A&A, 525, A119+

Monaghan, J. J. 1992, ARA&A, 30, 543

Mühle, S., Seaquist, E. R., & Henkel, C. 2007, ApJ, 671, 1579

Narayanan, D., Cox, T. J., Kelly, B., et al. 2008, ApJS, 176, 331

Narayanan, D. & Hopkins, P. F. 2013, MNRAS, 433, 1223

Narayanan, D., Krumholz, M., Ostriker, E. C., & Hernquist, L. 2011, MNRAS, 418, 664

Nikola, T., Stacey, G. J., Brisbin, D., et al. 2011, ApJ, 742, 88

Nordlund, Å. K. & Padoan, P. 1999, in Interstellar Turbulence, ed. J. Franco & A. Carraminana, 218

Norman, C. A. & Ferrara, A. 1996, ApJ, 467, 280

Oka, T., Geballe, T. R., Goto, M., Usuda, T., & McCall, B. J. 2005, ApJ, 632, 882

Ossenkopf, V. 2002, A&A, 391, 295

Ossenkopf, V. & Mac Low, M.-M. 2002, A&A, 390, 307

Paglione, T. A. D., Jackson, J. M., & Ishizuki, S. 1997, ApJ, 484, 656

Paglione, T. A. D., Tosaki, T., & Jackson, J. M. 1995, ApJ, 454, L117

Pan, L. & Padoan, P. 2009, ApJ, 692, 594

Panuzzo, P., Rangwala, N., Rykala, A., et al. 2010, A&A, 518, L37

Papadopoulos, P. P. 2010, ApJ, 720, 226

Papadopoulos, P. P., Thi, W.-F., Miniati, F., & Viti, S. 2011, MNRAS, 414, 1705

Parravano, A., Hollenbach, D. J., & McKee, C. F. 2003, ApJ, 584, 797

Pelupessy, F. I. 2005, PhD thesis, Leiden Observatory, Leiden University, P.O. Box 9513, 2300 RA Leiden, The Netherlands

Pelupessy, F. I. & Papadopoulos, P. P. 2009, ApJ, 707, 954

Pelupessy, F. I., Papadopoulos, P. P., & van der Werf, P. 2006, ApJ, 645, 1024

Pérez-Beaupuits, J. P., Wada, K., & Spaans, M. 2011, ApJ, 730, 48

Pietsch, W., Vogler, A., Klein, U., & Zinnecker, H. 2000, A&A, 360, 24

Pilbratt, G. L., Riedinger, J. R., Passvogel, T., et al. 2010, A&A, 518, L1

Pineda, J. E., Goodman, A. A., Arce, H. G., et al. 2010, ApJ, 712, L116

Pon, A., Johnstone, D., Kaufman, M. J., Caselli, P., & Plume, R. 2014, MNRAS, 445, 1508

Portegies Zwart, S., McMillan, S., Harfst, S., et al. 2009, New A, 14, 369

Press, W. H., Teukolsky, S. A., Vetterling, W. T., & Flannery, B. P. 2002, Numerical recipes in C++ : the art of scientific computing

Robitaille, T. P. & Whitney, B. A. 2010, ApJ, 710, L11

Röllig, M. 2011, A&A, 530, A9+

Röllig, M., Abel, N. P., Bell, T., et al. 2007, A&A, 467, 187

Röllig, M., Ossenkopf, V., Jeyakumar, S., Stutzki, J., & Sternberg, A. 2006, A&A, 451, 917

Rosenberg, M. J. F., Kazandjian, M. V., van der Werf, P. P., et al. 2014a, A&A, 564, A126

Rosenberg, M. J. F., Meijerink, R., Israel, F. P., et al. 2014b, A&A, 568, A90

Rosenberg, M. J. F., van der Werf, P. P., Aalto, S., et al. 2015, ApJ, 801, 72

Rosolowsky, E. 2005, PASP, 117, 1403

Russeil, D., Schneider, N., Anderson, L. D., et al. 2013, A&A, 554, A42

Saito, T., Iono, D., Yun, M., et al. 2013, in Astronomical Society of the Pacific Conference Series, Vol. 476, Astronomical Society of the Pacific Conference Series, ed. R. Kawabe, N. Kuno, & S. Yamamoto, 287

Salpeter, E. E. 1955, ApJ, 121, 161

Savage, C., Apponi, A. J., Ziurys, L. M., & Wyckoff, S. 2002, ApJ, 578, 211

Schilke, P., Walmsley, C. M., Pineau Des Forets, G., et al. 1992, A&A, 256, 595

Schneider, N., Csengeri, T., Klessen, R. S., et al. 2014, ArXiv e-prints

Schöier, F. L., van der Tak, F. F. S., van Dishoeck, E. F., & Black, J. H. 2005, A&A, 432, 369

Schwarz, J., McCray, R., & Stein, R. F. 1972, ApJ, 175, 673

Scoville, N., Sheth, K., Aussel, H., Manohar, S., & ALMA Cycle 0 Teams. 2013, in Astronomical

Society of the Pacific Conference Series, Vol. 476, Astronomical Society of the Pacific Conference Series, ed. R. Kawabe, N. Kuno, & S. Yamamoto, 1

Scoville, N. Z., Sargent, A. I., Sanders, D. B., & Soifer, B. T. 1991, ApJ, 366, L5

Shetty, R., Glover, S. C., Dullemond, C. P., & Klessen, R. S. 2011, MNRAS, 412, 1686

Shull, J. M. & Beckwith, S. 1982, ARA&A, 20, 163

Silich, S. A., Franco, J., Palous, J., & Tenorio-Tagle, G. 1996, ApJ, 468, 722

Smith, R. J., Glover, S. C. O., Clark, P. C., Klessen, R. S., & Springel, V. 2014, MNRAS, 441, 1628

Snow, T. P. & McCall, B. J. 2006, ARA&A, 44, 367

Sobolev, V. V. 1960, Moving envelopes of stars

Solomon, P. M. & de Zafra, R. 1975, ApJ, 199, L79

Solomon, P. M., Downes, D., & Radford, S. J. E. 1992, ApJ, 387, L55

Solomon, P. M., Rivolo, A. R., Barrett, J., & Yahil, A. 1987, ApJ, 319, 730

Springel, V. 2005, MNRAS, 364, 1105

Springel, V. 2010, MNRAS, 401, 791

Springel, V. & Hernquist, L. 2002, MNRAS, 333, 649

Stahler, S. W. & Palla, F. 2005, The Formation of Stars

Sternberg, A., Hoffmann, T. L., & Pauldrach, A. W. A. 2003, ApJ, 599, 1333

Takano, S., Nakajima, T., Kohno, K., et al. 2014, PASJ, 66, 75

Tielens, A. 2005, The Physics and Chemistry of the Interstellar Medium (Cambridge University Press)

Tielens, A. G. G. M. 2013, Reviews of Modern Physics, 85, 1021

Tielens, A. G. G. M. & Hagen, W. 1982, A&A, 114, 245

Tielens, A. G. G. M. & Hollenbach, D. 1985, ApJ, 291, 722

Usero, A., García-Burillo, S., Martín-Pintado, J., Fuente, A., & Neri, R. 2007, New A Rev., 51, 75

van der Tak, F. 2011, in IAU Symposium, Vol. 280, IAU Symposium, ed. J. Cernicharo & R. Bachiller, 449–460

van der Tak, F. F. S., Belloche, A., Schilke, P., et al. 2006, A&A, 454, L99

van der Tak, F. F. S., Black, J. H., Schöier, F. L., Jansen, D. J., & van Dishoeck, E. F. 2007, A&A, 468, 627

van der Werf, P. P., Isaak, K. G., Meijerink, R., et al. 2010, A&A, 518, L42

Vasyunin, A. I., Sobolev, A. M., Wiebe, D. S., & Semenov, D. A. 2004, Astronomy Letters, 30, 566

Vazquez-Semadeni, E. 1994, ApJ, 423, 681

Wada, K. 2001, ApJ, 559, L41

Wada, K. & Norman, C. A. 2001, ApJ, 547, 172

Wada, K. & Norman, C. A. 2002, ApJ, 566, L21

Wada, K. & Norman, C. A. 2007, ApJ, 660, 276

Wada, K. & Tomisaka, K. 2005, ApJ, 619, 93

Wakelam, V., Smith, I. W. M., Herbst, E., et al. 2010, Space Sci. Rev., 156, 13

Weiß, A., Requena-Torres, M. A., Güsten, R., et al. 2010, A&A, 521, L1

Wheeler, J. C., Mazurek, T. J., & Sivaramakrishnan, A. 1980, ApJ, 237, 781

Wolfire, M. G. 2011, in EAS Publications Series, Vol. 52, EAS Publications Series, ed. M. Röllig, R. Simon, V. Ossenkopf, & J. Stutzki, 141–146

Wolfire, M. G., Hollenbach, D., & McKee, C. F. 2010, ApJ, 716, 1191

Wolfire, M. G., Hollenbach, D., McKee, C. F., Tielens, A. G. G. M., & Bakes, E. L. O. 1995, ApJ, 443, 152

Wolfire, M. G., Hollenbach, D., & Tielens, A. G. G. M. 1989, ApJ, 344, 770

Wolfire, M. G., McKee, C. F., Hollenbach, D., & Tielens, A. G. G. M. 2003, ApJ, 587, 278

Xu, C. K., Cao, C., Lu, N., et al. 2015, ApJ, 799, 11

Xu, X., Narayanan, D., & Walker, C. 2010, ApJ, 721, L112

Yang, B., Stancil, P. C., Balakrishnan, N., & Forrey, R. C. 2010, ApJ, 718, 1062

Indicatoren van Mechanische Verwarming in Stervormende Sterrenstelsels: Samenvatting in het Nederlands

De aardatmosfeer bestaat voornamelijk uit stikstof en zuurstof en voor een klein deel uit andere chemische bestanddelen. De straling van de Zon wordt door de moleculen en stofdeeltjes in de atmosfeer verstrooid. Op een heldere dag resulteert deze interactie in een blauwe kleur. In ons dagelijks leven zien we vaak wolken. Deze wolken bestaan uit water en hebben verschillende eigenschappen die afhangen van de hoogte waarop ze worden gevormd. In het bijzonder hebben ze een dichtheid die verschilt van de gemiddelde dichtheid van hun omgeving. Wolken zijn er in verschillende vormen en afmetingen. Ze hebben een wisselwerking met het zonlicht, waarbij ze een deel van het spectrum van het licht blokkeren en op die manier werken ze als een filter. Wanneer het zonlicht dus op de wolk valt, zal een deel van het licht worden geabsorbeerd een deel wordt gereflecteerd, en het overige licht (straling) bereikt onze ogen.

Het concept van een wolk in de atmosfeer van de aarde kan verder worden doorgetrokken naar andere omgevingen, zoals sterrenstelsels. Sterrenstelsels bestaan uit sterren, gas en stof. De materie dat zich tussen de sterren bevindt, neemt het grootste deel van het volume in en wordt door sterrenkundigen als het interstellaire medium aangeduid (afgekort ISM). Sterlicht heeft op eenzelfde manier een wisselwerking met het ISM als de straling van de Zon met de wolken in onze atmosfeer.

Het ISM bestaat uit gas dat een lage dichtheid heeft. De eigenschappen van dit gas verschillen nogal met de gassen die aanwezig zijn in de atmosfeer van de Aarde. In een kubieke centimeter lucht, ongeveer de grootte van een ijsblokje, zitten 10^{19} atomen, terwijl hetzelfde volume van het ISM tenminste een miljoenste van een biljoenste keer ijler is met een dichtheid die in het algemeen varieert van 10^{-3} tot 10^4 atomen per cm^3. Wanneer we naar de thermische eigenschappen kijken, zien we dat de aardatmosfeer wordt gekenmerkt door verschillende lagen met temperaturen tussen de 200 en 300 Kelvin (wat correspondeert met $-172.15\,°$C tot $30\,°$C). Dit is in tegenstelling tot het ISM, dat verschillende fasen heeft met een veel grotere variatie in temperatuur, namelijk tussen de 10 en 10^5 K, (wat correspondeert met $-263.15\,°$C tot ongeveer $99700\,°$C). Onder deze omstandigheden kunnen atomen en moleculen op allerlei manieren worden aangeslagen die zich in de aardatmosfeer niet gauw voordoen.

De fysische verklaring voor hoe verschillende kleuren worden geproduceerd wanneer straling een interactie aangaat met materie, wordt gegeven door de kwantumfysica, en

in het bijzonder door de kwantumstructuur van atomen en moleculen. Sterstraling treedt in wisselwerking met het gas en brengt de verschillende stoffen in het ISM in een aangeslagen toestand. Wanneer de ultraviolette straling van de sterren wordt geabsorbeerd door het gas worden de elektronen in het gas in een hogere energietoestand gebracht. In het geval van moleculen komen, naast de aangeslagen toestanden van de elektronen, ook minder energetische energie overgangen voor. Deze toestanden corresponderen met energieverschillen die ongeveer honderd keer lager kunnen zijn dan die van de aangeslagen toestanden van elektronen. Deze aangeslagen toestanden worden geassocieerd met de rotaties en vibraties van het molecuul. Terwijl de aangeslagen toestand van de elektronen bijvoorbeeld kan resulteren in ultraviolette straling, produceren de rotaties van het molecuul infraroodstraling (IR, golflengtes van 1 μm tot1 mm) en sub-millimeter fotonemissie. De UV-straling dringt niet diep door in een interstellaire wolk, net zoals zonlicht maar beperkt doordringt in de wolken van de aardatmosfeer. Dit in tegenstelling tot infraroodstraling die veel dieper in de interstellaire wolk door kan dringen dan de UV straling. Als we dit en het feit dat de wolken in het ISM het visuele en ultraviolette straling blokkeren, in acht nemen, kunnen we zeggen dat het stof dat veel voorkomt in het ISM transparant is voor infraroodstraling, en dat deze straling kan worden gebruikt om dit stof zelf te bestuderen.

De straling, die wordt geproduceerd door wolken, kan worden waargenomen met daarvoor speciaal ontworpen telescopen. De meest gevoelige en modernste telescoop die voor dit doel geschikt is, is het Atacama Large Millimeter Array (ALMA) in Chili. ALMA kan zeer zwakke signalen detecteren. In het algemeen geven submillimeter- en infraroodstraling een indicatie van stervorming in speciale gebieden die functioneren als zogenaamde "sterrenfabrieken". In ons sterrenstelsel (de Melkweg) wordt bijvoorbeeld ongeveer 1 ster per jaar geboren. In stervormende sterrenstelsels kunnen tot wel 10 000 sterren per jaar worden geboren. De gebieden waar heel heldere sterren worden geboren zijn ook de gebieden waar ze dood gaan. Het snelle tempo waarin sterren worden geboren, verhoogt ook de kans op het vormen van zeer zware sterren (tot 1000 keer de massa van de Zon). Wanneer deze sterren sterven, exploderen ze in een van de sterkste explosies van het universum, zogenaamde *supernovae*. Deze explosies zijn 100,000,000,000,000,000,000,000,000 keer krachtiger dan de meest krachtige nucleaire bom die ooit op aarde tot ontploffing is gebracht. Op deze schaal veroorzaken ze schokgolven en turbulentie in het gas, waardoor het gas wordt verwarmd. Dit verwarmde gas zendt straling uit, die heel anders is dan in rustiger wolken.

De temperatuur van een lichaam wordt gewoonlijk gemeten met een thermometer. Vanuit ervaringen in ons dagelijks leven weten we dat deze werkt door direct contact te maken met het lichaam waarvan we de temperatuur willen meten. Nadat hij lang genoeg met het lichaam in contact is geweest, bereikt het een evenwicht, omdat er geen warmte meer wordt uitgewisseld tussen de thermometer en het lichaam. De temperatuur kan worden afgelezen door de schaalverdeling op de thermometer te gebruiken. Dit is mogelijk in het geval van een analoge en een digitale thermometer. Wanneer we nu het geval bekijken van buitenaards object en we willen de temperatuur ervan meten, dan is het duidelijk dat we geen directe metingen meer kunnen uitvoeren. We moeten daarom indirecte methoden benutten om de temperatuur en andere fysische eigenschappen van

het gas tussen de sterren te bepalen. De meest algemene indirecte methode maakt gebruik van kleuren en hun bijbehorende golflengten. Om te begrijpen hoe dit werkt, geven we een voorbeeld uit ons dagelijks leven. We weten bijvoorbeeld dat gesmolten lava rood gloeit. Deze rode kleur geeft aan dat de temperatuur van het lava ongeveer 1000 graden Celsius bedraagt. Een hete vlam die ontstaat tijdens het lassen van metaal gloeit met een blauwe kleur, wat betekent dat de temperatuur ongeveer 6000 graden Celsius bedraagt. Deze verschuiving in kleur komt door een verandering in de verdeling van de energie van de fotonen in het elektromagnetisch spectrum. In het eerste geval lag de piek van de verdeling van de fotonen bij fotonen met een rode kleur (lagere energie en langere golflengten), met erelatief weinig fotonen in het blauwe deel van het spectrum, terwijl dit in het tweede geval juist omgekeerd is. Nu ligt de piek van de verdeling van de fotonen bij de blauwe fotonen (hogere energieÃńn en kortere golflengten) met relatief weinig fotonen in het rode gebied. Wanneer de moleculen door warme of invallende straling in een aangeslagen toestand worden gebracht, zenden ze straling uit op discrete golflengten. Dit staat in tegenstelling tot de bovengenoemde voorbeelden waar de uitgezonden fotonen een breed golflengtegebied beslaan. Verschillende typen aangeslagen toestanden resulteren in emissie op verschillende golflengten. Een goede kennis van de relatieve intensiteiten van de verschillende emissie van de moleculen kan worden gebruikt om de temperatuur en de dichtheid van het gas te bepalen. De heldere emissie van HCN op 88 GHz ten opzichte van CO 115 GHz geeft hoge temperaturen aan in een stervormend sterrenstelsel van rond de 100 K. Dit is bijvoorbeeld een indicator voor hoge temperaturen (ongeacht de oorzaak van deze hoge temperatuur is). Deze moleculaire overgangen kunnen niet alleen worden beschouwd als een "thermometer" van het ISM, maar ze kunnen ons ook hints geven over bepaalde mechanismen die ervoor zorgen dat deze overgangen kunnen plaatsvinden. We kunnen de emissie van deze moleculen beschouwen als "lange afstand detectives" voor het ISM.

In dit proefschrift bestuderen we de effecten van de geabsorbeerde turbulente energie, mechanische energie, op de emissie van de eerder genoemde moleculen zoals HCN en CO. We hebben laten zien dat een kleine hoeveelheid turbulentie genoeg is om grote invloed uit te oefenen op de stralingsintensiteit van verschillende soorten moleculen. We hebben in het bijzonder het belang van de relatieve intensiteiten van de emissie van of HCN, HNC, ^{13}CO en de verschillende overgangen bestudeerd door middel van het opsporen van de thermische eigenschappen van het ISM. De relatieve intensiteiten van deze verschillende chemische stoffen werden onderzocht onder uiteenlopende omstandigheden, waarbij de invloed van mechanische verwarming in tabelvorm is gezet. Deze tabellen kunnen worden gebruikt om de mate van mechanische verwarming te kwantificeren in stervormende sterrenstelsels waarvan waarnemingen beschikbaar zijn. Bovendien kan informatie over de mechanische verwarming worden geanalyseerd, waarbij een model van mogelijke bronnen voor dergelijke turbulente omgevingen kan worden gepostuleerd. Dit is fascinerend en uitdagend omdat we, terwijl we ons ver van andere sterrenstelsels bevinden, op deze wijze toch belangrijke informatie kunnen afleiden uit een beperkte hoeveelheid gegevens.

143

Diagnostics for Mechanical Heating in Star-forming Galaxies: Summary in English

The atmosphere of the Earth is mainly made up of nitrogen and oxygen and a smaller fraction of many other chemical components. Radiation from our Sun interacts with these species and scatters. On a clear day this interaction results in a blue color. In our everyday life we often experience the presence of clouds. These clouds are composed of water and they have different properties according to the altitude at which they form. In particular, they have densities different from the average density of their surroundings. Clouds come in many shapes and sizes. They interact with the Sun light, blocking part of its spectrum and eventually acting as filters. Thus, when the solar radiation interacts with these clouds, part of it gets absorbed, some it is reflected and the remaining light (radiation) reaches our eyes.

The concept of clouds can be extended to other environments such as galaxies. Galaxies are formed of stars and gas and dust. Matter between the stars occupies most of the volume and is referred to as the *Interstellar Medium*, labeled with the acronym *ISM*. Light from stars interacts with the clouds in the interstellar medium in a similar way as the radiation from our Sun interacts with the clouds in our atmosphere.

The ISM is filled with gas of very low density. The properties of this gas are quite different from that present in the atmosphere of the Earth. For example, in one cm^3, that is the size of e.g. an ice cube, the atmosphere has 10^{19} atoms, while the gas of the ISM is at least 1 millionth of a billion times less dense with a range of densities that spans from 10^{-3} up to 10^6 atoms per cm^3. In terms of thermal properties, the atmosphere of the Earth is characterized by several layers whose temperature varies in between 200 and 300 K (corresponding to $-172\,°C$ up to $30\,°C$). In contrast, the ISM has different phases with a much wider temperature range between 10 and 10^5 K, i.e. from $-263\,°C$ up to roughly $99700\,°C$). In these conditions, atoms and molecules can be excited in more diverse and various ways.

The physical explanation how different colors are produced while radiation interacts with matter relies on quantum physics, in particular on the quantum structure of atoms and molecules. The radiation from the stars interacts with the gas and excites the chemical species inside the ISM. When the ultra-violet (UV) radiation of stars is absorbed by the gas the electrons get excited into higher energy levels. In the molecular case, in addition to electronic excitation, smaller energy differences that are about a hundred times lower are

possible. This excitation is associated with the rotation or the vibration of the molecule. While the electronic excitation can result in ultraviolet emission, the rotational transitions produce infrared (IR, wavelengths from 1 μm up to 1 mm) and submillimeter photon emission. The UV radiation has a low penetration depth, just as sunlight interacting with clouds in the atmosphere whereas IR photons can penetrate much larger clouds compared to the UV radiation.

The infrared radiation emitted from clouds can be detected with specially designed telescopes. The most recent and sensitive currently in operation is the Atacama Large Millimeter Array (ALMA) in Chile that can detect very weak signals. Generally IR and submm emission is indicative of star formation in special regions that work as star "factories". For example, in our Galaxy (the Milky Way) around 1 star is born each year. In star forming galaxies, up to 10,000 stars can be born each year. Regions where very luminous stars are born are also regions where they die. The fast rate of stars being born also increases the probability of having stars that are very heavy (up to 1000 times the mass of our Sun). When these stars die, they explode in one of the strongest explosions in the Universe known as *supernovae*. These explosions are 100,000,000,000,000,000,000,000,000 more powerful than the largest nuclear device detonated on Earth. At this scale they cause the gas in the vicinity to get mixed up and heated due to shock waves and turbulence. The heated gas results in various emission that is different from these of quiescent clouds.

Measurement of the temperature of a body is usually performed using specific instruments called thermometers. As we have experienced several times in our everyday life, this functions by having direct contact with the body whose temperature we are interested in. After the thermometer is in contact for a long enough period with that body, it reaches equilibrium as no heat is transferred anymore between the thermometer and the body. A reading of the temperature can be done using the scales available on the thermometer itself, both in the case of analogue or digital apparatus. When we move to the case of extraterrestrial bodies and we wonder about their temperatures it is evident that such direct measurements are not possible; eventually, indirect methods should be adopted in order to determine the temperature and other physical properties of gas between the stars. The most common indirect way adopted makes use of colors and their wavelengths. To appreciate how this works we can use everyday life experiences; for example, we know that molten lava glows red. The red color indicates that the temperature is about 1000 degrees C. A hot metal welding flame glows with a blueish color indicating that the temperature is about 6000 degrees C. This shift in the color is due to a different distribution of the energies of the photons in the electromagnetic spectrum. In the former case, the peak of the distribution of the photons is towards the red (lower energies and longer wavelengths), with a relative deficit in the blue part of the spectrum, whereas it is the opposite in the second case, i.e. the peak of the distribution is towards blueish photons (higher energies and shorter wavelengths) with relatively fewer photons in the red range. When excited through heat or incident radiation, molecules emit radiation in discrete wavelengths, as opposed to the previous examples, where the emitted photons have a broad distribution. Different types of excitation result in different types, wavelengths of emission. The relative intensities of the different emission of the molecules can be used to determine the temperature and the density of the ambient gas. For example, bright emission of HCN at

146

88 GHz relative to CO 115 GHz indicates temperatures in a star-forming galaxy around 100 K. This is for example a diagnostic for high temperatures (irrespective of what is causing this high temperature). These molecular transitions can be considered not only as a "thermometer" of the ISM, but they can also give hints on particular mechanisms that allow these transitions to occur. We can think of the emission of these molecules as "long distance detectives" for the ISM.

In this thesis, we study the effect of the absorbed turbulent energy, mechanical energy, on the emission of molecules such as HCN and CO mentioned earlier. We have demonstrated that small amount of turbulence are enough to have a big signature on the emission of molecular species. In particular we have studied the importance of the relative intensities of the emission of HCN, HNC, ^{13}CO and their various transitions in tracing the thermal properties of the ISM. The relative intensities among these chemical species were studied under different conditions where the impact of mechanical heating was tabulated. These tables can be used to quantify the amount of mechanical heating in star-forming galaxies for which observations are available. Moreover, information on the mechanical heating can be analyzed, where a model of possible sources for such turbulent environments can be postulated. This is fascinating and challenging because being far from other galaxies we can derive important information with a limited amount of data.

Publications

1. **M. V. Kazandjian**, I. Pelupessy, R. Meijerink, F. P. Israel, M. J. F. Rosenberg, M. Spaans "Constraining Cloud Parameters Using High Density Gas Tracers in Galaxies", (submitted)

2. **M. V. Kazandjian**, I. Pelupessy, R. Meijerink, F. P. Israel, M. Spaans "CO and ^{13}CO Emission Map Construction for Simulated Galaxies", (submitted)

3. **M. V. Kazandjian**,R. Meijerink,I. Pelupessy, F. P . Israel, M. Spaans "Diagnostics of the Molecular Component of Photon-dominated Regions with Mechanical Heating. II. Line Intensities and Ratios", 2015, *A&A*, 574, A127, 33

4. M. J. F. Rosenberg, **M. Kazandjian**, P. P. van der Werf, F. P. Israel, R. Meijerink, A. Weiss , M. A. Requena-Torres , and R. Gusten "Radiative and Mechanical feedback into the molecular gas of NGC 253", 2014, *A&A*, 564, A125, 12

5. **M. V. Kazandjian**, J. R. Touma, "The Doubling of Stellar Black Hole Nuclei", 2013, *MNRAS*, 430, 1, 2732-2738

6. **M. V. Kazandjian**, R. Meijerink, I. Pelupessy, F. P. Israel, M. Spaans, "Diagnostics of the Molecular Component of PDRs with Mechanical Feedback", 2012, *A&A*, 542, A65, 26

7. J. R. Touma, S. Tremaine, **M. V. Kazandjian**, "Gauss's Method for Secular Dynamics, Softened", 2009, *MNRAS*, 394, 2, 1085-1108

Curriculum Vitae

I was born on a sunny spring day on the 6th of April 1983 in Beirut, Lebanon, where I was raised with my brother in an Armenian and Lebanese community. I attended Armenian schools until I graduated from high school. Being the son of two electronics experts, I grew up around lots of gadgets and machines, where I learned and fed my curiosity about my surroundings.

I spent one year of self-studying physics before joining university in 2001, after which I joined the American University of Beirut as a physics major sophomore student. During my second year, I met Prof. Jihad Touma, my future mentor, with whom I worked as a research assistant on the stellar dynamics of star clusters around super-massive black holes. I graduated with a BSc degree in 2006. I continued working on my undergraduate project for my MSc thesis that I defended on the summer of 2008. The title of my masters thesis was "m=1 instabilities in near Keplerian potentials". From 2008 to 2010, I worked as a research assistant at the American University of Beirut, after which I joined Leiden Observatory for my PhD degree under the supervision of Prof. Frank Israel and Dr. Rowin Meijerink. The topic of my PhD project, presented in this thesis, is "Diagnostics for Mechanical Heating in Star-forming Galaxies". I attended several conferences and meetings on Galactic Dynamics, Radiative transfer, turbulence in the ISM, and high-performance computing in The Netherlands, USA, Germany and Cyprus and I presented part of my work in the 68th Dutch Astronomy Conference in Belgium.

I started working in industry as scientific software engineer as a consultant at Shell Project and Technology in Rijswijk on April 1, 2014, which is currently my daily occupation. But I still work on galactic dynamics and interstellar medium as side projects.

Acknowledgments

I would like to start by acknowledging my girlfriend Carla Maria Coppola for her help and support throughout the challenging, interesting, sometimes boring task of editing and proof-reading most of the thesis. Grazie Carla for being with me in tough periods and making this thesis possible.

This thesis is the culmination of five years of work in Leiden. Leiden Observatory has provided a fruitful and unique scientific environment to improve and deepen my scientific knowledge in Astronomy. I would like to thank Dr. Inti Pelupessy and Prof. Marco Spaans for useful suggestions and guidance throughout the thesis. I would also like to thank all my collaborators for the fascinating problems we solved together in our papers.

I am thankful to thank my colleagues in the observatory: Alessandra, Carl, Heather, Irene, Isabel, Koen, Marco, Nicola, Sascha, Silvia for the memorable moments and enjoyable time in The Netherlands. I would like to thank Francisco for all the cigarettes during the stressful last few months at the observatory; and Emanuele, for all the embarrassing moments in the Kaiser lounge.

For my friends from outside the department: Guilia, Noemi, Manthos, Dionis and Maraijka, JJ, and especially Hadi, Waseem, Daniele, thank you for making Holland feel like my second home.

I would like to thank Prof. Jihad Touma for inspiring ideas and encouragement throughout the years while working on this thesis.

Finally, I dedicate this thesis to my parents, Houda Ziedan and Vatche Kazandjian to whom I owe my love and passion to learning, science, maintaining high standards, and perseverance in trying to achieving perfection.